In-situ lithiation of lithium manganese oxide in a transmission electron microscope

Dissertation

zur Erlangung des mathematisch-naturwissenschaftlichen Doktorgrades

"Doctor rerum naturalium"

der Georg-August-Universität Göttingen

im Promotionsprogramm ProPhys
der Georg-August University School of Science (GAUSS)

vorgelegt von

Torben Erichsen

aus Bremen

Göttingen, 2022

Betreuungsausschuss

Prof. Ph.D. Cynthia A. Volkert, Institut für Materialphysik, Uni Göttingen
.....
(Name, Abteilung/Arbeitsgruppe, Institution)

Prof. Dr. Sven Schneider, Institut für Anorganische Chemie, Uni Göttingen
.....
(Name, Abteilung/Arbeitsgruppe, Institution)

Prof. Dr. Peter E. Blöchl, Angewandte Theoretische Physik, TU Clausthal
.....
(Name, Abteilung/Arbeitsgruppe, Institution)

Mitglieder der Prüfungskommission

Referentin: Prof. Ph.D. Cynthia A. Volkert, Institut für Materialphysik, Uni Göttingen
(Name, Abteilung/Arbeitsgruppe, Institution)

Korreferent: apl. Prof. Dr. Michael Seibt, IV. Physikalisches Institut, Uni Göttingen
(Name, Abteilung/Arbeitsgruppe, Institution)

ggf. 2. Korreferent/in: .....
(Name, Abteilung/Arbeitsgruppe, Institution)

Weitere Mitglieder der Prüfungskommission:

Prof. Dr. Jörg Behler, Institut für Physikalische Chemie, Uni Göttingen
.....
(Name, Abteilung/Arbeitsgruppe, Institution)

Prof. Dr. Christian Jooß, Institut für Materialphysik, Uni Göttingen
.....
(Name, Abteilung/Arbeitsgruppe, Institution)

Prof. Dr. Vasily Moshnyaga, I. Physikalisches Institut, Uni Göttingen
.....
(Name, Abteilung/Arbeitsgruppe, Institution)

Dr, Marcel Risch, Chemische Energie, Helmholtz Zentrum Berlin
.....
(Name, Abteilung/Arbeitsgruppe, Institution)

Tag der mündlichen Prüfung: 22.03.2022

Contents

1. Introduction

Storing electrical energy and making it available at later times as well as transportable, has been a wish since the discovery of electricity. This was possible earliest with simple capacitors like the Leyden jar, but the research in this field made the first leap in 1799 as Alessandro Volta invented "the pile" – the first battery [1, 2]. Sixty years later, in 1859, the first secondary battery, that could reversibly be charged and discharged, was developed by Gaston Plante 1859 – the lead acid battery [3]. These batteries worked well enough for the first electric car in 1832 [4], but demands on batteries were and are much higher. Especially today with uses in electromobility and microelectronics like smartphones, not forget increased stationary storage requirements with the rising amount of fluctuating renewable energy supply.

There are three general ways to improve batteries: To increase the potential between both electrodes, to reduce the mass of the components and to make the electrolyte stable towards the electrodes and voltage to prevent it from being consumed. The first batteries meet all three criteria were the NiMH and lithium-ion battery [5]. The latter of both, though more expensive, has a higher specific energy and was the basis of the 2019 Nobel Prize for chemistry. This is partially due to the higher voltage and the principle of inserting the lithium ions into the cathode without strongly altering the host structure (intercalation), which was first described for a TiS_2-cathode ($< 2.5\,V$ vs. Li/Li+)[1] by Whittingham, et. al. [7] This principle of structure retention upon uptake of lithium was then expanded to 4 V with $LiCoO_2$ and todays other most used materials by Goodenough, et. al. ($Li_x MO_z$ with M being Co, Ni or Mn)[2] significantly increasing the energy density [10]. Due to the principle of intercalation that the electrode stays mostly structurally the same, lithium-ion batteries will generally show cycleability and less hysteresis in comparison to conversion electrode-based ones [11].

The (Ni, Mn, Co)-dominated cathodes first commercialized in the 90s are still very prevalent today. The first two commercial batteries were both based on a coke anode with a $LiCoO_2$ or $LiNiO_2$ cathode, which have a layered structure allowing 2D lithium diffusion [12]. Alternatively there are the manganese-based cathodes of spinel structure that allow 3D diffusion. The search for improvements in energy density and especially

[1] Intercalation is used for anode and cathode, but due to its higher weight the cathode plays a larger role in the specific energy of the whole battery. With research ongoing, anodes are often either carbon, silicon or a mixture with a potential of a few 0.1 eV vs. Li/Li+ [6].

[2] today often a mixture of those with some additional dopants like aluminum [8] or the following discovered olivine $LiFePO_4$ (lower voltage, heavier due to iron) [9]

stability of many charge/discharge cycles has lead to cathode materials with mixtures of many, different cations (e.g. $LiNi_{1/3}Mn_{1/3}Co_{1/3}O_2$) [13,14], but the layered cathodes have inherent problems: First, the layered structure is only stable with a certain amount of lithium in it, so that not all lithium can be used for energy storage. If the battery is charged too much, this can lead to oxygen release in the cathode material leading to fires [14]. Battery systems, that limit the range of lithium cycled, need to be applied to balance all different cells in a battery [15–17]. They aim to prevent local deep (dis-)charge which can nevertheless occur due to differing internal resistances and capacities [18]. Second, both nickel and cobalt are toxic to the environment, undermining their dedication to be used in a more sustainable future. Despite all efforts to use as little Ni or Co as possible and replace them with other cations, newer generation batteries still require a significant amount of them to achieve the layered structure and a high voltage [13]. Third, with more and more use of Ni and Co in high performance applications like the automotive industry, the elements are becoming an increasing cost factor - too high for mass market. Which has lead to developments like Tesla starting to revert to less energy dense, but much more stable and cheaper $LiFePO_4$-cathodes in 2021 [19] and R&D departments trying to lower cobalt contents of layered cathode materials even sacrificing some performance [8].

In contrast, manganese is non-toxic and the 10th most abundant element in earth's crust and the second most common heavy metal only to iron with average of 0.1% of every rock [20]. Manganese-rich cathodes as used in power tools, medical applications and also some electromobility [18]. They are of the cubic spinel structure $Li_xMn_2O_4$, but are less energy-dense for $0 < x \leq 1$ with $148\,\mathrm{mA\,h/g}$ [21]. This is because only 1 Li per 4 oxygen atoms are used as $Li_xMn_2O_4$ undergoes a phase-separating phase transition to a tetragonal structure for $x = 1$, as the Jahn-Teller distortion of the manganese atoms dominates as soon as the valence drops to 3.5 or below. At the same time all Li moves from tetrahedral sites to octahedral sites for $x > 1$. If this region had a well-reversible behavior more than $100\,\mathrm{mA\,h/g}$ specific capacity, were to be gained by using it up to $x = 2$ [22].

Generally, spinel is the most stable crystal structure for most lithium transition metal oxides [22], which also shows through the fact that spinel can often be found on the surfaces and as intergrowth in the layered cathode materials [8]. Spinel could also be the base of a new generation of cathodes as the high-voltage spinel $LiNi_{0.5}Mn_{1.5}O_4$ yields 4.7 V thus increasing specific energy, but at the moment this voltage is too high for the common electrolytes - causing decomposition [23]. This might be no problem when new electrolytes are developed. Cathodes like $LiCoO_2$ also needed new electrolytes in the past [12] and a lot of research has already gone into the development of solid electrolytes for future batteries [24]. Still, dissolution of Mn^{3+} into the electrolyte discovered in 1981 [25]is listed as a major factor hindering better performance of $LiMn_2O_4$ (compare e.g. [26]). According to results by Xia, et. al. from 1997 this accounts for less than 35% of capacity losses [27]. Also, this could be supressed by

e.g. surface coating [28–30] and new electrolytes have since been developed – at least – reducing this further [31]. This is critical as it has been shown, that all non-stable structures, see the delithiated layered surfaces, decay into the stable spinel or an inactive rocksalt structure [32].

All this knowledge of failure mechanisms described so far is mostly based on electrochemical and XRD measurements of whole electrodes. This is summarized generically as either a progressive decay in capacity or increase in internal resistance, electrolyte interactions or material decay [33]. Still, "(...) it has been recognized that mechanical degradation becomes a dominant factor for battery service life during long-term operation." [34] Despite that, there are common rules of thumb: Firstly, every reduction of charging voltage by 0.1 V is said to double the cycle life. Secondly, it costs 10% in capacity to reduce by 70 meV. [35]. It is also common to make conclusions about mechanical failure on the basis of few, ex-situ obtained, large-scale images of the state of an electrode after 100 cycles (compare [33]). Similarly, it is well-accepted that tetragonal $Li_2Mn_2O_4$ will form in $LiMn_2O_4$ under the high-rate conditions (e.g. [21]) needed today, based on ex-situ TEM observations published 1998 [36].

Still the loss mechanisms of $LiMn_2O_4$ are not fully investigated. Therefore, in-situ methods are necessary as concluded in a review by Conder, et. al., because ex-situ samples are mositure sensitive and can relax or alter prior to analysis, especially for metastable states [37]. Especially, there have been no TEM studies on micrometer-size particles – only on $LiMn_2O_4$ nanowires. However, those showed an unexpected intermediate phase and no insights into why the tetragonal phase might lead to capacity fade [38, 39].

In this work, an in-situ TEM setup is used to lithiate the samples, which allows higher spatial resolution than in previous works. This provides insights into the phase transformation and the role of defects. By this we also ensure, that the samples don't change between lithiation and following characterisation. Further on, the fine structure in electron energy loss spectroscopy is used to analyze the interface between cubic and tetragonal phase in $Li_xMn_2O_4$ to gain chemical information like manganese valence and in addition to quantifying elemental composition. For this, commercially available $LiMn_2O_4$ particles of micron size are prepared as thin samples in a way to preserve large dimensions in 2D, which allows for more realistic insights than many other TEM studies performed ex-situ on nanoparticles. This can lead to insights to the following questions: Are there other factors responsible for the capacity decay besides the pure tetragonal transformation? Which influence do defects have on the lithiation behavior? And given the coordinated behavior necessary for the transformation[3]: Are there intermediate steps in the transformation?

[3] change of Li from tetrahedral to octahedral sites, tetragonal deformation and increasing Jahn-Teller effect with decreasing valence

Structure After this introduction, this thesis is structured as follows: The next chapter introduces the state of the art of in-situ experiments, battery and electron energy loss spectroscopy (EELS) basics as well as the current understanding about lithium manganese oxide spinel. Additionally, phase transitions and defects are reviewed as a basis for this work. Chapter 3 describes the sample material and instruments used, the process of sample preparation and the experimental procedure. Chapter 4 shows which methods of EELS are most suitable for analysis of $LiMn_2O_4$ and establishes their reliability. The results regarding microstructural analysis and diffusion behavior are presented in Chapter 5. Possible explanations, implications and their impact are discussed in Chapter 6. The work is summarized in Chapter 7.

2. Basics / Scientific Background

This chapter starts with a basic introduction into batteries. This is followed by a long overview of information regarding $Li_xMn_2O_4$, which also includes related compounds to help with the understanding of $Li_xMn_2O_4$ properties and structure. Some important defect types and tetragonal phase transformations are briefly summarized afterwards. The next section introduces some basic information about electron energy loss spectroscopy, while the last section is dedicated to a summary of notable (in-situ) microscopy experiments that show the realm of the possible.

2.1. Battery basics

The concept behind most lithium based secondary batteries has been very concisely been described in a paper by van der Ven, et. al. [40] to most of the extent needed within this work:
"The Li-battery designs in current use typically consist of a carbon (graphite) based anode and a transition metal oxide intercalation host as cathode. In the charged state, Li ions reside between the graphitic sheets in the anode while the transition metal oxide is Li deficient. Thermodynamically, the Li ions between the graphitic layers would much rather occupy the empty interstitial sites of the transition metal oxide cathode material. However, a spontaneous chemical reaction involving the transfer of Li from the anode to the cathode is prevented in a Li battery due to the presence of the electrolyte, which only allows passage of Li^+ ions (as opposed to neutral Li atoms). The Li^+ can only trickle through the electrolyte if an external circuit through which electrons can travel connects the anode and the cathode. In this way, the resulting electrochemical device converts the change in free energy due to the transfer of Li from the anode to the cathode into electrical work."

This can be extended by using one of the many textbooks available one the topic of batteries/electrochemistry. In this case information from a book by Besenhard is used, if not otherwise indicated. [21] As previously already stated a battery is based on two separate reactions at the two electrodes

negative electrode: $A \longrightarrow A^+ + e^-$

positive electrode: $B^+ + e^- \longrightarrow B$

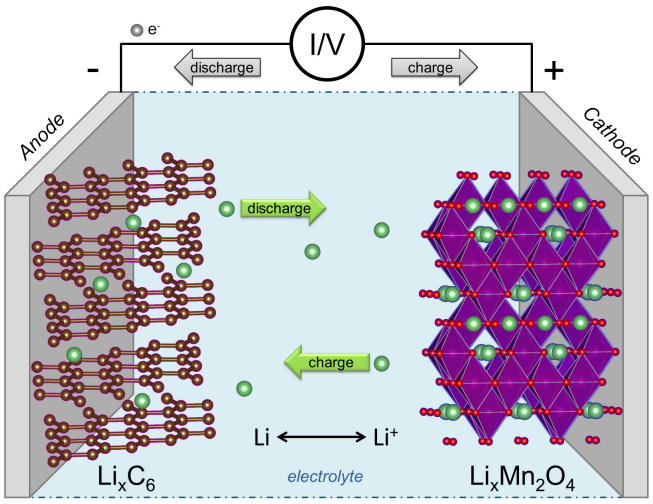

Figure 2.1.: A simple scheme of secondary lithium battery to introduce and clarify the concept. Many technical details and concepts crucial to real batteries are simplified or consciously left out.

that can be broken down to an oxidation and reduction process separated by an (only) ion-conduction electrolyte and therefore require the electron transfer by an external conductor. To give a comparison this organic electrolyte often has a conductivity of $\kappa = 10 \times 10^{-2}$~$10 \times 10^{-1}\, 1/(\Omega\,\mathrm{cm})$, which is comparable to that of seawater. The anode/negative pole is determined as the electrode where the oxidation dominates during discharge.

The potential of a battery can be predicted by comparing the single electrodes potentials in comparison to a reference electrode like the standard hydrogen reference H/H^+ or $\mathrm{Li}/\mathrm{Li}^+ = -3.02\,\mathrm{V}$, in comparison to the hydrogen electrode, which is often used in battery publications and has the lowest overall potential. The ideal voltage of the cell $\Delta\varepsilon_{00}$ can then be calculated by the difference between elements $\Delta\varepsilon_{00} = \Delta E^0(X/X^+)$, which relates to the Gibb's free energy of the full reaction by

$$\Delta G = -\Delta\varepsilon_{00} \cdot zF$$

with the exchanged electrons z and the Faraday constant $F = e \cdot N_A = 1.602 \times 10^{-19}\,\mathrm{C} \cdot 6.023 \times 10^{23}/\mathrm{mol} = 96485\,\mathrm{C}/\mathrm{mol}$.

One of the main ideas behind lithium-ion batteries is making the reaction reversible through charging by applying at least $-\Delta\varepsilon_{00}$ (secondary battery) instead of just using a single-time chemical reaction. This is only possible if both materials allow lithium to be incorporated into the electrode without (large) changes and damage to the structure

- called interacalation[1]. Because both the charge and discharge process as well as the potentials are dependent on dynamical processes another important parameter is the speed of those called the C-rate, the (dis-)charge current divided by the nominal capacity, therefore being the reciprocal value of the time in hours, written as e.g. 2C for a battery charged in 30 min.

The "development of lithium-ion batteries" was awarded the 2019 Nobel Prize for chemistry to John B. Goodenough, M. Stanley Whittingham and Yoshino Akira and involved exploiting above mentioned intercalation into the electrodes leading to the development of the first 4 V battery based on coke and cobalt oxide in 1986, which was introduced into the mass market by Sony in 1991. [42] Since then, manifold transition metal oxides have been tested and used as cathode materials. Those can be mostly classified by their structural type, which also determines the dimensionality of the lithium transport. From the 1D olivine structured $LiFePO_4$, the 2D layered $LiCoO_2$ and the 3D spinel-type $LiMn_2O_4$, which, of course, over time have been modified and improved by additives and substitutes to for example produce the commercially sucessful $LiCoO_2$/$LiNiO_2$-based lithium-manganese-nickel-cobalt-oxides and lithium-nickel-cobalt-aluminum-oxides. A good review of all kinds of different cathode materials, their characteristics and preparation methods was given by Bensalah and Dawood [43].

Obviously, real secondary lithium-ion battery are much more complex composites as they include active material, polymeric binder, conductive additives like carbon black and need to be sufficiently porous for electrolyte penetration. This still leaves out topics like e.g. the electrolyte, the electrolyte interfaces at the electrodes and the seperator. A more technical analysis of all those aspects relevant in lithium-ion batteries can be found in [18].

2.2. $LiMn_2O_4$, other manganese oxides and elementary chemical information

This section will give an overview of $LiMn_2O_4$, but also include an overview of special characteristics of lithium and manganese. Additionally, because not every aspect of $LiMn_2O_4$ has been investigated and understood it will also provide sections that highlight properties of $LiMn_2O_4$ and how these relate to other (battery) materials or how some characteristics can be compared to other alloys for a broader picture of this work. This also explains how experimental results are comparable, relatable and applicable.

[1] compare with the official definition of intercalation by IUPAC: "Reaction, generally reversible, that involves the penetration of a host material by guest species without causing a major structural modification of the host (`https://goldbook.iupac.org/html/I/I03077.html`, i.e. [41])."

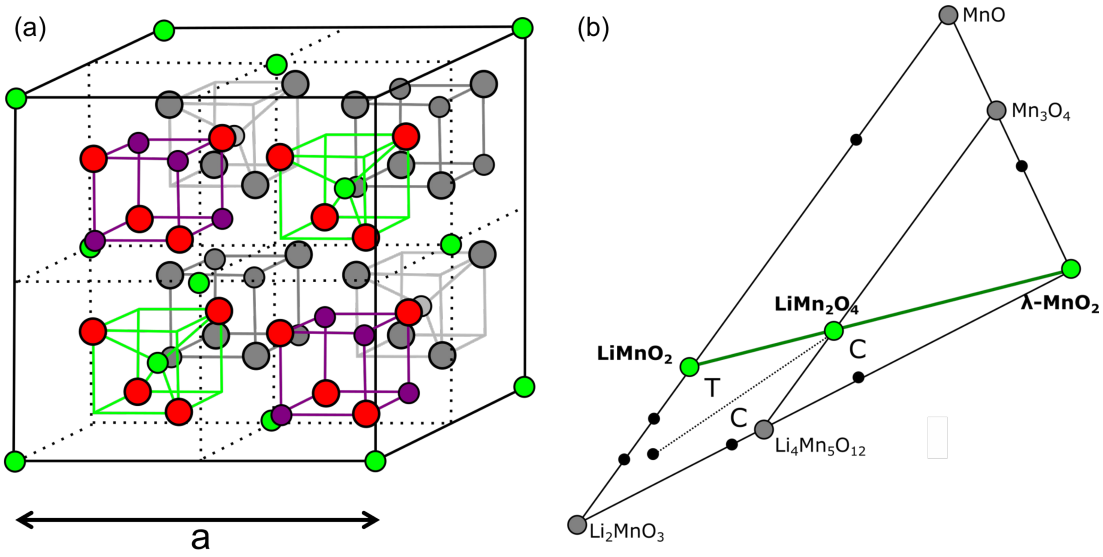

Figure 2.2.: Sketch of the spinel structure of $LiMn_2O_4$ (a) extended and colorized on the basis in [51], which is found in the central part of a ternary phase diagram for battery application materials in (b) (adapted from [52]). The green line shows the phases related to each other purely by de/lithiation.

2.2.1. $Li_xMn_2O_4$

Lithium manganese oxide $Li_xMn_2O_4$ as a battery material is usually used in the structural range of $0 \leq x \leq 1$ and has a nominal capacity of 148 mA h/g of which 140 mA h/g can be realised [27]. This is equivalent to 520 W h/kg within a voltage range of 3.5 – 4.5 V versus Li/Li^+ [44]. As a cathode material $LiMn_2O_4$ has semiconducting characteristics and is antiferromagnetic. It transports current by movement of small polarons with an activation energy for electron hopping of 0.16 – 0.41 eV, due to the Jahn-Teller distortion of Mn^{3+} that accompanies the electron during movement [45–47]. This leads to measured conductivities of up to $\sigma = 5 \times 10^{-4}$ S/m [45, 48, 49], while it is also reported lower 1×10^{-6} 1/Ωcm to 1×10^{-5} 1/Ωcm at 300 K [50].

The spinel form of $LiMn_2O_4$ is one of the central and most common phases within the lithium manganase oxides (comp. Fig. 2.2 (b)). The structure is named after $MgAl_2O_4$ (spinel: AM_2X_4 - $Fd\bar{3}m$ - No. 227) and was first prepared and characterized in the 1980s [25]. The large unit cell is made up of a few simple motifs as shown in Fig. 2.2 (a): The main cubic structure is formed by a close-packed face-centered oxygen lattice (position 32e), that is twice as long as the normal fcc unit cell. Half of the octahedral voids (16d) are filled with managanese, while only the 1/8th of the tetrahedral sites are filled with lithium. Those tetrahedral sites (8a) are different to the others (8b,48f) in sharing

faces only with empty octahedral sites (16c) so that they are farthest away from other lithium or the manganese [53]. If the arrangement of the cubic and tetrahedral motifs in Fig. 2.2 (a) were any different the unit cell would be smaller and contain less than 56 atomes (8 times the chemical formula of $LiMn_2O_4$). The spinel arrangement is often written by marking the tetrahedral and octahedral cations: $(Li)_{tet}[Mn_2]_{oct}O_4$ or even dropping the subscripts to denote the sites just by () and [].
Alternatively, one can think of the structure as alternating layers in (111) where one layer is purely filled with manganese octahedra that build a network of rhombs. The other only has a third of these octahedra at the corner positions of the other layers rhombs and is otherwise host to the lithium in the tetrahedral voids farthest away from the manganese. In this picture, it is also understandable that the different stochiometry of the layers and oxygen that has three bonds with manganese and one with lithium in tetrahedral coordination will not stay exactly in the positions described before but a concerted slight movement takes place on all oxygen positions [54, 55].

Delithiating the basic phase of $LiMn_2O_4$ with a lattice parameter of $a_c = 8.239(3)$ Å at about 4 V (see also Fig. 2.3) versus Li/Li^+ forms another spinel of $Li_\varepsilon Mn_2O_4$ called λ-MnO_2 ($a_c = 8.045(6)$ Å). Those two phases only differ by the tetrahedral 8a site filled or void of lithium [56]. λ-MnO_2 is metastable and can only be formed by this way of delithiation or by removing the tetrahedral cations in acid, [25, 57] since pure manganese dioxide otherwise crystallizes in the rutile structure β-MnO_2 [58]. The small edge in the presented voltage curve gives a hint at a process or intermediate phase for $0 < x < 1$. The consensus is that this is due to some lithium ordering at intermediate lithium content, but without agreement on the conditions, reason and exact nature of the order. According to X-ray diffraction, a lattice parameter of $a_c = 8.142(2)$ Å is present [56]. But next to conforming measurements [59] and DFT calculations [60], other phase separations are [61–64] and complex superstructures [65] are also reported. Some reports claim that the differences are either due to rate effects or deviations in oxygen stochiometry [61, 66]. The main takeaway from this is that due to coulombic and other interactions lithium will often prefer some ordering for further energetic optimisation and this should be true for all phases in the Li-Mn-O phase diagram, even if those effects are only studied in the battery application range, so far.

A different behavior occurs for additional lithiation of $LiMn_2O_4$. Unlike above the symmetry is not preserved and instead a tetragonal phase $Li_2Mn_2O_4$($I4_1/amd$ - No. 141) with $a_T = 5.649(2)$ Å and $c_T = 9.253(5)$ Å is observed. This transformation occurs immediately upon adding any additional lithium [67]. As shown in fig. 2.4, which depicts the crystallographic relationship of the two phases, due to the broken symmetry a smaller unit cell is necessary. The tetragonal a-axes are in $<110>_C$ direction and therefore without distortion should be $a_T = a_C/\sqrt{2}$. On comparison with the previous cubic structure the c-axis expands by 12.3 % and the a-axes shrink by 3 %, which works out to a volume expansion of 5.6 % [56]. As is supposed to be visible in fig. 2.4 the oxygen octahedra coordination stays the same during the transformation. The symmetry and

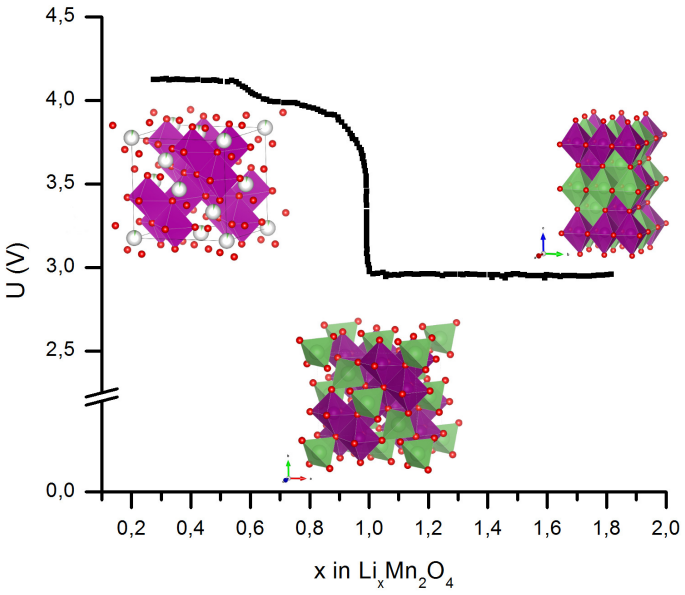

Figure 2.3.: The diagram of open-circuit voltage versus lithium concentration $Li_xMn_2O_4$ (measured in [56]) shows the three known phases of stoichiometries λ-MnO_2, $LiMn_2O_4$ and $Li_2Mn_2O_4$ (from left to right). The structure is fully preserved on delithiation with Li just continously leaving the tetrahedral sites. On lithiation a phase transformation from cubic spinel to a tetragonal structure takes place. The constant voltage in this region also shows that it is a two-phase region. Oxygen red, lithium green, manganese purple.

unit cell change stems from the coordinated behavior of all lithium. As soon as additional lithium was to be added to additional tetrahedral sites those would now not be surrounded only by empty sites, but instead either side sharing with manganese octahedra or short-distance edge-sharing with other lithium. This leads to the coordinated movement of both the additional as well as the already present Li to the octahedrals sites that are now filled. Since the cation to anion ratio is now 1:1 this is often called a (ordered) rocksalt phase of $Li_xMn_2O_4$ [51, 60, 68].

As soon as additional lithium is introduced the local Mn valence drops to 3. At this valence manganese oxide is known to exhibit a Jahn-Teller (JT) distortion (see further explanation later in sec. 2.2.3), while $LiMn_2O_4$ was previously only locally distorted in its MnO_6 octahedra with average valence of 3.5, where the distortions also pointed in differing directions overall averaging out to a cubic unit cell. This leads to a first-order phase transition and the c/a ratio of 1.16 [64]. The two phases $LiMn_2O_4$ and $Li_2Mn_2O_4$

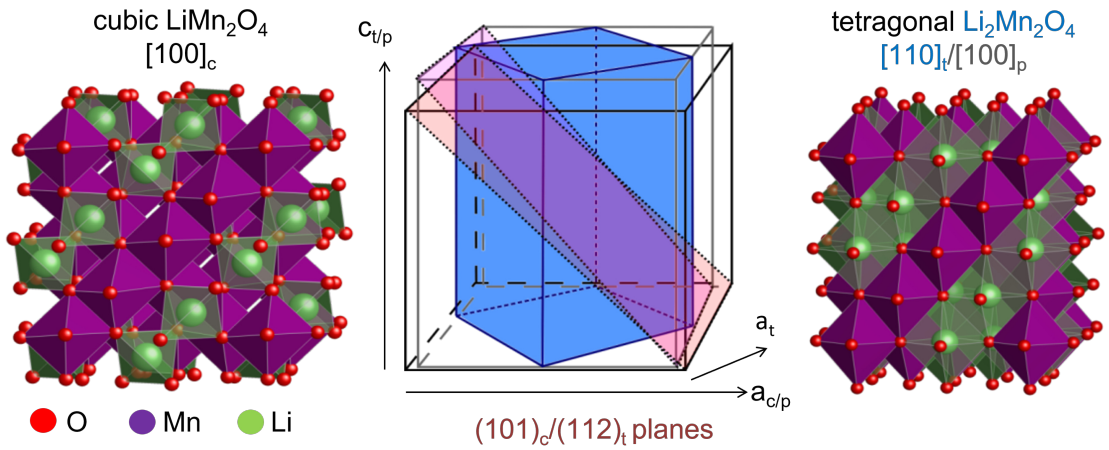

Figure 2.4.: Comparing the two crystal structures of cubic $LiMn_2O_4$ and tetragonal $Li_2Mn_2O_4$ (cut through the center parallel to the image plane for better comparison). Both crystal structures have a differently oriented unit cell, so the relationship between the two structures is outlined in the center. The common oxygen octahedral on the diagonal should be visible. This figure also appeared in [69] (compare fig. 5.6) and is reprinted with permission by the publisher.

demix at the same time due to JT instability to any lowering of the Mn valence below 3.5. This phase separation also shows in the voltage curve in fig. 2.3 as a flat potential of 3.0 V for $x > 1$. According to [67], this strong drop in voltage ($\frac{dG}{dn}$) can be explained mainly by the change in enthalpy $\frac{dH}{dn}$ (no large change in entropy) and is therefore caused by the energy of the octahedral site that additional Li is moving into and at the additional energy required to move the present Li to higher energy octahedral sites.

The common manganese-oxygen structure in both phases also motivates describing the $Li_2Mn_2O_4$ structure by a different, face-centered cell ($F4_1/ddm$No. 141) and a notation that makes for easier comparison and is equivalent to smallest-possible tetragonal unit cell. In this case the direction of all axes stay parallel to the previously cubic ones and are just shrunk or elongated so that the 'hkl' notation of any crystallography is more similar. This will be called the pseudo-cubic notation throughout this work and abbreviated with p in comparison to c,t. Multiplying a_T with $\sqrt{2}$ then yields the lattice parameters for this structure a = 8.0 Å, c = 9.3 Å and directly shows the c/a-ratio often referred to in literature. This kind of notation is encountered in other TEM studies for similar reasons (e.g. [70]).

The width of the phase separating region between $LiMn_2O_4$ and $Li_2Mn_2O_4$ does not fully extend to $x = 2$, but instead ranges to values of $x \approx 1.7$ as visible by the onset of another voltage drop in the open-circuit voltage in many papers including the early

ones of David, Thackerary, et. al. [55, 68] As with the previous discussion of lithium ordering in $Li_xMn_2O_4$ ($x < 1$) there is speculation about the exact arrangement of Li in the voids if $x < 2$. Structural refinement of neutron scattering data shows better agreement if some tetrahedral sites are kept occupied and relaxed towards empty sites, which would allow 40% of the previous tetrahedral to stay occupied [68]. Experimental work and DFT calculations consider all octahedral sites to be occupied [51, 60]. David, et. al. [68] assume that $x \approx 1.7$ is where the addition of Li becomes energetically less favorable due to additional repulsive forces than the transformation of further $LiMn_2O_4$. This additional repulsion of the lithium atoms by each other might also explain that not much lithiation into the tetrahedral voids of the rocksalt structure of $Li_2Mn_2O_4$ is possible, which is reported to be destroyed at $Li_xMn_2O_4$ with $x > 2.25$ [55].

According to DFT calculations, it is the antiferromagnetic ordering of lithium manganates at room temperature that provides their high stability [71]. However, based on changes in this order or charge order and the temperature dependence in the order of the JT distortions transformations in the crystal structure can also occur at low temperatures, leading to tetragonal phases, other monoclinic and orthorhombic phases [45, 72]. Technically, these changes start to occur at 250 K with a transformation to an orthorombic structure (Fddd) where the symmetry of the cubic $LiMn_2O_4$ is broken and the length of the axes changes independently to values in the range of 8.20 – 8.25 Å, which is less than 0.5% from the cubic lattice parameters [73–75]. Only at 65 K is the structure comparably tetragonal ($I4_1/amd$) as measured by XRD and neutron diffraction [75, 76].

Not all material science aspects of especially concerning defects are fully discussed in the current state of the research landscape on $LiMn_2O_4$. Therefore, it will be necessary to draw some conclusions on the basis of comparison to other materials sharing some characteristics with $Li_xMn_2O_4$. These links and key distinctions(!) shall be discussed in the following sections. They become relevant towards the discussion of this work and might be skipped by the reader for now, if desired. One necessary information from the following part: Due to the fact that the samples were later used in the vacuum of a TEM, it is important to mention that for lithium mangenese oxides $LiMn_2O_{4-\delta}$ only very small oxygen deficits of $\delta \leq 0.025$ are obtained upon preparation and only at elevated temperature [77]. In these studies, $LiMn_2O_4$ was also shown to coexist with Li_2MnO_3 and Mn_2O_3 phases when the stoichiometry of the mixture of preparation materials is different. The effects of lithium deficiency are discussed with the other links and distinctions.

2.2.2. Understanding the properties of $LiMn_2O_4$ by comparison...

2.2.2.1. ... with spinels in general

As previously mentioned, the spinel structure has the chemical formula AB_2X_4 and is named after $MgAl_2O_4$ with the characteristic diamond lattice of Mg and Al on half of the

octahedral sites of the oxygen fcc lattice. Despite that the spinel structure is incredibly versatile and forms on the basis of diverse transition metal oxides. Some examples are $Li_{0.5}Al_{2.5}O_4$ and $CoFe_2O_4$ based on oxygen, but also $CdCr_2Se_4$, $CuTi_4S_4$ and other Sulfites, Selenides and Tellurites are possible. The best studied spinel is magnetite Fe_3O_4, though. This diversity is only possible, because of the versatility of spinel that has three parameters to react to those different stochiometries: The relaxation of the anions from the ideal position $u = 3/8 + \delta$, the inversion of the occupation of tetrahedral and octahedral site i and the lattice parameter a. The adaption via the lattice parameter a was already described before in the case of $Li_xMn_2O_4$ $(0 \leq x \leq 1)$ and will show up as a motif in some other cases later. Inversion is common and either seen as perfect inversion in inversion spinels like magnetite $(Fe^{III})[Fe^{II}Fe^{III}]O_4$ or partial inversion like in $MgAl_2O_4$ where $i <= 0.2$ of the tetrahedral sites are filled with the octahedral species [53, 78].

The inversion factor and which cation will occupy a certain void in a transition metal spinel is difficult to predict. Sickafus et. al. describe one of the influences, the valence, the following way: “However, high-valence cations generally possess small ionic radii and, thus, according to Pauling’s first rule, they may be sufficiently undersized to »rattle« in their confining cages between anions. Pauling’s rule states »as cation valence increases, small interstices and small coordination numbers become preferable.«” Other factors and structures are presented online[2], where also the valencies and LFSE (ligand field stabilization energies) are discussed as influencing factors, showing that theoretical calculations are necessary for good predictions. Not really suprising considering that spinel can accomodate valences from (2,3)-spinels ($NiFe_2O_4$) to (6,1)-spinels (WNa_2O_4). But I wasn’t able to find another example of the $Li_xMn_2O_4$ spinels (-,4) for x=0 and (1,3.5) at x=1. Nevertheless, a part of the structural characteristics like the beforementioned layering along the <111> directions are true for all spinels [78].

There are other well-known Li spinels that allow intercalation reactions. Those can help to pin-point effects in $LiMn_2O_4$ and help discussion of the results later. Lithium titatium oxide spinel ($Li_4Ti_5O_{12}$) is occasionally used as an anode material in batteries as it transforms without change of crystal structure all cubicly with therefore high cycleability but with a mid-range voltage of 1.6 V making it neither a very attractive cathode nor anode except for special applications. But despite the homogeneous structure there still is a phase separation to the fully lithiated phase. [79] In contrast, $LiMnTiO_4$-spinel undergoes a $LiMn_2O_4$-like transition ($Fd\bar{3}m \leftrightarrow$ rocksalt $Fm\bar{3}m \leftrightarrow$ tetragonal $I4_1/amd$) but upon charging as the Mn valence is $Li_{1-y}Mn^{3+y}TiO_4$. With a c/a-ratio of 1.08 and $a = 8.34\,\text{Å}$, $c_T = 5.753\,\text{Å}$ it shows a smaller JT effect, but an irreversibility of 30 – 40 % of the material is measured by XRD [80]. This shows by comparison that the tetragonal distortion in $LiMn_2O_4$ is caused the JT effect in manganese and is not a

[2] https://www.adichemistry.com/inorganic/cochem/spinels/spinel-structures.html (accessed 2019-10-17)

characteristic of the spinel rocksalt structure.

2.2.2.2. ... with other pure manganese oxides

It makes sense to highlight a few key structural characteristics and phases of manganese oxides, to better understand the influence those have on the behavior of $LiMn_2O_4$. On global average every rock contains 0.1% mangananese as the second most abundant heavy metal after iron. It thus comes as no suprise that there are more than 30 different Mn minerals [20, 81]. As Post summarizes it in his comprehensive review on most manganese oxides [81] all their structures and consequently their powder diffactions are very similar, since they are based on the same MnO_6 octahedra with manganese valences of two to four. The difference lies in how those assemble with changes in manganese-oxygen ratio with the most common motifs: edge, face or corner sharing octahedra. One should be aware that many of the basic manganese structures are based on edge-sharing octahedra or face sharing chains of octahedra that therefore form tunnel-like strucutures, e.g. Pyrolisite (β-MnO2) rutile structure with single octahedra, Ramsdellite (MnO2) with double chains, Nsutite (γ-MnO2) an intergrowth phases of both Pyrolusite and Ramsdellite as well as large tunnel-structure hollandite were motif-wise the single-octahedra in rutile structure are replaced by face-sharing octahedra. But those structures are of less significance as they are much less closely packed than $LiMn_2O_4$ and one thus wouldn't expect a transformation into this direction or intergrowth of this kind. Furthermore, they are not particularly stable intercalation compounds and are rather used in primary batteries [8,81]. The same reasoning applies for the many layered variants of manganese oxides, but they also all either depend on water or additional elements for stablization [81] and shouldn't be present in $LiMn_2O_4$.

α-Hausmannite Mn_3O_4 with its tetragonally distorted spinel structure ($I4_1/amd$, $a = b = 8.14\text{Å}$, $c = 9.42\text{Å}$) [58] is the most insightful and likely pure manganate to be encountered in this work and despite its tetragonal distortion it has one third of the manganese - the Mn(II) - residing in the tetrahedral sites keeping its uninverted spinel arrangement in contrast to Fe_3O_4 [81]. The same is true for γ-Mn_2O_3 that is also a tetragonally distorted spinel [54], in which case it probably helps to read it as $Mn_{2.67}O_4$ to understand that it has some vacancies in comparison to a fully occupied spinel structure like Mn_3O_4.

As both of the structures occur naturally they need to be kept in mind as results of off-stochiometry in the samples or as a result of oxygen loss, since they are higher than 1:2 manganese-to-oxygen ratio. But as Post states in his review of manganese oxides the "Mn-O bond distances (...) can provide insights into the Mn valence state" [81] and with this correlation in combination with other techniques off-stochiometries causing valence changes in Mn are well-characterisable in the TEM.

2.2.2.3. ... with other compositions and their effects

Multiple battery material used in commercial secondary lithium batteries like the early utilized $LiCoO_2$ are layered in their structure [82]. They also include the motif of arranged transition metal MO_6 octahedra. Other than the alternating 3:1 ratio of Mn octahedra in the {111} layer of the spinel, here the lithium is only incorporated into the otherwise emtpy layers. This is one reason why other decay mechanism like e.g. cation diffusion into these layers and therefore cation diffusion mechanisms are much more discussed. Plus, other factor like extreme discharges can play a role that are less(!) of a problem for spinel as fully emptied layers can become stable and lead to rearrangement in the structures [14]. In many cases when layered materials leave thermodynamic stability they can form spinel (for instance at the end of discharge or at the surface) [14] showing that spinel is the more stable crystal structure at many given stochiometries. So some prominent effects/defects discussed in battery research are related to the layered structure and not transferable to $Li_xMn_2O_4$ even when the stochiometries sound comparable. Examples can be layered $LiNi_{0.5}Mn_{0.5}O_2$ or layered $LNi_xMn_xCo_xO_2$ with $x = 1/3$. Due to different relaxations in the otherwise also close-packed oxygen lattice the unit cell in those cases is monoclinic (C2/m) [83]. Layered, monoclinic $LiMnO_2$ for example can only be synthesized on the basis of $NaMnO_2$ by substitution [84]. The stable layered phase of the layered lithium-manganates is Li_2MnO_3, but written differently $Li(Li_{1/3}Mn_{2/3})O_2$ all octahedra are filled (cation:anion = 1:1) and it is already at a Mn valence of 4, making it chemically totally inactive [32].

Due to the higher thermodynamic stability of spinel this structure is also used with other stochiometries. E.g. Nickel-based spinel can also be synthesized, but more than one type of cation is more common. With nickel operating at a voltage of 4.7 V $Li[Mn_{1.5}Ni_{0.5}]O_4$ is often deemed the “high-voltage spinel” and since it operates the two redox pairs $Ni^{3+/4+}$ und $Ni^{2+/3+}$ it also keeps manganese from Jahn-Teller distortion (compare the good review by Li, et. al. [34]). This strategy can in general be applied by mixing in any cation that is more active than Mn [32]. The details of other substitutions like Al, etc. can be seen in [85]. These substitutions all aim at preventing a manganese valence of 3 thereby preventing tetragonal distortion.
Another strategy for suppressing the onset of the JT effect is lithium substitution of manganese in $Li_xMn_2O_4$. The most common approach is stable lithium superstoichiometry in spinel, $Li_{1+\alpha}Mn_{2-\alpha}O_4$, to lower the manganese valence, which could postpone the onset of JT distortion [67]. The substitution will lead to lithium in octahedral sites of the spinel and works up to $\alpha = 1/3$ [86]. For further information on most details of lithium manganese oxides the review by Thackeray is the best starting point [22].

To summarize, these effects play a very important role in real application batteries to tweak the behavior of the cathode material and suppress unwanted structural transitions, but they come at the trade-off of either lowering some parts of the discharge potential, the amount of active lithium per unit cell or come at the cost of expensive

substitutional cations. For pure lithium manganese oxides this is equivalently true as most manganese dioxides can take up lithium until rocksalt stochiometry is reached ($x_{Li} + x_{Mn} = x_O$) [22]. This reduces the region of stochiometries of interest to phases between the spinel line of Mn_3O_4 to $Li_4Mn_5O_{12}/Li_{1+0.33}Mn_{2-0.33}O_4$ and the rocksalt line of MnO and Li_2MnO_3.

2.2.2.4. ... with oxygen deficient $LiMn_2O_{4-\delta}$

The sensitivity of $LiMn_2O_4$ to oxygen loss that plays a large role in many manganates needs to be looked at as it is later used inside the vacuum of a TEM. Multiple groups have investigated the oxygen deficiency δ in $LiMn_2O_{4-\delta}$, which occurs upon calcination of $LiMn_2O_4$ in atmosphere during the preparation process at onset temperatures in the range of 750 – 800 K and is visible in an increase of the stochiometric lattice parameter of $a = 8.236$ Å [87,88]. The reported values for the maximum possible deficiency vary with values up to $\delta = 0.2$, which in turn leads to a Mn valence of $3.5 - \delta$, which increases the amount of Jahn-Teller-active manganese atoms and creates tetragonal distortion [64, 89]. At deficiencies above the threshhold a decay of the sample material occurs into all kinds of phases mostly $LiMnO_2$ and Mn_3O_4, though, while at values below 0.07 the material remains cubic [87, 89]. A possible explanation is that the deficiency doesn't cause oxygen vacancies, but rather metal interstitials[3], since they have a lower formation energy [90]. This kind of compensation of missing oxygen would then also explain the general tendency for the mild c/a distortions (< 1.07) in comparision to a full $Li_2Mn_2O_4$ transformation [77, 86].

Oxygen deficiency can lead to all kinds of effects degrading the long-term cycling behavior of $LiMn_2O_4$, but only shows minute effects on the lattice parameter for small δs and Li deviations, that were in detail characterized and summarized in [66]. Notably, in Li-rich $Li_{1+\alpha}Mn_{2-\alpha}O_4$ with $\alpha = 0.07$ higher overall oxygen deficiencies of $\delta \geq 0.13$ can be prepared, however deliberate annealing in Ar atmosphere. TEM characterization showed tetragonal regions in the particles after preparation, some even with lamellar twinning, and c/a ratios of up to 1.16. But no local chemical analysis was performed on those regions and the XRD spectra of the samples remained cubic to a large part and also showed some decay through the formation of Li_2MnO_3 peaks [70]. This hints at the fact that the sample is not stochiometrically uniform and that the effects are connected solely to the bulk values of α and δ.

To sum up the tetragonality caused by stochiometric deviations close to $LiMn_2O_4$ can be distinguished from the effect caused by $Li_2Mn_2O_4$ transformation due to its more continous nature and lesser magnitude. But based on reports by Hao, et. al. any oxygen deficiency could be removed by annealing 500 °C for 4h [91] and is therefore fixable if of significant concern.

[3] Mn^{II}, which don't create a distortion

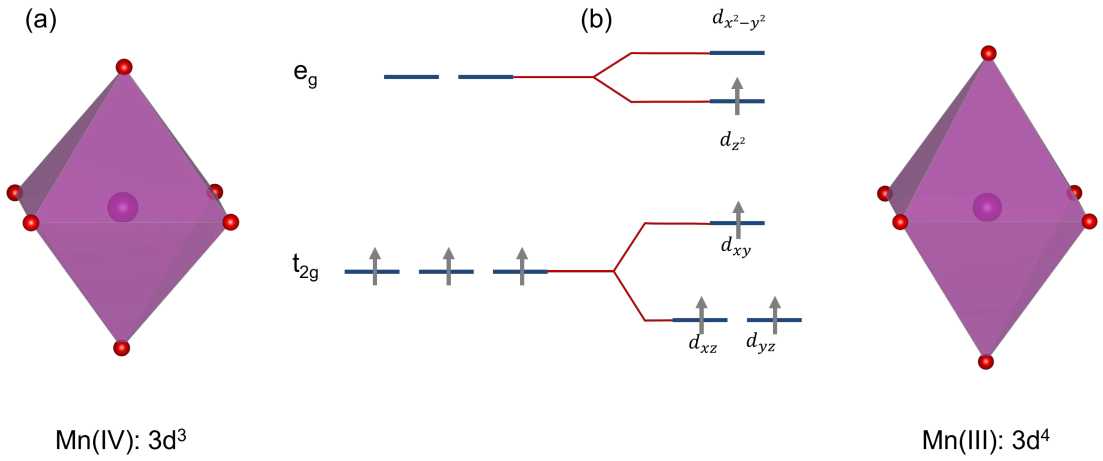

Figure 2.5.: Scheme of the energy levels of the octahedral 3d orbitals of Mn(III) (a) and Mn (IV) (b). The elongation of the octahedra by 16% is shown to scale.

2.2.3. Manganese and the Jahn-Teller effect

Manganese's electronic structure will be shortly reviewed here, because it is a determining factor for the trainsitions investigated within this work:

Manganese is a 3d transition metal and thus has five orbitals in the d-shell ($2l+1=5$ with $l=2$). The orbital configuration corresponds to [Ar]$4s^2 3d^5$, which allows a variety of valence states. Among these, the most abundant are Mn(II), Mn(III) and Mn(IV) [92]. But manganese is known to go up to oxidation states of Mn(VII) [93]. In all structures of the relevant battery materials the transition metal oxides the manganese atoms are mainly octahedrally coordinated. A slightly distorted MnO_6 is therefore also the basic configuration of Mn, in which the 5 d orbitals are split by the crystal field into 2 e_g orbitals (pointing towards the anions) and 3 t_{2g} orbitals (pointing between the anions) [32].

Jahn and Teller first proposed in 1937 that "all degenerate electronic states of nonlinear molecules are unstable" [94]. Nie, et. al. summarized the consequences of this nicely, so that I will closely stick to their summary: Due to the degeneracy the system is unstable and will form a system of lower symmetry and energy without degeneracy. In the ocatahedral field environment the five 3d orbitals are already split into the triplet (t_{2g}) and doublet (e_g). The JT effect or JT distortion often occurs, when e_g is occupied by an odd amount of electrons. In case of Mn(III), the octahedra can now distort in two possible ways by either lengthening the bonds along the z-axis (d_{z^2}) while shortening the xy-plane bonds or the other way around ($d_{x^2-y^2}$). Both can lower the overall energy [95]. For $Li_2Mn_2O_4$ with all states of Mn(III) the additional electron in the d_{z^2} of Mn

causes a strong repulsion p_z of O and pushes the oxygen anion away in z-direction (or now c-direction crystallographically) [96]. The case of lengthening in z-direction is sketched in fig. 2.5. In case of battery materials both Mn(III) and Ni(III) have singe electrons in the e_g and are therefore susceptible to JT-distortion with the energy of the occupied level being lower and the unoccupied raised [32]. The differential energy of the e_g electron for $Li_2Mn_2O_4$ with the involved transformation is thus what causes the abrupt decline in battery cell potential [96].

2.2.4. Lithium

Lithium is the first element of the alkaline metals and thus highly reactive. Because of its light weight it is designated for the use in batteries requiring high charge/power densities.[4] It can be stored e.g. in vacuum, inert atmosphere or pure hydrocarbons to protect it from oxidizing. If lithium is exposed to the atmopsphere, it reacts to form lithium nitride or hydroxide (via lithium oxide if moisture is present) [97]. The reaction of lithium with atmposphere can be checked directly by its color as it is shiny, metallic in its pure initial state. Li_3N can still easily donate Li and looks black in its amorphous state, expected in our case, but can turn red when annealed at higher temperature [98]. This is probably why it's sometimes also reported as brown or violett. The fast reaction kinetics are reported for the oxidation, so that the first reaction layer will always be Li_2O, in presence of oxygen [99]. This will dull the metallic shine of the lithium and will turn into a blueish white when moisture promotes the reaction to LiOH [97].

Regarding our experiments the exact nature of reaction products on the surface can't be determined. We hope to supress any reaction, though. The reaction wouldn't be a problem, though, as Li_3N is one of the best ionic conductors with $\sigma = 1.2 \times 10^{-3}\,\mathrm{S/cm}$, $1 \times 10^{-5}\,\mathrm{S/cm}$ and $6 \times 10^{-4}\,\mathrm{S/cm}$ (depending on the crystal direction [100]) with many other similar observations on this topic [101–104]. At the same time the electronic conductivity is low (LiN_3: $10 \times 10^{-12}/(\Omega\,\mathrm{cm})$ [105]) making it a good solid electrolyte. Reports on ionic conductivity of Li_2O and LiOH are more sparse with reported values in the range of 1.7×10^{-9} – $1 \times 10^{-13}\,1/(\Omega\,\mathrm{cm})$ (calculated for 300 K based on [106]) and other consistent reports with the electric conductivity presumed to be bad, since di-lithium oxide in anti-fluorite structure is an ionic compound [107, 108]. This would make lithium itself a good electric conductor as a pure metal.

2.2.5. Diffusion

During normal battery operations the transfer across the solid-electrolyte interface is the limiting factor for the kinetics, [109] so that diffusion in the cathode isn't noticed as

[4] M=6.941 g/mol/ $\rho = 0.53\,\mathrm{g/cm^3}$ with the highest standard potential of −3.04 V SHE and a specific charge density of 3.860 Ah/kg (F/M).

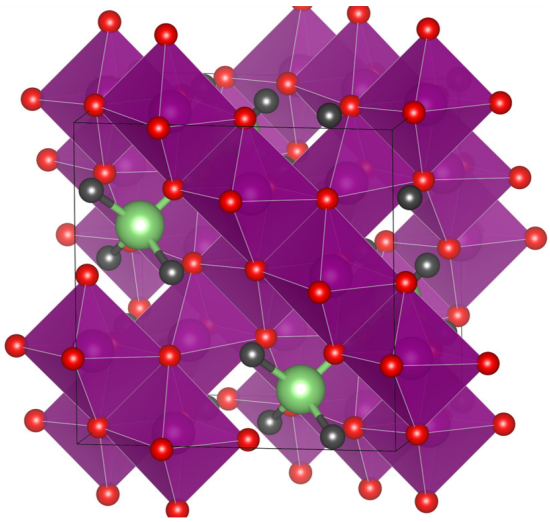

Figure 2.6.: $LiMn_2O_4$ structure showing the diffusional pathway by indicating the octahedral voids (grey) next to the filled tetrahedral positions, which are the connection to other tetrahedral sites. The orientation is visible by the cube of the unit cell.

a bottleneck.[5] In spinel based materials this is especially true, since they have a three-dimensional system of pathways for lithium movement. This distinguishes them from the layered-materials like e.g. $LiCoO_2$ (2D) and tunnel based systems like olivines e.g. $LiFePO_4$ (1D). This is important to keep in mind as diffusion has two governing parameters: the possible pathways (dimensionality) and the activation energies. The diffusion in $Li_xMn_2O_4$ spinel and rocksalt play an important role in other battery materials as they often form on the surface of other intercalation compounds. [32]

Diffusion in $Li_xMn_2O_4$with $x < 1$ occurs via a diamond network of the initial tetrahedral site a neighboring, empty octahedral site and the final tetrahedral site via a single-vacancy mechanism [40]. Fig. 2.6 visualizes the three-dimensional diffusion by showing the spinel structure highlighting the green Li atoms in tetrahedral sites additionally indicating the four neighboring octahedral sites in grey. This relatively simple pathway is much further investigated literature, which has shown multiple parameters influencing the diffusion behavior. For $Li_2Mn_2O_4$ the pathway stays the same as the Mn-O structure is unchanged apart from the tetragonal distortion. The lithum only resides in the octahedral vacancies now and moves the network created by the connected tetrahedral sites.

In the spinel region of $Li_\epsilon Mn_2O_4$ to $LiMn_2O_4$ a multitude of influences are discussed.

[5] These bottlenecks can and are overcome by changing electrode characteristics like particle size, electrode thickness, porosity and so on, that come with other trade-offs.

The influence of the intermediate phases and the corresponding lithium orders are supposed to be a key factor [22], but as there is still no consensus about the intermediate lithium-ordered phases in this region, they won't be discussed in detail here. A possible mechanism behind the influence of lithium order one diffusion can be understood by imagining how lithium order will locally change the available diffusion paths. The local lithium concentration is correlated to the valence of the sourrounding manganese atoms. Ouyang, et. al. calculated that the migration barrier for lithium diffusion is lower in the vincinity of Mn^{4+} in comparison to Mn^{3+}, which predicts better diffusion at lower lithium contents. This is due to the fact that the Jahn-Teller polarons in Mn^{3+} are limited in their motion, making the barrier for lithium diffusion near valences of three higher [110, 111].

The influence of cations neighboring on the diffusion path has been calculated on differently doped $LiM_{0.5}Mn_{1.5}O_4$ spinels and summarized to have a large effect as the diffusion barrier for two 8a sites through 16c can thereby vary in the range of 200 – 550 meV [112]. Since, the diffusion through this octahedral 16c site is equivalent to the passing through the central hole of a ring of six manganese octahedra in the {111} plane many other theoretical calculations have been performed on differing configurations. E.g. replacing a single Mn atom in this ring by Co leads to the diffusion barrier dropping from 0.4 eV to 0.2 eV (DFT: GGA+U), [113] allowing to estimate the magnitude of the local valence without including changes in local Li concentration or Jahn-Teller distortion. The same six cation ring has also been used to calculate the influence of manganese valence with results showing that Mn^{4+} (less lithium) lowers the diffusion barrier. The diffusion barrier for three MnId/MnIv each is the highest, though, being slightly higher than the ones of one and two MnId] in the ring. The parameters of influence discussed are manifold as a combination of electrostatic effects in form of positive charge localization, the change in Mn-O bondlength and as a consequence the change of the Li 16c vacancy size [114]. The local effect of Mn-O bond length shorting due to a higher O 2p hybridization on higher Mn^{3+} count and an increasing vacancy site might also play a role in the diffusion of $Li_2Mn_2O_4$. Moreover, high internal strains are given as a possible reason for a mixture of both valencies leads to the highest diffusion barrier and high stresses are to be expected at least at the interface of the lithiation.

As described earlier in the $LiMn_2O_4$-$Li_2Mn_2O_4$ spinel rocksalt region the diffusion still occurs on the same network, but Li now resides in the octahedral sites and moves through the tetrahedral site, with the energy levels of the sites obviously changed due to the phase transition. The diffusion in transition metal rocksalt has been theoretically well described by works of Ceder et. al. [115, 116]: Diffusion in rocksalt strongly depends on the cation order as the spinel version has a perfect 3d network of diffusion paths and any deviation from this order reduces the amount of low-barrier pathways reducing diffusion through worse percolation as investigated by Monte-Carlo methods. This also includes considerations of the different configurations of cations sourrounding the tetrahedral vacancies Li passes through. Either neighbored by two other Li or two

cations with first both having a barrier of approximately 300 meV vs. 600 meV without much dependence on the type of transition metal oxide. There also tetrahedral sites completes encapsulated by cations that therefore cannot participate in the transport. This group of Ceder laid out nicely how this interaction leeds to different content z of necessary Li in the rocksalt $Li_zMn_{2-z}O_4$ to make diffusion possible with a percolation network based on just 0-TM diffusion or the more costly 2-TM vacancy. The spinel structure would still allow diffusion with a lithium content of $z = 0.542$, almost half the stochiometric amount, reaching pure 0-TM diffusion at 0.77, whereas disordered rocksalts even need $z > 1$. These results compare well with summarized results in a review by Radin, et. al. describing Diffusion for x>1 as more complex, sluggish in disordererd rocksalts but "relatively facile" in cases of Li-excess. Most importantly they expect the Li diffusion coefficient to "drop drastically with increasing Li content" towards two as the amount of vacancies for transport decreases. This allows the conclusion that $Li_xMn_2O_4$ is pretty insusceptible to low to medium amounts of disorder in the structure as the connectivity of the network is high as long as the lithium content is not nearing $x = 2$. So any kind of point defect shouldn't play a major role in the lithiation kinetics.

The role of planar defects on the diffusion of lithium has only more gotten attention lately. Moriwake, et. al. used STEM observations of low-energy twin boundaries in thin films of $LiCoO_2$ to calculate that the chemical potential near the twist boundaries was decrecreased. They also found that the activation energy for migration along the interface was 0.2 eV lower than for the migration across the boundary and concluded that grain boundaries must have a detrimental effect in all-solid-state lithium-ion batteries [117]. The preferental transport of lithium along planar defects was also observed by in-situ TEM lithiation of SnO_2 nanowires, where the presence of growth twins along the center lead to the preferred transport of lithium along the center. DFT calculations confirmed lithium concetration there energetically favorable and lead the authors to suggest controlled microstructure engineering to enhance and steer lithium transport [118]. But grain boundaries can also lead to a hindered conductivity in all directions as in the case of Li-rich anti-perovskite Li_3OCl where four types of low energy grain boundaries ($\Sigma3(111)$, $\Sigma3(112)$, $\Sigma5(210)$ and $\Sigma5(310)$) in most cases lead to additional energy of > 0.15 eV being required for activation and one magnitude lower lithium conductivities at 500 K.

Since those effects can't be taken into account for measurement of diffusion coefficients the experimental values span a large range from 10×10^{-13} – 10×10^{-8} cm^2/s at room temperature [119–121]. Where more detailed studies with knowledge of the microstructure showed PLD produced thin films to be on the lower end (10×10^{-11} – 10×10^{-12} cm^2/s decreasing with decreasing Li content) [122] as well as for electrodeposited and sintered thin films with 50 nm grain size (10×10^{-11} – 10×10^{-9} cm^2/s [123] and the Li diffusion coefficient significantly dropping for thick electrodes (10×10^{-11} – 10×10^{-8} cm^2/s for 304 – 112 μm electrode thicknesses) [124]. It can also be experimentally shown to depend on the stochiometry and was determined to be in the range

of 1×10^{-13} – $1 \times 10^{-10}\,\mathrm{cm}^2/\mathrm{s}$ for the pure spinel in large particles [125]. The upper limit can be expected to be $< 1 \times 10^{-8}\,\mathrm{cm}^2/\mathrm{s}$ as this is the self-diffusion coeffictient for Li^+ estimated from neutron scattering at 400 K in $LiMn_2O_4$ and $Li_{1.1}Mn_{1.9}O_4$ [126].

To put those numbers into perspective simulated surface self diffusion energies on different surfaces from 0.14 – 0.41 eV [127] and a non-aequous $LiPF_6$-based battery electrolyte has a diffusion coefficient of 10×10^{-6} – $10 \times 10^{-5}\,\mathrm{cm}^2/\mathrm{s}$ [124]. This is close to reported surface diffusion coefficients of Li on (001) tungsten (1×10^{-7} – $1 \times 10^{-5}\,\mathrm{cm}^2/\mathrm{s}$ at 300 K) [128] and on graphite ($5 \times 10^{-6}\,\mathrm{cm}^2/\mathrm{s}$) with an activation energy of 0.16(2) eV [129].

2.3. Simple, multidimensional defects in crystals

This section will give a quick summary of defects that can be expected for $Li_xMn_2O_4$ and can be investigated by the methods of TEM used in this work. This will leave out any point defects, e.g. vacancies and interstitial atoms as well as cation disorder in $Li_xMn_2O_4$, as their investigation exceeds the possibilities of this in-situ focused work. Their occurence´is to be expected, though, as they are the common means of diffusion and "are present as part of a structure in thermal equilibrium" [130]. Instead, types of defects more common for spinels are going to be introduced on a basic, textbook level[6] and supplemented by specific information regarding spinels or $Li_xMn_2O_4$. As common dislocations occur in any materials the focus will lie on *antiphase boundaries, stacking faults and twins*.

2.3.1. Antiphase boundaries (APB)

APBs can only be formed in compounds that consist of a sublattice: In the case of $LiMn_2O_4$ this is the fcc oxygen lattice that is filled by two different motifs of manganese ocatehedra and lithium tetrahedra. Alternatively this can be understood visually by going back to fig. 2.4 (a), where the spinel unit cell was sketched as a large cube made up of eight smaller cubes of two different motifs arranged in a way that motif A would only share faces with motif B and vice versa. Switching motif A by B and B by A in a region of the sample would result in what is an APB. This is illustrated in fig. 2.7.

APBs can occur when a lattice exits in such a way that two generally equivalent sites exist in which two different atoms can order into different kinds of sublattices. In spinel (AB_2O_4) this is the case, as the oxygen forms a fcc lattice that has generally equivalent octahedral voids, but once B is positioned in the lattice the characteristic rows of B determine the tetrahedral voids for A, though B could have initially also taken the octahedral voids in the A rows.

[6] The general information on those defects can be taken from any good textbook on material science. In this case the book by Cahn and Haasen [130] was used.

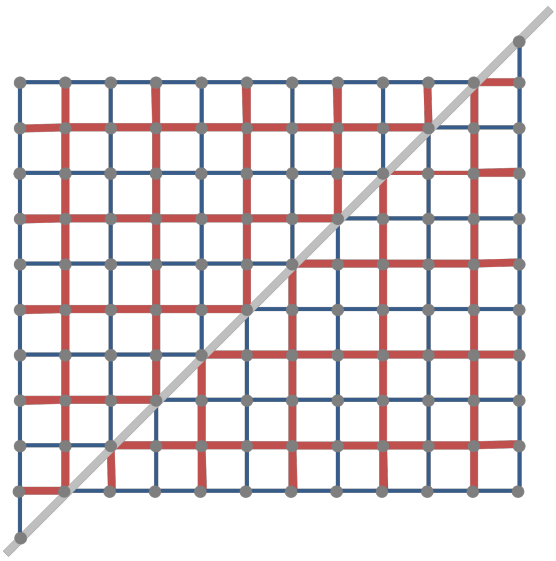

Figure 2.7.: Sketch to illustrate the nature of an antiphase boundary. The two domains of an antiphase boundary share the same basic structure (gray points) but the sub lattice occupation represented as blue and red lines is switched.

The APB can form either when different domains grow into each other upon heterogeneous nucleation or also by mechanical deformation. This is, since APB are *special cases of stacking faults* in which the burger's vector $\vec{b}$ of the stacking fault is a displacement vector $\vec{u}$ that goes from one sublattice to the other. In the case where $\vec{u}$ lies in the APBs interface, which is always but not exclusively the case for mechanical deformation, the interface energy is relatively low. This is deeemed a type I antiphase boundary.

APBs are expected for spinel [131], but contrary to the claim in the cited paper they should also be able to persist in the further lithiated $Li_2Mn_2O_4$ as the manganese structure persists and thus two different octahedral sites of Li and Mn. An interchange of those two species would lead to an antiphase boundary. This also relates to the most well-known example of rocksalt NaCl, which is made up of two identical lattices of Na and Cl (in this case fcc) that are shifted by half a unit cell to form the full structure (Halite structure).

2.3.2. Stacking faults

The principle of stacking faults is most easily explained for closed packed structures like the fcc (or hcp) structure. The fcc structure consist of a certain alternating arrangement of the close-packed {111} planes as illustrated in fig. 2.8. Each close-packed layer has two possible positions for the next layer indicated in dark gray - thus giving a total of

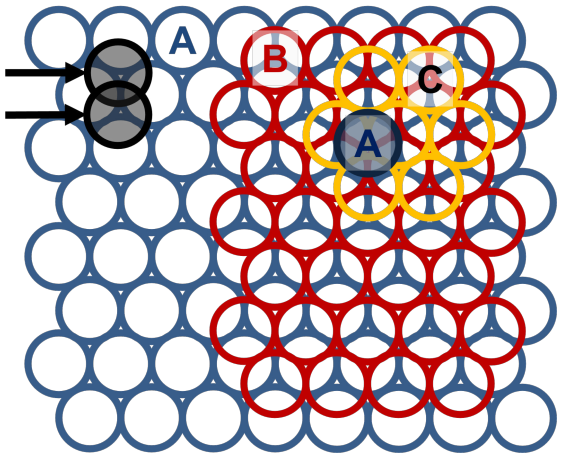

Figure 2.8.: Close atomic packing along a (111) plane in a simple fcc structure. Layer A (blue) has two possible positions for the next layer indicated in dark gray / the basis for the layers B (red) and C (yellow). The fcc structure consists of repeated layers of ABC.

three different positions A, B and C. Repeating the motif of ABC many times gives the fcc structural arangement.

Changing the stacking order, i.e. moving a layer to the second local energy minimum in a close-packed {111} plane, is not a full lattice invariant translation. Otherwise, it would not be noticeable as a fault in the stacking order, but instead is achieved by dislocations that are shorter than one full Burger's vector – *partial dislocations*[7]. As any other dislocation, partial dislocations can be visualized by the scheme of an introduced or removed half-plane. This is sketched in fig. 2.9 (a,b). There, two different kinds of stacking faults are shown on the left side of the according lattice, whereas the right side of the simple crystal is left unchanged. The color of the layers is supposed to guide the eye and make the differences more distuingishable. One can see that the originally undisturbed stacking sequence on -ABCABCABC- is transformed to -ABCA|CABCA- in the case of the removal of a half-plane while the insertion of a plane leads to -ABC|B|ABCABC- with the vertical lines indicating positions in the stacking sequence where the stacking direction is changed in comparison to the unchanged side. In reality and on a large scale, both sides distort to accommodate the defect. It is thus impossible to assign a removed/inserted half-plane[8], but one can count the number of

[7] In the case of a simple one atom fcc lattice this would be any type of $a/2<110>$ displacement that belongs to a suitable $\bar{1}11$ plane and yields a full translation, but can be split up into two partial dislocations, e.g. $a/6[211]$ and $a/6[12\bar{1}]$. Splitting a full dislocation into two *Shockley partial* dislocations is one way stacking faults are created under mechanical deformation.

[8] Note: a removed plane is also equivalent to two inserted ones.

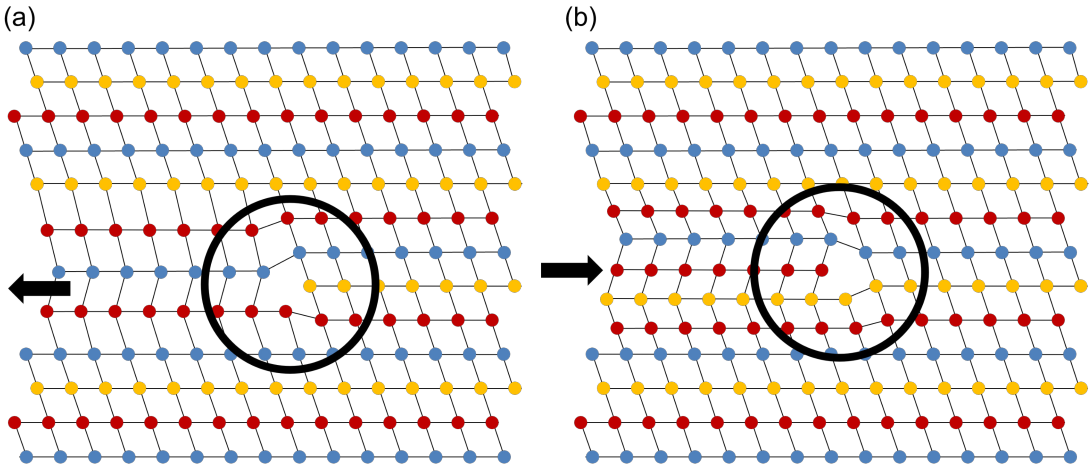

Figure 2.9.: Sketch of two types of stacking faults in 2D, where a fault is introduced by both the removal (a) and introduction (b) of a half-plane. This locally changes the stacking sequence (and bond direction), because the associated dislocations only yield no full lattice invatiant translation.

stacking changes: one stacking change is named an *intrinsic SF* and two an *extrinsic SF* ($\equiv$ example 1 / example 2).

For naturally occuring spinels the situation is a more complex, as spinel has a more complex structure than a one-atomic fcc lattice. Stacking faults in different spinels are observed both on {110} and {111} planes where the nature of the plane depends among other things on off-stoichiometry, the kind of cations and how the SFs were formed, i.e. during nucleation or mechanically. [132, 133] In case of SFs on a {111} plane the dislocations are $a/12$<112>, which is the Shockley partial dislocation of the anion lattice. [132]

2.3.3. Twinning

Another type of defect that is common both for spinels and during tetragonal deformations is twinning. Because Parsons' summary of twins is very concise it is a very good starting point:

> "A twinned crystal is an aggregate in which different domains are joined together according to a specific symmetry operation: the twin law. The diffraction patterns derived from different domains are rotated, reflected or inverted with respect to each other, depending on the nature of the relationship between the different domains, and weighted according to the quantity

> of a particular domain present in the crystal. The diffraction pattern measured during data collection is a superposition of all of these. Reflections from different domains may overlap and twinned crystals fall broadly into two categories in which either all reflections or only certain zones of reflections are affected by overlap. The former occurs when a crystal lattice belongs to a higher point group than the crystal structure itself; the latter frequently occurs when the twin law is a symmetry operation belonging to a higher symmetry supercell." [134]

In general, twinning is described by the plane on which it occurs and the associated twinning operation, which is often a rotation around the plane normal. According to Mallard's Law the twin elements are always rational and the plane is thus always a lattice plane and twin axis a lattice row [135]. The result of this can still get very complex, especially the more chemical species and complex unit cells are involved. Still, twins are quite common as the symmetry often leads to low interface energies between the twins. This is due to the fact that a twin boundary often leads to a low Σ[9] coincidence site lattice. Twins are often $\Sigma 3$ [136].

While twins can also form by other means, i.e. during crystal growth, twins often form under the influence of stress. This can occur during a phase transformation process when shear forces cause different regions to form different orientations of the new crystal structure. Additionally, twins can be formed by mechanical deformation by the movement of partial dislocations on neighboring planes. An indication could be seen in fig. 2.9 (b), where a minimal region of two planes was mirrored in respect to the rest of the lattice. With many planes involved this becomes more easily visible and can reach macroscopic extensions, which was nicely demonstrated in our group for fcc metal [137].

Twins often occur in spinels on {111} planes, [138] which is parallel to the faces of the XO_6 cation octahedra. Twinning leads to very characteristic changes in the surface shape of faceted particles or especially gems, which is shown in fig. 2.10 for the case of $MgAl_2O_4$ – the name giving compound.[10] But this kind of twinning also occurs in smaller spinel particles ($10-20\,\mu$m), where the full landscape of twinned particle shapes can be observed. [139]

[9] Overlapping the identical lattice of two different domains, Σ is the ratio of the unit cellv volume of the coincidence site lattice - representing the periodicity of the *Moire pattern* of both – divided by the unit cell volume of the phase of the single domains.

[10] Use of image `https://commons.wikimedia.org/wiki/File:Spinel-83077.jpg` by Rob Lavinsky, iRocks.com under licencse *CC-BY-SA-3.0* (`https://creativecommons.org/licenses/by-sa/3.0`).

Figure 2.10.: Image of twinning in a $MgAl_2O_4$ spinel gem (see text for reference). Indications for twinning, i.e. similar shapes of well-faceted particles, were also observed for $LiMn_2O_4$ in this work.

2.4. Phase transformations with a focus on cubic to tetragonal

The exact transformation between $LiMn_2O_4$ and $Li_2Mn_2O_4$ has only been studied very little while the phase diagram and the two adjoining phases are quite well known. This leaves some room for different kinds of phase transformations mechanisms. The most important ones and their most important characteristics will be summarized and specified in this section – limited to the detail necessary for this work. As this work is from Göttingen and the crystallography is one of the most important points the main source for this chapter will be "Physical Metallurgy" [130] with the most important chapter written by Wayman and Bhadeshia. Two things seem likely when adding additional lithium to $LiMn_2O_4$: In both cases, the additional Li is added to $LiMn_2O_4$ at a reaction front where it forms a metastable[11] state with more lithium than the cubic structure is supposed to contain. In the first case, now a spinodal decomposition occurs enriching one part of the metastable area to $Li_2Mn_2O_4$ and the other stays at $LiMn_2O_4$ In the other case, the whole region undergoes a cubic-to-tetragonal transfomation at a constant content of lithium in the region.

To classify a phase transformation and compare it with others two main criteria are often applied first: Is it *diffusive or non-diffusive/diffusionless*? This determines whether the diffusion of atoms over distances of multiple unit cells are required to form the microstructure present after transformation. And is it a *civilian or military* transformation? Meaning whether the atoms change position in an uncoordinated, one-by-one diffusion-like process or in a coordinated fashion without changing their nearest neighbors. Classic examples of those combinations are precipitation (diffusional, civilian), massive transformations[12] (diffusionless, civilian) and the martensitic transformation

[11] likely both temporal and spatial

[12] Massive transformation: A transformation in which the crystal structure changes while staying at the

(non-diffusive) for which the term military was coined.

One main difference between the massive and the martensitic transformation is the *athermal* character of martensite formation, i.e. the amount of martensite formed is a function of the temperature[13] not the holding time at that temperature [140]. This is the case because the chemical driving force of the transformation is so large that it needs no thermal activation or fluctuations to overcome a activation barrier, so that it cannot be prevented by infinitely-quick cooling. This can only work because military transformations have an *orientation relationship* to the parent phase, which is not necessarily the case for massive transformations even though they also occur at a higher speed compared to precipitation reactions, but slower than martensitic transformations.

Historically, there is a strong differentiation between the transformation types based on the reaction mechanism, but it has been shown (compare e.g. [141]) that the crystallographic descriptions developed for martensitic transformations like in e.g. steels, Cu–Au, Fe–Ni, Ni–Ti, but also some ceramics, also holds for *diffusional-displacive transformations* and some other transformations. This also has implications on the mechanism of the transformation, [142] and means that a further look at the characteristics of the martensitic transformations like habit-plane, orientation relation, their crystallography, interfaces, etc. is needed.

Different phenomenological theories were developed that are mathematically equivalent by Wechsler, Liebermann and Read as wells as Bowles and Mackenzie [143]. The simplest way to understand the basic relationships between the cubic and tetragonal structures aand the processes necessary for a transformation is the model of the *Bain transformation*. For this, the relationship between both lattices – previously already established – as shown in fig. 2.11 (a) in form of the pseudo-cubic lattice is necessary. The pseudo-cubic (x_p) and tetragonal (x_t) lattice are transformable through

$$\begin{pmatrix} a_p \\ b_p \\ c_p \end{pmatrix} = \begin{pmatrix} 1 & 1 & 0 \\ -1 & 1 & 0 \\ 0 & 0 & 1 \end{pmatrix} \begin{pmatrix} a_t \\ b_t \\ c_t \end{pmatrix}, \tag{2.1}$$

where the lengths are thus related by $|a_p| = |b_P| = \sqrt{(2)}|a_t|$, $|c_p| = |c_t|$ [70]. The pseudo-cubic lattice, in turn, can be produced from the cubic lattice by one of the following transformation matrices[14]:

$$U_3 = \begin{bmatrix} \alpha & 0 & 0 \\ 0 & \alpha & 0 \\ 0 & 0 & \beta \end{bmatrix}, \qquad U_2 = \begin{bmatrix} \alpha & 0 & 0 \\ 0 & \beta & 0 \\ 0 & 0 & \alpha \end{bmatrix}, \qquad U_1 = \begin{bmatrix} \beta & 0 & 0 \\ 0 & \alpha & 0 \\ 0 & 0 & \alpha \end{bmatrix}, \tag{2.2}$$

same stoichiometry, but with movement of more than a next-nearest neighbor distance.

[13] Most phase transformations occur and are studied by changing temperature as the parameter at a fixed composition, which is not the case in this work.

[14] This is named the Bain strain, which converts the austenite to the martensite bravais lattice for martensitic transformations. But there are other transformation models than the Bain model.

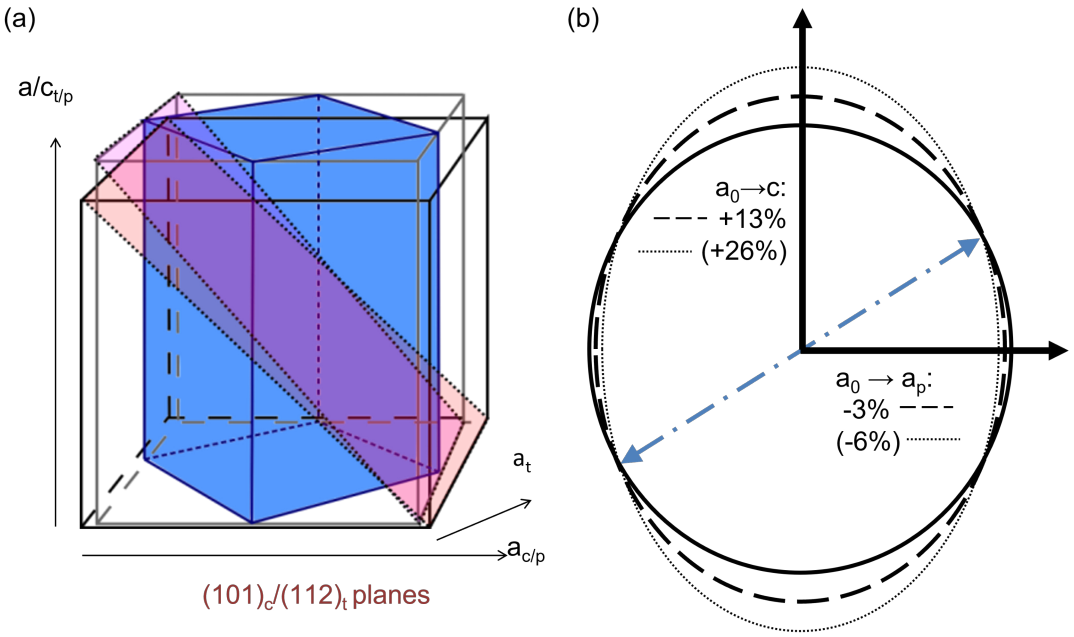

Figure 2.11.: Sketches showing the lattice correspondence between $LiMn_2O_4$ and $Li_2Mn_2O_4$. (a) The tetragonal $Li_2Mn_2O_4$ unit cell can be produced by Bain strain of the cubic phase with the help of a pseudo-cubic lattice. (b) Drawing the two different distortions of the axes in 2D shows an invariant line (blue) at the intersection between the cubic cell as a circle (solid line) and the tetragonal ellipsis (dashed, dotted - exaggeration).

with $\alpha = a/a_0$ and $\beta = c/c_0$. It is important to note, though, that any correspondances of lattice planes as well parallelity of the principal axes cannot yet be evaluated for an orientation relationship between parent and product phase of the transformation in a transformed sample.

The transformation between parent and product phase has to occur via a *(semi)-coherent glissile interface* as the lattice correspondence has to be conserved. For this, it is necessary that both phases share a common plane that remains (almost) undistorted throughout the transformation. This *invariant-plane strain* state would thus give the *habit plane*. Fig. 2.11 (b) sketches the distortion of the principal axes in 2D by changing a circle (cubic) to an ellipse (tetragonal axes), that determines an undeformed line (blue, dotted). The transformation can then occur via a combination of a shear s along an undistorted line and an elongation δ perpendicular that accounts for the change in volume during the transformation.

During transformation the global shape of the sample changes across the common

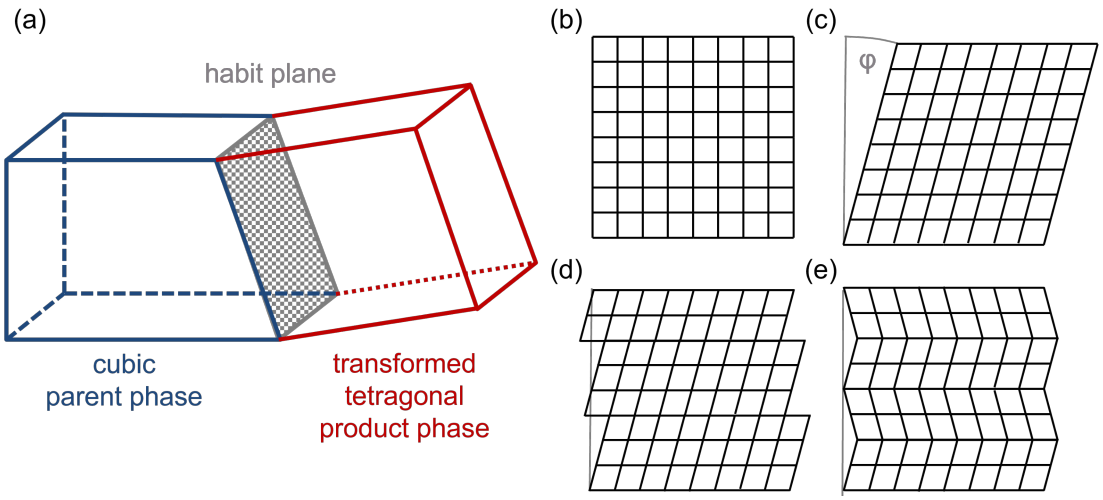

Figure 2.12.: Transformation would lead to a bulk shape change along the habit plane (a) due to the (simplified) distortion of the parent phase (b) into the product phase (c). The bulk shape can only be retained by either deformation through slip (d) or twinning (e).

habit plane as sketched in fig. 2.12 (a). If the sample weren't constrained by external forces, those changes would be large. But shape change is often minimized by two different strategies. To illustrate this fig. 2.12 (b,c) show a parent phase and product phase of a transformation that produces a slight shear parallel to the horizontal habit plane (or rather line in 2D). Thus, the whole sample would also deform by an angle of φ.[15] The shear component of the transformation can be compensated by the two mechansims sketched in fig. 2.12 (d,e), i.e. either a lattice slip parallel to the shear direction (or any combination of slips resulting in a net slip in shear direction) as well as the formation of twins to minimize the bulk deformation.

In practice, any combination of those two occur and additionally the fact that the cubic parent phase has three equivalent principal axes that can transform into a c-axis makes the situation complex. But this not only occurs to minimise the shape change of the whole sample, but also to minimize the strain energy at the transformation interface, i.e. parent-product-interface. This is often necessary, because in most cases there is no invariant-plane strain and perfect habit plane as this would require transformation a less simple transformation with three different strains in the feformation matrix - one of them being very close to $b/b_0 = 1$.[16]

[15] This can be the case and is utilized in shape memory alloys that have special material properties like a high resistance against shearing of lattice planes.

[16] This is mathematically more complex and genereal as just quickly summarized here. The main idea

It is important to note that the shear component of the transformation parallel to the habit plane can be compensated by deformation and combination of different transformation variants, i.e. c-axes with their possible twins, but the *volume change cannot be compensated*. In the end, all the characteristics of the transformation rely on the total energy of the sample. The sample will tend towards a local energy minimum, that includes the energy of defect formation like strain energies and any interfaces in the sample, but also local energy minimization by formation of a different variant compensating strains generated by previous transformation.

In the end, the orientation relationship (given by a pair of parallel planes and directions) is strongly determined by the habit-plane developing between the parent and product phase of the transformation. It can be predicted for some cases, where a plain-strane is present. Klostermann discusses many of the relevant implications of the habit-plane for the orientation-relationship in [143]. But often it can only be determined experimentally: with some of the most common ORs named after famous metallurgists, e.g. Kurdjumov-Sachs, Nishiyami, Greninger-Troiano. For more details on those please consult a textbook like by Cahn and Haasen [130].

The reversibility is the last very important aspect of a phase transformation. One can assume, that for transformation sharing the crystallography with martensitic transformations, the criteria for reversibility might be similar. Reversibility is of most interest and thus well studied in shape memory alloys, where this aspect is actively used and therefore critical. The necessary requirement, and often thought to be sufficient, is the presence of a glissile interface. This is equivalent to the mathematical condition of $\lambda_2 = 1$ mentioned before, which is also discussed further in terms of hysteresis and the energy of the interface between parent and product phase in [144] with the conclusion that this at least minimizes hysteresis. But Dunne finds this not to be solely sufficient and lists many other factors of influence like low volumen change, spacing of the transformation twins and others [140]. This is supported by Hornbogen, who describes transformation fatigue to mechanical effects like defect accumulation/cracking and other factors, e.g. brittle grain boundaries, structural incompatibilites and likely very important for $Li_xMn_2O_4$ interference of diffusion [145]. From a crystallographic viewpoint *weak transformations*, where parent and product phase share a finite common symmetry group lead to no plasticity and are thus reversible [146]. The concept behind this is that sharing a common symmetry group leads to the backtransformation only having the possibility to revert to the original structure, whereas in other cases it can be possible that multiple equivalent orientations of the parent phase are possible

though is, that the whole transformation between both phases can be decomposed into the eigenvalues. If the middle one of them is one $\lambda_2 = 1$, with $\lambda_1 < \lambda_2 < \lambda_3$, a perfect habit plane exists with an invariant-plane strain state. In this case no defects at the parent-product interface would be expected and also single-phase transformation is possible – meaning the formation of only one c-axes without any twinning or shear. The eigenvalues also have other implications on the properties of the transformations.

thus leading to a different outcome than perfect reversibility.

2.5. Electron Energy Loss Spectroscopy (EELS)

The following section is supposed to give the electron microscopy or EELS novice a general understanding of the method and therefore relies heavily on textbook and review sources [130, 147, 148]. Those or the book by Egerton, et. al. [149] also provide an excellent start to dive deeper into the topic and the information of the following section can be found there, while only more specific facts are uniquely cited.

Electron energy-loss spectroscopy (EELS) determines the energy distribution of the electron beam that passed through the sample. This is happens by the beam passing through a magnetic-prism that disperses it by its energy and allowing the resulting spread beam (=spectrum) to both be recorded and filtered and recondensed. This allows all classical TEM methods to be performed with an energy-filtered beam.[17]

In comparison to the other spectroscopy method of energy-dispersive X-ray spectroscopy (EDXS) common in electron microscopy EELS comes with some key differences; and advantages in the case of this thesis. EEL spectroscopy is generally performed in the region up to approximately 2 keV and can detect chracteristic energy losses of very light elements starting at $Z = 2$, $Z = 3$ (He, Li). EDS can detect any element with $Z \geq 5$ and X-ray energy >100 eV. While characteristic X-rays are uniformly emitted as a spherical wave over 4π sr this information is contained in the forward scattered and thus much less divergent electron beam, which under normal circumstances leads to order of magnitude higher detection efficiencies in EELS and shorter aquisition times. Whereas the energy resolution in EELS is mostly determined by the energy of the electron beam (1 eV) it is larger than 1 eV for EDS. But importantly EELS is able to detect many kinds of losses upon interaction within the sample; not only ionization/generation of characteristic X-ray radiation.

The energy losses inside the TEM and visible in the beam are a combination of plasmon excitation, excitations of the conduction band (creating secondary electrons), decelaration in the coulombic field of the atoms, phonon excitations and ionization of inner shells. These decay via Auger electrons or the characteritic X-ray emission mentioned above. Because any EEL spectrum contains a combination of the aforementioned processes the interpretation is less straight forward than EDXS. An example of a typical EEL spectrum for $LiMn_2O_4$ can be seen in fig. 2.13.

The zero-loss peak (ZLP) is located at 0 eV and its shape already indicates the achieved resolution in the data, because it is generally the shape of the incoming beam but may include some phonon contributions. This is the reason why the resolution of a spectrum is often slightly informally given as the full width at half maximum (FWHM) of the ZLP.

[17] This in not to be confused with a monochromator, where the beam is filtered within the source before interacting with the sample.

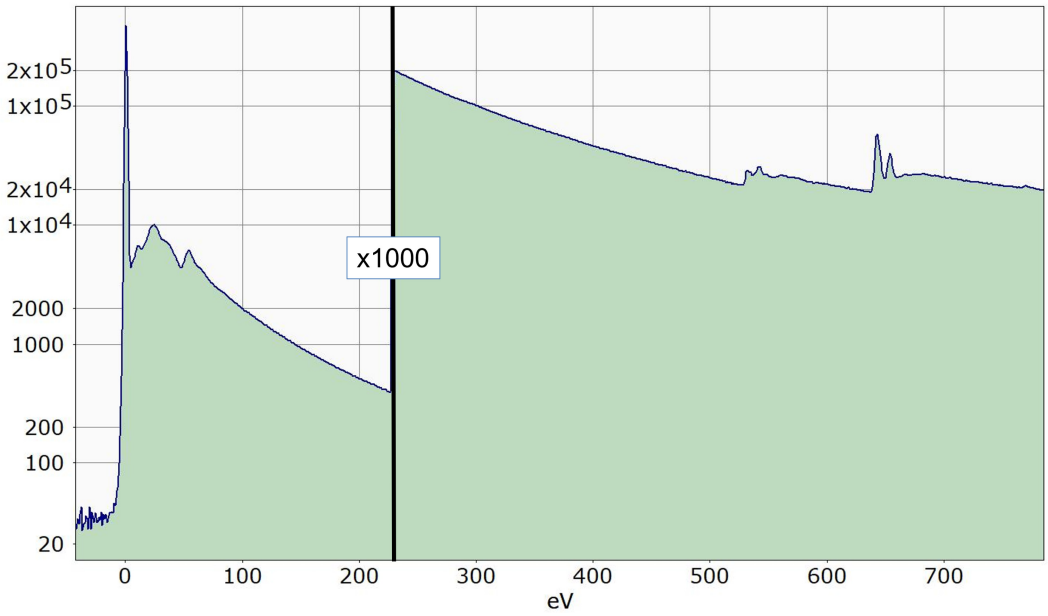

Figure 2.13.: Example of a typical electron energy loss spectrum. This case shows the MnO_2 data from the *EELS Atlas* [150] included in `Digital Micrograph`.

With a field emitter gun it is often approximately 1 eV and could be reduced to below 0.2 eV with a monochromator, but this costs around 90% of the beam brightness.

Everything below an energy loss of arbitrarily chosen 50 eV is called the low-loss region of the spectrum and as described by Grogger, et. al. contains most of the information available also by optical spectroscopy like the band structure and the dielectric properties. In EELS this whole information is summed up under the name *plasmon peak* as it contains most of the intensity besides the ZLP and can become dominated by the surface plasmons when working with nanoparticles or -structures. It also already visually gives a first hint at the sample thickness as a thicker sample will cause more electrons to experience an interaction and therefore the intesity of the ZLP will decrease while the plasmon peak will increase. While a thicker sample will increase the chance of interaction with the electron beam and thus increase any elemental signal, it also increases the chances of an electron interacting more than once thus combining the losses and making the spectrum more complicated. This leads to a sweetspot of thickness depending on the investigation.

Everything above 50 eV is deemed the high-loss region and contains a rapidly decreasing background despite the logarithmic[18] y-axis. This also explains why EELS is

[18] Most of the other spectra in this work are plotted linearly as they don't span as much energy difference in one spectrum and the linear scale is more intuitive to the human eye.

shell	n & l	j	edge
K	1s	1/2	K
L	2s	1/2	L_1
	2p	1/2	$L_{2,3}$
		3/2	
M	3s	1/2	M_1
	3p	1/2	$M_{2,3}$
		3/2	
	3d	3/2	$M_{4,5}$
		5/2	

Table 2.1.: EELS edges are named on the basis of their quantum numbers. Edges occuring close to each other in the spectrum, i.e. only differing by spin, are grouped.

not often used for any signals with energy losses above 2 keV, as previously mentioned, due to the increasing aquisition time. Also note that signal needs a factor 1000 multiplication despite this to show the signal in the range higher than 500 eV. This background is made up of random, inelastic plural scattering events and can be described by a power-law function of type $A \cdot E^{-r}$ with $2 < r < 6$. On top of this the ionization edges are visible. Those are named based on their quantum numbers of the electron shell n, the angular momentum l and the total momentum j. The naming scheme for $n \leq 3$ is shown in tab. 2.1. The example spectrum in fig. 2.13 shows three ionization edges at roughly 50 eV, 530 eV and 640 eV. They already show that in comparison to the delta-like shape in EDXS their shape differs from the simple hydrogenic saw-tooth like `Mn-M` to the more complex `O-K` and `Mn-`$L_{2,3}$ (in order).

One spectrum on its own is not as informative as spatially-resolved spectroscopy and this is where TEM has one of its strengths. This can be achieved by spectrum imaging (SI) creating a three-dimensional data cube of both spatial and spectral information (x,y,E) as shown in fig. 2.14. This data are also called SI (spectrum image) and are most often obtained by scanning the beam across the region of interest on the sample and recording a spectrum at each x/y-coordinate as indicated by the red, vertical bar in the image. Additionally, it can also by recorded by energy-filtered TEM (EFTEM) through recording an energy-filtered conventional TEM image at each energy of the required spectrum – shown as an orange slice in the figure.

Each of the two recording methods have their (dis-)advantages. As any aquistion of a SI will automically generate a large dataset and require aquistion times >5 min, it is an advantage to avoid it, if possible. EFTEM can be used well for this if there are easily discernible features in spectrum or strong changes occur within the sample, because this allows to just record single slices/energy-filtered images at the energy of those features. Additionally, chemical mapping can be performed without recording

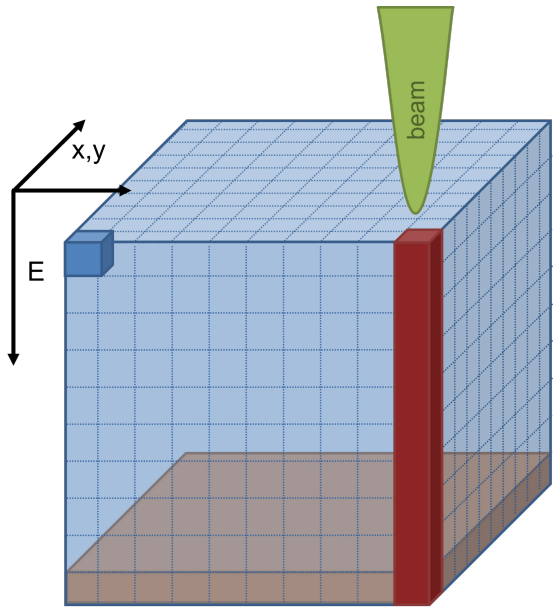

Figure 2.14.: Sketch of spectrum imaging (SI). Spectrum imaging obtains a three dimensional cube of data (x,y,E), that consists of voxels (blue) and can be aquired by EFTEM (orange) or scanned spectrum aquisition (red).

a full cube as a method using three images to estimate the background and extract the signal is enough (lookup *three-window method* for more detail). EFTEM also, in principle, has the same spatial resolution as a conventional TEM image. But as the size of the smallest slit is larger than the selectable dispersion (eV/ch) of a single spectrum the energy-resolution is limited.

Vice versa, due to time and data restrictions the amount of recordable voxels is limited and thus for scanned aquisition of a SI the region of interest has to be chosen carefully as the associated STEM image will rather be limited to multipes of hundreds of pixels in x and y. Those SIs can be looked at in all spectral details as a full high-resolution spectrum is recorded at each pixel. This also quickly allows correction of energy-drift within the data cube between each spectrum whereas in EFTEM this leads to changes in the dispersion. Spatial drift is easier to detect during aquisition, which allows a re-recording or can be avoided by regualar automated checks.

This work will focus on STEM-based aquisition of SIs to use small details in the spectra to detect chemical information. Which leads directly into the next subsection.

2.5.1. Fine structure (ELNES)

As Grogger, et. al. summarize it EELS has some characteristics of absorption spectroscopy, as the excited electrons can go into any state above the Fermi level. Due to this the ionization edges have intensity fluctuations starting at the edge threshold – the so-called energy-loss near-edge structure (ELNES). "These structures are related to the momentum resolved density of unoccupied states at the site of the excited atom. The ELNES has been found to be dependent on the local atomic environment such as coordination, valence and type of bonding." [147, p. 204] This enables spatially resolved recorcding of not just elemental/compositional but chemical information. Comparable other methods that can access this chemical information are x-ray photoelectron / absorption spectroscopy especially using X-ray absorption near-edge structure (XANES), though the used edges can strongly differ in energy. If a TEM with monochromator can be used for the spectroscopy the spectra can be quite comparable on the same edges as many features have a natural line width broader than both methods (XAS: $<0.1\,\mathrm{eV}$, m-EELS: $\sim 0.2\,\mathrm{eV}$).

The excitation of any electron in an edge can generally occur into the continuum and therefore with all energies that are larger than the critical energy for ionization. However, with increasing energy this processes cross-section decreases, which gives most edges the basic saw-tooth like shape that also contributes to the overall background for higher energy signals. But an excitation is already possible into the lowest possible unoccupied state accessible to the electron. Therefore, the edge starts early and probes the available states therefore giving a projection of the density of states (DOS) just above the Fermi level. To illustrate this, the basic principles behind the shape of the two highest energy edges of manganese dioxide - the O–K and Mn–$L_{2,3}$ - in fig. 2.13 can be explained hereafter.

The basic shape of the O–K-edge at circa 530 eV is often described as the *p-projected density of unoccupied states*.[19] This is due to the nature of oxygen with the configuration of $[\mathrm{He}]_2 s^2\,2p^4$. As O–K is a transition from the state of $n = 1$, $l = 0$ the dipole selection rule $\Delta l = \pm 1$ only allows scattering into p states. The lowest being 2p, which has holes because of the strong bonding with the manganese 3d states [150]. This also shows that the O–K-edge will also show changes of the manganese chemistry due to this interaction.

The whitelines in the Mn–L-edges are also governed by the density of unoccupied electron states with a possible symmetry or angular momentum l. The Mn–$L_{2,3}$ visible

[19] Note of warning: From a pure quantum-mechanical standpoint those states only exist once the electron transitioned so that this also includes the electron hole near the core. According to [151] this is not a large problem as theO 2p states screen the hole.

at 640 eV and 651 eV are the result of excitations from the $2p_{3/2}$ and $2p_{1/2}$ states of manganese. The energy difference of ~ 11 eV between is due to spin-orbit splitting. The reason for their brightness, though, is the fact that with $n = 2$, $l = 1$ and $j = 1/2, 3/2$ they can transition into s and d states, but d states are available with a sharp onset in the 3d conduction band. Once again any change in chemistry of manganse involving a change in the conduction band should thus be visible in the spectrum.
The basic expectation for the difference in intensity between both states of $\mathrm{Mn\text{-}L_3}$ and $\mathrm{Mn\text{-}L_2}$ is that due to a higher degeneracy $(2j+1)$ the $2p_{3/2}$ should have twice the intensity of $2p_{1/2}$. It's not exactly this simple as experiments show, but the $\mathrm{Mn\text{-}L_3}$ signal generally holds much more counts.

2.6. Notable in-situ TEM experiments and state of the art of battery research methods

As this thesis is based on in-situ electron microscopy, this section will give a short account of previous work done by (in-situ) electron microscopy and spectroscopy methods. This is to show the state of the art of in-situ TEM microscopy and also to show other methods that may yield similar results. The publications described in the following are by no means a full account, but only a limited selection.

Work on the battery cathode materials discussed in this thesis work started out with "classical" electro-chemical methods still used today: current-voltage scans yielding capacity information, voltage information, cyclability etc. This was often supplemented with X-ray diffraction characterization of the developing phases and their stability as well volume fractions - basically the concetration dependent phase diagram. For an example compare with the data provided in the long review on "manganese oxides for lithium batteries" from 19997 by Michael M. Thackeray [22].

At least for $LiMn_2O_4$, it was then also Thackeray in 1998 that introduced a new layer of discussions to the reasons for capacity loss as additional use of TEM characterization yielded the result that $LiMn_2O_4$ may experience structural fatigue by $Li_2Mn_2O_4$ cell voltages higher than the approximately 3 V needed to form $Li_2Mn_2O_4$. The aforementioned observations of $Li_2Mn_2O_4$ crystallites in discharged $LiMn_2O_4$ cathode material [36, 79]. This opened up questions about characteristics and mechanisms of electrode particles, which needed electron microscopy to be adressed.

2.6.1. Developments in in-situ electron microscopy relevant to this thesis

One of the first electron microscopy studies done on $LiMn_2O_4$ was already an in-situ experiment, which studied the temperature-induced also Jahn-Teller-driven transition at a temperature of 230 K, which shows a charge ordering effect [152]. But this is not an in-situ experiment with lithium as the varying parameter, which had proven

useful using diffraction techniques like neutron diffraction to Li order in $Li_xMn_2O_4$ for $x \leq 0.5$ [61], showing that the particle size strongly determines the phase boundaries of the $LiMn_2O_4$-$Li_2Mn_2O_4$ phase transition by ex-situ XRD with many intermediate measurements [153] or the initial lattice parameter dependency measurements necessary for general understanding of $Li_xMn_2O_4$ [62, 67, 154]. TEM in itself had proven its importance to battery reasearch, too, e.g. in studies on $LiFePO_4$ adding insight into the core-shell transformation discussion of the times by using HRTEM and especially EELS to study interfaces in the particles [155].

But especially the ex-situ TEM studies could always be questioned for the area studied not being representative, the particles changing during transfer, et cetera. The change came with the introduction of a STM-holder for the TEM as it allowed voltage/current measurement/applications and was first used in studies on individual gold rows [156] and semiconducting nanowhiskers [157].

Anode materials were the starting point for in-situ lithium reactions that first followed the setup of an anode material nanowire as the sample contacted by a Li donating material immersed in an ionic liquid electrolyte (ILE) on a metal tip. In the first experiment those were SnO_2 nanowires lithiated by applying a -3 – $-3.5\,\mathrm{V}$ bias to them, while in contact with a ILE/$LiCoO_2$ on the tip. Showing a distance to $\sqrt{t}$ behavior for transformation accompanied by high dislocation density at the interface due to the massive expansion during amorphisation of the sample [158]. Very similar results were obtained for Si nanowires with the same setup in a longer study also using electron diffraction [159]. Many more publications could be mentioned here with very similar procedures (see [160–165]), but two more are worth mentioning as they brought some innovation. By using Li metal with its Li_2O surface as a solid electrolyte problems withe ILE coating the sample surface and the vacuum could be circumvented [166]. This also allowed first experiments on aluminum nanowires including multiple de-/lithiation cycles and involving EELS characterization of the Li distribution [164].

Cathode materials show less extrem reactions than e.g. the swelling of silicon or graphite upon lithiation so that studies include more methods to study the reactions and are sparser. In-situ studies on the $LiFePO_4$ transformation behavior mentioned before thus required samples and conditions suitable for high-resolution imaging [167, 168]. Another study on spinel cobalt oxide nanoparticles was able to track individual particle's transfromation using STEM supplemented with diffraction also using a STM-TEM holder [96]. The work closest to this thesis was performed by Lee, et. al. on $LiMn_2O_4$-nanowires without [38] and with a growth twin [39] using an approach involving ILE: They were able to measure CV curves on single and bundles of their 100 – $200\,\mathrm{nm}$ thick nanowires with currents in the range of -10 – $10\,\mathrm{pA}$ (ex situ: $2\,\mathrm{mV/s}$ scan rate) and -250 – $250\,\mathrm{pA}$ (in-situ: 10 nanowires at $2\,\mathrm{mV/s}$). Interestingly they observed a addi-

tional orthorhombic intermediates phase reported nowhere else that also extended over many 10s of nanometers without growth twin, which in the nanowires with growth twin was very sharp and showed only a lattice rotation that hasn't been seen elsewhere. They also didn't report any capacity loss on multiple cycles. Those results may be due to the unique geometry of the nanowires and their mechanical contraints as [153] showed the previously mentioned particle size dependence of phase boundary.

The advantage of the use of ILE of being able to contact multiple nanowires with a stable contact comes at the disadvantage of the ILE only allowing snapshots and limited time experiments due to beam and vacuum interaction. For other manganese dioxides cycling has also been possible with the Li metal contact. E.g. the lithiation at $-2\,\mathrm{V}$ and delithiation at $4\,\mathrm{V}$ of the tunnel structured α-MnO_2 [169].

Other approaches should not be left out, but differ in their amount of control and reliability. A very simple approach is the fact that **Li_2O decomposition** under the electron beam can be used by putting both it and sample material on a mesh grid, lithiating the sample material by starting lithium surface diffusion by beam irradiation of the Li_2O. Though with no direct control it has been sucessfully used for carbon, silicon and FeF_2 [170–172]. Another option is the preparation of **miniaturized whole batteries** that despite some holography of the potentials [173, 174] are often more proof-of-principle and require extensive sample preparation as they are based on a layered sample preparation process like PLD of more than five layers [175–177]. The approach of using a **liquid cell holder** also involves a full battery setup circumventing the problems with the electrolyte and thus also allowing studies of electroly cathode interaction like SEI formation (compare [178, 179]) but at the cost of a thickness were much more than a little contrast at low resolution or EDX is very difficult [180].

2.6.2. Additional microscopy and spectroscopy methods used in cathode materials

Using any TEM based method has the disadvantage of sample thickness requirements. Thus, either only small particles are assessable without time-consuming sample preparation. And when interpreting the results of the small regions inspected, it is important to compare with results from techniques yielding similar results.

One method able of accessing both structural and chemical information is **X-ray absorption spectroscopy (XAS)**. First by extended X-ray absorption fine structure (EXAFS) and second by X-ray absorption near-edge spectroscopy (XANES). Both are performed on the `Mn-L` and `Mn-K` edge. With results from those the first structural refinements of the Mn-O bonds were possible to show that both Mn^{3+} and Mn^{4+} are present in the samples and distortions of the MnO_6-octahedra can reach local extends of the bulk distortion for $Li_2Mn_2O_4$ [181]. As wells as the influence of different manganese

oxides and lithium contents and thus valence on the O−K and Mn−L edges [182].

But Qiao, et. al. nicely summarize the problems of spectroscopy on the XANES-Mn−K edge: "Although hard X-rays benefit from deep penetration depth and non-vacuum instrumentation, the dominating signal of MnK-edge XAS is from the 4p states, which are not the valence state of transition metals." [183] That's why extensive studies of samples with intermediate Li content on the Mn−K edge need additional theoretical calculations of the manganese and oxygen density of states (compare results of [59]). On the other hand, **X-ray photo electron spectroscopy (XPS)** provides insights from all the EELS-accessible edges Li−K, Mn−L, Mn−M and O−K, but os only sensitive to the surface of the samples. [184, 185]

Methods that are able to do the kind of mappings possible in STEM-EELS are also becoming adapted in X-ray-based methods. The first example of this is localized XANES on the Ni edge at 8343 eV and even tomography on micron-sized particles of $LiNiMnO_4$ [186]. Even more impressive are operando measurements using softer X-rays to map the kinetics of lithium in $LiFePO_4$ by scanning transmission x-ray microscopy (STXM) [187].

3. Materials and methods

This chapter will give information regarding the sample material, the method of sample preparation and the procedure of the in-situ experiments.

3.1. Sample material

The $LiMn_2O_4$ material used for the experiments is a commercial powder from SIGMA ALDRICH *Lithium manganese(III,IV) oxide, electrochemical grade* with the PubChemID *24871819* and a nominal size of $\leq 5\,\mu$m. Two other powders were also tested.[1] The former proved to be difficult due to the small particle size in the sample preparation process, as agglomerates would have had to be worked with, and in addition, for in-situ experiments the small particles would only have had small grain in which the observation and investigation of an interface would have unnecessarily difficult. This was also true for the second sample, since these turned out to be very large, but apparently sintered, agglomerates of even smaller particles.

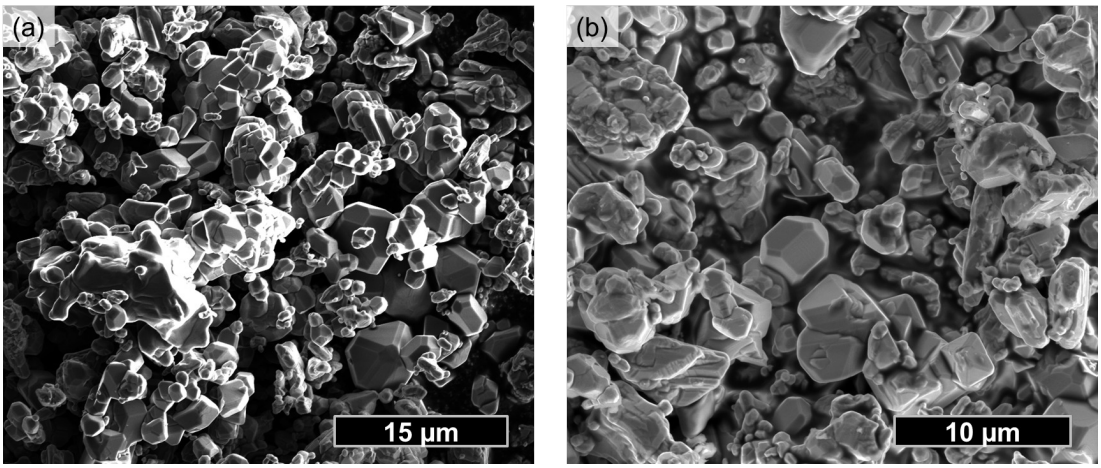

Figure 3.1.: Overview micrographs of the SIGMA ALDRICH-$LiMn_2O_4$ sample powder in its pristine state on a SEM stub.

[1] SIGMA ALDRICH (*Lithium mangenese oxide*, *329764133*, $\leq 0.5\,\mu$m) and ALFA AESAR (*Lithium mangenese oxide, 99.5%*, —, $\leq 50\,\mu$m).

For further use and investigation, the powder was pressed onto a SEM stub using a carbon pad and then tapped to coarsely remove loose particles. Overviews of this type of sample are shown in Fig. 3.1. It can be seen that the particles are not uniform and that, in addition to large, faceted grains, a wide variety of other shapes occur, which don't deliver any hint regarding their crystallinity with regard to grain size and multiplicity as well as orientation.

In spite of the quality specifications of the manufacturer, employees of the institute were able to observe extensive areas with increased sodium content in the same material (cf. [188]) and precipitates and possibly phase boundaries or other phases in other battery materials, which were also specified as pure phase (cf. [189]). In this work (see sec. 5.1.3) particles were found which were more like $Li_2Mn_2O_4$ and tetragonal. Therefore, the powder was additionally characterized by us $\theta - 2\theta$-X-ray diffraction and showed the expected lattice constant for cubic $LiMn_2O_4$ was $a = 8.247(4)$ Å. No further peaks could be identified as an alien $Li_xMn_2O_4$ phase (see fig. A.1).

As the used FIB-based sample preparation method is very time-consuming, additional thought was put into further identification of suitable particles via the readily available SEM imaging used anyways during the FIB process. Despite large facets on the surface, which indicate good crystallinity, stacking faults (see sec. 5.1) and other defects were later found in the particles. It is therefore worthwhile to look at a few typical particles, which are large enough for preparation in the FIB. Fig. 3.2 shows four of these particles. With the in-situ experiments requiring single crystalline regions on the order of $1\,\mu$m, the particles in fig. 3.2 (a,b) can be used. They are uniformly faceted and symmetrical, although in Fig. 3.2 (b) the edge in one of the facets and the reduced symmetry suggest that there is probably a twin (compare with surface morphologies of twins in the spinel $MgAl_2O_4$ [139]) or another grain. Fig. 3.2 (c) on the other hand already indicates defects onthe surface that can only be observed under very good imaging conditions in the FIB. A comparison with contrasts in other materials suggests that these are *channeling* effects as used in Electron Channeling Contrast Imaging (ECCI) (e.g. [190] or shortly described in [130]) in SEM. These can mark stacking faults, nano twins and dislocations on smooth surfaces (preferably in the BS signal) [191, 192]. In some cases, however, defects can already be recognized by clear steps in the morphology of the particles. The particle in fig. 3.2 (d) only partly shows a structured surface even though it is of sufficient size. This kind of particle was also deemed to have a high risk-reward-ratio and therefore not considered for preparation.

In the hope of further insights by using the nature of the facets to predict whether a particle might be cubic or tetragonal additional attention was paid to the possible surface terminations. Fig. 3.3 shows some resulting particle shapes assuming different relative surface energies of the facets. Both on the basis of theoretical calculation and experimental observations a *truncated octahedron* shape dominated by {111} surfaces is expected for $LiMn_2O_4$ particles as visualized in Fig. 3.3 (b) [193–195]. The fig. 3.3 (a,c) show two other particles as a help for a more general comparison regarding symmetries

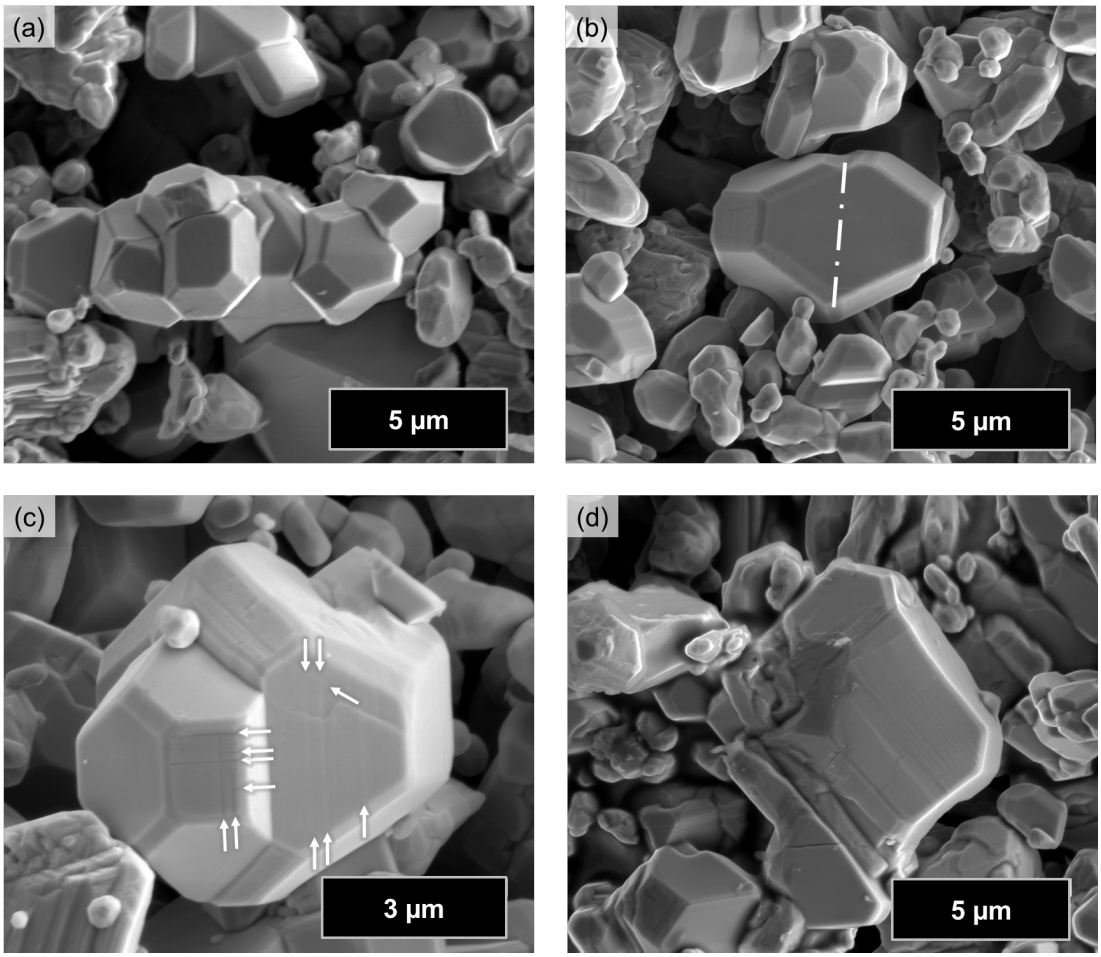

Figure 3.2.: Four typical particles size-wise suitable for FIB preparation. (a) and (b) with their continuous facets suggest large single crystalline volumes. The contrasts in (c) as indicated by some exemplary arrows hint at the possible presence of stacking faults or small twins. The particle in (d) is large enough, but the surface morphology and reduced symmetry in comparison makes it too high of a risk to use.

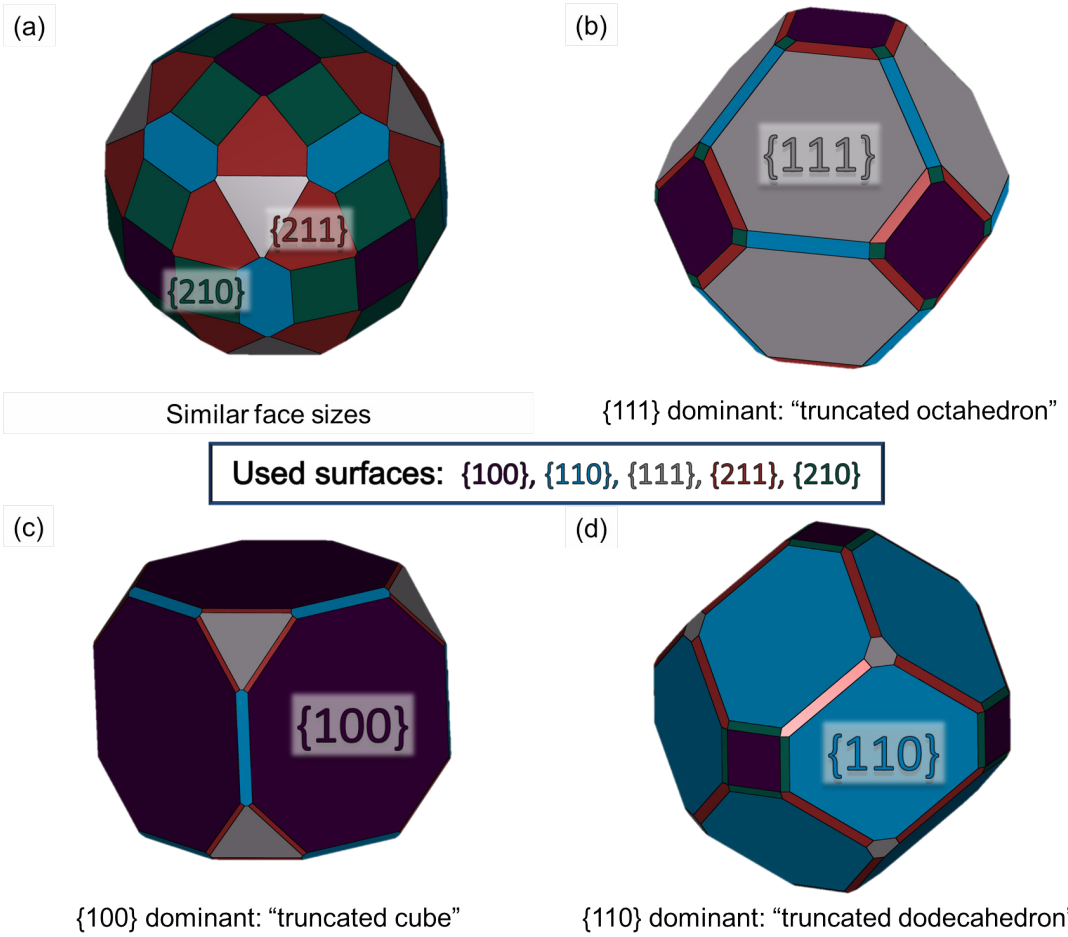

Figure 3.3.: Ideal typical single crystal particle shapes constructed with the different surface terminations that can be expected for $LiMn_2O_4$. (a) An abstract particle shape using approximately equal surface sizes of all terminations. The most probable particle shape for $LiMn_2O_4$ with dominating $\{111\}_c$ surfaces is shown in (b). (c,d) show two differing particle shapes with two other termination often reported in other materials as a means of comparison.

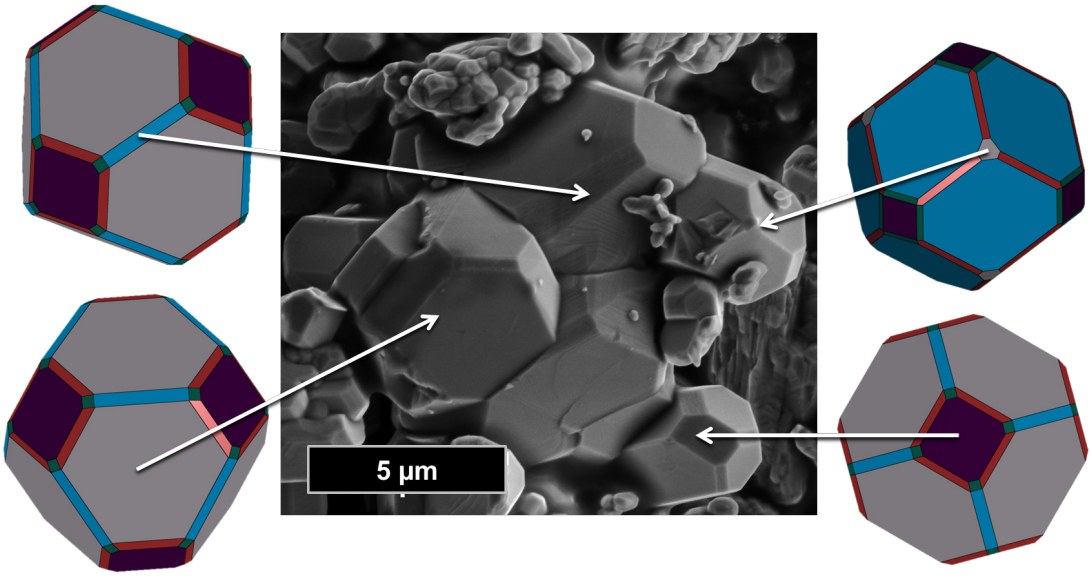

Figure 3.4.: Comparison of theoretical particle shapes with an observed particle agglomerate. In general mostly truncated octahedra were observed as shown, but this example was chosen to demonstrate that there are truncated dodecahedra present. This image was also used for comparison in [196].

and orientation. Fig. 3.3 (d) is of another importance, though. Looking back at the relationship between the cubic spinel and tetragonal phase, during the transformation $\{111\}_{c=p}$ stays the close-packed oxygen layer. Therefore, one might expect that in the tetragonal $Li_2Mn_2O_4$ phase the $\{101\}_t = \{111\}_p$ could be dominating.

We didn't further investigate the relationship whether the presence of truncated dodecahedra in the sample material (compare Fig. 3.4) is directly correlated to the tetragonal samples pre-characterized in the TEM. It would provide an explanation for the observed differing particle morphology, though. Also, the presence of an additional particle morphology is an additional indicator of particles with a different stoichiometry as this would also yield different surface energies explaining a different termination.

3.2. Used instruments and modes

As most of the instruments and methods in this section are regularly used in material science, the section purely acts a quick reminder. The information described hereafter can be found in any of the many textbooks on electron microscopy like [148, 149] or in a general textbook of material physics like [130].

3.2.1. Dual Beam Microscope: Scanning Electron Microscope (SEM) and Focus Ion Beam (FIB)

The SEM scans a focused electron beam across the samples surface with acceleration voltages in the range of 1 – 30 kV, which requires the sample to be in a vacuum to supress unintentional scattering of the electrons. The imaging can be performed using different detectors, most commonly the secondary electron detector that yields the best impression of sample topography, but dedicated SEMs often include others for energy dispersive X-ray or backscattered electrons, that can both yield contrast based on changes in sample stochiometry.

The SEM imaging presented in this work was mostly restricted to the SEM unit inside the used dual beam FEI NOVA NANO 600 LAB that also included a focused ion beam and micromanipulator for TEM sample preparation. As the parameters were chosen for a quick workflow in sample preparation, i.e. imaging times of less than a minute, the electron beam current was on the order of 1 nA leading to a realized resolution on the order of 10s of nanometers at the surface of the particles.

Additionally, to the imaging capabilities of the electron beam, a focused ion beam due to its higher particle mass allows targeted sputtering of selected parts of a sample surface and thus can be used for sample manipulation, i.e. exposing certain parts of a sample and cutting them. Combined with capability to introduce a precursor gas into the sample chamber that on interaction with electron or ion beam leads to the deposition of a platinum-hydrocarbon-mixture deposition that can be used as a glue or protection layer, preparation and transfer of thin TEM samples of chosen particles is possible. For those preparation processes using the ion beam voltages comparable to those of the SEM and beam current ranging from pA to 20 nA can be switched between according to requirements of the processing step and required damage prevention as well as cut quality.

3.2.2. [Scanning] Transmission Electron Microscope ([S]TEM)

Since the complexity of a TEM (in case of this work a FEI TITAN ETEM G2 and PHILIPS CM30) does not allow for a fully sufficient explanation within the scope of a few paragraphs, the reader is encouraged to visit a textbook for more details. Here the main terms and modes are supposed to be mentioned by the suprisingly instructive comparison with a light microscope.

As both light and transmission electron microscope work by shining a uniform source through a thin sample their ray diagrams are comparable. But as electrons of 300 keV have a much smaller wavelength the theoretical resolution, which in reality is limited by much worse electromagnetic lenses, is higher. Those lenses also require much more physical space and the focal lengths are often on the order of 1 m making TEMs much larger. Additional requirements like the vacuum to reduce scattering of the electron

beam and the required sample thickness of approximately 100 nm for electron transparency are among the key differences.

Because of the differing nature, wavelength and energy in comparison to visible light the matter interactions also differ, but can be differentiated into elastic and inelastic interactions. Elastic diffraction is one of the main reasons for contrast in the samples and can be used for structural analysis in the diffraction (focal) plane by direct imaging that is an indicator for the reciprocal lattice of the sample or by the selection of spots in the focal plane for imaging. This limitation of imaging information only to (mostly) the central beam is called bright-field imaging (BF) whereas excluding the undiffracted beam is called dark-field imaging (DF). Both allow insights into the micro- and defect structure of the sample. Within the realm of electron microscopy many of the inelastic electron interactions with the sample can be imaged or investigated. In the case of the TITAN, it is a GATAN IMAGE FILTER (GIF) electron energy loss spectrometer below the imaging screen – an energy-dispersive imaging system to investigate the sample-transmitted beam- allowing to perform both energy-filtered imaging (EFTEM) or record an electron energy loss spectrum (EELS).[2]

As the FEI TITAN is equipped with an image-corrector the nominal resolution is better than 1 Å, but cannot be achieved in the sample prepared for in-situ use, but the correction still helps a lot with the samples prepared as a compromise between differing requirements in sample thickness for in-situ performance, diffraction as well as high-resolution/STEM imaging and spectroscopy.

In addition to imaging by homogeneous illumination the FEI TITAN can also be used to scan the sample similarly to the SEM with the difference, that the strongly focused beam is transmitted through the sample and different signals can be recorded for imaging. For example, BF- or DF-STEM imaging with different beam diffraction angles similar to instroducing an objective lens above or, as often the case in this work, the localized EEL spectra of a region of interest (ROI) in the sample.

3.3. Sample preparation

For TEM sample preparation in the FIB, regularly replaced powder samples as described in the previous section were used as starting material. The search for a suitable particle was then performed on this sample in the electron beam image. For reference, the search for a suitable particle can take from five to 45 minutes, depending on luck and whether special requirements (e.g. clearly single crystalline, separate particle) have to be met. As discussed regarding Fig. 3.3 in principle the comparison to ideal particle shapes can yield the possibility to prepare a very specific sample orientation. In reality,

[2] Some capabilities of the FEI TITAN where not used within this work: E.g. the beam monochromator, the environmental TEM capabilities allowing to introduce gas into the sample area and other detectors like the energy-dispersive X-ray spectroscopy (EDS) system

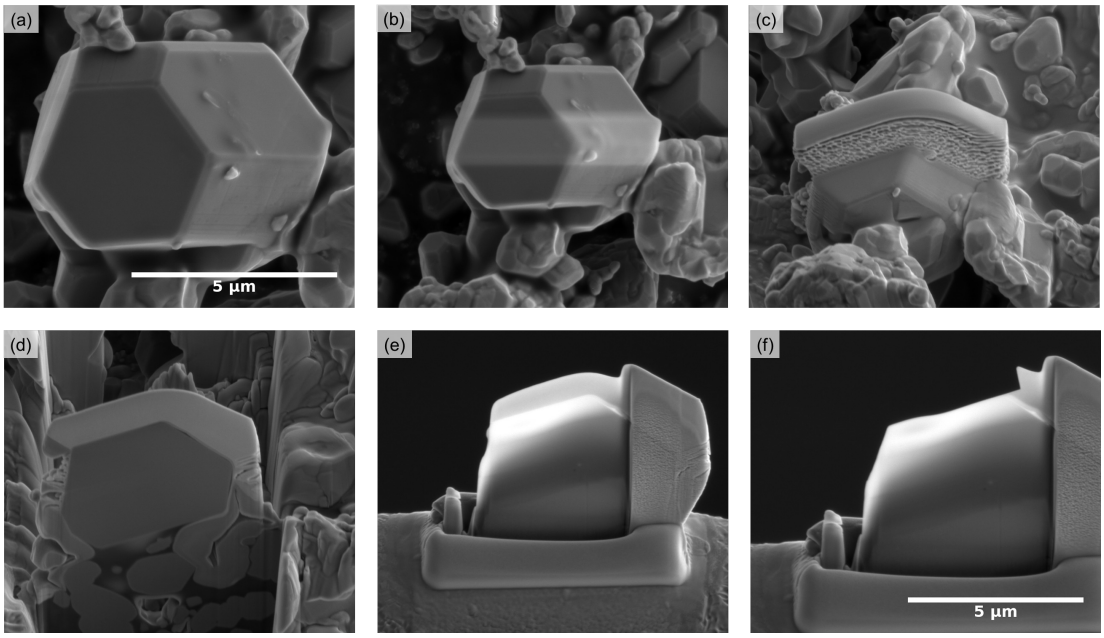

Figure 3.5.: Example of a typical FIB preparation process. The biggest deviations from the conventional procedure are the T-shape (as seen from above) of the lamella and the final removal of the platinum protective layer. Additionally, a very high emphasize is placed on trying to prepare the sample with a rather homogeneous thickness and without holes.

the already long search for a particle often doesn't allow for this. Especially considering that the sample can basically only be rotated and depending on the rough surface of the powder sometimes be slightly tilted. Additional factors can also play a role: For example, a low particle density on the carbon pad can lead to strange charging effects and separated particles or ones with very little contact to others are more prone to mechanical instabilities as well as drift during the preparation process. Therefore, particle selection and orientation was mostly limited to selecting a strongly facetted particle and orienting it to a symmetry axis close to the longitudinal axis of the particle (ensemble). This is important to make it more probable to reach a (low index) zone axis with single tilt capacity of the in-situ TEM holder.

In general, the FIB sample preparation as illustrated by the series of the important steps in Fig. 3.5 follows the conventional process used for TEM lamellae. After previously described selection and orientation (comp. Fig. 3.5 (a)) electron beam platinum and ion beam platinum is deposited on the selected particle $0.2\,\mu$m and $0.5 - 2\,\mu$m (see fig. 3.5 (b,c)). During initial experiments, sample preparation was undertaken without this step, to prevent contamination and only slight damage to the sample was detected.

However, the platinum prevents *curtaining* effects and contributes significantly to a more uniform cutting behavior and thus a more homogeneous lamella due to a more even upper edge.

In Fig. 3.5 (d), the particle can be seen after cutting a trench with 7 nA adapted in size to the particle. It is observed that the particles may have a height of 1 – 5 μm and voids may be present below. So placing the cuts for the lift out process may require additional rotation by 180° and the cuts must be placed accordingly to avoid holes in the lamella and to ensure mechanical stability.

The thinning shown in Fig. 3.5 (e) is performed in three steps with decreasing ion beam current and decreasing section width. In comparison to the more standard H-shape (as seen from above while thinning) a T-shape lamella is cut so that contacting the sample later in experiment is easier. These are again adjusted to the appearance / size of the particle after transfer, but are approximately 1 nA and 5 μm, 300 pA and 4 μm, and 100 pA and 3 μm. At the beginning the lamella is tilted by 1.2° to the beam. Ideally, the last step should not be performed with any additional tilting, because unlike H-structured lamellae[3] a thin spot or a hole in the middle can cause strong bending and then the samples are not suitable for the in-situ experiments. Unfortunately, this also happens to very thin specimen, which would be ideal for high resolution. Another problem with very thin samples is that they often already bend extensively during the thinning process.

The process was optimized to achieve the largest possible area of uniform thickness in the lamellae. The process was stopped either when the protective platinum was completely removed during thinning or when the lamella achieved electron beam transparency, recognizable by certain contrast changes in the 2 kV or 5 kV electron beam image. If a platinum layer is still present after thinning, later prohibiting easy contact to the sample, it is removed with 100 – 300 pA and tilting the sample to −10 – 0°. Preview images and *Reduced Area Scanning* should be used to avoid long illumination of the sample from the side and possible damage during this alignment.

3.4. Description of setup and procedure of an in-situ lithiation process

3.4.1. Nanofactory STM holder

The in-situ lithiation experiments where performed in a NANOFACTORY STM-TEM holder. This kind of holder is introduced in the Publications by Larsson, et. al. and Svensson, et. al. [157, 197] Although some changes to the exact layout of the holder have since

[3] Attempts with H-shaped lamellas to work with thinning only on one side (more like a U) were not promising, because in the in-situ experiment the contact point to the lithium was not always clearly visible.

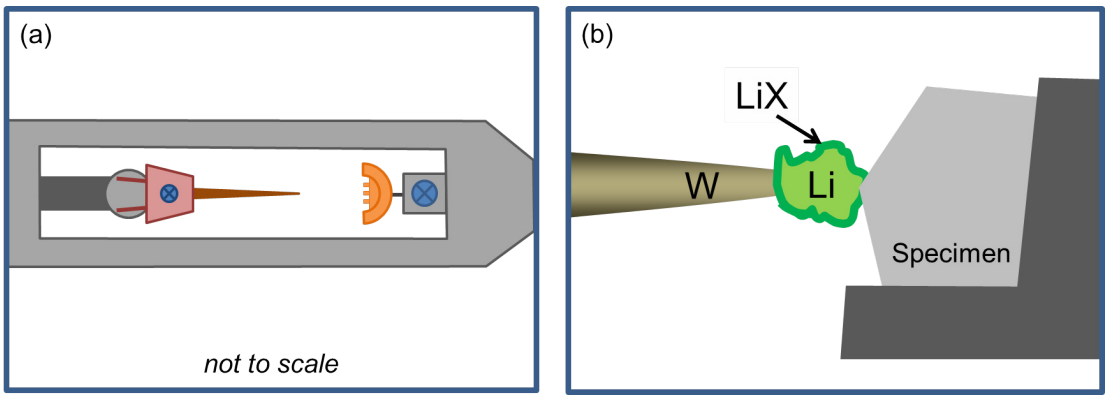

Figure 3.6.: Schematics of (a) the TEM holder used for the in-situ experiments and (b) how this holder is set up to form a small battery. (a) shows that the pole piece part of the holder is made up by a small hat with a screwed-in tip that can be moved by a piezo and a sample mount on the right with the possibility to apply a bias between them. (b) depicts the situation after both have been brought into contact, with the tip representing the current collector, Li/LiX being the anode/solid electrolyte and the specimen representing the cathode.

been made the principle is still the same. As shown in Fig. 3.6 (a) it is a single-tilt TEM holder which consists of a piezo-controlled movable hat that can carry a tip and a mount that can take up any kind wire or spring construction to introduce the sample into the holder. As is discussed in [197] the movement of the tip and its accuracy are subject to a lot of influences the most important being the tightness of the legs of the hat/spider. It is most important to know that the inertial sliding or coarse movement of the tip can bridge a maximum distance of 2 mm and the pure piezo elongation or fine movement of the tip is capable of 0.7 μm, which requires a close installation of the sample.

With the holder a bias can be applied between the tip and the sample mount - due to its STM-dedication. Despite this, the holder can be used for all kinds of other experiments, e.g. from this institute, ranging from inducing a temperature change [198], applying a mechanical load [199], measuring electrical characteristics of a sample [200] or as in this case using it for electrochemical experiments.

3.4.2. Experimental procedure

To conduct an electrochemical experiment inside the TEM the FIB-prepared, pre-characterized sample is glued onto the flattened part of copper wire with Pt glue[4], which

[4]Using a soft, flattened copper wire instead of a spring simplifies the process of getting the sample to the right height in the holder. Additionally, it sometimes allows some coarse adjustments of the sample

is then mounted into holder (right side of Fig. 3.6 (a)). The tip is formed by electrochemical etching of a tungsten wire mounted into the hat. Once everything, but the tip is assembled and positioned, the tip can then be scratched across a freshly cut lithium surface covered by n-pentane[5] (ChemSolute), which protects the tip from fast oxidation while the holder is introduced into the microscope's vacuum.

Once the holder is inside the TEM a micro-battery as shown in Fig. 3.6 (b) needs to be assembled for the lithiation process. This requires contact between tip and sample with the lithium then acting as anode, the slightly reacted LiX surface as the solid electrolyte[6] (compare sec. 2.2.4) and the sample being the cathode. To get tip and sample into contact almost the full distance has to be covered with the coarse movement mode while ensuring that the tip is and stays on the same height as the targeted point of contact. This can be assured by using tilt, wobbler and/or focus as also described in [157]. Final contact can then best be made in bright field imaging conditions by lowering the tip slightly, carefully approaching until a slight overlap of sample and tip occurs and then lifting the tip. The moment of contact can be determined by a change in the movement behavior of the tip as well as the movement of the bending contours in the sample. During the experiments this should be retested by a small tip movement every once in a while, because drift and cross-talk can lead to loss of mechanical contact.

The experiment can be controlled through the bias applied to the sample via a KEITHLEY SOURCEMETER while the tip is connected to the ground of the microscope. To keep experiments comparable and to counteract possible charging of the sample by the generation of secondary electrons (compare e.g. [202]) the sample was brought to $-5\,\mathrm{V}$, while recording an in-situ video under bright field conditions. To stop the reaction it was most effective to remove mechanical contact. This can be interpreted as the general proceeding with characterisations possibly carried out in pauses, if not otherwise indicated.

Afterwards the sample was first post-characterized in the single-tilt holder before exposing it to atmosphere again, then removed, the copper stem cut off and built into a sample holder and either directly post-characterized by all kinds of techniques or stored in the vacuum pumping stand as the residual lithium at the point of contact otherwise creeps over the sample and reacts (compare sec. A.8).

It has to be taken into account that the controller of the STM-holder is a big electronic device with sufficient electromagnetic fields to influence the EEL spectrometer. If EEL spectra therefore are supposed to be recorded the tuning has to have been per-

orientation to emulate a second-tilt axis though this requires steady hands. The fact that the sample needs to be glued for this is a necessary trade-off – that cost some in-situ sample in the process of removing the copper stem to make it post-characterisable.

[5] In principle, the n-pentane protects the Li like the oils it is sometimes stored in as it is also a pure hydrocarbon. The difference is that it evaporates quickly and therefore vanishes fully inside the vacuum.

[6] Liquid electrolyte has been used in many in-situ electrochemistry publications, but this can lead to many practical problems as tested out by Timo Wuttke [201] and has other disadvantages.

formed under unchanged state of the controller. This includes things like power status and position of the controller in the room. Some influences can still not be excluded as the controller can introduce some high frequency oscillations that can not be corrected and therefore influence the width of the peaks by temporal broadening during the acquisition, which worsens the spectral resolution.

4. Using electron energy loss spectroscopy to investigate a $LiMn_2O_4$-$Li_{1+x}Mn_2O_4$ phase boundary

EELS investigations on the structures occurring during the in-situ experiments of this work and the examination of phase boundaries, especially lithium variations as well as manganese valence and also general stoichiometry fluctuations play a decisive role in the results. Since there was no experience with those characterizations regarding $Li_xMn_2O_4$ materials in our institute, different known methods were tested in detail. It had to be investigated which methods could be used (maybe also in-situ), how stable these methods are under the present conditions and how reliably the data can be extracted from the in-situ samples that were not optimized for EELS investigations alone. This chapter therefore also includes some discussion elements, so that the next chapter can focus on material science results and EELS can just be viewed as an experimental method like many others.

For this purpose, this chapter relies on data, which will only fully be explained in a later chapter (see paragraph 5.2). This is data obtained from an in-situ lithiated sample with a clearly visible boundary inside the region of interest. This boundary area was recorded over a large area and at relatively low magnification with spatially resolved STEM-Dual-EELS, resulting in four-dimensional data sets, i.e. *Spectrum Image (SI)*, of this area. Within the SIs further away at opposite sides of the interface can be used as the two different phases of the reaction. So using this data the different methods can be explained and tested for their suitability.

To generally motivate the use of EELS to investigate those different material properties mentioned above, fig. 4.1 based on data measured by Paterson and Krivanek show the EEL spectra of differing manganese oxides. All kinds of changes in the peaks of `O-K` and `Mn-L` are visible for the shown common manganese oxides (MnO, MnO_2, Mn_2O_3 and Mn_3O_4) of different valence (2+, 4+, 3+, 2.66+). The strength of these changes and the different shape of the eight different edges already makes it clear that there are different possibilities to draw conclusions about the basic properties of the sample.

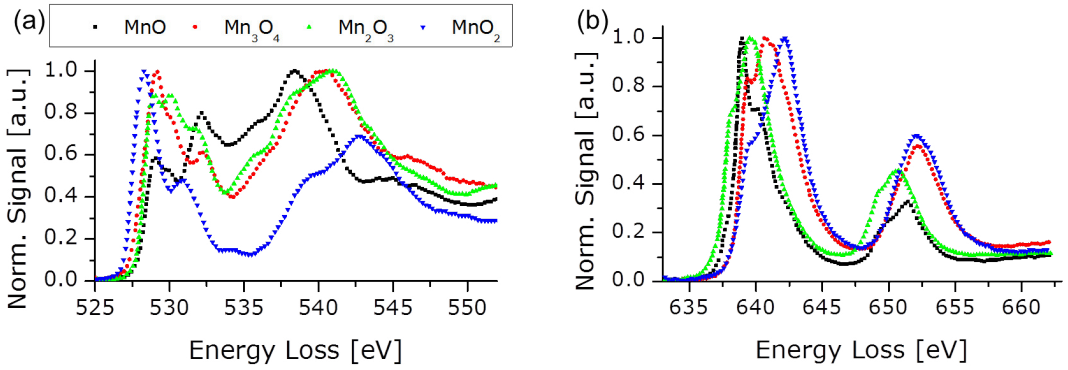

Figure 4.1.: EEL spectra from different manganese oxides (extracted from [203]). The spectra show the combined influencing factors, for example different stoichiometries and thus valences, but also coordination. The lower energy losses correspond to the O–K-edge and the higher ones belong to the Mn–L-edge to oxygen and the spectra were recorded with energy resolution better than 0.5 eV and therefore show some more fine structure than the spectra of $Li_xMn_2O_4$ shown later.

4.1. Comparison of the spectra of both areas

As already mentioned above, the data used in the following demonstration are not single point spectra. Instead, the data[1] from fig. 5.8 is used, since here the interface is located vertically and approximately in the middle of a $(520\,\mathrm{nm})^2$ large area with 100x100 pixels and thus both areas can be easily separated.

This has the advantage that it is not necessary to compare spectra that are collected from different samples and under different conditions. Instead, the spectra are obtained under the same beam conditions, same thickness, comparable orientation, etc. This is also one of the disadvantages of drawing conclusions by direct comparison of EEL spectra, since it is not always easy to ensure the same conditions [204].

In Fig. 4.2 the four important edges and additional features of the $LiMn_2O_4$ and additionally lithiated $Li_{1+x}Mn_2O_4$ are plotted for comparison. In fig. 4.2 (a) the full energy range of 0 – 70 eV is after the data has been deconvoluted. Besides the changes visible in the elemental edges highlighted in the square and magnified for fig. 4.2 (b) two additional significant changes are visible. On the one hand, the peak in the region of about 10 eV decreases into a shoulder upon lithiation. This energy range is commonly attributed to intraband transitions [205, 206] and changes are also observed in other lithium-containing energy materials (compare $LiFePO_4$ [207, 208] or Li-Mn-Ni-Oxide

[1] 2.5 mm-aperture; dual EELS pixel recording times: 0.005 s (low-loss) and 0.02 s (high loss); FWHM roughly 1.3 eV; dispersion: 0.1 eV/ch; $d = 0.8t/\lambda$

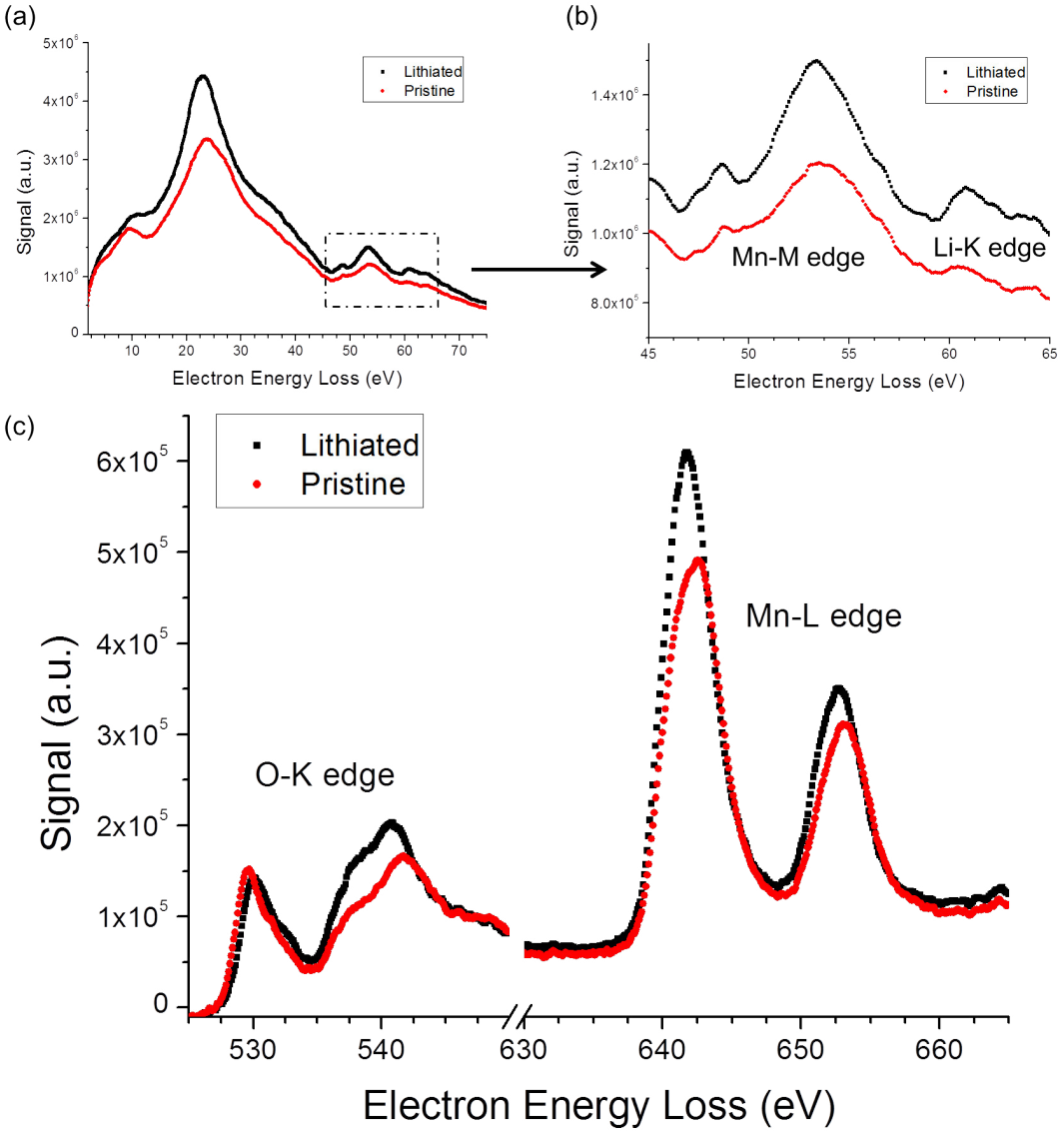

Figure 4.2.: Overview of different changes between the region of pristine material $LiMn_2O_4$ (red) and additionally lithiated $Li_{1+x}Mn_2O_4$ (black). The low-loss data was deconvoluted and in the high-loss range a background correction was performed. Besides an intraband transition and shifts in the plasmon area (a), the element-specific peaks of Mn−M and Li−K (a,b), O−K_a, O−K_b, Mn−L_3 and Mn−L_2 (c) and their characteristic changes are shown.

spinels [206]). On the other hand, a shift and slight change of shape of the most probable energy loss, i.e. the plasmon peak is observed.

If we look at the area of the manganese M (Mn−M) and lithium K (Li−K) edge, shown enlarged again in Fig. 4.2(b), more precisely changes can be seen in both edges. For the Mn−M starting at about 45 eV with its maximum at about 53 eV, the *pre-peak* is more pronounced, while the size of the entire edge changes little. This is clearly different for the Li−K, which is shown at 58 eV. Although it lies on the spurs of the previous manganese edge, it is already clearly recognizable in its original state and, as expected according to Eq. 4.5, shows a clear increase in size during further lithiation, which also confirms the successful lithiation.

The two further edges in fig. 4.2 (c) belong to oxygen and manganese. The oxygen K-edge (O−K) consists of two parts (within this resolution): the pre-peak and the main edge, which has a more complex shape. In the literature, there are differing names for these edges, depending on how highly resolved the spectra are and which features are of special interest. In the following, however, the first peak is designated by the common O−K_a, which is marks the start of the edge, and the second peak is designated O−K_b. One can observe during lithiation that the oxygen edge shifts by 0.5 eV from 529.6 eV to 530.1 eV. In addition, there is a clear change in the relative intensity of O−K_a and O−K_b, whereby the pre-peak is much more pronounced in the lithiated case. The formation of these partial peaks and their exact meaning with respect to the individual energy levels in oxygen are explained in detail in [209]. For a detailed interpretation, however, a better energy resolution is missing in the case of these data.

The manganese L-edge (Mn−L), consisting of the two peaks Mn−L_3 and Mn−L_2, shows a shift, just like the oxygen edge during lithiation, but in the opposite direction to lower energies. In the case shown in Fig. 4.2(d) this corresponds to a change of 0.9 eV from 642.7 eV to 641.8 eV. The lithiation also affects the shape of the Mn−L_3 peak, which takes on a much more symmetrical shape when the Mn^{3+} fraction is increased by lithiation. [2]. In addition to this, the L_3/L_2 ratio increases, i.e. the ratio of the integrated surfaces under the edges Mn−L_3 and Mn−L_2.

4.2. Low-Loss Methods

The spectra of low energy loss already shown in para. 4.1 can be used for a number of different evaluations. In addition to the identification of the plasmon center and the chemical quantification, for which a detailed explanation follows, this range can be routinely determined by means of a standard function in Digital Micrograph to determine the thickness of the sample t in relation to the mean inelastic scattering length λ. Physically, this method is based on $I(t) = I_0 \cdot \exp(-t/\lambda)$ (the LAMBERT-BEER

[2] $LiMn_2O_4$ at a valence of 3.5 corresponds to a 1:1 mixture of the Mn^{3+} and Mn^{4+} ions, while $Li_2Mn_2O_4$ at a valence of 3 has only Mn^{3+}

LAW, e.g. in [148]), so that the thickness of the sample can be determined by integrating the intensity of the zero loss peak I_0 and the inelastically-scattered intensity in the low loss spectrum I_t. So that

$$t/\lambda = -\ln\left(\frac{I_t}{I_0}\right) \tag{4.1}$$

can be calculated. Since the intensity decreases by orders of magnitude towards higher energies and the correlation is exponential, the dispersion almost doesn't matter, though the value remains an estimate. For manganese, λ is approximately 135 nm (see sec. 6.2 based on [150]) with the usual sample thicknesses used in TEM t being up to 1.5, depending on the application.

4.2.1. Plasmon center

As already shown in fig. 4.2, the lithiation of $LiMn_2O_4$ results in a significant shift of the plasmon peak, which can be used to localize the interface. This is shown in fig. 4.3, which is based on the data used in the previous section. To generate this data, a Gaussian function was fitted to the deconvoluted plasmon peak at each point on the map within `Digital Micrograph` using a 7.5 eV wide window (19.5 eV to 27 eV). The center is then extracted as the signal for plasmon maps. The color scale shows two clearly separated areas at about 23 eV and 24 eV which are additionally separated by a clear interface. Since the values are not used for any further calculations, the phenomenological use of a Gaussian that only describes the used energy window reasonably well has no consequences.

In this case, a more accurate quantification can be achieved by averaging the data vertically in fig. 4.3 (b) so that the standard deviation is also available as a statistical error. This data clearly reflect the previous visual impression and can be analyzed, once again phenomenologically, using a Fermi function of type

$$f(x) = A_2 + \frac{A_1 - A_2}{1 + \exp((x - x_0)/dx)} \tag{4.2}$$

and the values $A_1 = 24.03(1)$, $A_2 = 23.130(3)$, $x_0 = 223(1)$ nm and $dx = 23(1)$ nm, to allow for a flexible transition region in the fit parameters. Thus, the plasmon peak of $LiMn_2O_4$ is reduced by 0.9 eV during and the transition constant dx. It can be seen that 50% of the change is distributed over a width of about 50 nm. This quite localized considering the fact that the interface is not perfectly aligned in vertical direction and most probably does not have an interface parallel to the z direction.

Changes in the plasmon peak during lithiation are to be expected due to different known effects. For example, textbooks of electron microscopy (e.g. [148, Abs. 39.5])

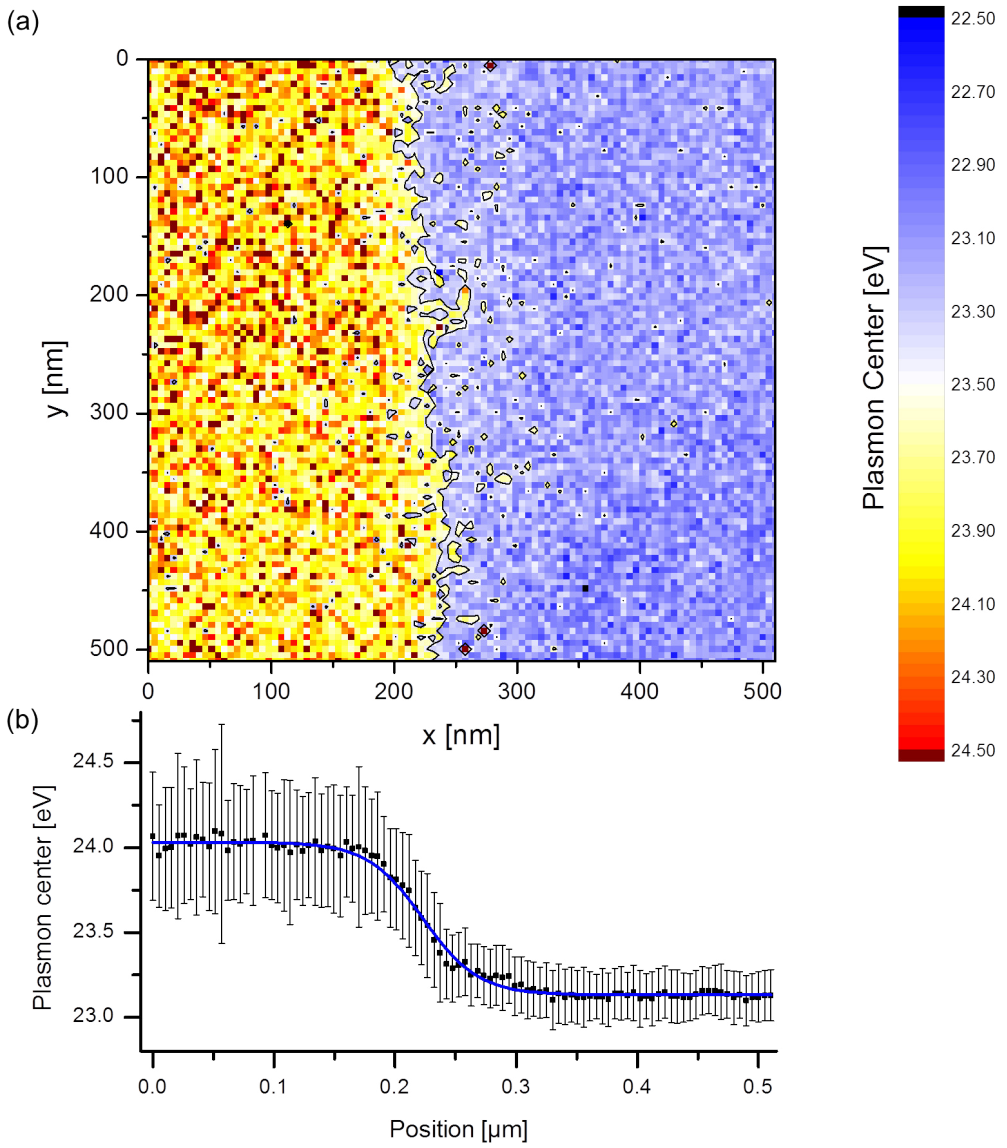

Figure 4.3.: Plasmon map of a vertical interface generated by in-situ lithiation. The additional lithium in $Li_{1+x}Mn_2O_4$ (right) generates a shift of the plasmon peak in comparison to the pristine $LiMn_2O_4$ (left). The shift amounts to almost a SI1eV as can be extracted from the vertically averaged data in the line plot below.

state a correlation between the average energy loss of the electrons $\overline{E}$ and the average nuclear charge number of the material Z in the form of:

$$\overline{E} = 0.7 \cdot Z^{0,36} \tag{4.3}$$

This suggests a lowering of Z by lithiation and consequently a reduction $\overline{E}$, which should also be visible as a plasmon peak shift. The other well-known relationship

$$E_\mathrm{p} = \frac{h}{2\pi}\omega_\mathrm{p} = \frac{h}{2\pi}\left(\frac{ne^2}{\varepsilon_0 m}\right) \tag{4.4}$$

between the plasmon energy E_p, the plasmon frequency ω_p and the free electron density n is only valid for free electron structures and can therefore not be applied to $LiMn_2O_4$, so that more insights would need support by simulations.

The increased standard deviation of the center of the gaussian fit in the left region can be explained by the broader shape of the $LiMn_2O_4$ plasmon peak, which leads to a less-well defined center. Physically, a more inhomogeneous material and thus a larger standard deviation would rather be expected on the additionally lithiated $Li_2Mn_2O_4$side on the right. However, a shift of the plasmon peak as in this case has elsewhere already been reported other lithium-containing materials. For example in the case of Kübel, et. al. on $LiFePO_4$, a shift of 0.3 eV between lithiated and unlithiated iron phosphate was observed, which corresponds to a third of the shift observed here. [208].

The significance of this clear change between the two stochiometries is therefore rather that this method provides an easy way to differentiate the two, while at the same being a low-loss method, which can generally be recorded with shorter exposure times, lower doses or less binning in evaluation. Due to the shorter times required for recording such a map, the suitability for in-situ experiments is thus more likely to be given than with approaches based on high loss data.

4.2.2. Chemical quantification

This work is experimentally based on changes in the lithium content of the samples. So the chemical quantification concentrates mainly on the low-loss region of the EEL spectrum, where the `Li-K` edge is found (see fig. 4.2 (b)). With the size of the edge and the periphery to the `Mn-M` edge this means that the lithium content can only be determined in comparison to the existing manganese, since oxygen has no visible edge in this area and a certain dispersion is required to make the quantification possible under these circumstances. Methodically, however, quantification according to the same principles as for the low-loss range (`Li-K` and `Mn-M`) can also be used for the high-loss range (`O-K` and `Mn-L`). For this some additional things like the edge shape or ELNES must be taken into account, though.

Since the quantification depends on the quality of the spectra, it should be mentioned that it is worthwhile to use the DUAL EELS also for the low-loss range. In these cases,

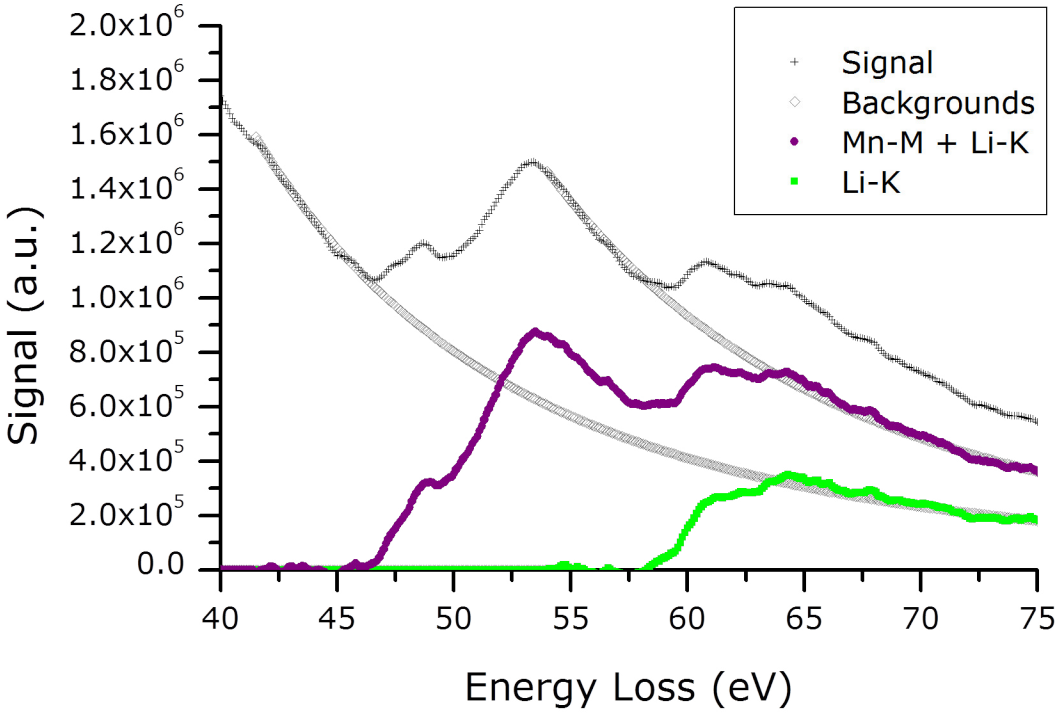

Figure 4.4.: Low-Loss EEL spectrum (black) of $Li_{1+x}Mn_2O_4$. After subtracting the background (gray) in the form of a power function, the manganese `Mn-M`edge (violet) is obtained, which still includes the lithium `Li-K` edge (green) starting at about 60 eV. The quantification is performed in the edge regions of homogeneous form at about 55 eV and 65 eV.

the integrated SPLICE function of DIGITAL MICROGRAPH is used to combine zero loss peak and signal. However, this excludes simultaneous recording of the high energy edges, so that it is necessary to weigh options, since sufficient spectral quality can also be achieved by subsequent binning.

Similar to EDX elemental analysis, stoichiometric determination based on EELS is based on two basic principles, which are linked in Eq. 4.5: The intensity I of an edge in the spectrum is proportional both to the local density of that material n penetrated by the electron beam and to the respective interaction cross-section of the material σ and the intensity of the incoming beam. Therefore, the relative atomic composition of two materials can be described as

$$\frac{n_{\mathrm{Mn}}}{n_{\mathrm{Li}}} = \frac{I_{\mathrm{Mn}}(\Delta_1)}{I_{\mathrm{Li}}(\Delta_2)} \cdot \frac{\sigma_{\mathrm{Li}}(\Delta_2)}{\sigma_{\mathrm{Mn}}(\Delta_1)} \tag{4.5}$$

where Δ represents the window over which the intensity of the edge was integrated. The exact interaction cross-sections and the expected intensities for edges that are further apart depend on further factors such as e.g. the spectrometer aperture angle β and the acceleration voltage of the TEM. For a more detailed discussion of these factors, please refer to the textbook on EEL spectroscopy by Egerton. [149, Abs. 4.5] However, their influence on the following measurements is also small, since in the following only measurements under the same conditions within a spectroscopy map are compared for which factors remain the same.

`Digital Micrograph` has an automatic calculation of the interaction cross-sections based on the recording conditions stored in the data. However, to exclude those parameters from this work, absolute quantification will be omitted, and only the above basic principle

$$I \propto n \tag{4.6}$$

will be used. This is also more intuitive for the use on $LiMn_2O_4$: doubling with doubled content in comparison to the theoretical relative change of the atomic content $33\%_{\text{at.}}^{\text{Li}}$ to $50\%_{\text{at.}}^{\text{Li}}$ and $67\%_{\text{at.}}^{\text{Mn}}$ to $50\%_{\text{at.}}^{\text{Mn}}$ when quantifying the `Li-K` and `Mn-M` edges when only lithium content changes. An experimental confirmation that this holds true explicitly for the `Li-K` edge has been demonstrated by Graetzet. al. [210] and also been used on lithium-containing materials. [211, 212]

In order to exclude thickness effects and since the two edges are very close to each other, a 4.5 eV wide area in front of the manganese edge and a 5 eV wide area in front of the lithium edge were used to adjust a monomial power function as a background, as shown in Fig. 4.4. For the integration of the edges, a window should then be selected which is not influenced by large changes in the edge shape like ELNES for all compounds occurring in the sample and in which this still applies even if a small `chemical shift` or energy drift occurs despite DUAL EELS and drift correction. For manganese, a window of 53 – 58 eV is suitable, while for lithium a 15 eV wide window starting with 59.5 eV worked well. The window is intentionally set relatively large to suppress the influence of noise at this smaller edge, but this requires a well adapted background for all occuring $Li_xMn_2O_4$ compounds.

The result of above choices can be seen in fig. 4.5. That the spectra already showed significant increase in lithium content is visible across the interface. A much higher binning (5x5) is needed because integration is more susceptible to noise than position determination by fitting. Even though a trend is visible, reliable quantification can only be done by vertical averaging (or summation), which then yields a line profile across the interface displaying two different levels of lithium content.

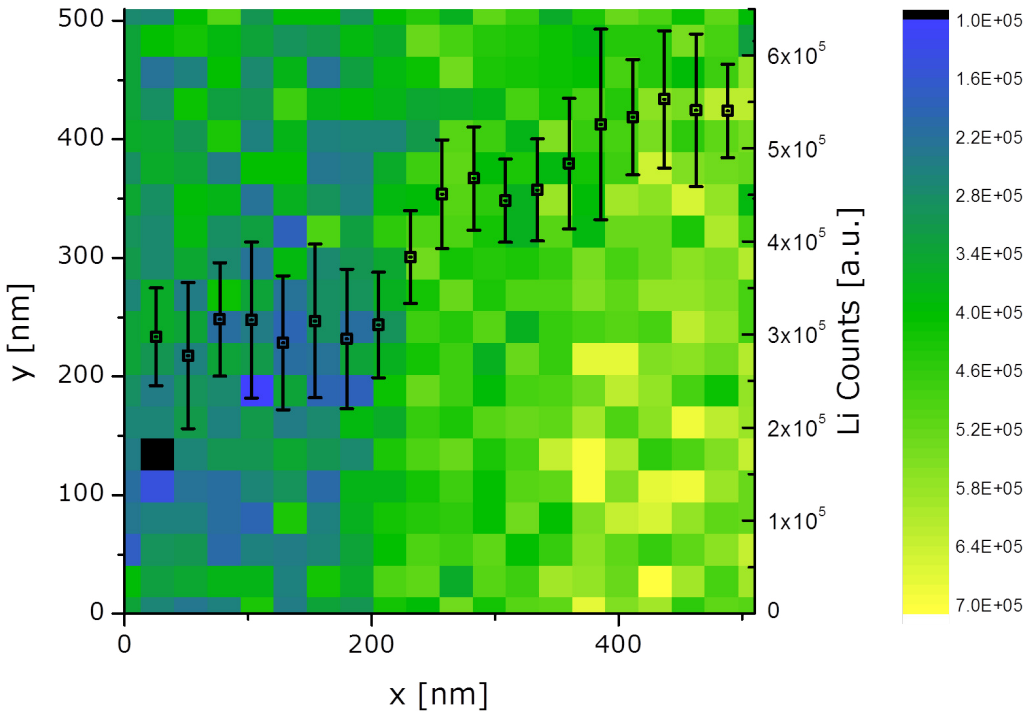

Figure 4.5.: Under the right circumstances lithium mapping becomes possible. Even with 5x5 binning in comparison to the plasmon map only the trend is visible, but the vertically averaged data in the line plot shows to plateaus and the standard deviations of both areas don't overlap.

4.3. High-Loss Methods

The prospect of gaining access to information about atomic bonds and local chemistry, rather than just the elemental composition, is one of the properties of EELS that set it apart from EDS, and one of the reasons why it is increasingly being used to characterize materials [150]. For this purpose the analysis of the exact edge shape of the involved elements plays a decisive role, because these are projected densities of state of the unoccupied states, which allow the above conclusions. The opportunities, which exist in respect to $Li_xMn_2O_4$ and their actual implementation, shall therefore be discussed in the following. Since manganese is a transition metal one would expect it to carry most of the chemical changes in the material and therefore show the most significant

changes.

4.3.1. Manganese L_3/L_2-Ratio

For the experimentally measured data the manganese L_3-L_2-ratio can be calculated with the help of a script for `Origin`. This is based on an implementation started by Daniel Mierwaldt, which was used in various ways to determine the L_3-L_2-ratio and the manganese valence in manganate-perovskite (see e.g. [200, 202, 213]). The procedure in the script and the exact processing of the data during the evaluation is based on a paper by Varela, et. al., who performed the calibration using $La_xCa_{1+x}MnO_3$ [214].

Theoretically, the edges of manganese should not differ much in different materials with the same valence, but experimentally (as mentioned in sec. 2.5) there is a dependence of the ELNES on other factors like the crystal structure. A very early paper from 1994 still showing this very nicely was published by Garvie and Craven [215]. Therefore, the above script was extended by further methods and calibrations, which were tested for their suitability for $Li_xMn_2O_4$. The procedure will be explained in the following.

It is possible to pass a large amount of spectra to the script, which should have been previously deconvoluted in `Digital Micrograph` to suppress thickness effects. Thus, binning of maps is not necessary to reduce the number of spectra, but only to make the edges contained in the data visible in such a way that fits converge well and the signal-to-noise ratio is low enough for integrations performed within the methods. A corresponding spectrum, which then also contains the `O-K` edge, looks like the one previously shown in fig. 4.2 (c), but with a much higher noise level, since much less binning is used for point spectra.

The script then starts to find the maximum in the data, i.e. the `Mn-`L_3 edge. This step serves to make it independent of absolute energy calibrations and to align all further energy windows relative to it. This is already the case for the next step, in which in a window 41 – 6 eV in front of the edge the background is adjusted and subtracted in form of a power function. Afterwards a position determination of the `Mn-`L_2 edge takes place by adjusting a Gaussian function relative to the maximum in the window 5 – 18 eV. This is refined by a fit in a window of -2 – 2 eV relative to the center of the previous fit. In contrast to Varela, et. al. [214], however, this step is repeated for the `Mn-`L_3 peak in the following and a variable distance between the two `Mn-L` edges is assumed. The two fit windows are -6 – 6 eV relative to the maximum and -2 – 2 eV around the center of the first fit. Fig. 4.6 shows an example of the result that fit routine, so that the energy difference between `Mn-`L_3-`Mn-`L_2 is also a measure available.

To remove the continuum contributions of the spectrum, the data is then normalized by dividing by the 3 eV average behind the white lines. This then allows the substraction of a HARTREE-SLATER function exported from `Digital Micrograph` for the `Mn-L` range, as used by Varela, et. al. However, other groups also use a differing correc-

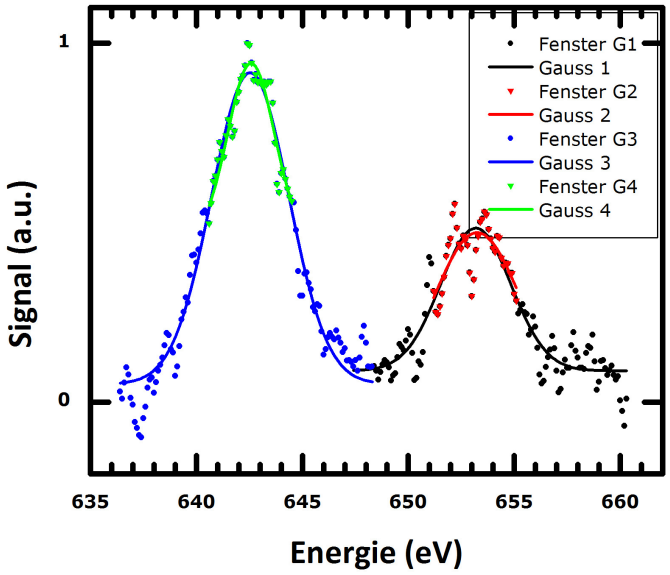

Figure 4.6.: Fit and position determination of the two Mn−L edges. Image shown is just a regular example of the output produced by the script for a random point spectrum. The narrowing fit windows are indicated by color change.

tion for this (comp. van Aken, et. al. [216]), that is also implemented, where a linear combination of two arctan functions in the form

$$f(\Delta E) = \frac{h_1}{\pi}\left[\arctan\left(\frac{\pi}{w_1}(\Delta E - E_1)\right) + \frac{\pi}{2}\right] + \frac{h_2}{\pi}\left[\arctan\left(\frac{\pi}{w_2}(\Delta E - E_2)\right) + \frac{\pi}{2}\right] \tag{4.7}$$

is used. The values are chosen in such a way that the two turning points of the function E_1 and E_2 are located on the first turning points of the previous Gaussian functions. The value $w_1 = w_2 = 1$ should approximately correspond to the spectral resolution or FWHM of the zero loss peak. The contact points of the function with the data of the spectrum are given by the subtracted background in front of the edges, the previously normalized area behind the edges and the minimum between the two Mn−L peaks averaged over ten points. The results for both methods can be compared in the appendix (see fig. A.2). Although the substraction of this continuum contribution by both functions also reduces the effects of sample thickness, deconvolution of the data should not be omitted for better comparability unless the samples are explicitly very thin like for pure STEM investigations.

After the previous steps the areas under the two Mn−L white lines can now be determined by integrating them numerically of 4 eV, 8 eV and 10 eV width, which depends on the particular calibration to be used (cf. [92, 214, 217]). An error estimation is possible

by doing the same integration after shifting the windows by e.g. 1 eV or by varying the size of the windows by 2 eV up and down as in this case. This helps to estimate noise sensitivity.

Two factors that limit the usability of this method in practice are the following: It turns out that for materials that contain other transition metals, some of these also change their valence, although this was not expected theoretically (e.g. nickel containing Li(TM)O_2). This is not the case here, but needs to be kept in mind if the methods should be applied to other materials. In addition, oxygen apparently also plays a more decisive role in the uptake of electrons, since in $Li_{1-x}CoO_2$ the cobalt edge appears quite constant despite lithiation (compare [204, para. 8.4.2]). Furthermore, the high sensitivity of the integration of the edges to the signal-to-noise ratio is a problem, especially if good spatial resolution has to be achieved and binning the spectra a little more is out of question. For atomic resolution, additional processing of the spectra like PCA (see [214]) is needed to suppress the noise.

One way to suppress the effects of noise and also get a better quantification of the error would be to fit a function to the peaks (for comparison tried here with a simple Gaussian functions). If one only uses the maxima of the functions resulting from the fits, promising results are already obtained (see later fig. A.4). However, in order to be able to use them, a separate calibration using reference standards would be necessary. Furthermore, it should be considered whether in this case the use of other functions can describe the full shape of the two edges even better and one can then use the calculated edge area instead of the maxima.

Using the L_3/L_2 ratio for the calculation of the manganese valence is also dependent on the width of the edges, which of course also depends on experimental resolution i.e. zero-loss peak, because a fixed window width is used for integration. In addition, the width of the two edges also depends on the structure of the materials used, which means that either separate calibrations have to be made or calibration measurements on other materials have to be found. Riedl, et. al. have compiled a very detailed overview of the effects of slightly different methods and other effects [218].

Therefore, this data is not usable without suitable calibration. Therefore, Fig. 4.7 shows measurement data and calibrations of the three selected routines deemed most suitable taking into account our experimental conditions. They all chose a differing mathematical function to describe their calibation data [92, 214, 217]. But on the other hand, they also chose three different methods of calculation.

Varela, et. al. has multiple different valences in the range of three to four, which can be calibrated with the linear function

$$|\text{Varela, et. al.:}| \qquad R^{\text{V}}_{\text{Mn}} = 5.0(4) - 0.73(11) \cdot V_{\text{Mn}} \tag{4.8}$$

which is good at confirming the expected general trend and uses a simple fit function. Even though it is not calibrated by lithium containing samples, it has previously been

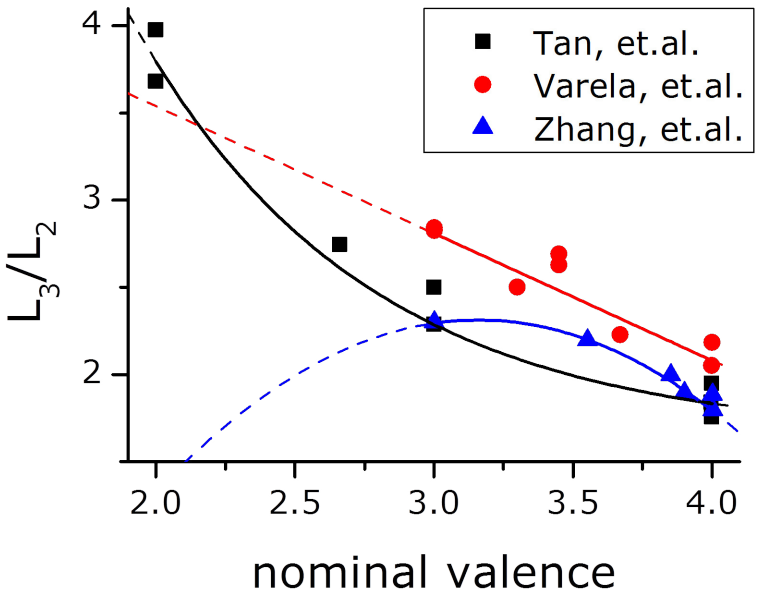

Figure 4.7.: Calibration data and curves from the literature (see [92, 214, 217]), which show how much the reference curves and data can differ depending on the method and how important it is to use a variety of suitable materials with different valence values during calibration.

used in other publications on $LiMn_2O_4$ [219]. The data from Tan, et. al. has the great advantage of extending over the broadest valence range. It is apparent in the curve shape of

$$|\text{Tan, et. al.:}| \qquad R^{\text{T}}_{\text{Mn}} = 24(9)\cdot\exp\left(-V_{\text{Mn}}/0.83(11)\right) + 1.64(8) \tag{4.9}$$

that this yields a higher sensitivity for changes in the anterior range near +II in comparison to +IV. Unfortunately intermediate values for calibration between +III and +IV are missing. And since the calibration data of Zhang, et. al. are very similar at both points measured, a strongly changed calibration curve could have been expected when also calibrating in this region. The curve

$$|\text{Zhang, et. al.:}| \qquad R^{\text{Z}}_{\text{Mn}} = -0.734\cdot(V_{\text{Mn}})^2 + 4.638\cdot V_{\text{Mn}} - 5.014 \tag{4.10}$$

has a square shape for this reason. Such a shape is also observed, for example, in another case on pure manganates, which could indicate that this method is problematic for manganese evalutation, since the function is not injective [220].

This one of the general conditions for using these methods for manganese valence determination, because if the data does not follow a monotonic trend in the range of

interest it is not unambiguous and invertible. Another problem with inverting calibration data is that the arithmetic error becomes very large due to the inversion of the curves, which are affected by errors. Thus, e.g. the inversion of the linear function alone results error bars of $\sim 0,5$ in the absolute values of valence, while the trends are working. Because of this reason this inversion-error is not permanently shown in the following data, because it would dominate any data quality errors and dominate any data trends that are otherwise cleary there looking at the pure $\mathrm{Mn{-}L_3/Mn{-}L_2}$-ratio. But even if only the statistical error is shown, which results from calculations with more than one datapoint, the absolute value error of the peak ratio method has to be kept in mind.

4.3.2. Distance between O-K_a- and Mn-L_3-edge

As already shown and explained in par. 4.1, oxygen plays a more active role in Li(TM)O_2 compounds than expected. While basic chemistry always assumes a fixed valence of minus two for oxygen, the EELS shows significant changes of the edge shape. But the $\mathrm{O{-}K}$ edge is reported to include transition particularly in the pre-peak associated with a transition from 1s-states to 2p-states hybridized with manganese [209]. These can also be used to draw conclusions about the manganese valence. Combining this with the fact that both edges move into opposite directions (compare fig. 4.2 again) upon changes in the oxidation state the energy difference between the oxygen pre-peak i.e. $\mathrm{O{-}K_a}$ and the $\mathrm{Mn{-}L_3}$ white line can be used as valence change mapping method. The fact that this method relies on edge position instead of area under the curve allows the comparison of different calibration strategies.

For example, the asymmetry observed in the $\mathrm{Mn{-}L_3}$ for a mixed manganese valence like $Mn^{3.5+}$ previously described is a disadvantage for both methods. It can affect both the placement of the integration window and maximum determination. But determining the maximum of an edge should not be influenced by zero-loss peak width deviations as much as an integration method. Thus, the paper by Zhang, et. al. shows that even with a ZLP of 1 eV ZLP and $0.2\,\mathrm{eV/channel}$ dispersion good results in valence quantification can be achieved [92].

These conditions are much closer to those that can be achieved with the in-situ samples. The materials used by Zhang, et. al. are different materials $(0.3-0.4t/\lambda)$, each with a different crystal structure with manganese valence of three (Mn_2O_3, MnOOH) and manganese valence of four (twice MnO_2) and four different cryptomelanes (valences of 3.55, 3.85, 3.85 and 3.9), which were produced by a combination of manganese oxide with small amounts of potassium, molybdenum and vanadium. This also better represents the conditions expected in experiment. On the one hand, calibration is performed on samples that are mainly manganese oxides with few additions of other materials. In addition, different crystal structures are also taken into account in the calibration.

An evaluation of the data with respect to the oxygen edge has been included into the script and is automatically performed if the oxygen edge is present in the data by choosing a suitable dispersion during experiment. In the implementation this means that the spectra may start at 525 eV at most. This allows the fitting of several Gaussian functions to the oxygen edge in the window of 525 – 550 eV. A Gaussian function is fixed at the position of 530 eV for the first iterations to ensure a better fit and to know which peak converges to the pre-peak and only in the course of the process is this limitation removed. Once the position of the pre-peak is found, its position is determined more accurately using a PSEUDO-VOIGT function (linear combination of LORENTZ- and Gaussian function) in a window of -1.5 – 1.5 eV, since this function calculates the position of the pre-peak more accurately in case of a very pointed shape. To intentionally show a non-ideal example a fit is shown in fig. 4.8. In this case noise is still very present in the oxygen pre-peak, but the fit still converges at an acceptable position, even the edge shape is not well described. Still peak position determination of the pre-edge is much more prone to runaway fits at higher noise than the $\mathrm{Mn\text{-}L_3}$ position determination and is the main driver of errors in the data. Though, the advantage is that those fits always yield data that is orders of magnitudes of in the valence calculation afterwards and can be filtered out well.

The relationship between the manganese valence the energy difference ΔE between the positions of the $\mathrm{O\text{-}K_a}$ and $\mathrm{Mn\text{-}L_3}$ edges is given as

$$\Delta E = 2.65(6)\,\mathrm{eV} \cdot V_{\mathrm{Mn}} + 103.45(23)\,\mathrm{eV} \tag{4.11}$$

by Zhang, et. al. [92]. As demonstrated in fig. 4.6 the fits also work with noisy data as long as the pre-peak is already visibly pronounced against the background noise. Experience shows that the fit of the oxygen edge works well upwards of an intensity of about 500 – 1000 1 after the background has been subtracted, with a slight dependence on the signal-to-noise ratio. The influence of noise will be later discussed in more detail when comparing the results of both methods. But the binning of the data before evaluation should be done so that sufficient counts are present in each pixel spectrum. Experimentally, however, the acquisition time of the spectra should ideally be chosen rather low, but so that the oxygen edge just barely becomes visible, since then corrections regarding drift and more can be made separately on the individual spectra before binning.

Since the oxygen edge, as summarized by Kurata and Colliex, extends over a range of up to 50 eV and the prepeak in particular is associated with the transition of hybridized states this method also has its limitations [209]. As soon as significant amounts of other transition metals are present the $\mathrm{O\text{-}K}$ edge would consist of a combination of different transitions and a conclusion on the manganese valence alone could be impossible.

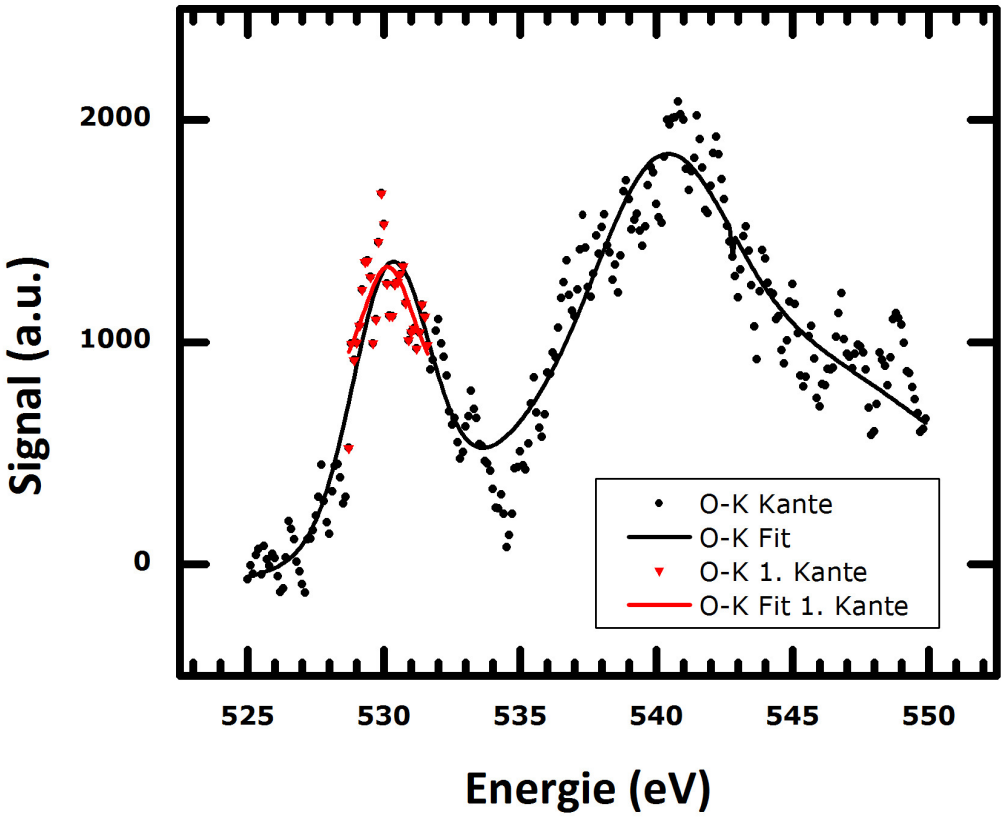

Figure 4.8.: Original plot produced by the fitting routine implemented for the O–K_a pre-peak position determination. Black marks the measured spectrum and the initial multiple Gaussian fit of the whole O–K-edge. The following separate fit of the determined pre-peak data is shown in read and fitted with a sharper function.

4.3.3. Additional possible methods to determine manganese valence

Although the two methods described in detail above represent the most frequently reported or most promising materials for our experimental questions numerous other methods that can be used to identify manganese valence. Some of these were also tested in the course of this work, but were not implemented in the end. Nevertheless, these will be briefly discussed here to classify them and explain why they were not used or to show possibilities to extend the analysis in the future.

The basis of the second method is the shift of the Mn-L_3 edge when the valence changes. A **absolute quantification of the edge position** therefore also allows conclusions about the valence (see e.g. [217]). The problem with absolute energy quantification is that it requires very careful calibration. This should include an edge of an independent material to recorded to use as a calibration standard. This was not the case in our samples. Additionally, depending on the energy differences that need to be quantified high demands are placed on the dispersion tuning.

To get around these problems, according to Zhang, et. al. the **distance between Mn-L_3- and Mn-L_2 edge** can be used. However, this method is less sensitive, especially in the range of valences between +III and +IV, and an inversion for valence determination by the curve shape might prove difficult [92]. Since the positions of the two edges were automatically determined in this work anyways, it was confirmed that it proves not to be sensitive enough for our use case.

In an extensive comparison of different methods on iron (see [216]), the **Adjustment of a linear combination of reference spectra (MLLS)** was determined as the best method. However, an absolute calibration of the energy scale is once again necessary, because small energy drift can already lead to deteriorating fit quality, and the reference spectra of differing materials must be recorded. Additionally, the reference spectra need to approximately match the recording parameters of the collected data for a good fit. Furthermore, MLLS is based on the fact that the experimental spectra also represent a linear combination of the references, which need not be the case with the fine structure of an edge.

According to Graetz, et. al., the fine structure in the form of the Mn-L edges could be used to determine the occupation of the 3d band by evaluating the **normalized total intensity of both Mn-L edges**. The data behind this is intriguing, because it gives a general relationship for different transition metals at the same time and over a broad range of d occupancy [221]. This method without calibration was also programmed and tried, but due to the integration also proved to be very noisy. Another attempt also relying on integration, which would have been very easy to implement is the direct substraction of two *slices* (i.e. images including the signal of a certain energy region of the EEL spectrum) of the intensity of the edges of Mn-L_3 and Mn-L_2 in Digital Micrograph. This showed no contrast at useful binning, although the idea behind this method was successfully used for imaging in EFTEM on manganates [222]. Own

attempts to bypass the noisiness of the integration by determining the **height ratio of the Mn−L_3 and Mn−L_2 peaks through a fitting-based approach** looked promising (see fig. A.4 in the appendix), but need to be calibrated on the basis of a larger library of standards. And while working well in one sample in give a well-distinguishable measure of both sample regions the pure height measures is certainly dependent on recording conditions, so that transforming it into a fitting-based approach that yields area under the peaks would have to be considered.

The **ELNES-form of the O−K-edge** again contains a very complex structure due to the strong hybridization with manganese, from which according to Kurata and Colliex almost all binding information can be deduced [209]. The method used in this thesis is an example of this, but with a good energy resolution in the order of a FWHM of 0.3 eV more information could be extracted. For example about the **distance and relative intensity of O−K_a- and O−K_b-edge** [214]. However, this method requires a good fit of the O−K_b edge, which did not work out so reliably when trying to implement it. In addition, a new calibration would also be required for $Li_xMn_2O_4$ due to the materials. This and the drive to understand the fundamental mechanism prompting the changes in the O−K edge have led to the start of a cooperation with **simulation-based generation of EELS reference spectra** to compare characteristic features in the edge to the measured data in the continuing CRC project. Many theoretical publications on the simulation of EEL spectra that is not totally tailored to our research questions has already been performed, though, e.g. the Li−K edge [223] or low-loss region [224].

4.3.4. Sensitivity of the methods for valence determination and interface detection

Calculation of all above mentioned, scripted methods takes time, especially if one aims for the highest possible local resolution and therefore lowest binning, which also means the highest possible amount of evaluated spectra. Further, it is important to know why a certain *SI* doesn't show any variation when evaluated. Whether it is because the underlying spectra are of poor quality or there is just no existing material change. For this reason a rather arbitrary measure of spectrum quality has been introduced into the evaluation routine. It works by calculating the standard deviation of the area used for the background fit in front of the Mn−L edge after the background is removed. This value should get smaller and smaller with decreasing noise and to make the value a little more descriptive and comparable it is divided by the mean value of the manganese edge behind the white lines, that is also used to normalize those (comp. fig. 4.6). This way it is easily explainable that no useful quantifications can be performed if the noise value is close to the signal of the edge even if the white-lines are more intense than the rest of the edge.

Based on the data already for all this chapter, Figure 4.9 shows some noise values for different binning in the data. Median spectrum number is just an arbitrary descriptor of

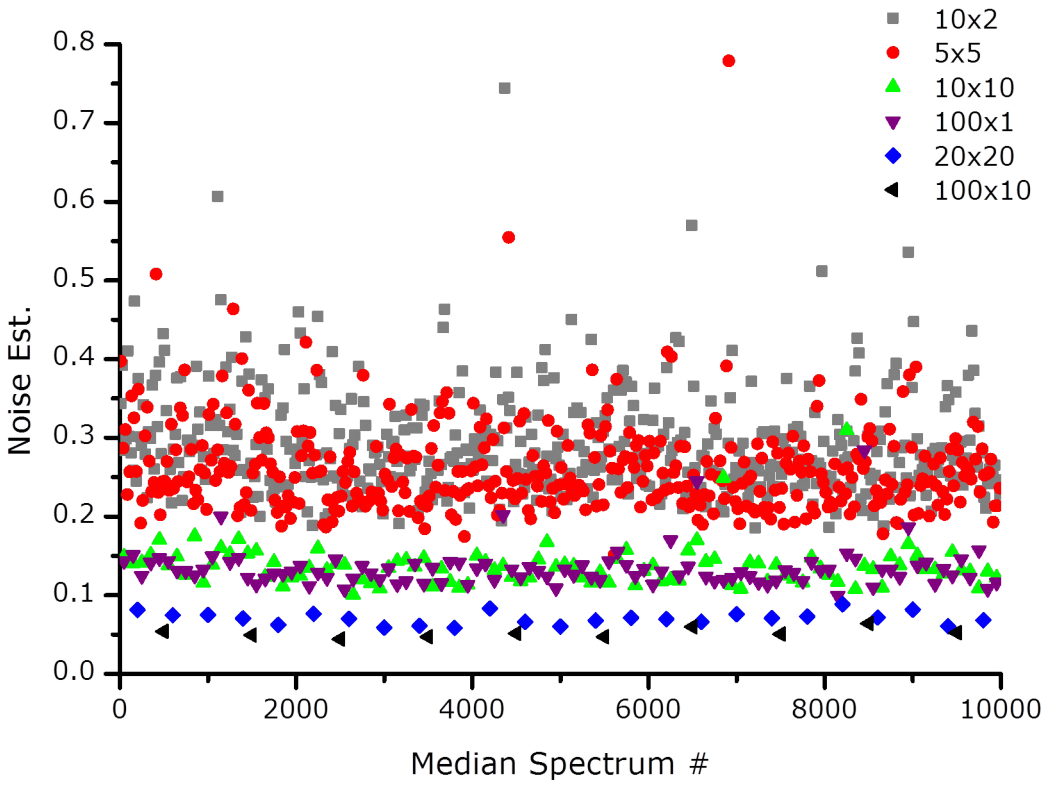

Figure 4.9.: Results of the noise estimation data of the spectrum image used in this chapter. As the data shows binning more spectra leads to a reduced signal-to-noise ratio as would be expected. The plot also shows that for this data any binning of less than 20-25 spectra (not shown here on purpose) and therefore noise estimate higher than 0.5 would make it reasonable not to expect a reliable quantification result.

the spectrum in the row of all 10000 spectra that means that spectra at same x position are binned data based comparable region of the sample, because the two-dimensional data is exported by `Digital Micrograph` as a row of vertical lines. The basic trends one would expect for the noise estimate. First, a higher binning leads to a lowered relative noise. Just taking a quick look at the plot the noise also looks stochastic as binning four times more spectra leads to halving of the noise estimate (compare green/violet with blue).[3] This is not totally surprising as the way the noise estimate is set up, it should be proportional to the inverse of a standard signal-to-noise-ratio. Second of all, binning the same number of spectra leads to a comparable noise estimate as can nicely be seen for 10x10 binning in comparison to 100x1 binning (green/violet). This has the advantage that a high resolution in one direction is desperately needed it can be achieved by an asymmetrical binning. Third of all, looking at $\propto 1/\sqrt{N}$ relationship another way it is visible that benefits of binning wear of quickly. Comparing 5x5 binning with 10x10 binning yields a dramatic improvement, which is also visible in the noise estimate data itself, whereas 20x20 to 100x10 has a really high payoff resolution-wise. Given the acquisition times typical for a spectrum image (often $20-40$ min) quadrupling the pixel number at otherwise constant conditions parameters to double the resolution is not feasible at a certain point. This illustrates why it is so important to find the method still working reliably at a higher noise level.

Taking into account that the region at hand used for this analysis should mostly consist of two different stoichiometries this can be tackled by looking at the resulting histogram of all implemented methods and check at which binning it becomes bimodal. This is shown for three different approaches in fig. 4.10 (a). The first thing to note is that manganese L_3/L_2-ratio seperates into a two peak distribution at a very high binning, which demonstrates that all methods show the same trend and are consistent. But at a resolution of a then 5x5 map this is not a feasible method in comparison to the other two histograms, that are much clearer at 16x more pixels or four times higher resolution. That both are almost equivalent is not surprising as they both involve the $\mathrm{Mn}\text{-}L_3$ peak. The obvious advantage of the third method (red) as shown in the map in fig. 4.10 (c) is that it can be translated into a manganese valence value by the literature-given calibration. Nonetheless, it should be noted that the two maps are identical except for remaining noise, especially in distinguishing the two phases and in identifying the position of the interface. This will be taken advantage of in the following chapters as sometimes higher dispersion EELS data has been recorded that then doesn't include the oxygen edge. But as shown can still be analyzed at the same noise constraints excluding a calculation of manganese valence value.

Same holds true for plasmon maps previously shown (comp. fig. 4.3) that also yield a high resolution due to their high signal in the low-loss region. They can therefore also

[3] If the noise is simply stochastic it should only grow by $\sqrt{N}$ by summing up N spectra, while the integrated signal of the manganese is proportional to the amount of spectra ($\propto N$.)

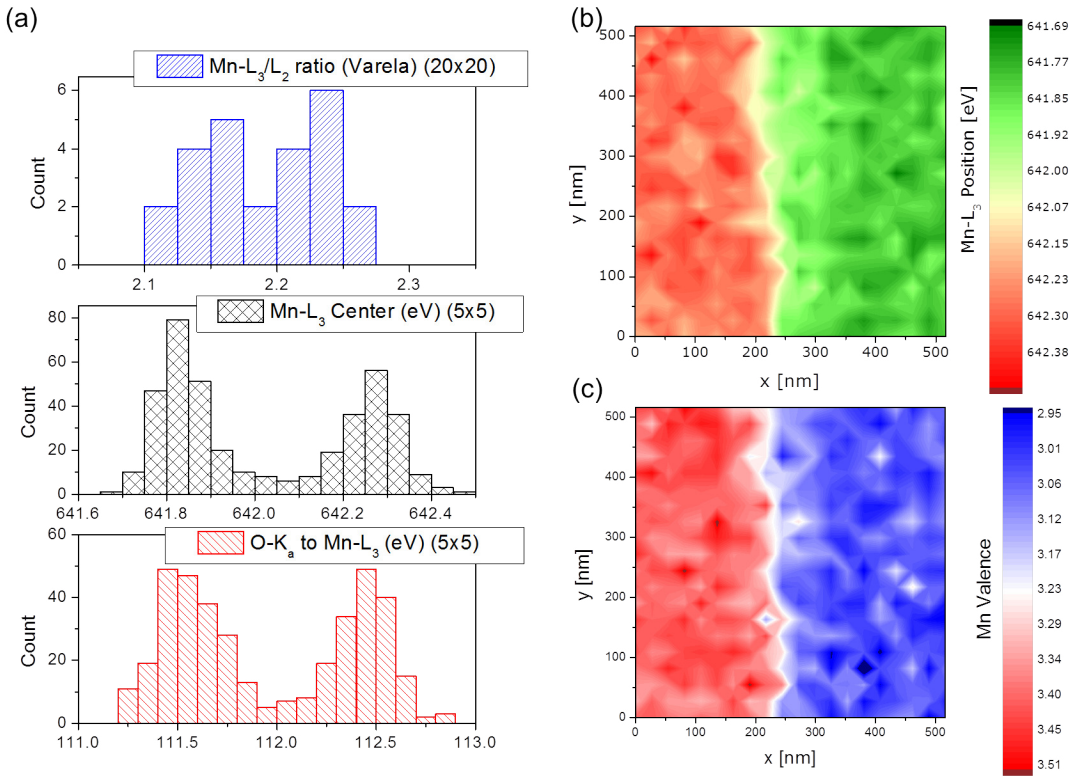

Figure 4.10.: Comparing different approaches of identifying the phase separation in a spectrum image. (a) shows the histograms of one L_3/L_2-ratio, the pure center position of the Mn−L_3 edge and the approach additional using the position of O−K edge. First method needs a four time higher binning, but still shows two regions in the end, while the other two methods are comparable. This is also visible in the maps belonging to those approaches (b,c).

be used if the highest resolution chemical interface localization is required. Most of the other methods implemented have also been compared against each other to investigate their suitability. Two additional figures for this purpose with a slightly different way of presentation have been added to the appendix.

5. Results

In the course of this thesis, 15 lamellae were investigated in-situ. Since not all investigations could be carried out in one lamella, different effects and investigation methods are described in the following using the best example of each lamella, but indicating how representative those results were.

This chapter will summarize the experimental results of this thesis grouped by topics. The first section examines samples like they were after sample preparation, which includes confirming the spinel structure. It also includes the characterisation of some defects observed without in-situ lithiation.

The second part is the paper published in ACS Applied Energy Materials [69], which focuses on establishing the microstructure resulting from in-situ lithiation, the interface between both phases and the dynamics of the reaction. The paper is included without large changes in text. Only the references to the supporting information have been changed as those have been included and often extended in other parts of this thesis. This also identifies some parts that have been published as part of the supporting information, though they should be independently marked most of the time.

Sections sec. 5.3, sec. 5.4, sec. 5.5 offer additional insights to the data shown in the paper by further analysis. Afterwards, the last three sections focus on the effects of defects on the lithiation behavior (sec. 5.6), attempts of delithiating a previously lithiated sample (sec. 5.7) and various control experiments performed (sec. 5.8).

In-situ videos unfortunately cannot be made permanently available to the reader of this thesis. Even though image sequences are provided for the most significant in-situ observations, the in-situ results of this work are more easily understood and appreciated, if one is able to see the corresponding in-situ recordings of the reaction front propagating into the sample. One video is available as a supplementary material[1], because it is a part of the paper included in this thesis [69]. Even though the image needed to be compressed for online display and is thus at lower resolution and slightly less sharp, it gives an impression of the speed of the reaction, the behavior of the reaction front and at least somewhat that moving images make it much easier to understand the contrasts.

[1] https://pubs.acs.org/doi/abs/10.1021/acsaem.0c00380

5.1. Precharacterization of prepared samples before in-situ use

5.1.1. General characterisation by bright field, dark field and diffraction pattern

Before the samples were used in in-situ experiment, they were precharacterized each time. Mostly diffraction images of different zone axes and some associated bright field and dark field images were recorded. In addition to checking the expected **$LiMn_2O_4$ spinel** structure, this verified the preparation quality with respect to **homogeneity of thickness** and strong contrasts due to stresses caused by bending of the lamella during thinning, as well as to check whether the sample was single crystalline or at least a **large grain** would be accessible for in-situ lithiation.

Special attention was on which zone axis is closest to the initial orientation of the sample and thus approximately represents the plane normal of the lamella, which may allow conclusions in the evaluation of the in-situ experiments. In addition, this provides an overview of whether a and which zone axis might be accessible later in the in-situ experiment with the single-tilt holder.

Fig. 5.1 shows four exemplary precharacterization images of a lamella later used in in-situ experiment (results in sec. 5.2). As shown in (a) and (b), the two zone axes can be indexed by the crystal structure of $LiMn_2O_4$[2] and also shows that the particle is single-crystalline. In general three different orientations were used for a full crystallographic confirmation, which also included a comparison of the necessary main holder tilt $\Delta\alpha$ (and secondary tilt $\Delta\beta$, if properly recorded).

Thus, major damage to the sample by FIB (e.g. oxygen loss) as well as significant lithium loss should show up in the diffraction patterns. With a significant delithiation, the lattice parameters would not have been suitable for indexing, since a shrinkage of up to 3% should take place here (compare sec. 2.2.1) and the $Li_\varepsilon Mn_2O_4$ was always used as a possible structure for comparison during indexing would have been more suitable, if this was the case. In fig. 5.1 (a) it can be observed that the plane normal of the lamella is very close to $[011]_c$ and has to be tilted by roughly $\Delta\alpha = 50°$ to reach the $[001]_c$-orientation, which shows that one of the $\langle 100\rangle$-directions has to be almost in the plane of the lamella. Note that, as expected from the spinel structure, the 400-spots have much more intensity than the other spots visible in fig. 5.1 (b), due to the complex symmetry of spinel.

BF (c) and DF (d) images shown in fig. 5.1 confirm that the sample is single-crystalline and thus the ideal result of a TEM specimen preparation (single-crystalline over a large area and otherwise free of visibly large defects), though slightly thinner would be bet-

[2] Initially, a script by Timo Wuttke was ported and extended in Matlab to compare the diffaction patterns with almost all conceivable (lithium) manganese oxides as a precaution. This also included not only the geometry of the diffraction patterns, but also the lattice parameter via the diffraction constant of the used TEM.

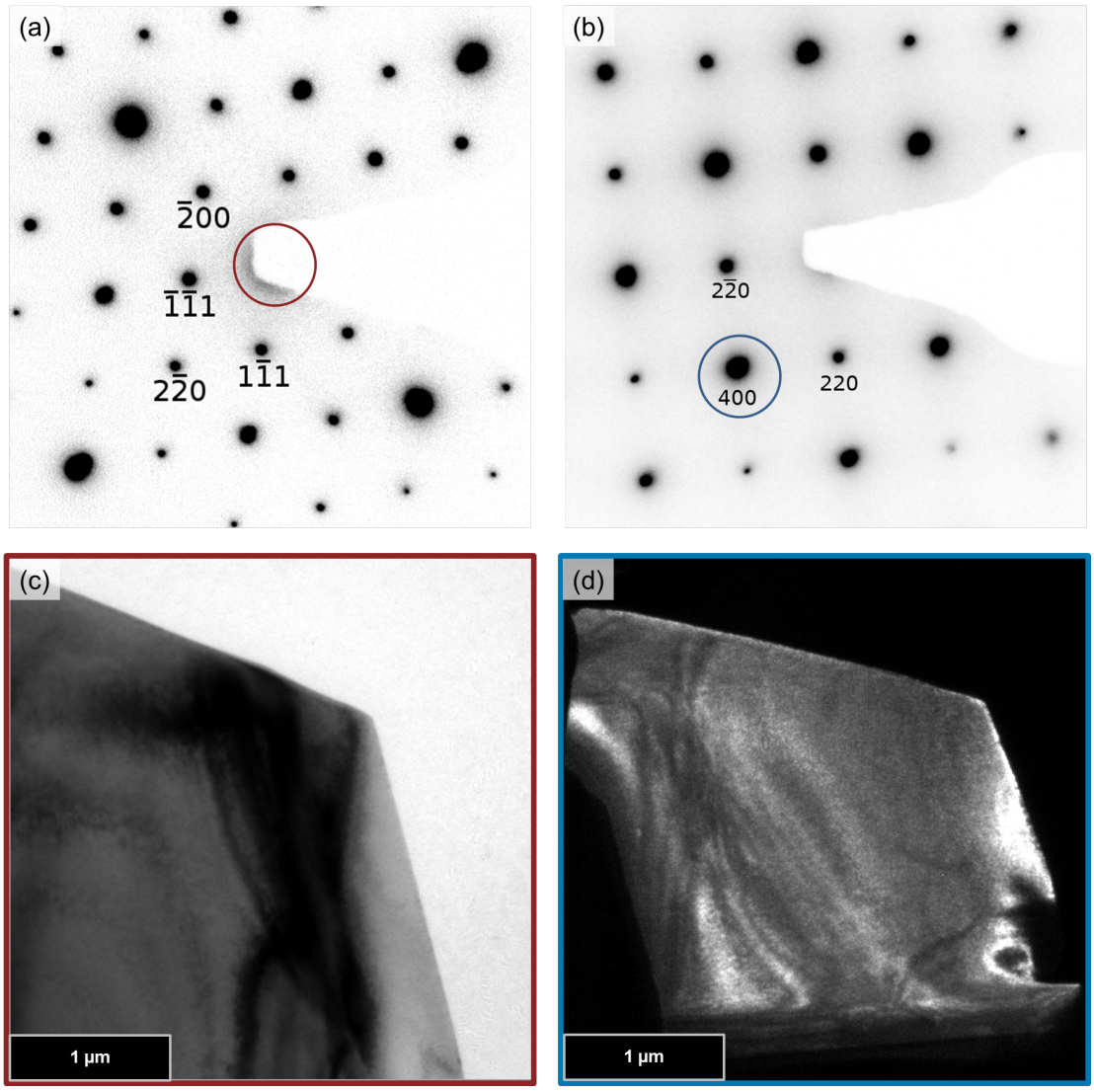

Figure 5.1.: General charactization previous to in-situ usage. (a,b) Images of two diffraction images of different zone axis confirming the spinel structure of the sample after FIB preparation. The $[011]_c$ orientation in (a) has been used for a BF shown in (c) and is close to the plane normal with $\alpha = 0°$. (d) shows an example of a DF image using the $[400]_c$ spot in the $[001]_c$ orientation of (b) at $\alpha = 50°$. The DPs confirm an intact spinel sample and BF/DP show that the sample is free of major defects and FIB damage.

ter. Additionally, the sample does not show much thickness contrast. Only bending contours are visible, which are hardly avoidable in the T-shape of the samples due to the slightly reduced mechanical stability compared to a H-shape version. Thus, several square micrometers of projected sample size are available for examination during lithiation.

An alternative method of sample preparation using the PIPS was also tested in the hope of higher sample output and better pre-selection of particles for in-situ experiments, but preliminary tests were not promising enough to invest more time (compare fig. A.6).

5.1.2. Stacking faults in the sample material

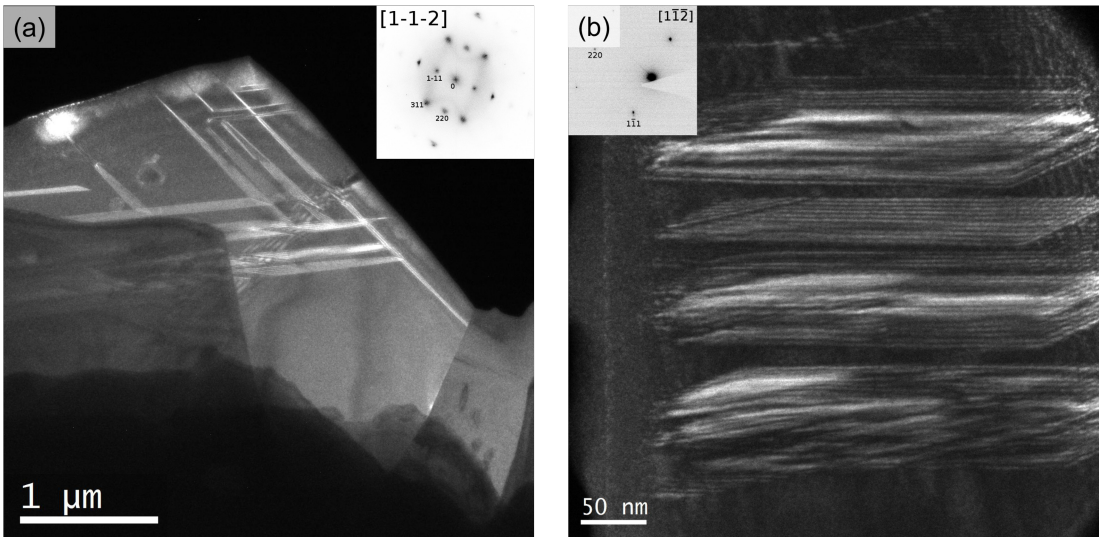

Figure 5.2.: Dark field images of pre-existing stacking faults. In a FIB-prepared lamella (a) and in tip for APT measurements (b).

During the pre-characterization of the samples, it was found that the samples were often not completely free of defects. These planar defects can be seen in Fig. 5.2. In the $[1\bar{1}\bar{2}]_c$-zone axis in (a) the planar character of the defects is clearly visible. The oscillating contrast already indicates that the defects are stacking faults. Because the $1\bar{1}1$ spot is perpendicular to the beam in this zone axis, a group of these stacking faults almost disappears and can only be recognized by a weak contrast in the center of the image.

In fig. 5.2 (b) again the oscillating contrasts of the stacking faults are shown in an image of a TAP-tip, which was created in the collaboration within SFB1073 project C05. The zone axis here was almost acessible despite a single-tilt holder which according

to B. Pfeiffer is presumably due to the facetting of the particles and the way tips were prepared from them. The longitudinal axis of the truncated octahedral shapes when used as an axis of symmetry in TAP tips and FIB lamellae, often brings a zone axis close to the plane normal.

Unfortunately, we cannot make any further statement about the exact character of these stacking faults. It is not known whether the stacking faults are intrinsic or extrinsic and what the atomic arrangement of/in or between the stacking fault planes looks like.

5.1.3. Tetragonal $Li_2Mn_2O_4$ particles/regions in the sample material

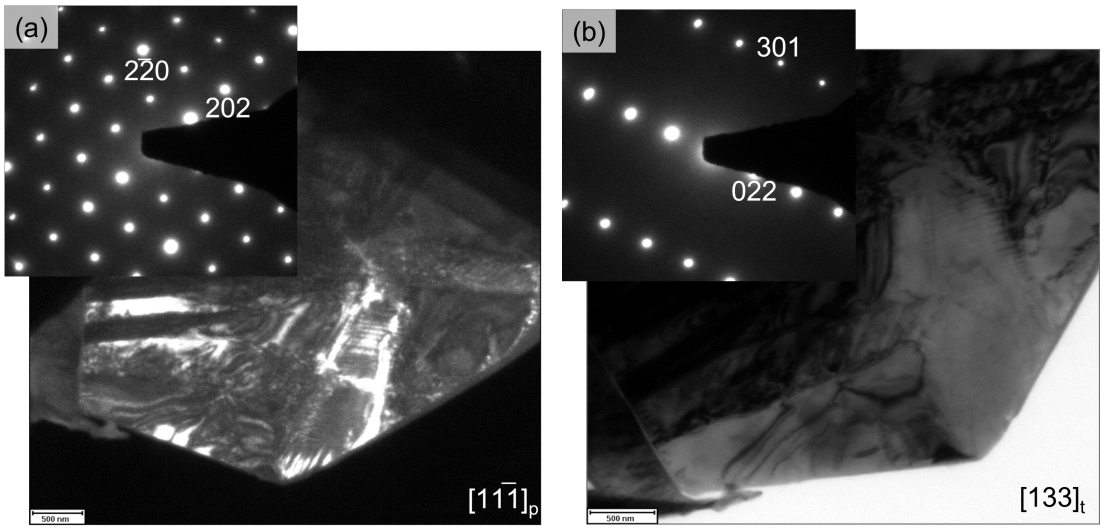

Figure 5.3.: BF/DF/DPs of a tetragonal particle in the sample material. The diffraction patterns in this as-prepared lamella from the sample material can be indexed by the $Li_2Mn_2O_4$ structure parameters. Both the dark field (a) and bright field (b) images show a lamellar structure.

Although as discussed in par. 3.1 and shown in Fig. A.1 no extraneous phases should be present in the material, at least three times after FIB preparation tetragonal structures were found that did not reflect a spinel structure. Three such examples will be shown here and were characterized, but as they are not the main focus of this work, this will be kept brief.

As fig. 5.3 shows, samples of tetragonal particles are well distinguishable from the desired one by their microstructure alone. This also shows in the diffraction patterns, that fit the tetragonal $Li_2Mn_2O_4$ structure. The brightfield image in fig. 5.3 (b) already shows that the sample has many contrasts/defects and should therefore not be used for

lithiation anyway. These lamellar contrasts can be seen even more clearly in the dark field fig. 5.3 (b) and several domains of different orientation can be seen, which show different lamella spacing.

The diffraction image in fig. 5.3 (a) also shows the similarity of the cubic and tetragonal phases of $Li_xMn_2O_4$ nicely. At first glance, except for a slight distortion the $[11\bar{1}]_p$-zone axis hardly differs from the $[011]_c$-zone axis (see fig. 5.1). This makes it difficult to easily identify the different phases by diffraction images during sessions at the TEM.

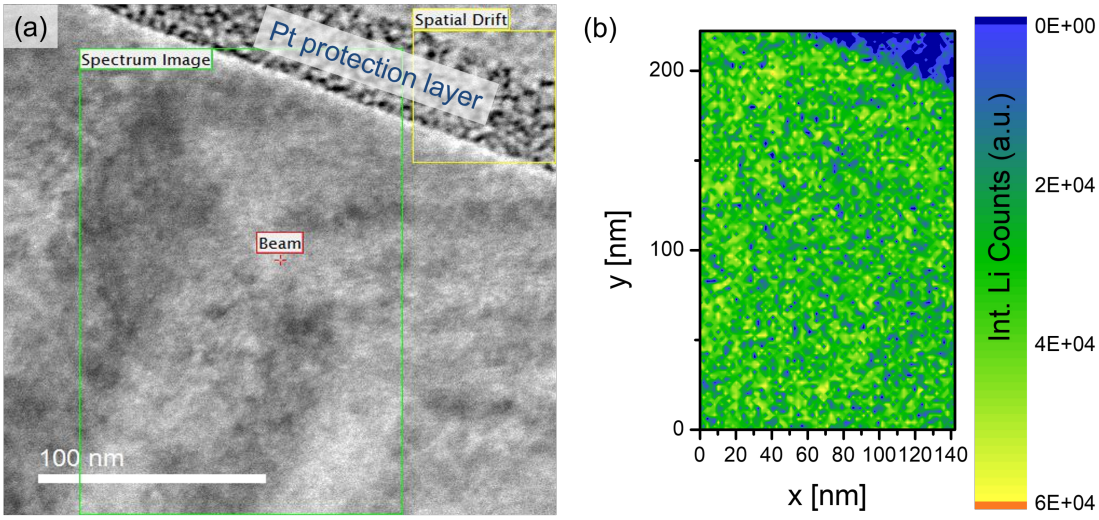

Figure 5.4.: Lithium map for a tetragonal region in the sample material. The overview image of the EELS map shows a fishbone like lamellar structure, that suggests twinning (a). The EELS map (b) of the spectrum image region shows that the region contains lithium and doesn't correlate with the fishbone structure. The region of the platinum protection layer can be clearly distinguished as it does not contain Li.

Although, the diffraction patterns suggest the presence of $Li_2Mn_2O_4$ particles, it needs to be confirmed by EELS that they contain lithium and that the manganese valence values fit. Otherwise, the particles could also be another tetragonal phase like Mn_3O_4. This was tested using another FIB sample in fig. 5.4. The STEM overview image in fig. 5.4 (a) shows the region elected for this purpose (green), comprising two domains with differently aligned lamellar structure (like fishbone). The upper region of protective Pt layer was used for drift correction. Neither the different domains nor the lamellar structures are found as contrasts in the lithium map in fig. 5.4 (b), which suggests a stoichiometrically homogeneous sample. Testing with other methods like a plasmon center or $Mn\text{-}L_3$ position mapping (both not shown) is consistent.

The previous characterisation was performed with a dispersion not allowing simul-

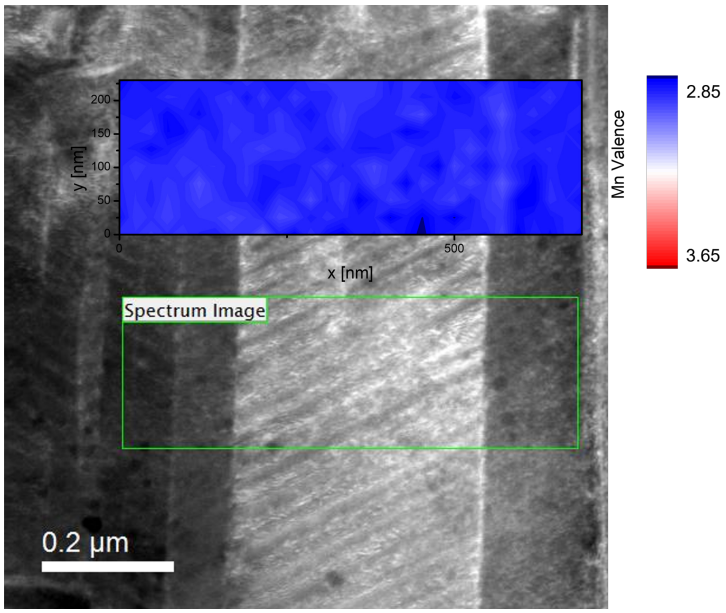

Figure 5.5.: Mn valence mapping on the tetragonal phase in the sample material, where the STEM overview image shows lamellar structures, again. The Mn valence mapping, offset upwards, from the region of interest is homogeneous at a valence of roughly 2.9.

taneous recording of the O–K edge, thus not allowing manganese valence calculation. This was performed on a third case shown in fig. 5.5. The Mn valence map shown above of the region of interest is homogeneous with an average valence of $2.91(3)$ (calculated with the 299 data points). This is 0.08 below the expected value of 3 for $Li_2Mn_2O_4$, but further from 2.67 of Mn_3O_4. Again, the contrast of the lamellar structures is not mirrored in the map within the available spatial resolution.

5.2. ACS Applied Energy Materials: Tracking the diffusion-controlled lithiation reaction of $LiMn_2O_4$ by in-situ TEM

TORBEN ERICHSEN, BJÖRN PFEIFFER, VLADIMIR RODDATIS AND CYNTHIA A. VOLKERT

Abstract

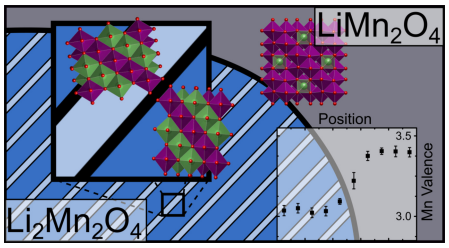

Spinel lithium manganese oxide ($Li_xMn_2O_4$) is used as an active material in battery cathodes. It is a relatively inexpensive and environmentally friendly material but suffers from capacity fade during use. The capacity losses are generally attributed to the formation of the tetragonal phase (x > 1) due to overpotentials at the surfaces of the micrometer-sized particles that are used in commercial electrodes. In this study, we investigate the mechanisms of tetragonal phase formation by performing electrochemical lithiation (discharging) in situ in the transmission electron microscope (TEM) utilizing diffraction and high resolution imaging as well as spectroscopy. We observe a sharp interface between the cubic spinel (x = 1) and the tetragonal phase (x = 2) that moves under lithium diffusion control. The tetragonal phase forms as a complex nanotwinned microstructure, presumably to relieve the stresses due to expansion during lithiation. We propose that the twinned microstructure stabilizes the tetragonal phase, adding to capacity loss upon deep discharge.
KEYWORDS: lithium manganese oxide spinel, tetragonal $Li_2Mn_2O_4$, EELS, twinning, defects, interface, lithiation

5.2.1. Introduction

The need for lightweight power sources with high energy density is ever growing with increasing demand in all fields of application like electrified transport and temporary energy storage for alternative energy production. Many of today's secondary battery technologies involve cathodes containing significant amounts of expensive and poisonous cobalt. An alternative is transition metal based spinels that have been extensively studied over the last few decades mostly by non-local methods such as cyclic voltammetry and x-ray diffraction (XRD). However, they show problems in capacity retention, as summarized by Thackeray, et al. [79], which limits their applicability.

$Li_xMn_2O_4$ spinel (LMO), which is a low-cost and environment-friendly material, is able to accommodate lithium up to x = 2 per chemical unit while retaining the same basic arrangement of manganese-oxygen-octahedrons. In the range of $0 < x < 1$,

where the crystal structure remains cubic, only the lattice parameter changes with x ($Fd\bar{3}m$, a = 8.02 – 8.24 Å). [22] Upon increasing the lithium content above x = 1, the previously tetrahedrally coordinated lithium immediately shifts to octahedral sites while leaving the oxygen-manganese arrangement unchanged. This lowers the Mn valence below the x = 1 value of 3.5 and produces Jahn-Teller (JT) mediated tetragonal distortion. [60] The high energies of having neighboring tetrahedral and octahedral sites populated by lithium lead to low solubility between the x = 1 and x = 2 phases and to a large miscibility gap between the two phases. The atomic structures of the cubic x = 1 and tetragonal x = 2 phases are shown in Fig. 5.6. The primitive tetragonal unit cell ($I4_1/amd$, a = 5.7 Å, c = 9.3 Å) is rotated by 45° relative to the cubic unit cell. [55] However, since the Mn and O atoms shift only slightly during the transformation, it is often simpler and more instructive in the discussion of crystallographic relationships to describe the tetragonal phase using a non-primitive tetragonal unit cell ($F4_1/ddm$), a = 8.0 Å, c = 9.3 Å) where the a and c axes are parallel to the ones of the cubic spinel system. [55] This has been referred to as the pseudo-cubic unit cell and vectors in this system are labeled with a subscript "p" to distinguish them from the cubic "c" and primitive tetragonal "t" systems. [70]

The known degradation mechanisms of LMO include dissolution of manganese into the electrolyte [27, 28, 225, 226], mechanical degradation due to volume changes of the electrode particles during de-/intercalation [36, 227] and capacity loss due to the fact that the cubic to tetragonal transformation at x > 1 is not entirely reversible [22]. This limits the Li uptake to half its achievable value in commercial application, since only the cubic region is used. But residual tetragonal regions have also been detected by TEM in LMO electrode particles cycled within 0 < x < 1, presumably due to the formation of the tetragonal phase in overpotentials. [36] To improve capacity retention and reversibly extend the lithium range to x > 1, a variety of costly methods have been introduced, such as using nanoscale particles for better stress accommodation [228], surface coatings [29], and partial substitution of manganese by other transition metal which reduces manganese dissolution and shifts the onset of the tetragonal transformation to larger values of x. [28] These approaches have produced moderate improvements in capacity retention, but usually the cost and environmental advantages of LMO as well as some capacity are partially or fully lost. It is somewhat surprising then that the exact mechanisms of capacity fade in micrometer-size particles due to the tetragonal transformation have not yet been fully investigated.

LMO has so far only been studied with in-situ TEM for the case of $LiMn_2O_4$ nanowires, in which a cubic-to-tetragonal phase transformation was confirmed by electron diffraction upon lithiation. [39] But in contrast to previous reports, the transformation was fully reversible and proceeded via an intermediate orthorhombic phase. It was suggested that this could be due to particle size effects previously observed by XRD on large ensembles of LMO particles. [153] A closer study to better understand and confirm these

observations requires higher spatially resolved methods such as have been applied to $LiMn_{1.5}Ni_{0.5}O_4$ [186] and $LiFePO_4$ [187] using x-ray methods. Comprehensive TEM-based studies including STEM-EELS (which have been applied to e.g. LiFePO4 [208]) could not be performed on the nanowires probably due to their thickness limiting the applicability of EELS and STEM.

As a first step in understanding how the tetragonal phase may lead to capacity fade in LMO, we track the microstructural changes during electrochemical lithiation of LMO electrode particles using in-situ TEM studies. With the help of in-situ TEM, diffraction, STEM and EELS and laser-assisted Atom Probe Tomography we are able to track the phase boundary and the associated changes in microstructure during lithiation above $x > 1$, i.e. deep discharge. The unexpected formation of a twinned microstructure indicates an important role of lithiation-induced stresses and may stabilize the tetragonal structure against delithiation thereby providing a possible specific mechanism for capacity fade.

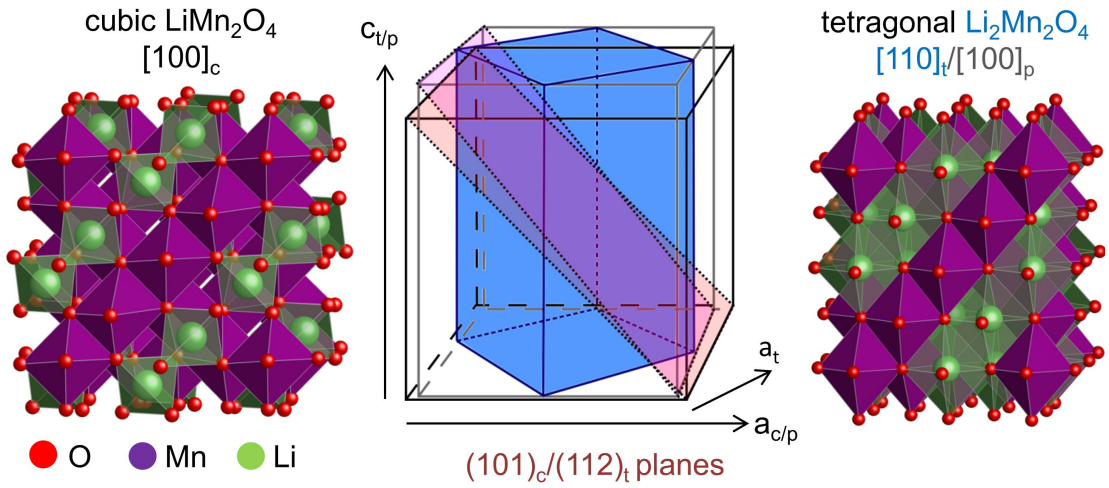

Figure 5.6.: The crystal structure of $Li_xMn_2O_4$. Equivalent cuboids viewed along $[100]_c$ in cubic $LiMn_2O_4$ (left) and along $[110]_t/[100]_p$ in tetragonal $Li_2Mn_2O_4$(right). The MnO_6 octahedra (violet) are distorted, but their arrangement remains unchanged upon transformation between the phases. The central sketch shows the relationship between the unit cells of the two materials, including the labeling conventions. It also shows the tetragonal twinning plane $(112)_t/(101)_p$ which lies close to the cubic $(101)_t$ plane.

5.2.2. Results and Discussion

In-situ lithiation of a LMO specimen prepared by FIB from commercially available micron-sized particles was performed in the TEM by mechanically contacting the foil with a lithium tip (see Methods section for more detail). Bending contours in bright field (BF) imaging clearly reveal a reaction front moving from the contact with the Li tip into the LMO sample (e.g. Fig. 5.7 (a)). The reaction front movement is accelerated by applying a $-5\,\mathrm{V}$ bias and can be stopped during the experiment by mechanically separating the foil from the lithium source. Although the reaction proceeds without the application of an external bias, we apply a bias here to compensate for any voltages generated in the sample by electron beam illumination [202] and to overcome possible chemical potential barriers between the tip and sample. [158]

The portion of the sample shown in Fig. 5.7 (a) is completely lithiated within $180\,\mathrm{s}$, which corresponds to a very high charging rate of approximately 20C. A video of this reaction is available in the Supporting Information (online). Bending contours are visible directly after contact with the lithium tip and move with the reaction front into the sample. The bending contours are localized directly at the interface, presumably because the phase transformation involves distortion of the original cubic spinel lattice to a tetragonal crystal structure (Fig. 5.6), helping to identify the interface shape and movement.

Diffraction patterns (Fig. 5.7 (b)) confirm that the sharp boundary observed in the TEM (Fig. 5.7 (a)) is the phase interface between the initial $LiMn_2O_4$ and lithiated $Li_2Mn_2O_4$. The diffraction pattern with $a = 8.2(2)\,\text{Å}$ of the initial material (Fig. 5.7 (b) top), though wit a large uncertaintydue to the large sports of nanodiffraction, is consistent with $[111]_c$ with the same lattice parameter determined by XRD measurements on the pristine sample material (see sec. A.2) and within the expected value of $a = 8.24\,\text{Å}$. [22] Upon lithiation, the material transforms into the tetragonal structure without rotation of Mn and O octahedra, so that the $<100>_c$ and $<100>_p$ directions are the same. The resultant diffraction pattern (Fig. 5.7 (b) top) has fewer spots due to the smaller unit cell [68], and is consistent with the known tetragonal structure. A careful examination of the lamellar structure in the transformed region reveals domains with the three different possible in-plane orientations $<100>_c = <100>_p$, rotated relative to each other by 120°. This is consistent with the three-fold symmetry of the $[111]_c$ zone axis and indicates that the lamellar structures have specific crystallographic orientations.

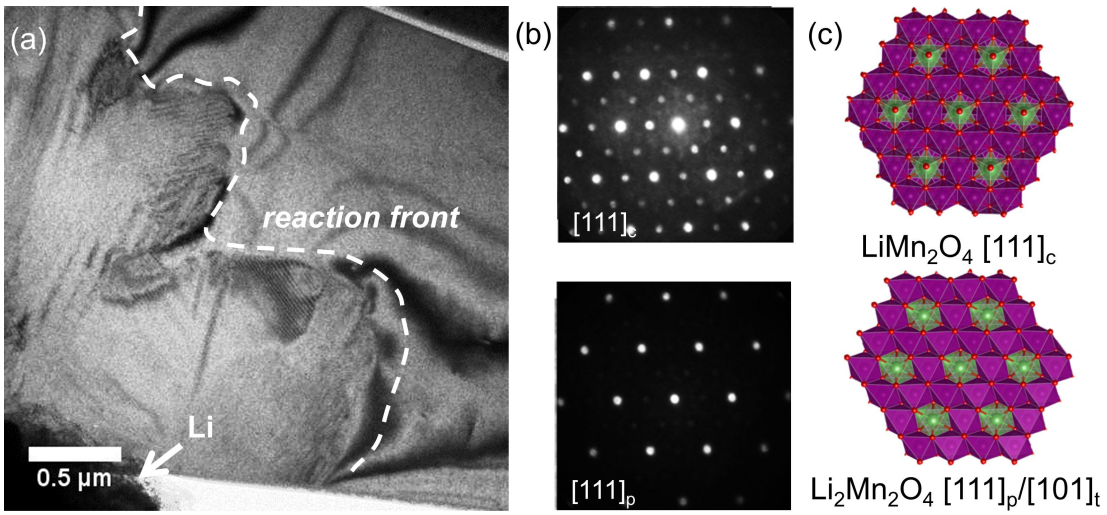

Figure 5.7.: In-situ lithiation of LMO. (a) BF image of an initially single crystalline LMO specimen during lithiation. The lithium tip is visible in the lower left corner. Strain and microstructural contrast reveal a sharp interface (dashed line) between the untransformed single crystal on the top right and the lamellar structure in the transformed region on the bottom left. (b) Diffraction patterns from a scanning nanodiffraction analysis confirm the initial spinel structure in a near $[111]_c$ orientation (top) and the structural transformation to the tetragonal phase in a near $[111]_p$ orientation (bottom). (c) Sketches of the crystal structures viewed along the [111] direction show the similarity between the phases.

A partially in-situ lithiated $Li_xMn_2O_4$ TEM specimen containing a phase interface between $x = 1$ and $x \approx 2$ was characterized using high-resolution TEM and STEM-EELS (Fig. 5.8). The electronic structure of the sample is studied in both the low- and high-loss regions of the EEL spectra. The transformation from $x = 1$ to $x \approx 2$ causes the plasmon peak to shift by 0.9 eV to lower energies (Fig. 5.8 (a)), which is used in Fig. 5.8 (c) to map the interface between the phases. This peak shift is in the same direction but three times larger than the energy shift observed and used to map lithium content in (Li)$FePO_4$ [208]. Plasmon peak shifts have also been observed in other transition metal oxides ($Li_{0.5}Ni_{0.5}Mn_{1.5}O_4$ [206], various manganese oxides [229]) and indicated a change in electronic properties. An unidentified broad peak present at 10 eV, lying at a similar energy as an intraband transition observed in (Li)FePO4 [208], diminishes upon lithiation. Furthermore, the height of the `Li-K` edge at 58 eV in Fig. 5.8 (a) increases by 75 %, while the `Mn-M` edge only slightly changes in intensity while keeping the same shape.

In the high-loss region (Fig. 5.8 (b)), the `O-K` edge, which corresponds to the transi-

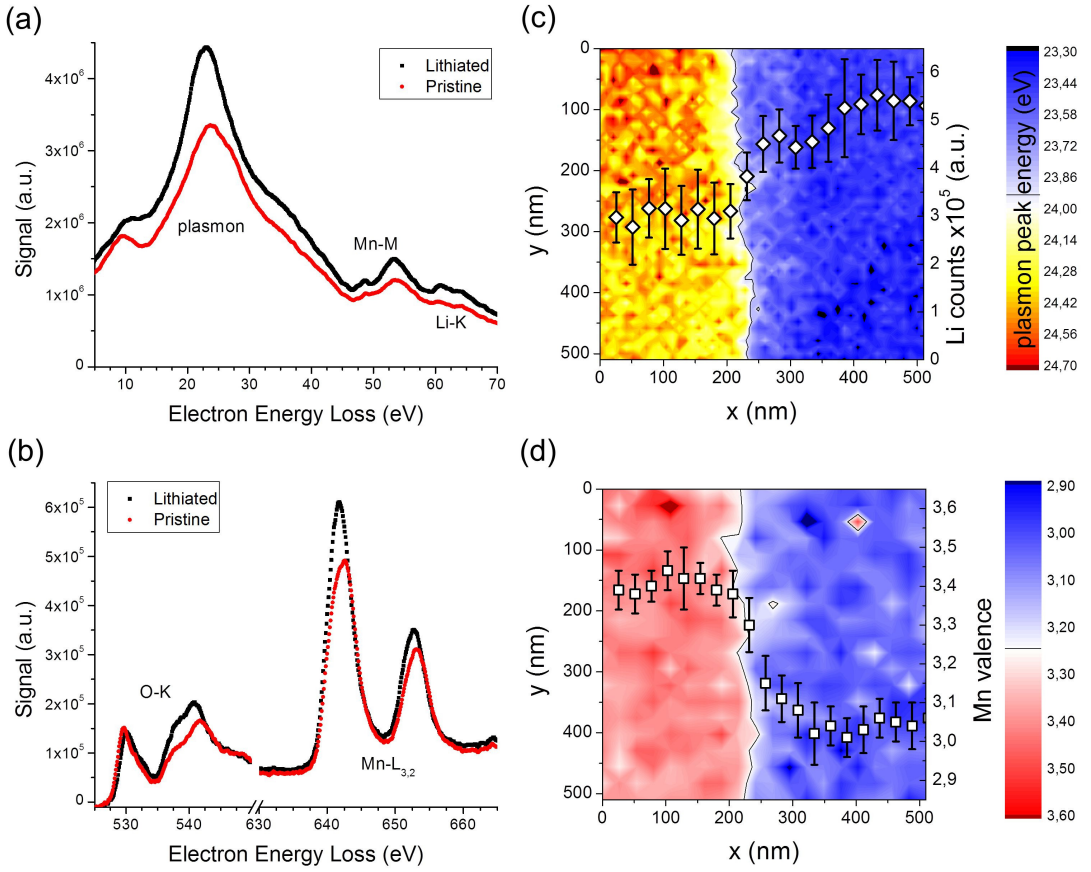

Figure 5.8.: EELS of a phase interface region. (a) Dual low-loss EEL and (b) high-loss EEL spectra from the pristine and transformed regions of the sample. (c) Plasmon peak energy map of the phase interface region overlaid with the `Li-K` edge counts summed along the direction parallel to the interface (error bars are the standard deviation). (d) Mn valence map of the phase interface region overlaid with the Mn valence averaged along the direction parallel to the interface, showing a change from 3.45 to 3.05 across the interface.

tion from the O 1s to the hybridized bands of O 2p and Mn 3d [230], shows a shift in the first peak maximum from 529.6 – 530.1 eV as a result of lithiation. Additionally, the intensity ratio of the first to second peak of the O–K edge increases. This trend has been observed in multiple EELS studies upon lowering manganese valence due to the interaction of above mentioned states in the MnO_6 octahedra. [209, 214, 229] The Mn–L_3 edge moves from 642.7 eV lower to 641.8 eV upon lithiation. Moreover, an increase in the Mn–L_3/Mn–L_2 ratio can be observed also indicating a drop in valence. [92, 203, 209, 214, 217, 229] The more symmetric shape of the $x \approx 2$ Mn–L_3 peak is consistent with a pure Mn^{3+} state while the shoulder on the $x = 1$ Mn–L_3 peak suggests a mixture of $Mn^{3.5+}$ states. The intensity ratios of the first two oxygen peaks as well as the Mn–L_3/Mn–L_2 intensity ratio have been widely used to map Mn valence changes in the literature. However, intensities are somewhat more sensitive to background signal and detector noise than peak positions. [214] Therefore, the change in absolute energy difference between the O–K and Mn–L_3 edges can provide a high signal-to-noise measure of Mn valence. [92]

The position of the phase boundary is clearly shown in Fig. 5.8 (c) using a map of the plasmon peak energy. It correlates well with the Li–K peak counts which have been vertically averaged in the map region and overlaid on the map. The lithium counts almost double across the interface, as expected.

The manganese valence map in Fig. 5.8 (d) also clearly marks the same position for the interface. The slightly lower resolution follows from higher binning needed to process the data. The change in valence of 0.4(2) from 3.45(12) on the left to 3.05(11) on the right is slightly smaller than the expected 0.5 for the $x = 1$ to $x = 2$ transformation, but valence quantification in the TEM and particularly in an in-situ sample is difficult and requires careful calibration standards and/or theory calculations.

The EELS maps of electronic structure at the interface (Fig. 5.8 (c,d)) show that the interface is rough, suggesting that the interface is not crystallographically sharp, not planar or not parallel to the electron beam. Thus, the approximate 100 nm interface transition width observed in both lithium and manganese electronic structure and the 50 nm width observed in the plasmon map serve as upper limits of the phase boundary width.

Further ex-situ analysis of a single domain of the lamellar structure was performed in a double-tilt holder directly after an in-situ lithiation (Fig. 5.9). The inset SADP (Fig. 5.9 (a)) reveals a twinned tetragonal phase with a twinning plane of $(112)_t$ / $(101)_p$, indicated by a dashed line. This is the most common twinning plane in tetragonal minerals. The closely spaced diffraction spot pairs correspond to the $(004)_t$ / $(010)_p$ and $(220)_t$ / $(001)_p$ reflections of the two twin variants. This

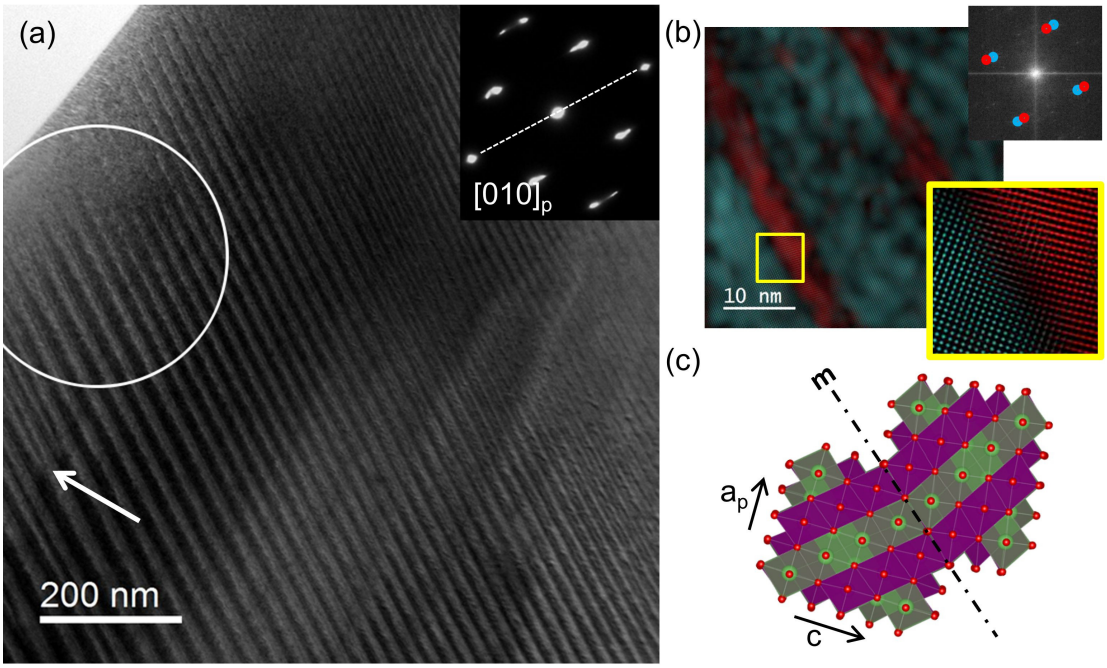

Figure 5.9.: Lamellar structure of $Li_2Mn_2O_4$. (a) BF image of an in-situ transformed LMO sample showing lamellar contrast with a periodicity of approximately 30 nm. The inset SADP, taken from the circled area at a tilt of $\approx 37°$, shows that the contrast stems from two variants of tetragonal LzMO that are twinned along a $(112)_t$ plane (indicated by dashed line). (b) Bragg-filtered HRTEM images of the lamellar microstructure in the $[1\text{-}10]_t$ orientation. Twins are revealed by selecting the $\{220\}_t$ (red) and $\{004\}_t$ (blue) planes in the FFT; the twin boundaries are narrow but non-flat. (c) Atomic structure sketch of the $[010]_p$ / $[1\text{-}10]_t$ zone axis showing the orientation and possible position of the twin plane.

is confirmed in Bragg-filtered HRTEM images in Fig. 5.9 (c) that is color-coded using the spot selection shown in the FFT of the image. While the interface plane between both variants is not perfectly planar it is close to the $(101)_p$ twinning plane.

Both BF and Bragg-filtered HRTEM imaging allow the periodicity of the twin variants to be determined as between 20 – 50 nm. The thickness of the twins is not constant across the whole specimen (Fig. 5.9 (a) and Fig. 5.11 (a,b)); in particular there is evidence for a decrease in twin thickness by twin splitting in regions where the TEM specimen is thinner (see arrows in Fig. 5.9 (a)). Note that the lamellar structure seems to completely disappear in the thinnest regions at the edge of the TEM specimen (Fig. 5.9 (a)). Scanning nanodiffraction analysis of the twinned sample in Fig. 5.9 using a beam diameter of 2 nm reveals a majority twin variant thickness of 25 – 30 nm, a minority twin variant thickness of 5 – 10 nm and a boundary width of 1.5 – 4 nm (see sec. 5.3.1).

A sketch of the mirror plane and the two twin variants, excluding any distortions at the interface, provides a possible visualization of the twinned crystallographic structure (Fig. 5.9 (d)). It demonstrates that the $(112)_t/(101)_p$ twinning plane is parallel to edges of the MnO_6 and LiO_6 octahedra, allowing them to be joined across the twin boundary in the same way they are joined in the original spinel phase. However, the Jahn-Teller distortion points in different directions in the two variants, resulting in 6° and 9° misalignments between the lattice planes measured in Fig. 5.9 (b). The exact arrangement of the octahedra at the interface and possible deviations in chemical composition could not be detected by HR-TEM, HR-STEM or STEM-EELS in our in-situ samples.

Laser-assisted atom probe tomography (APT) is used to look more carefully for any possible variations in composition within the twinned structure. We use here the same APT method that has been successfully applied previously to investigate lithium distributions in LMO by Pfeiffer and Maier, et al. [231, 232] In this case, a fine needle was cut directly from the in-situ TEM lithiated specimen in Fig. 5.9 using FIB, and then analysed with laser-assisted APT (Fig. 5.10). The Li to Mn ratio is roughly double of what has been found in previous APT reconstructions of $LiMn_2O_4$, further confirming that the in-situ TEM lithiated material is the $Li_2Mn_2O_4$ phase. The reconstruction of the APT analysis of the twinned $Li_2Mn_2O_4$ specimen showed no evidence of chemical heterogeneity (Fig. 5.10 (a)). In particular, a careful analysis of the lithium composition averaged perpendicular to the twin planes (along the cylinder sketched in Fig. 5.10 (a)) showed no evidence of heterogeneities above the noise level (see sec. A.6). This is additionally visualized in Fig. 5.10 (b) showing a homogeneous lithium distribution in a planar slice of the

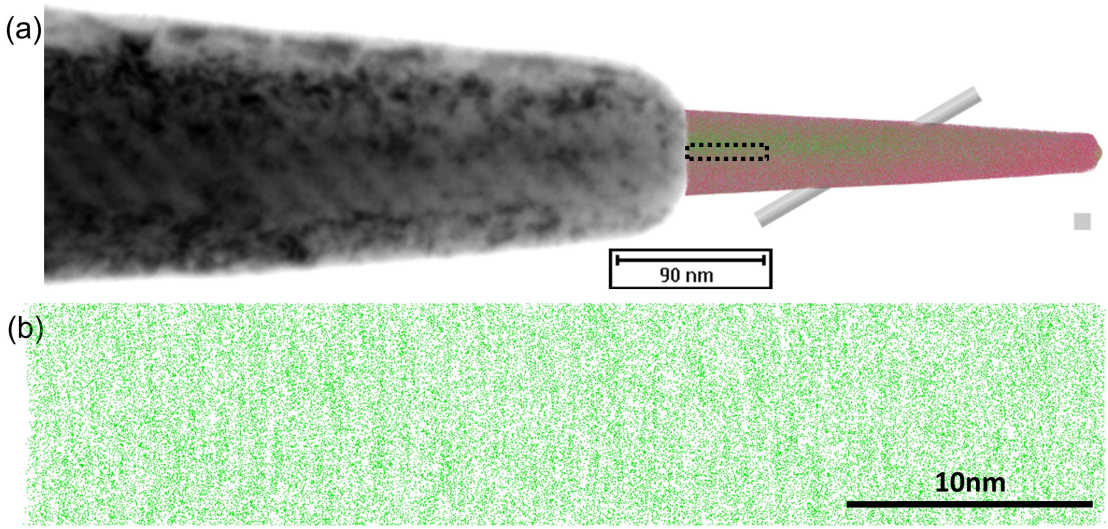

Figure 5.10.: APT analysis of in-situ lithiated $Li_2Mn_2O_4$. (a) BF-TEM image of the needle after APT analysis of the specimen from Fig. 5.9 and the APT reconstructed volume (Li: green, Mn: red). Analysis of the local lithium concentration along the 10 nm diameter cylinder perpendicular to the twin planes showed no evidence of lithium heterogeneity (see fig. A.8). (10 nm box for scale) (b) Planar slice of a part of the reconstructed volume closest to the lamellar contrast still visible at the tip (rectangle in (a)) showing a homogeneous lithium distribution.

reconstructed volume directly at the tip of the remaining needle (dotted rectangle), where lamellar contrast is still visible in BF-TEM image (Fig. 5.10 (a)).

We have investigated the kinetics of the reaction by recording the rate of propagation of the phase interface away from the contact to the Li tip. Fig. 5.11 provides an overview of the reaction front motion for the in-situ lithiated specimen shown in Fig. 5.7 (a). A TEM image of the fully lithiated specimen is shown in Fig. 5.11 (a), while a sketch showing the progression of the phase interface, the resultant domain structure and the twin spacing and orientations are shown in Fig. 5.11 (b). One sees that the reaction front velocity varies strongly from position to position along the boundary, leading to a rough interface. Nonetheless, a plot of the mean and median distances of the reaction front from the contact point shows a clear trend with time (Fig. 5.11 (c)). Due to the fact that the video was only started after contact between the lithium tip and the sample had already been established, the reaction

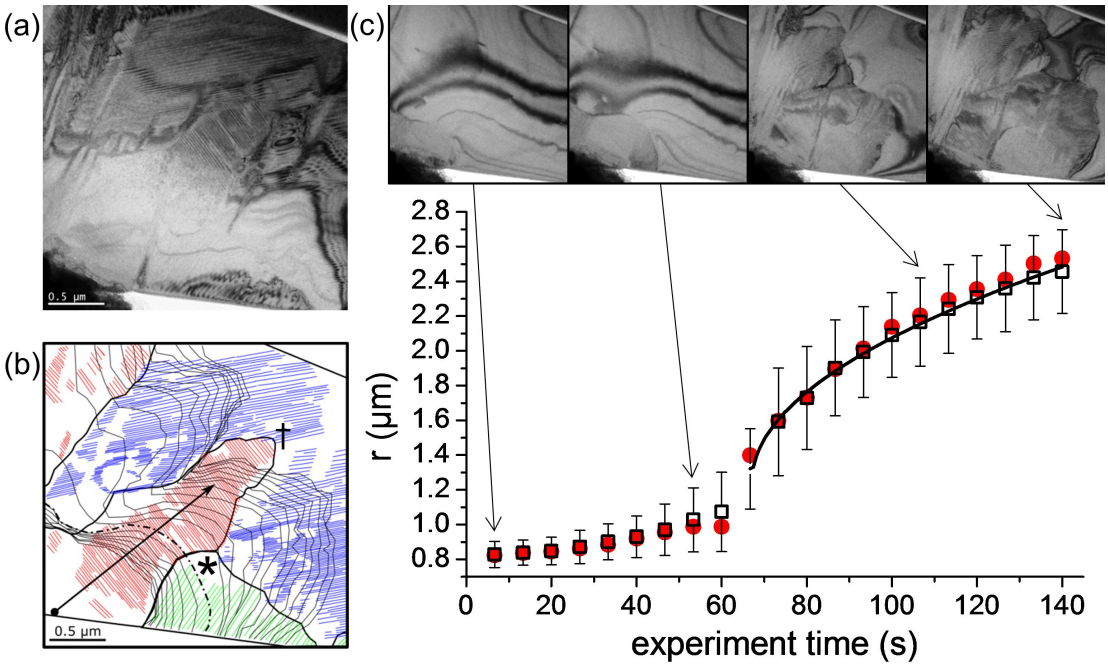

Figure 5.11.: Lithiation kinetics. (a) A bright field image of the specimen from Fig. 5.7 after lithiation is complete. (b) Position of the reaction front for every 20th frame (ca. 7 s) of the image series (thin black solid lines). The twin boundaries are marked where they could be detected in different colors to indicate the different domains. Domain boundaries are marked with thick black solid lines. The contact point with the lithium tip is indicated by a dot and the position of the front at 60 s is indicated by the dashed-dotted line. (c) The evolution of the mean (black squares) and median (red circles) distance of the reaction front from the contact point. The solid line shows a square root fit to the data for times greater than 60 s.

front had already moved around $0.8\,\mu$m into the sample. After this, the bias was ramped up at $0.1\,\mathrm{V/s}$ to reach $-5\,\mathrm{V}$ within $60\,\mathrm{s}$ and the boundary arrived at the position shown by a dotted-dashed line in Fig. 5.11 (b). After a stable bias of $-5\,\mathrm{V}$ is reached, the boundary moves more rapidly but with a steadily decreasing velocity. This behavior is well fit with a square root function (Fig. 5.11 (c)), indicating that the reaction front movement is diffusion limited. Exact solutions for diffusion-limited growth laws are complex, but in many cases the boundary position can be expressed as $r(t) = \alpha\sqrt{(D(t-t_0)} + r_0$ [233], where α is a dimensionless constant that varies between around 0.1 and 10.0 depending on the lithium concentrations at the interface and far away from the interface, and depending weakly on the dimensionality of the problem. Thus, the square root fit with $\alpha = 1$ yields an order of magnitude estimate for the diffusion coefficient of lithium in the transformed $Li_2Mn_2O_4$ region as $D = 2\times10^{-10}\,\mathrm{cm^2/s}$. This is in reasonable agreement with reported values for bulk diffusion of lithium in polycrystalline $LiMn_2O_4$, $D = 3.4\times10^{-8}$~$1.71\times10^{-12}\,\mathrm{cm^2/s}$, where single crystalline samples tended to have smaller diffusivities. [121] This is also multiple orders of magnitude smaller than the surface diffusion coefficient of lithium on graphite ($D = 5\times10^{-6}\,\mathrm{cm^2/s}$) [129], which allows us to conclude that the reaction front is controlled by lithium diffusion in the twinned single crystal $Li_2Mn_2O_4$ phase.

We analyzed the data in Fig. 5.11 (b) in detail to understand the reasons for the strongly heterogeneous interface velocities. The propagation of the reaction front is strongly hindered at the interface between the red and upper blue domains, but not at any of the other interfaces, so that a connection between interfaces and front propagation is not immediately obvious. Plots of the local interface velocity (magnitude and direction) as a function of local twin orientation also did not show a clear correlation (see sec. 5.5). We also found no systematic effect of the estimated local foil thickness (which is thinner near the edges) or experiment time on either the local front velocity or the twin spacings. In contrast, in-situ lithiation of several other samples showed that existing stacking faults in the $LiMn_2O_4$ strongly hindered front propagation. The specimen shown in Fig. 5.11 did not contain stacking faults in the pristine state, however the presence of dislocations and point defect clusters cannot be ruled out. Thus, we presume that the main factor causing the locally variable front propagation velocities are the presence of defects and stresses that we could not identify during pre-characterization.

In total, 15 in-situ TEM lithiation experiments were performed. All showed a sharp phase interface that propagated into the TEM specimen and the formation of a twinned structure in the transformed region. Between one and 3 different oriented twinned domains were observed with twin thickness periodicities between a few and 100 nm. A similar twinned microstructure was found in the tetragonal $Li_2Mn_2O_4$ phase contained within several of the investigated pristine $LiMn_2O_4$ particles (see sec. 5.1.3). This indicates that the twinned microstructure can occur in lithium manganese spinel even with-

out the extreme conditions used for the in-situ experiments (large overpotential, high C-rate and TEM irradiation). In particular, it shows that the minimum specimen dimensions (ca. 100 nm thick TEM foil versus 5 μm diameter particle) do not completely control phase stability, in contrast to the interpretation of electrochemical measurements in a previous report. [153] Generally, twinned microstructures with very similar microstructures result from stress-driven, diffusionless martensitic transformations from the cubic to tetragonal phase in a wide range of materials with similar c/a ratios. This introduces the idea that the martensitic-like microstructure observed here may be the result of stresses created by lithiation, or in materials that exhibit a Jahn-Teller distortion as a result of lithiation. A similar twinned microstructure in a lithium containing manganese oxide has to our knowledge only been reported in oxygen-deficient $Li_{1+\alpha}Mn_{2-\alpha}O_{4-\delta}$, which showed tetragonal distortion directly after calcination, [70] while twinning is not uncommon in other types of manganite spinels. [234, 235]

The TEM foils have a roughly equibiaxial plane stress state, so that stress-driven twinning should show a clear dependence on the out-of-plane orientation of the sample. The simplest test of this idea, which neglects stresses due to defects and accommodation stresses at the twin interfaces, is to compare the out-of-plane crystallographic orientation of the foils with the number of domains. If stress relief due to the plane-stress state of the foil is the dominant effect, then the c-axis should point as far as possible out of the plane, and the foils with near $<111>_c$ orientations, having all possible c-axes equally pointed out of plane, should contain three domains (e.g. Fig. 5.7), while foils with orientations further away from $<111>_c$ should contain one (e.g. Fig. 5.9) or two domains. A comparison of all 15 in-situ samples showed some tendency for the twin domains to form as predicted by stress relief (see fig. 6.2). However, evidence that driving forces other than the foil plane stress state are important can be seen directly in Fig. 5.11 (b). During reaction of the initially single crystal region, a new domain is formed (indicated by $\star$ in Fig. 5.11 (b)), and another domain ceases to grow (indicated by †). Since the initial plane stress state due to the foil geometry is homogeneous, we presume that the reasons for the observed domain selection during growth must be due to the interaction of the interface stresses [236] with defects that could not be seen during pre-characterization.

We found no clear connection between the twin spacings and the out-of-plane foil orientations. For example, if the foil plane stress state is decisive in driving twin formation, then twins are less likely to form in foils with an out-of-plane orientation along one of the $<100>_c$ cubic directions, since the 13 % expansion due to the lithium induced cubic-to-tetragonal transformation can occur unconstrained, leaving only the ca. 1 % contraction to be accommodated by in-plane stresses. However, we unfortunately never encountered a near $<100>_c$ out-of-plane oriented sample, and it is possible that strains on the order 1 % are already more than sufficient to initiate twinning as a stress relief mech-

anism.

The question remains of whether the nanotwins we have observed during in-situ lithiation and found as inclusions in pristine sample material (see fig. 5.36 and fig. 5.37) also form under in-operando battery conditions. There are a number of important ways in which our in-situ TEM studies differ from in-operando battery conditions, including the difference in stress state between the TEM foil and an intact particle, the effect of damage and fields introduced by the electron beam, and the absence of a liquid electrolyte. To test the importance of these differences on nanotwin formation, in particular due to the difference in the stress state between a particle and a thin TEM foil, we electrochemically lithiated fully intact micrometer-sized $LiMn_2O_4$ particles to form $Li_2Mn_2O_4$ in a typical battery electrolyte (see sec. 5.8.6). SEM images (fig. 5.36) show the formation of crystallographically oriented steps on the particle surfaces as a result of the electrochemical treatment. The orientation of those steps is consistent with twinning on $(101)_p$ planes as observed during in situ lithiation in the TEM. Low-voltage STEM images of thin foils prepared from the ex situ lithiated particles (fig. 5.37) reveal crystallographically oriented lamellar contrasts. Most of these are clearly nanotwins or stacking faults. Thus, despite the difference in stress states, battery electrode particles also appear to form nanotwins as a result of lithiation. This is perhaps not surprising since when Li begins to diffuse into a spherical particle, a compressive biaxial stress state is generated which is similar in sign and magnitude to what is formed in the TEM foil. [237] On diffusing further into the particle, more complicated stress states will ensue as a result of plasticity fracture, and coupling between stresses and reaction rates and diffusion, [237] perhaps accounting for the high defect density found throughout the particle (*Figure S7c,d*). We conclude that nanotwin formation can be expected at the surface of battery electrode particles as soon as they experience overpotentials.

Fig. 5.12 shows a high-resolution STEM image of the phase boundary. The serrated structure of the interface reveals the lenticular-shaped needle structure of the transformed material, which is typical for mechanical twinning. The twins themselves are not discernible by Bragg filtering since the twinning plane is not parallel to the beam as a consequence of the $[110]_p$ orientation of the sample. FFT analysis of the image shows local variations in the c/a-ratio and an average value of 1.12 which is 25 % smaller than the expected value of 1.16. Similar local deviations from the expected c/a-ratio have been observed in an Al-doped LMO and attributed to ferroelasticity and defects. [131] The sharp localization of bending contours at the interface plus blurring of the FFT spots provide evidence for strains near the interface. Nevertheless, Bragg-filtering of the image along the three principal directions

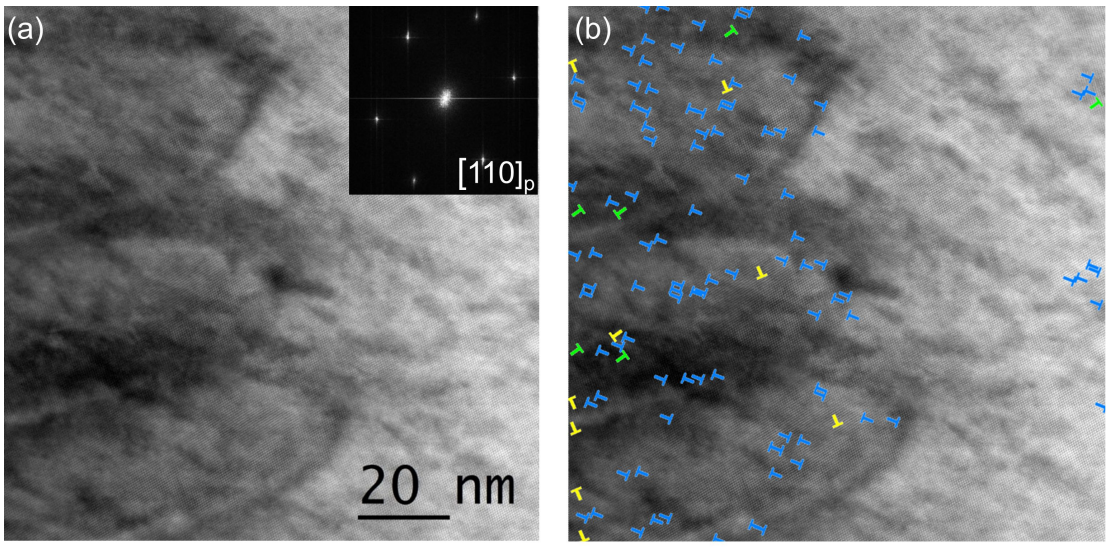

Figure 5.12.: Microstructure at the phase interface. (a) A high-resolution BF-STEM image in $[110]_p$ orientation (see FFT inset) reveals lenticular-shaped needles at the phase boundary, typical of mechanical twinning. (b) Single plane Bragg filtering allows three different dislocation types to be identified, indicated by three different colors including the direction of the inserted half-plane. The dislocations are mostly localized in the left, transformed region of the sample.

can be used, see Fig. 5.12 (b), to examine the coherency of the boundary by looking for interrupted planes. This shows that the left, transformed region is heavily populated by dislocations of mostly one Burgers vector direction, while only a few dislocations are located further ahead of the boundary in the untransformed material. This allows us to conclude, that although twinning presumably relieves some of the transformation stresses, it still involves dislocation formation and generation of a semi-coherent interphase interface.

The observation of both Li diffusion controlled motion of the interface and of the martensitic needle structure characteristic of mechanical twinning suggests that the transformation is a coupled diffusional/displacive transformation. [238] The differences to purely displacive transformations like the martensitic transformation are therefore in the kinetics due to the diffusional component. But the crystallographic martensitic transformation theory is still applicable, which also predicts dislocations in the planar interface between cubic and tetragonal phase. [141] Displacive transformations are often reversible, with the most notable case being shape memory alloys, where the boundary between both phases is highly glissile. However, a significant loss in reversibility is observed once the transformation causes plastic deformation and dislocation

accumulation. [239, 240] The highest reversibility is reached when the crystallography allows an undistorted habit plane between both phases and when there is no volume change to the unit cell. [241] For steel, the large volume change during the martensitic transformation is often given as the reason for irreversibility. [146]

In light of the large volume change $\Delta V \approx 5\text{˜}6\,\%$ associated with the Jahn-Teller distortion due to lithiation of LMO and the observed dislocation accumulation near the phase boundary (Fig. 5.12) a highly reversible transformation is not expected. In fact, attempts to reverse the movement of the lithiation front were not successful even at very high overpotentials up to 15 V. It is conceivable that the applied overpotential is not large enough to drive the in-situ reaction, as a result of charging from secondary electron emission [202] and possible potential barriers to moving the Li through the lithium oxide/nitride layers [242]. Nonetheless, successful delithiation of α-MnO_2 nanowires has been reported using a similar in-situ setup with a solid lithium electrode at a potential of 4 V [169], suggesting that the origin of the irreversibility observed here lies in the transformation itself and not in experimental complications.

We have demonstrated that in-situ lithiation of $Li_xMn_2O_4$ in the TEM leads to the expected phase transformation from cubic spinel ($x = 1$) to tetragonal spinel ($x \approx 2$) and that the two phases are clearly distinguishable by a sharp semi-coherent interface. We were able to verify the successful lithiation by both structural and spectroscopic analysis of the lithium content and manganese valence, but did not detect the orthorhombic intermediate phase previously reported in nanowires. [38] The deviations from the expected stochiometric values for the lithium content ratio (1.75 instead of 2) may be explained by the in-situ conditions and the difficulty of detecting Li, but is also consistent with a valence change of only 0.4. Furthermore, it is possible that Li vacancies are stable in the tetragonal phase, extending the equilibrium composition range to below $x = 2$, in which case the measured composition at the reaction front would be less than $x = 2$, reflecting a finite solubility of the $x = 1$ phase in the $x = 2$ phase. [55, 59, 153] The small measured deviations from the expected manganese valences are well within the typical range of accuracy for EELS, and depend critically on the method used to determine valence from the electron energy loss spectra. In fact, the possibility here to perform manganese valence determination across a chemical boundary within a single sample offers a rigorous test of the various methods to determine valence; in LMO the energy difference between the $\mathrm{O\text{-}K_a}$ edge and $\mathrm{Mn\text{-}L_3}$ edge seems to be more reliable, rather than the more widely used methods based on the $\mathrm{Mn\text{-}L}$ edge intensities. By analyzing reaction front movement, we conclude that the reaction is diffusion limited and were able to obtain a value for the lithium diffusivity in twinned single crystal $Li_2Mn_2O_4$, which is in the range of previously reported values for $LiMn_2O_4$, indicating that transport in the tetragonal phase is not a rate-limiting factor during battery operation. Our measurement provides a reference value of the diffusivity that can be used to identify roles of grain

boundaries, particle ensembles, polycrystallinity and cycling damage that have influenced previous measurements of rate-limiting transport.

5.2.3. Summary and conclusions

During the in-situ tetragonal transformation of the lithium manganese oxide, we observed the formation of a complex twinned microstructure with a well-defined crystal orientation relative to the initial cubic phase and strongly reminiscent of mechanically twinned microstructures. We conclude that the twin microstructure formation is stress-driven, although the lack of a clear dependence on the plane stress state of the foil points to the importance of stress fields from defects and from phase misfit. This twinned tetragonal phase could not be reversibly transformed back to the cubic phase, presumably due to the accumulation of dislocations at the phase interface. Evidence for twinning is also found at the surface of lithiated micron-sized particles, indicating that twin formation also happens during lithation of intact particles. In fact, residual tetragonal domains have been previously found in the TEM in $0 < x < 1$ cycled battery electrode particles and attributed to local overpotentials and named as a cause for battery fatigue. [36] Volume changes and Jahn-Teller distortions have long been associated with capacity fade in Li ion cathode materials [243] and a number of different mechanisms have been proposed. Here, we have identified a new mechanism, namely that the twinned microstructure hinders delithiation of the tetragonal phase and contributes to capacity loss in $Li_xMn_2O_4$-based batteries. Developing materials that can undergo reversible twinning during electrochemical cycling may be a promising direction for reducing battery fatigue. Some of the tactics used for reducing fatigue in shape memory materials by minimizing coherency stresses on the habit plan may prove beneficial even if the volume change inherent to lithium charging cannot be avoided.

5.2.4. Methods

Sample preparation. Sigma Aldrich lithium manganese(III,IV) oxide $LiMn_2O_4$ powder with a nominal particle size smaller than $5\,\mu$m was used. Large, facetted particles were selected and cut into TEM foils using a Focused Ion Beam microscope (FIB, FEI Nova Nano Lab 600 FIB-SEM). After depositing a Pt protective layer, a micron-sized block aligned to the main particle facets was transferred to a TEM half ring (Omniprobe grid) using a micromanipulator. There, one corner was thinned to TEM transparency with the FIB. The Pt protective layer was later removed from the edge of the foil to make the specimen edge accessible to contact by the lithium tip.

TEM characterization/in-situ method. Pre-characterization of the specimen was performed using a 300 kV TEM (Phillips CM30) to confirm the $LiMn_2O_4$ cubic spinel structure and characterize any grain boundaries or other defects. In situ experiments and subsequent ex situ characterization were conducted in a FEI Titan

microscope at 300 kV with an image corrector and a Gatan GIF Quantum 965 ER with Dual EELS capability.

The in-situ holder is a piezo-controlled Nanofactory STM-TEM single-tilt holder in which the FIB-prepared specimens were mounted. Immediately before inserting the holder into the TEM, the W tip of the STM-holder was scratched across a freshly cut Li surface covered in liquid n-pentane (ChemSolute). The n-pentane slows oxidation of the lithium while the W tip is mounted in the holder, the holder is inserted into the TEM, and pumped down, all in less than a minute. The n-pentane keeps the lithium from completely reacting, but allows a layer of lithium oxide/lithium nitride to form on the surface, which acts as a solid electrolyte during the experiment. [162, 165] Lithiation inside the TEM is initiated by mechanical contact between the tip and the specimen; the contact is confirmed by movement of the specimen, bending contours observed in bright field mode and small changes in the electrical currents. A bias of −5 V is applied between tip and sample to drive the reaction and counteract possible positive biases in the sample due to the secondary electron generation and the lithium oxide barrier. [158, 202] The reaction could be halted by breaking off the contact between sample and tip.

EELS characterization of the specimen. Energy drift correction and deconvolution of the low-loss EEL spectra were performed using built-in functionalities of Digital Micrograph. Li content near the reaction interface was obtained by mapping the Li–K-edge, integrated over a window of 15 eV behind the edge after a power-law background subtraction had been performed. Since all acquisition parameters were the same within a given map, the edge counts are proportional to the number of atoms in the beam path and therefore provide a direct measure of relative changes in lithium content [149], assuming that other element compositions do not vary during an experiment. The plasmon position was determined by a Gaussian fit to a 5 eV region surrounding the maximum.

The manganese valence was determined using a method established by Zhang et al. for manganese oxides based on the energy difference between the O–K_a edge and Mn–L_3 edge. [92] The energy difference was measured after of power-law background subtraction based on the background in front of the O–K edge and deconvolution using Digital Micrograph. We note that this method gave valences closer to the expected values than methods based on the Mn–L edge intensities. The error for this method is taken as the approximate 3.5 % of the value stated in the above publication, since the standard deviations calculated from our data are about equally large.

Atom probe tomography analysis and sample preparation. A tip with ca. 30 nm apex radius was prepared by FIB from a previously in-situ lithiated TEM specimen that was interim stored under vacuum. After transfer of the sample to a tungsten support wire, the tip was cut and sharpened using an established lat-

eral cut method. [244] Laser-assisted atom probe analysis was performed using a method developed for $LiMn_2O_4$. [231] The analysis temperature of 30 K immobilizes the lithium and allows determination of lithium concentrations at and across defects. [232]

5.2.5. Acknowledgments

The crystal structures in this work were sketched with VESTA. [245] Help in the display of the APT data by J. Arlt is gratefully acknowledged; we also thank C. Nowak for developing the APT methods used for analyzing $Li_xMn_2O_4$. Additional thanks go to M. Baumung for preparation of the ex-situ $Li_2Mn_2O_4$ particles shown in the sec. 5.8.6. We also thank C. Borchers, R.-T. Qu, M. Risch, and F. Schönewald for their critical reviews of the manuscript and helpful discussions. This work was funded by the Deutsche Forschungsgemeinschaft [CRC 1073 - Project C05 and Z02]. The use of equipment in the "Collaborative Laboratory and User Facility for Electron Microscopy" (CLUE, `www.clue.physik.uni-goettingen.de`) is gratefully acknowledged.

5.3. Additional characterisation of the reaction product $Li_2Mn_2O_4$

Some characterisations of the twinned $Li_2Mn_2O_4$ phase were not included in the previously included paper or were only added as supplementary information. Those results will be shown in the following sections.

5.3.1. Characterisation by scanning nano diffraction

Most of this section/image appeared as supplementary information of the paper

Scanning nano-diffraction with a 2 nm diameter beam and large convergence angle (to protect the CCD) was performed on a $[010]_p$ aligned sample with a large single twinned domain (compare fig. 5.13). Twin identification was performed using the ratio of the integrated intensities of the diffraction spots (yellow circles) from each twin variant[3]. All spots were integrated, but only spots were included in calculations, where intensities of the spots didn't overlap (arrows). A plot of the ratio of the integrated intensities along a linescan perpendicular to the twin planes allows the twin variant widths to be determined. The thicker variant has a width of 22 – 28 nm. The thinner variant has a width of 3 – 6 nm. The twin boundary widths alternate between 1.5 nm and 3 – 4.5 nm. This indicates that the 1.5 nm thick boundaries are parallel to the roughly 2 nm diameter electron beam and are planar over this length scale. In contrast, every second twin boundary has a measured width that is larger than the electron beam

[3] For this purpose the program FIJI was used [246]

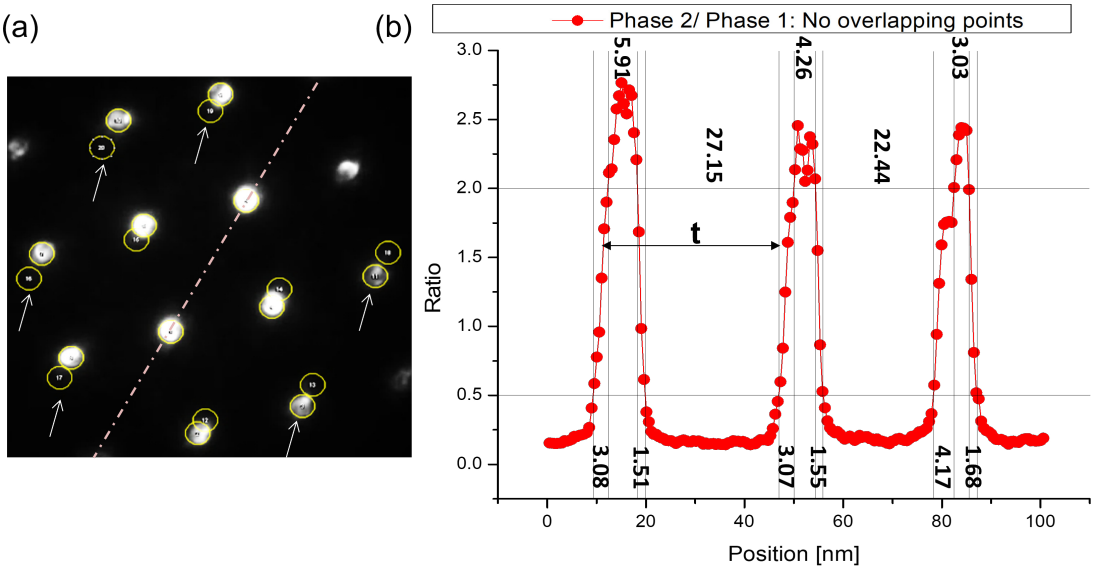

Figure 5.13.: Scanning nano diffraction of the twinned $Li_2Mn_2O_4$. (a) A typical nano-diffraction pattern reveals a twinned microstructure with a $(101)_p/(112)_t$ twinning plane (dash-dotted line). (b) A nano-diffraction line scan allows the widths of the twin variants and the twin boundaries to be determined. The thickness of both twins, i.e. twin spacing t is indicated by an arrow.

diameter, indicating that these boundaries are not perfectly parallel to the electron beam or have 3 – 4.5 nm roughness.

The diffraction pattern in fig. 5.13 (a) also shows how difficult it is to make the twinned, tetragonal phase visible. Only in this orientation $[010]_p$ are both twin variants in a zone axis orientation and thus bright in the diffraction pattern and also well separated. In conventional diffraction the lamellar microstructure also leads to striations connecting the spots of the two phases, but also distorting the other spots. Moreover, most in-situ samples have more than one domain of twins.

5.3.2. Chemical homogeneity of the twinned $Li_2Mn_2O_4$

Even though, the paper showed that the microstructure of the transformed region is made upof twins. Therefore, both of them are of the $Li_2Mn_2O_4$ phase, but still the microstructure often showed complex contrasts that depended on the mode and conditions of microscopy as well as the sample orientation. Fig. 5.14 shows STEM/EELS data that was recorded under the premise of trying to find out whether there might be chemical inhomogeneities within the twins or at the interfaces between them.

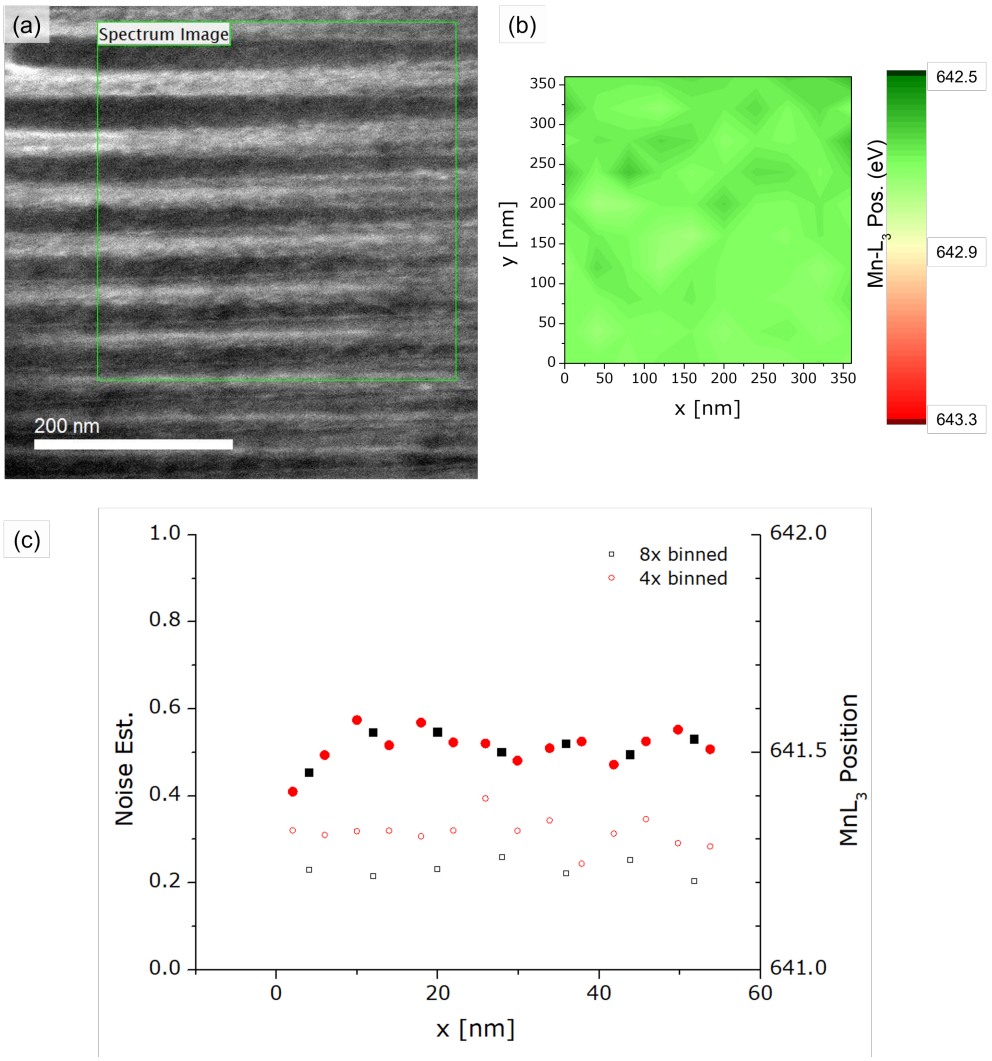

Figure 5.14.: EELS variation within a twinned $Li_2Mn_2O_4$ sample region. (a) shows the ABF-STEM overview image of the twinned sample region. (b) The $Mn-L_3$ edge mapping shows little variation. (c) Additional linescan data in $[010]_p$ orientation showing the edge position (solid) and the estimate of noise in the data (hollow).

Fig. 5.14 (a,b) show the annular bright field STEM image and the Mn−L_3 edge position mapping across multiple twin variants. Because the sample was not perfectly aligned in $[010]_p$ for (a,b), another linescan characterisation perpendicular to the lamellar contrast was performed in that orientation for fig. 5.14 (c). It can be observed in fig. 5.14 (a)[4], that the contrast of the lamellar structure is much stronger on the left whereas on the right some twins appear to be splitting.

Regarding the EELS data one has to take note of the differences in the energy scale of the Mn−L_3 edge. The automatic spectrometer tuning used for calibration of the instrument at that time can lead to some variations in the dispersion and energy offsets (compare fig. 5.14 (b,c)) between different sessions. This issue should not be the focus of this section, but will be addressed later.

The mapping of the Mn−L_3 edge position in fig. 5.14 (b)[5] shows little variation (mean: 642.70(3) eV). Especially no visual correlation with the lamellar contrast of the sample region mapped can be made out. This was confirmed by a linescan (fig. 5.14 (c)) perpendicular to the lamellar contrasts in $[010]_p$ orientation, which is the one shown in the previous section. For comparison two different binnings are shown with the noise estimate (hollow) for comparison. At these noise levels the edge position measurements should be reliable and variations could be interpreted as due to the sample. Unfortenately, the binning necessary to suppress the noise enough also reduces the spatial resolution. This kind of variation in the data was therefore not detailed enough to correlate it with contrasts in the associated overview image. Thus, one can only conclude that the twins are most likely very similar in stochiometry, but there might still be differences at the interfaces which were not within the resolution of the data.

5.3.3. High resolution imaging of the twinned microstructure

Similar to the defect analysis of the $LiMn_2O_4$-$Li_2Mn_2O_4$-interface shown in the paper additional high resolution STEM imaging was performed on the microcstructure within the $Li_2Mn_2O_4$ regions of samples with $[110]_p$ orientation. The interface between to domains with different twinning planes is quite irregular where they meet as is shown in fig. 5.15 (a). It certainly has no regular plane that it occurs on as in the projection of zone axis in which the image was taken some regions show overlapping of the lamellar contrast (e.g. see right region of the image) whereas the interace appears more localized in other regions. With this irregular shape of the interface a high dislocation density can be expected. Detailed analysis at a region of the interface shown in fig. 5.15 (b) confirms this. In the right of the both images dislocation cores are marked with 'T's through Bragg-filtering in the same way it was done for the paper. On the other

[4] This is similar to fig. 5.9 as this is the same sample.

[5] The color scale as well as the axis in (c) have been set to a range/contrast comparable to that in the EELS section where the $LiMn_2O_4$-$Li_2Mn_2O_4$-interface was mapped. Otherwise, any map will appear incredibly noisy.

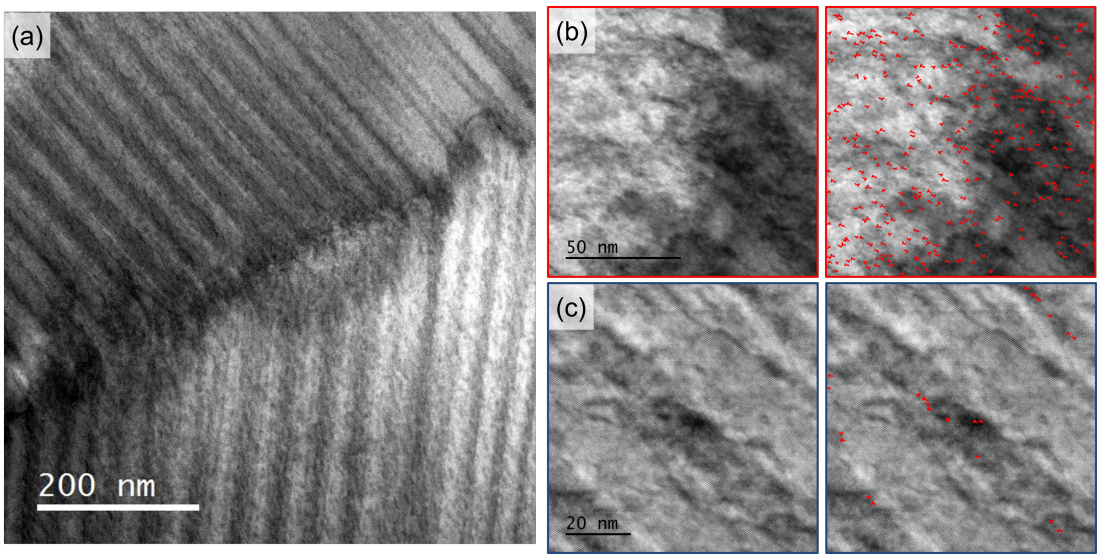

Figure 5.15.: BF-STEM characterisation of the defects within the $Li_2Mn_2O_4$ microstructure in $[110]_p$ orientation. (a) The interface between two domains is irregular. (b) Thus it shows a high density of dislocations marked on the right in detailed analysis. (c) Other regions further from the domain boundary have a smaller defect density.

hand fig. 5.15 (c) shows a selected image of three lamellar contrasts where the defect density is significantly lower. The defects tend to lie at regions where contrast changes occur. Therefore, one can conclude that those are likely interfaces, where defects would be expected.

5.4. Additional characterisation of the interface between $LiMn_2O_4$ and $Li_2Mn_2O_4$

Most of the characterisations of the interface between $LiMn_2O_4$ and $Li_2Mn_2O_4$ have already been shown in the paper section. During all experiments of this thesis one of the main questions has always been how closely the strucutural interface, i.e. twinned microstrucuture and crystal structure, of the reaction is co-located with the chemical interface, i.e. lithium content and manganese valence.

Different approaches were taken to get closer to an answer to this question. They will all not be shown here as they all paint the same picture as in the paper. In scanning nano-diffraction the sharpness of the interface determined by diffraction was approximately the same as that of the EELS-determined interface. This is plausible as the

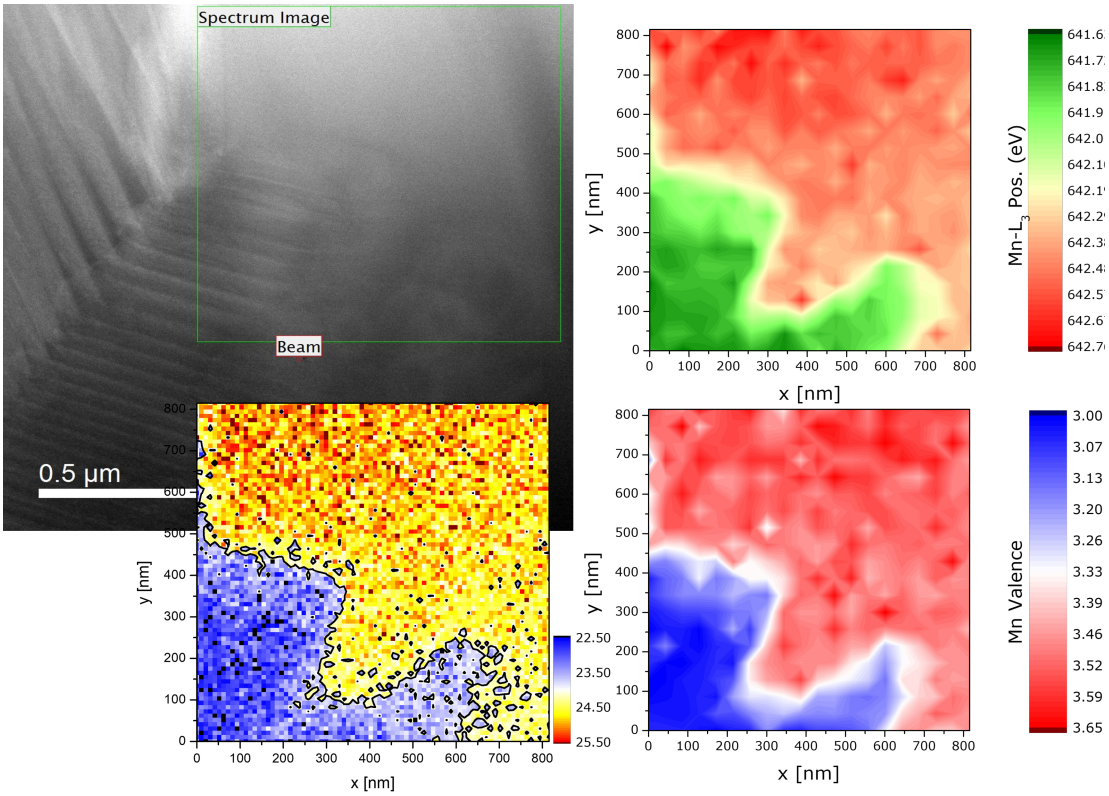

Figure 5.16.: STEM-EELS mapping of a more complex interface between $LiMn_2O_4$ and $Li_2Mn_2O_4$. The STEM image shows that the spectrum image area is close to end of the previously shown complex domain interface. in the lower right corner of teh STEM image bending contours are visible without a lamellar contrast. The three different EELS map methods plasmon center, $Mn-L_3$ edge position and Mn valence show the same shape of the interface. This shape rather resembles the bending contours.

interface between both phases is semi-coherent and therefore the distinction in diffraction is difficult. In almost all EELS maps recorded the chemical interface was at the position of the end/start of the contrast of the twinned microstructure, i.e. the sharp bending contour that is located there or very close. Therefore, this section will not show the many observations that all are exactly in agreement with fig. 5.8 – the EELS map of the paper. Instead, **one EELS mapping** is shown in fig. 5.16 that shows a hint that some transformation without immediate twinning might be possible.

The STEM image in fig. 5.16 shows the interface between domains (comp. sec. 5.3.3) in the lower left from which it was lithiated. Therefore, the top right is of even contrast and unlithiated. The clearly twinned structure visible in the image only reaches into the lower left part of the spectrum image region marked by the green square. But additional bending contours are weakly visible directly left of this square and further into it at the bottom righ edge.

The EELS data that was recorded within that region in fig. 5.16 was evaluated with three different methods. The fact that all three mappings show the same contour of an interface nicely confirms that all three methods can be interchangeably used. The interface visible in all maps is sharp, but the gradient between the regions with min and max of the scales of the maps (compare lower left to the top) shows a transition zone of more than 100 nm. It has to be taken into account, though, that the interface is most likely not parallel to the beam.

Comparing the contour of the chemical interface in all three maps with the STEM image (fig. 5.16) directly next to it shows that it more closely matches the one of the bending contours. When one takes a closer look at the left edge of all three maps there might be hints visible of the bending contours touching the region of the spectrum region in the STEM image. This might be a hint that some region of this sample is already structurally transformed and thus tetragonally distorted, hence the bending contours, but other than the rest of the sample has not immediately formed twins.

Fig. 5.17 shows an overview of the whole sample, after the in-situ experiment. The sample was lithiated from the top right area. The full in-situ lithiation behavior and geometry of the sample is described later, in sec. 5.6.2. This also explains the nature of the V-shape contrast above the white square. The lithiation has left the lower left and right part of the sample unlithiated. It appears that the V-shaped defects have lead to a complex stress state in the sample upon lithiation as a domain boundary runs diagonally through the image. Interestingly the nature of the domain boundary switches in the center of the image. In the top-right corner of the image the twin interfaces point to the top and to the right away from the diagonal. Whereas in the lower left part of the sample they point towards the left and to the bottom away from the domain interface.

It might be that region visible in the EELS maps that has been tranformed in the upper part of the indicated square, but is not visibly twinned is hindered by this complex stress state that has built up towards the end of the lithiation. Ultimately, this kind of observation has only been made in this sample. All other methods and samples

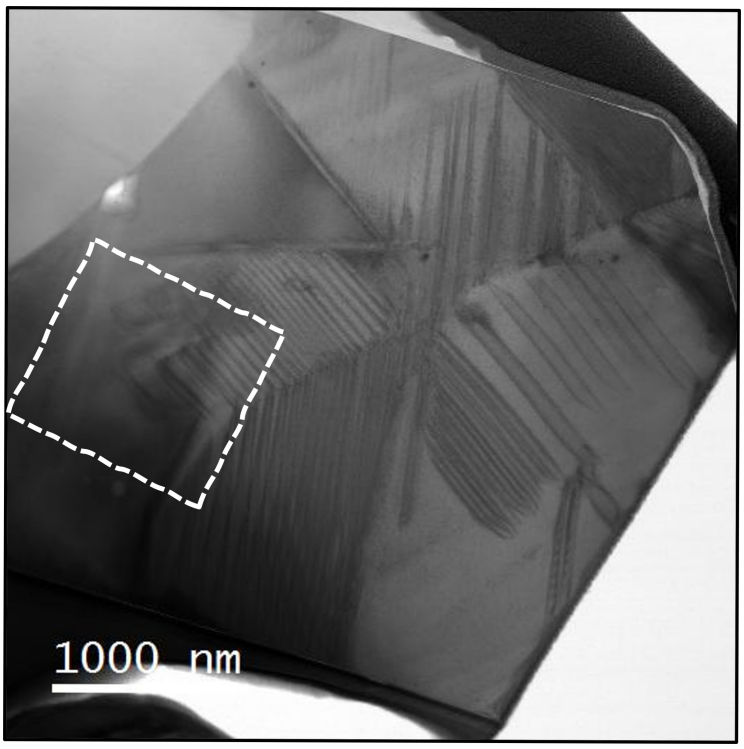

Figure 5.17.: Overview of the sample shown in sec. 5.4, 5.3.3 and 5.6.2. The white square marks the approx. region of the previous STEM image. Note the diagonal domain interface running through the sample.

showed strong bending contours co-located at the reaction front / front of the twinned microstructure.

5.5. Further analysis of the interface movement and microstructure

During this work the focus was not the observation to follow the full lithiation of the sample. Instead, e.g. the lithiation was often stopped within the sample, the videos were stopped in between to do characterisations, contact needed to be reastablished due to drift or magnification was changed. Thus, chracterisation of the lithiation kinetics was only done once for the sample shown in the paper. The data in this section relies on data from the in-situ lithiation shown in fig. 5.11. **The figures and texts of this section were also part of the supplementary information of [69].**

5.5.1. Directional dependence of front movement

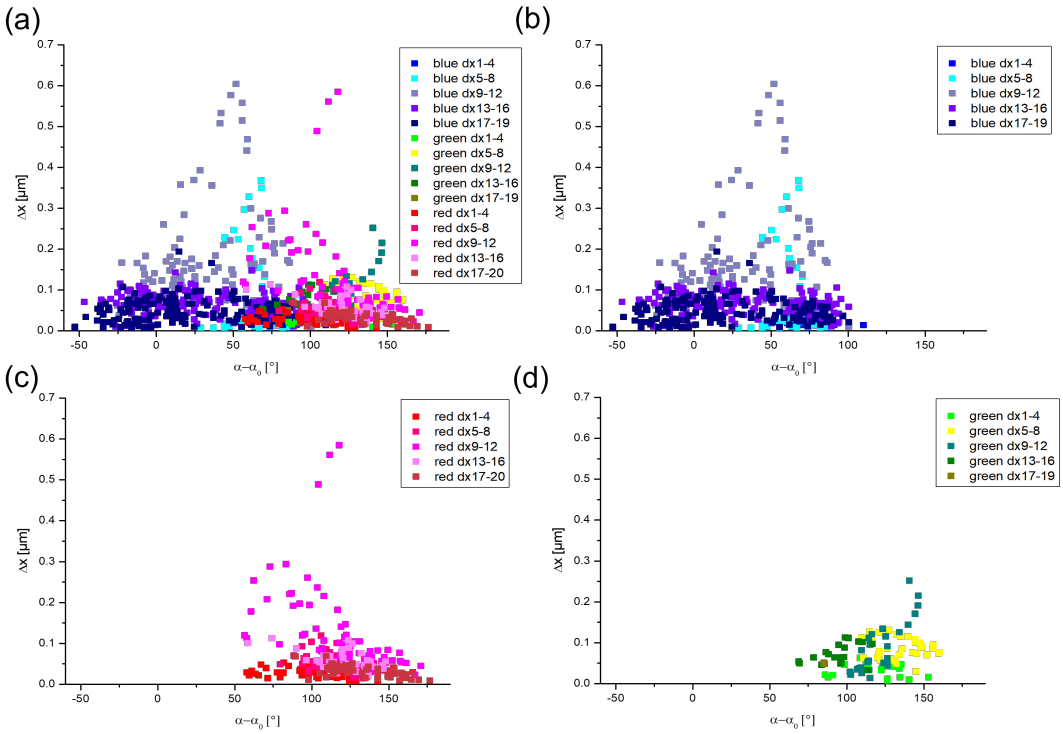

Figure 5.18.: Directional dependence of front movement. The Δx of the reaction front for the fixed time steps of the in-situ experiments has been mapped for four intervals. The x-axis corresponds to the difference between the local angle of the reaction front movement α and the direction of the twin boundary normal α_0. (a) shows all data as well as the data of the blue domain (b), the red domains (c) and the green domain (d) separately.

Fig. 5.18 shows the distance Δx the reaction front moved between to timesteps at which the reaction front was determined. This distance was mapped depending on the the direction of the movement compared to the normal of the lamellar contrasts / twin boundaries. The data is colored by the three different domains from fig. 5.11 and time steps are grouped into five different stages of reaction. All this data is shown in fig. 5.18 (a) with and separate for each domain shown in (b,c,d).

Despite all three domains exhibiting a direction of fastest motion, which roughly corresponds with the average diffusion direction for the domain, there is no correlation with the twin boundary orientations. Competition between domains as well as the fact that the propagation directions are limited to a range of only 90° due to the sample

geometry, likely limit how rigorously one can investigate possible correlations between the tetragonal phase microstructure and the front velocity. In any case, the lack of a clear dependency suggests that possible fast diffusion paths for Li, such as along twin boundaries, are not dominant.

5.5.2. Influence of sample position on $Li_2Mn_2O_4$ microstructure

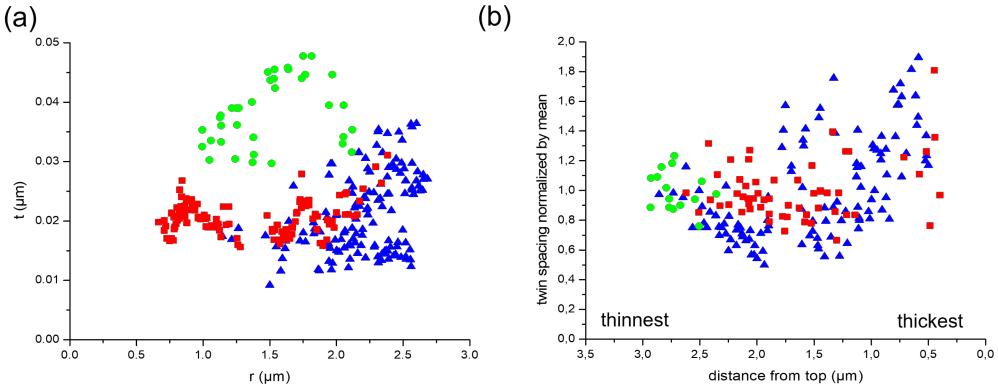

Figure 5.19.: Different scatter plots to evaluate the influence of various parameters twin spacing for the specimen in fig. 5.7/5.11. The (normalized) twin variant thickness is plotted against the distance r to the lithium contact point (a), which depends on experiment time, and against the distance from the top of the lamella image (presumed to linearly depend on lamella thickness) (b).

Further parameters were investigated for their influence on the measured twin spacing. Fig. 5.19 (a) shows a scatter plot of the twin spacing (10 – 50 nm) and the radial distance from the contact point. The distance should be an indirect measure for the reaction rate, as due to the diffusion dependence it should be slower at higher distance / later in the experiment. To compare the domains the twin spacing was normalized by the domain mean in fig. 5.19 (b) and plotted against the distance to the top of the sample in the image. This should be an indirect measurement for the sample thickness as FIB-prepared specimen are normally slightly wedge shaped, yielding a linear dependency of thickness to the distance from the free edge (at the bottom in the images).

Because the data of the green region is confined to a very small space it is not possible to see any trend at all. Both red and blue might show a slight trend in both fig. 5.19 (a,b). Due to the fact, that the data is very noisy it is not possible to make any conclusion here. Additionally, even if there is a trend it is then visible in both parameter dependences.

5.6. Interaction of the lithiation front with defects

The presence of planar defects has a strong influence on the lithiation behavior. This was observed in multiple in-situ experiments. The two following sections will describe the influence of two different kinds of defects on the movement of the reaction interface, i.e. lithium front. But, a high density of defects leads to more contrasts in the sample as the strains get more complex. Positions of the interface can thus be harder to observe in still images, but are deducible by careful frame-to-frame comparison.

5.6.1. Influence of stacking faults

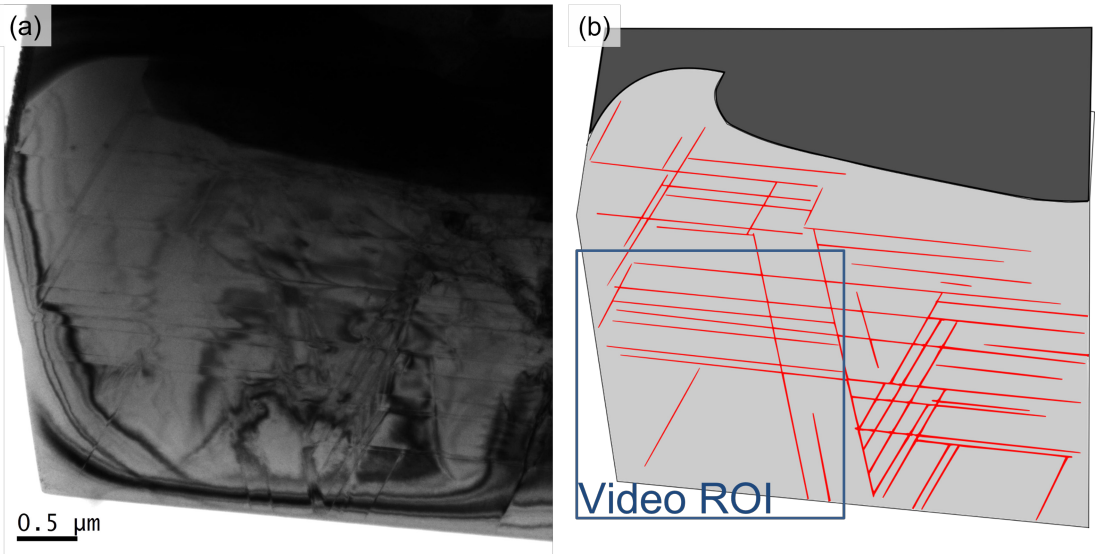

Figure 5.20.: Overview of a sample with a high stacking fault density. The bright field image of the sample (a) shows that the SFs lead to contrasts. Due to this a higher magnification including fewer defects was chosen for in-situ imaging (b).

The influence of stacking faults on the lithiation behavior was most clearly observable in the sample shown in fig. 5.20. Pre-charactersation showed that the sample was single chrystalline, but with a high defect density. Fig. 5.20 (a) shows a multitude of stacking faults that lead to a more complex contrast in the right region of the sample. The arrangement of SFs can be seen in the sketch in fig. 5.20 (b) made on the basis of the full pre-characterisation of the sample. Three different orientations of the SF projections are observed. It also has to be taken into account that lines were only drawn where a clear contrast was observed so that some SFs might extend further than sketched.

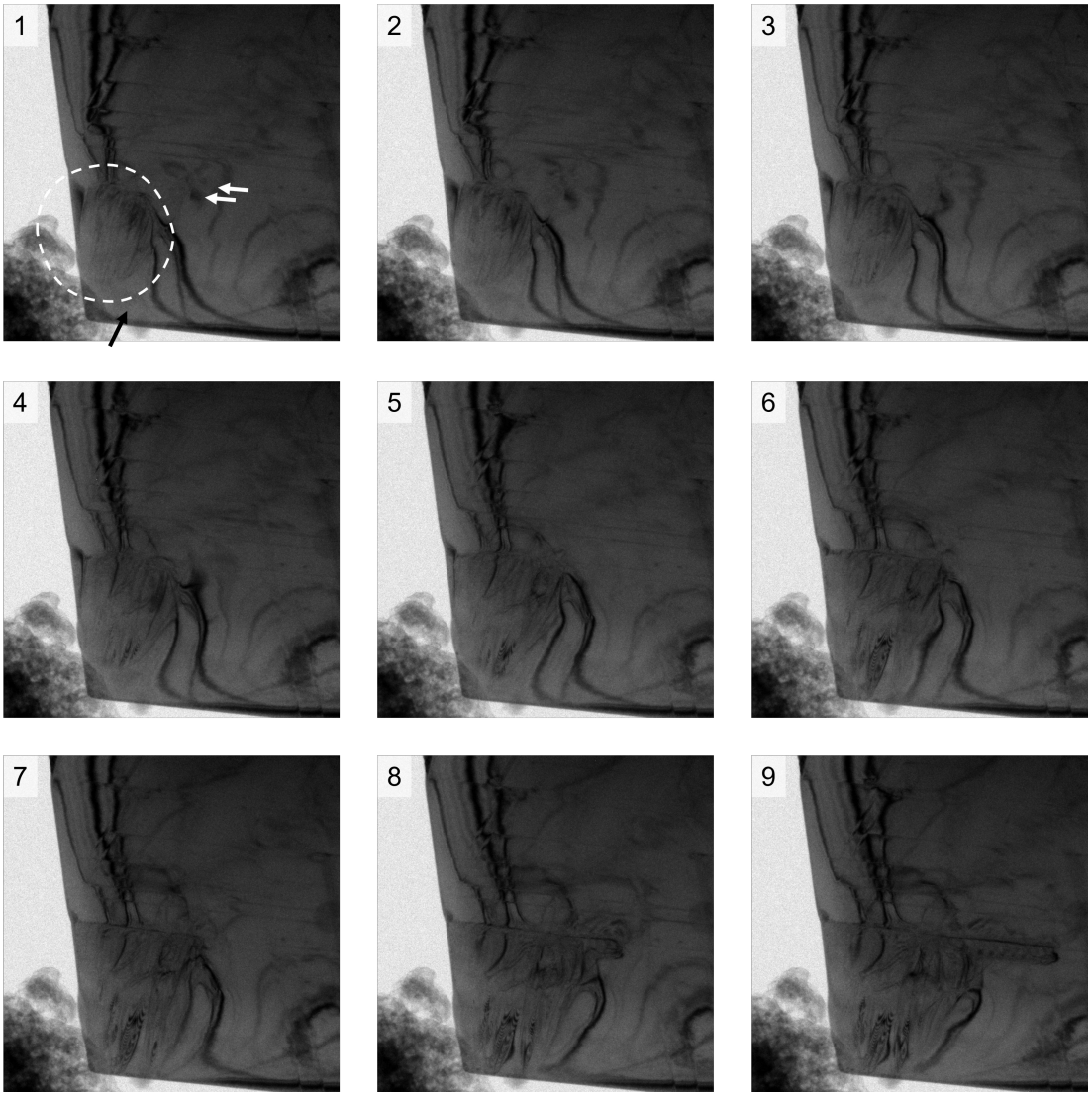

Figure 5.21.: Image sequence showing the influence of stacking faults. In the starting frame of the 140 s sequence the lithium has already reacted the encircled region of the sample. The reaction front moves normally, but also across a SF (black arrow) without visible resistance (1-6). Then (7-9) the reaction is speed up strongly between the SFs (white arrows). Field of view: $2.708\,\mu\mathrm{m}^2 \times 2.708\,\mu\mathrm{m}^2$

Additionally, the region chosen for the in-situ observation of the reaction is marked in fig. 5.20 (b), which was chosen due to more even contrast. The reaction of this sample region can be seen in the image sequence of fig. 5.21. The image sequence spans a time of 140 s starting when the sample has already been contacted by the lithium tip (lower left corner). A region of the sample has already reacted with lithium (circled) before the bias is applied.

To give a guide to the eye three stacking faults are marked with arrows pointing along the SF plane's projection. Those three SFs are used as examples for their influence on the reaction front during in-situ lithiation in the following paragraphs. But they also help the observation that throughout the whole in-situ reaction of this sample the lamellar contrasts of the twins are never parallel to the pre-existing defect's contrasts and thus should be different planes.

The sequence shows **three different influences of the stacking faults** on the lithiation behavior. During the first six frames (fig. 5.21 (1-6)) the reaction front moves similarly to the reaction front shown in the ACS paper. This includes the movement across a SF (marked by a black arrow in frame 1) without any notable change in diffusion behavior (**neutral**). But during the last third of the image sequence (fig. 5.21 (7-9)) the lithiation behavior changes notably: While the front is approximately circular in frame 7, in frame 8 and 9 the reaction moves forward much quicker between the two SFs marked with white arrows in the initial frame. Meaning that lithium transport is possibly **enhanced** along the direction of one of the SFs. Also, the reaction front is **blocked** by the upper of the two SFs as no crossing of the interface can be observed in the last frame.

Additional videos including ones at higher resolution were recorded subsequently. Due to the additional contrasts of the already transformed $Li_2Mn_2O_4$ region the further reaction is hard to observe the reaction front in their still images, though still possible by careful analysis. One of those image sequences is shown in appendix (sec. A.10 / fig. A.12), but the observed behavior is summarized in fig. 5.22. This shows the previously sketched overview of the stacking faults with the added information of how the reaction front moves upon further reaction.

Within the observable region of the in-situ videos the reaction first shows the expected reaction behavior previously reported in fig. 5.21 starting at the tip in the lower left and moving right. Afterwards the large front extends further out past the blue square region (1). After this, the following videos show that the next areas between stacking faults are reacting one after another (2/3/4) from the right side to the left. The stacking fault(s) marked by the left black arrow are passed by all lithium fronts. On the other hand, the SF marked right black appears to have a blocking effect on the lithium movement as reaction fronts two, three and four come from the right and move left, while the region to the right of the V-like structures of stacking faults remained mostly unlithiated.

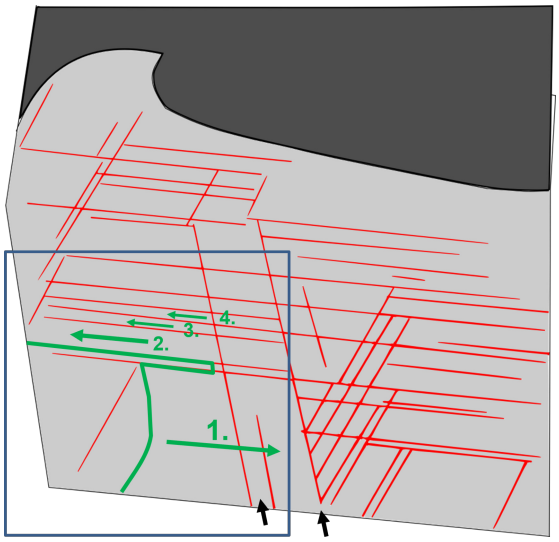

Figure 5.22.: Sketch of the behavior observed during in-situ lithiation of a sample with high stacking fault density. Numbers indicate subsequent lithiation in direction of the arrow.

5.6.2. Influence of three-dimensional defects

An additional type of defect in the sample material already showed as a planar defect with extended dimensions in comparison to the previous stacking faults. Even though this was only clearly visible under the right sample orientation. Two of those defects resembling a V-shape in the sample are marked by black arrows in fig. 5.23 (a). In an attempt to make the samples still more homogeneous in thickness[6], this sample has a protective layer of FIB-deposited remaining on it. At this starting point of the image sequence contact with the sample is already established and the standard bias of $-5\,\mathrm{V}$ is applied.

Within the 40 s of the image sequence shown from fig. 5.23 (a-d) the reaction moves more than $1\,\mu\mathrm{m}$ to reach V-shaped defect structure. Fig. 5.23 (b,c) show that multiple domains of twins form as multiple directions of lamellar contrast are visible. It is important to note, that at the time of the last still image the sample is already visibly bent by the tip, because the tip had some positional drift during this experiment. This leads to the worse contrast in comparison to the other frames. The in-situ lithiation was stopped by moving the tip away at his point with the goal of having the reaction front in the center of the sample. The contrast got immediately better as soon as the tip was

[6]The original idea was also to be able to rethin the sample. But thinner samples prepared this way yielded almost no contrast in-situ and also bent way to easily upon contact with the tip, making a sample orientation very difficult.

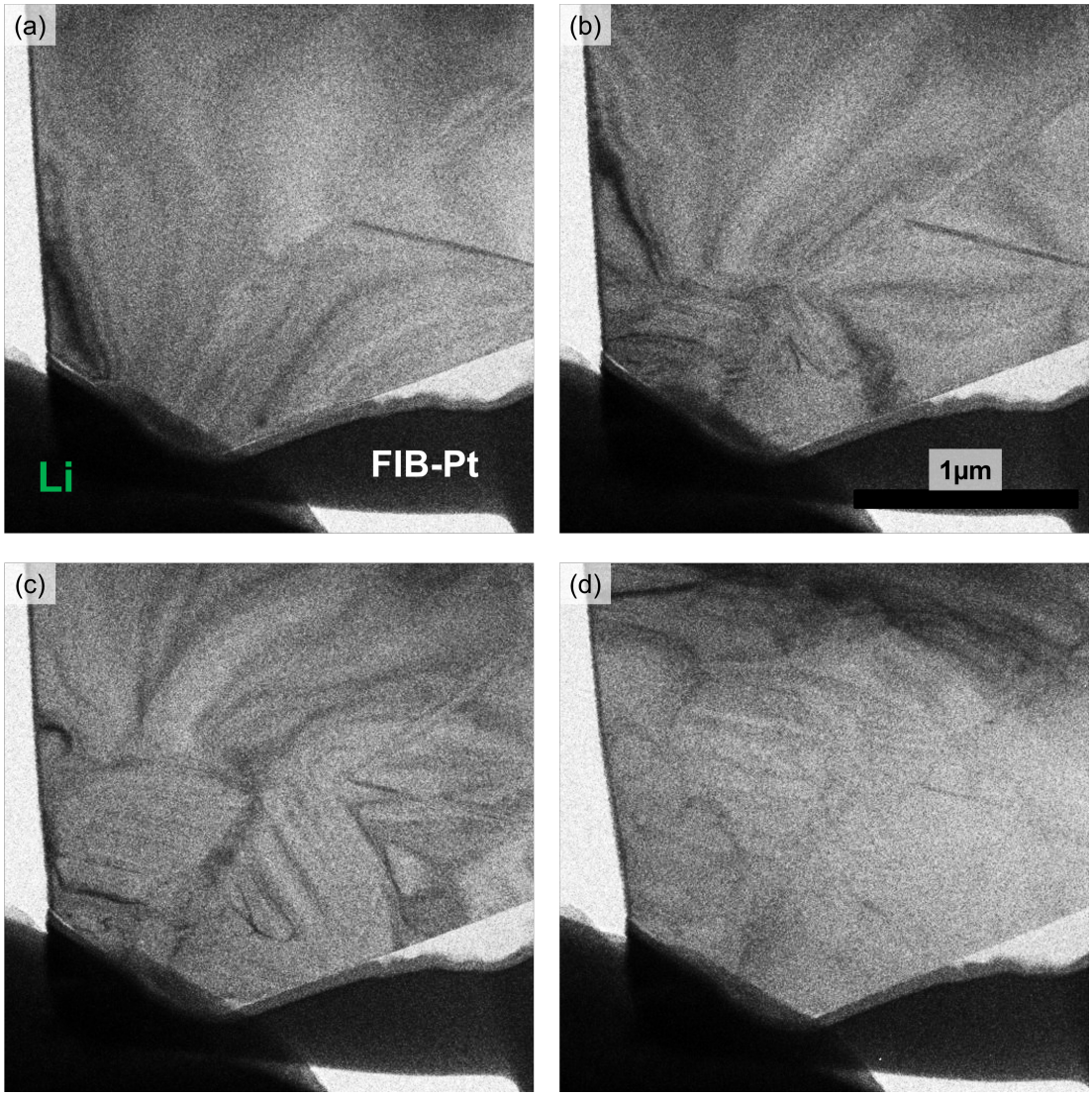

Figure 5.23.: In-situ lithiation image sequence with extended planar defects present. Those defects are indicated by black arrows in (a). Within the 40 s of the image sequence the reaction front moves past the V-shaped defect structure. At this point the lithium tip contact is removed. (Contrast has been increased for print)

removed, which will be shown later.

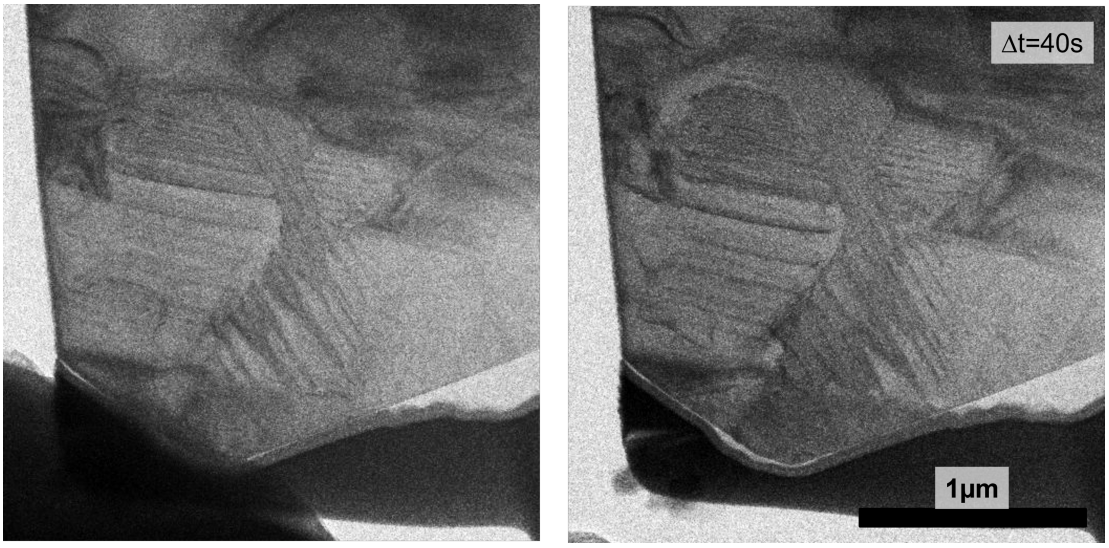

Figure 5.24.: Movement of the reaction front continues without Li tip contact. After additional 40 s the front has moved further past the V-shaped defect structure.

The reaction of the sample continues, despite the mechanical contact of the tip being removed. This can be seen in fig. 5.24 by comparing the two images separated by 40 s. The continued lithiation of further areas of the sample was only observed to this extend in this sample. The extent of the continuing lithiation is even larger than shown in this directly comparable images taken from the in-situ video, which showed when the sample was further investigated afterwards.

The ongoing reaction of the sample beyond the intended point suggests that the different sample preparation might have an influence. It is well known that the metals deposited in the FIB are not pure, but contain remains of the hydroxycarbons used as precursor gas [247]. As carbon is an active anode material for batteries a possible explanation could be that some lithium is moved into the protective layer later reacting with the cathode material $Li_xMn_2O_4$ as this energetically favorable in comparison to any LiC_x. This has to be kept in mind, if any further experiments with this type of sample preparation are going to be done in the future.

The main observation is the reaction front reaching the V-shaped defect structure during the in-situ lithiation, but not moving into the area enclosed by the defects. Fig. 5.24 shows the contrast of the twinned microstructure at approximately two thirds of the visible sample area, but it does not extend into the area right of the center. The area of the defects was afterwards investigated further by STEM-EELS to confirm and understand this.

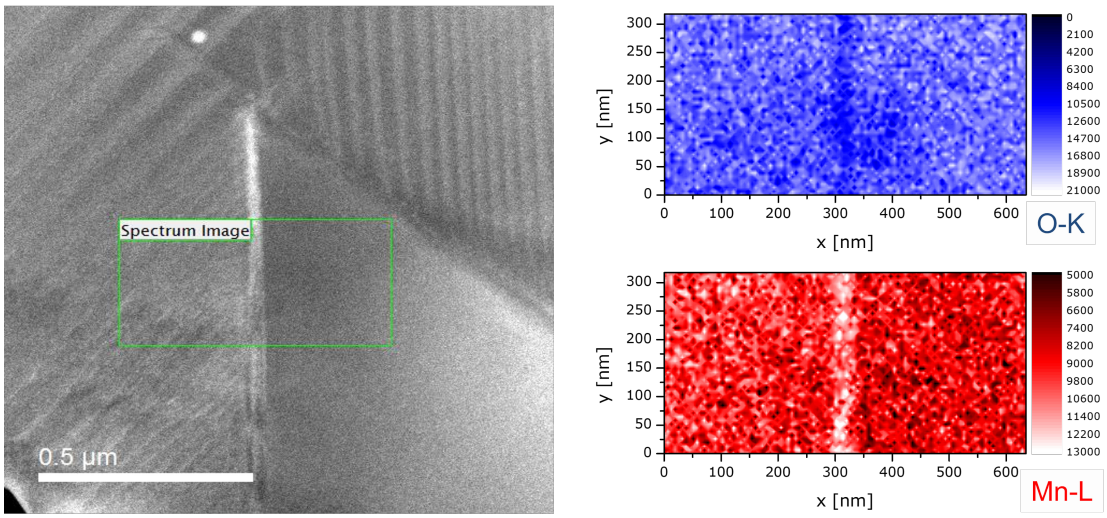

Figure 5.25.: STEM-EELS elemental analysis of an extended defect. The overview image shows that the twinned structure does not extend into the enclosed region. Chemical maps of the O–K and Mn–L edge show a distinct difference at the position of the defect. STEM rotation was used to have the defect vertical in the maps.

A few of the results of the STEM-EELS analysis are shown in fig. 5.25. The annular bright field STEM contrast used in the overview maps when the main goal was EELS analysis shows less bending contours than classical TEM-BF images. Thus, it can be clearly seen that the twinned microstructure is all around the region enclosed by the defects, but no reaction has taken place within. The chemical mapping via the quantification of the O–K and Mn–L edge shows that both lithiated and unlithiated regions show the same oxygen and manganese content. This is to be expected as pre-characterisation showed the defects as inclusions in a single grain. But a strong contrast is visible in both elemental maps. Manganese is enriched in comparison to the rest of the sample, whereas oxygen is diminished.

Those elemental maps plus of the ones of the edges not explicitly shown can be vertically averaged. This was done in fig. 5.26 (a) to give a quantitative idea of the defect and lithiation state. The data was normalized by the average of the first 253 nm, basically the whole side left of the defect. It can be seen that all edges are homogeneous with a slight trend to fewer counts towards the defect. Expectedly, the Li–K edge integration proves to be noisiest as it was just recorded with the zero-loss peak and the *Dual EELS* was used to record the O–K and Mn–L edges.

To the right of the defect the O–K and Mn–L edges show the same counts as on the left side. The Mn–M quantification deviates a little to lower counts. This is likely due

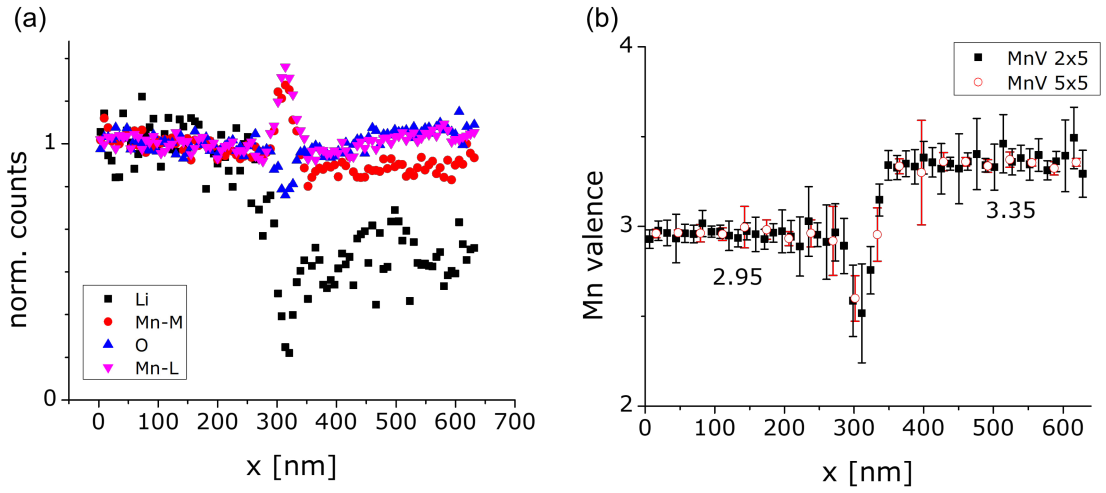

Figure 5.26.: Vertical average of elemental counts and manganese valence across the defect. (a) All counts for all available edges in the vertically averaged quantification were normalized to the average value left of the defect. (b) Mn valence quantification was averaged for two x-binnings prior to calculation.

to the change in the plasmon peak with varying lithium content shown in the EELS chapter (compare sec. 4.2.1), which makes perfect background substraction for the Mn−M edge difficult. The lithium counts drop significantly in the unlithiated region, which is expected.

The elemental quantification of the defect itself in fig. 5.26 (a) shows an increase of both manganese edges and a slight decrease in oxygen counts. Lithium counts drop to their lowest values at the center of the defect.

The emerging picture of left and right of the defect just differing by lithium content is supported by the manganese valence quantification shown in fig. 5.26 (b). The error bars correspond to the standard deviation of the vertical average of the manganese valence map it's based on. Higher lithium content on the left correlates with a valence of 2.95 on average, which is slightly lower than the expected 3. Valence quantification on the right side of the sample gives a valence of 3.35, which is lower than the 3.5 it should be. Directly at the defect the measured manganesethe drops to values almost as low as 2.5, which also points to a different stochiometry. The two different binnings used for the quantification show the same values and plateaus on the left and right of the defect, though coherently the data with less binning in x-direction (2x5) is noisier, but providing slightly more data points near the interface.

Table 5.1 shows the previously described changes quantitatively in comparison to the normalized left side. The average for the normalized left 40 datapoints $\bar{c}_{L40}$ is obviously 1 for all edges, but the higher error shows the noisier nature of the lithium counts.

	$\overline{c}_{L40}$	$\overline{c}_{C3}$	$\overline{c}_{R40}$
Li K	1.00(9)	0.24(8)	0.55(9)
O K	1.00(3)	0.815(14)	1.03(4)
Mn L	1.00(3)	1.27(3)	1.01(3)
Mn M	1.00(4)	1.21(3)	0.91(3)

Table 5.1.: Table summarizing the chemical quantification of the spectrum image in fig. 5.25. $\overline{c}$ are the average normalized counts for the left 40 (L40), right 40 (R40) and the central three (C3) data points on the defect.

Lithium being exactly half the counts in the fourty points on the right, unlithiated side (R40) in comparison to the lithiated side is at least within the error for 0.55(9). The comments made regarding the `Mn-L`, `Mn-M` and `O-K` in the previous paragraph hold true.

At the central three points (C3) located at the defect the oxygen counts drop by approximately 20% and manganese increases 27% on the more reliable `Mn-L` edge quantification compared to the basic stochiometry of the $LiMn_2O_4$ sample. The lithium counts drop by more than 75%. This data can be used to estimate the stochiometry of defect. In the basic sample the ratio O:Mn should be 2. Multiplying this by 0.815 and dividing 1.27 yields 1.3.

Also taking into account the manganese valence measured at the interface and the fact that in pre-characterisation and some HRTEM images the defect coherently fit into the structure of the $LiMn_2O_4$ grain, the most likely fit is Mn_3O_4. Mn_3O_4 has a tetragonally distorted spinel structure with similar lattice parameters and a theoretical valence of 2.67 (compare sec. 2.2.2.2) and the O:Mn ratio of 4:3 is very close to the measured 1.3.

A short speculation as this is not the focus of this thesis: The defects in this sample could therefore be inclusions of Mn_3O_4, which might have formed due to slight off-stochiometry during sample preparation and segregated to existing stacking faults on {111} planes minimizing their energy due to distortion and interface.

5.7. Attempts at delithiating an in-situ lithiated sample

In order to investigate the influence of the microstructure formed during lithiation on the delithiation process, three attempts were made in this work to reverse the phase interface movement between $LiMn_2O_4$ and $Li_2Mn_2O_4$ by applying a strong reversed bias (in comparison to the lithiation experiments). The results presented in this section originate from one of these experiments and are representative of the behavior of the microstructure in the other experiments. The results of this sample were selected because the sample was most homogeneous and had a well recognizable and STEM-EELS

accessible interface.

The lithiation process was performed as described above at a voltage of −5 V applied to the sample and the formation of the characteristic microstructure during the lithiation under BF imaging conditions happened similarly to ones previously shown. Subsequently, the contact of the sample with the lithium was mechanically interrupted and the sample was characterized with STEM including EELS. Afterwards, the contact between tip and sample was re-established, whereby a voltage of 10 V had already been applied to the sample to prevent further lithiation, which should easily lead to delithiation.[7] The behavior of the phase boundary was observed and after no change was detected within six and a half minutes, which in other cases were sufficient for complete lithiation (in this case the actual lithiation reaction occurred within less than two minutes), the voltage was increased again to 15 V. After almost ten minutes, the contact to the lithium source was mechanically disconnected and the sample was examined under the same conditions as before with STEM(-EELS).

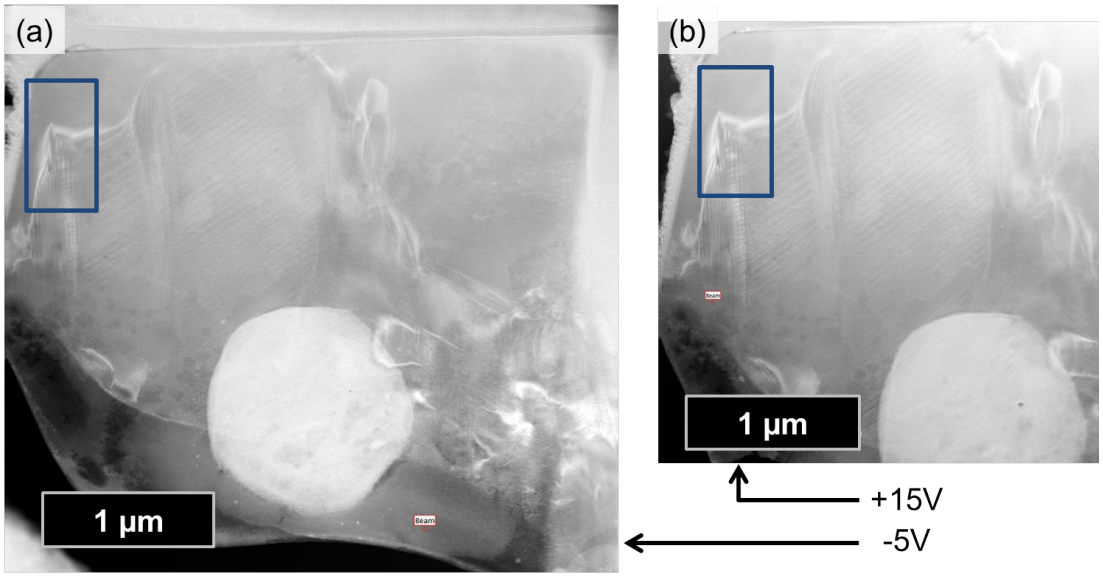

Figure 5.27.: (a) ABF-STEM overview image of the sample after successful lithiation at a potential of −5 V. (b) Overview image under comparable conditions with slightly altered image region following a delithification test with a potential of up to 15 V.

Fig. 5.27 (a) shows the sample after lithiation. In the bottom left corner a part of

[7] This an extremely high voltage was chosen to eliminate as much doubt as possible about all influnces on the voltage discuseed throughout this thesis, e.g. capacitative effects, beam induced charging, and a possible energy barrier of moving lithium back into tip.

the lithium tip is still visible. Furthermore, two artifacts can be seen: Firstly, there is a dirt particle in the lower central area that was attracted to the sample between precharacterization of the sample and mounting into the TEM. Considering the time required for all steps up to the in-situ experiment, a test was nevertheless performed on the sample. Secondly, it can be seen that the area at the bottom of the image (i.e. at the top in the FIB) became significantly thinner during sample preparation during thinning and was bent off. This was also the case in other experiments and did not noticeably affect the lithiation of the sample. Regular slight movements and their direct influence on the bending contrasts ensured a continuous mechanical contact of the tip with the sample. As the bending contours and lamellar contrasts in the upper half of the sample show, lithiation of the sample took place. The rectangle marks the area of the STEM-EELS map recorded for before/after comparison. Fig. 5.27(b) shows the sample under comparable imaging conditions. For better comparability, the magnification was adjusted to approximate that of (a). The lamellar structure is still visible and the bending contours do not show any extensive movement.

In order to find out whether a partial delithiation occurred nevertheless with no or only a slight change of the microstructure, e.g. by delithiating only one of the variants or with the distortion of the lattice remaining despite decreasing lithium content, STEM-EELS maps were recorded at the areas marked in Fig. 5.27. The results are shown in Fig. 5.28 for both manganese valence quantification and the position of the $\mathrm{Mn\text{-}L_3}$edge. Both maps agree to a large extent in the position of the interface. The serrated nature of the microstructure is more pronounced in the $\mathrm{Mn\text{-}L_3}$ maps, because the detection of both phases by $\mathrm{Mn\text{-}L_3}$ edge position is less prone to errors (compare to cha. 4). Considering that the maps might not be aligned perfectly and that the maps have a significantly higher noise level after the delithiation attempt, the maps match within the expected accuracy. The increased noise level is due to poorer data quality, since the previous scan produced a slight carbon contamination at the location. This is also very weakly visible in the BF/HAADF-STEM signals in Fig. 5.29 as a rectangular shadow. These images also show the exact shape of the phase boundary. It can be noticed that in both cases before and after lithiation the shape of the interface in both imaging and mapping correlate very well confirming again that microstructure formation and phase transition are correlated. The fact that this is also the case after the delithiation attempt with a notably high counter bias would suggest that the microstructure might stabilize the $Li_2Mn_2O_4$ against delithiation.

However, in order not to rely only on the visual appearance of the maps, the statistical values can also betaken into account. These are summarized in table 5.2. The median and mean values for both maps show that no shift of the valence has occurred within the map and thus no delithiation seems to have taken place. Furthermore, the 10% and 90% percentiles of the $\mathrm{Mn\text{-}L_3}$edge position show that the two phases have not changed. The shift of the percentiles for the manganese valence are presumably due to the poorer data quality and thus increased scatter, which does not shift the median and mean.

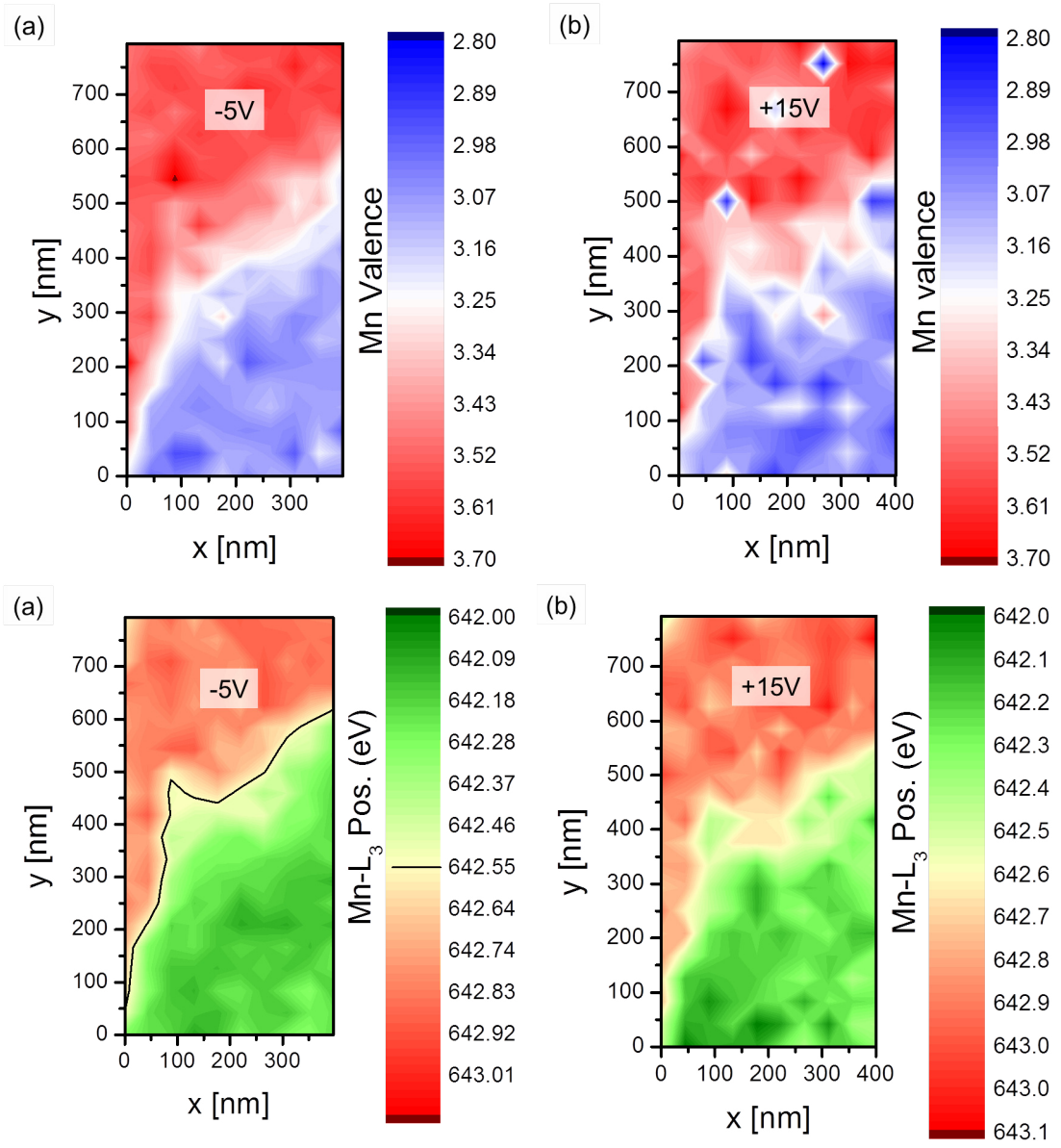

Figure 5.28.: Two types of EELS maps (manganese valence and $Mn-L_3$position) before and after the delithiation experiment to investigate the influence on the phase boundary.

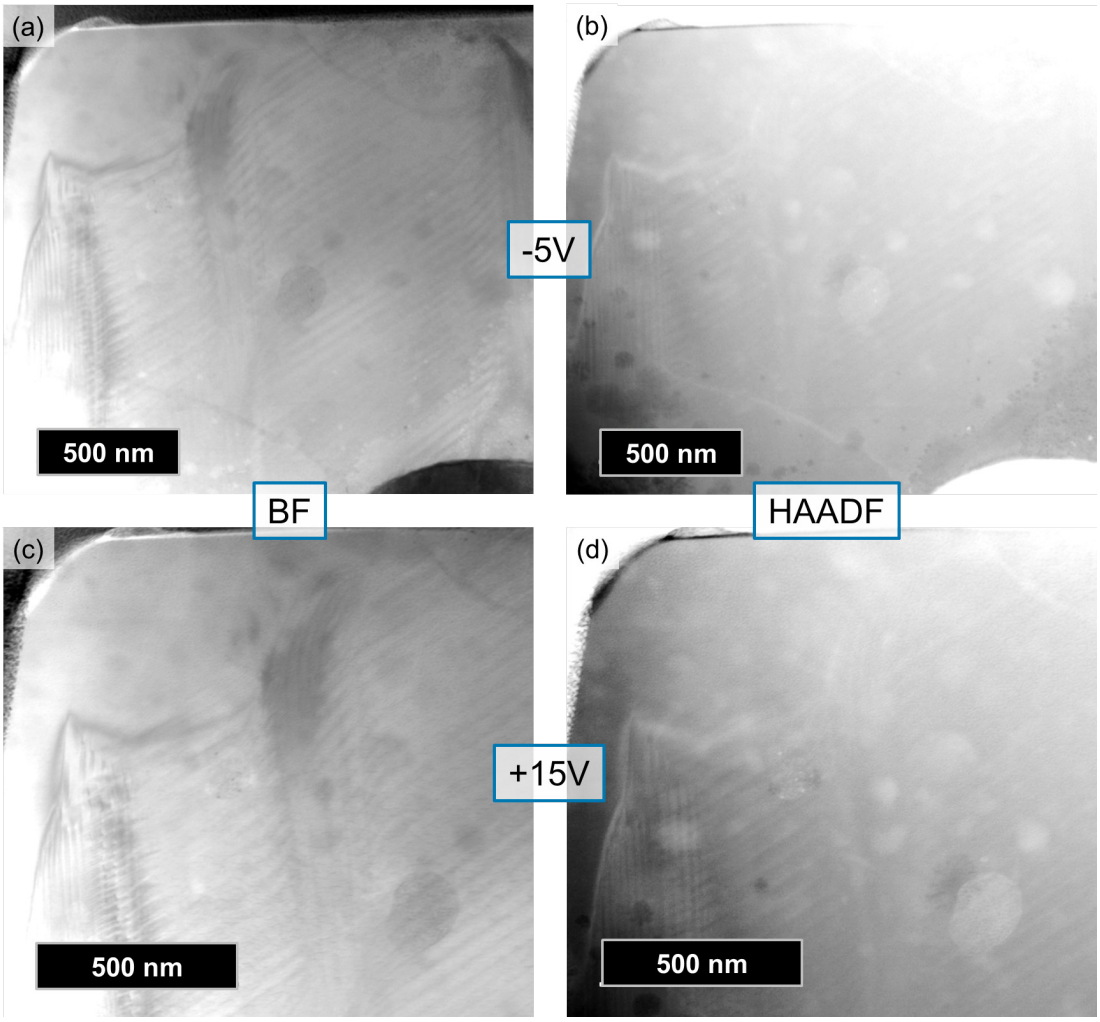

Figure 5.29.: system images ($L = 130\,\mathrm{mm}$) of the phase boundary before and after a delithification experiment show no clearly recognizable change in both BF and HAADF contrast.

		∅	median	10%-percentile	90%-percentile
−5 V	Mn-Val.	3.3(2)	3.33	3.07	3.57
	Mn−L_3-Pos.	642.5(3) eV	642.5 eV	642.16 eV	642.85 eV
15 V	Mn-Val.	3.3(2)	3.31	3.02	3.59
	Mn−L_3-Pos.	642.6(3) eV	642.6 eV	642.19 eV	642.86 eV

Table 5.2.: Tabulated summary of the most important statistical values of the four EELS maps shown in the section.

5.8. Control experiments

5.8.1. Lithiation also starts without bias

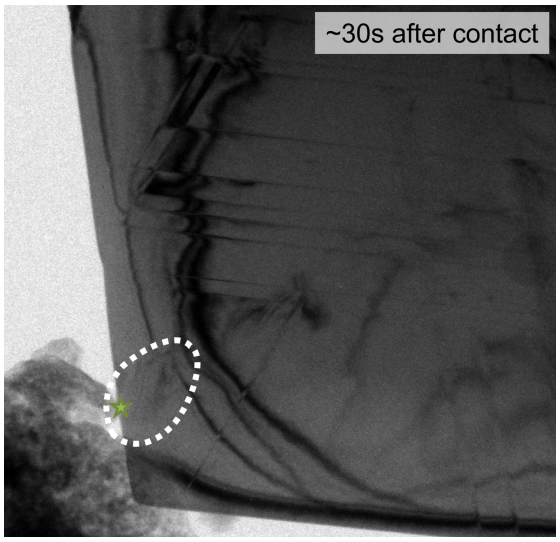

Figure 5.30.: Lithiation starts without bias. 30 s after contact a small region of the sample shown in sec. 5.6.1 has transformed without a bias applied. The star marks the contact point of the Li tip which could clearly be determined from the recorded video.

The reaction of the lithium on the tungsten tip was visible at the start of the in-situ experiment as shown in fig. 5.30. Thirty seconds after contacting the sample a small region has transformed even without a bias applied. This is highlighted by the white annotation. The contact point of the lithium tip is marked by the green star.

The bias was often only applied after contact was made and this was not the only time the start of reaction was already noticable. At the same time one can see that the contrast of the transformed region is not easy to identify. There were a multitude

of reasons why experiments where still performed at a bias: The most important one reproducibility as a bias was applied in the first experiments. Others include but are not limited to imitations in video recording length, reactions being easier to observe at higher speed, questions about sample charging and activation energy necessary to get through the LiX solid electrolyte layer. The latest experiments were even performed with bias before contact with the hope of less tip drift (crosstalk of the piezo with the bias) and stopping after short lithiation.

There was never any obvious difference in microstructure formed in the regions that where lithiated at the beginning without bias.

5.8.2. Contact and bias with pure tungsten tip

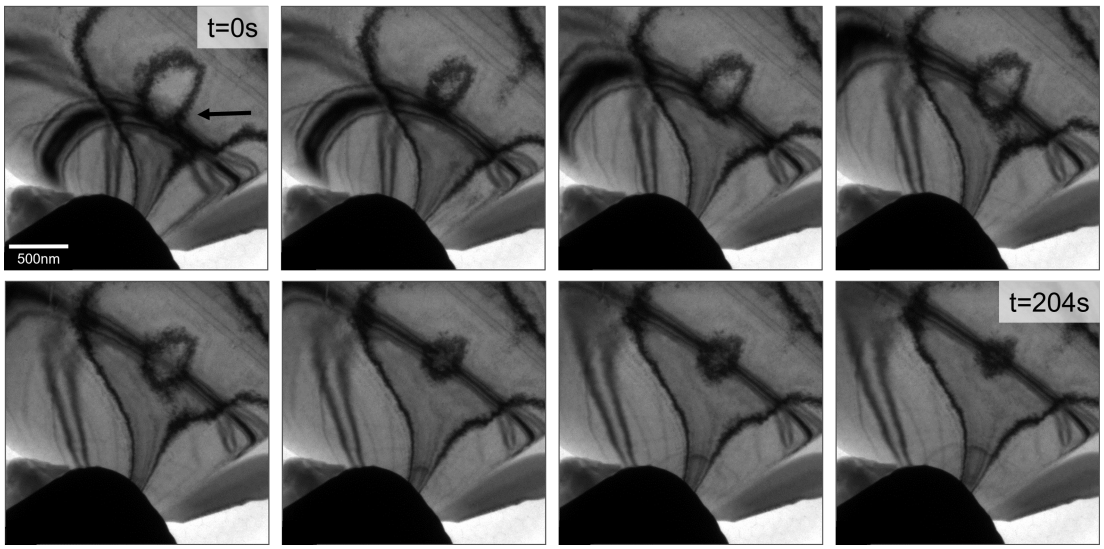

Figure 5.31.: Brightfield image sequence showing contact between a pure tip and a pristine $LiMn_2O_4$ sample at $-5\,V$. During the timeframe of a normal in-situ lithiation experiment of multiple minutes movement of some bending contours but no sharp interface can be seen.

Contact experiments with a pure tungsten tip were performed to make sure that the microstructure upon lithiation of $LiMn_2O_4$ is not influenced by pure current flow. Fig. 5.31 shows still images from the video sequence during the time (roughly three and a half minutes) the bias between tip and sample was held at $-5\,V$ – same as during in-situ lithiation. Movement of the bending contours is clearly visible in the region marked with an arrow in the first frame: The large band like contour moves through the image and the more elliptical bending contour gets smaller and smaller. This movement is

possibly due to a slight drift between tip and sample seen during many experiments, thus changing the stress applied to the sample. But no sharp interface developes comparable to the ones observed during in-situ lithiation. During in-situ lithiation changes in the sample and sharp bending contours near the tip were always visible, latest during appplication of the negative bias.

5.8.3. Beam stability of Li under STEM-EELS conditions

A previously already characterized region of interest was included again in a STEM-EELS mapping to investigate possible sample damage during typical investigations. The results are shown in fig. 5.32 in which no obvious damage to the sample can be observed in the overview image of the survey. When extracting the thickness map from the data, the previously scanned region is clearly visible by additional thickness (brighter green). This is due to carbon deposition because of imperfect vacuum, which was a long term problem of the instrument during this thesis.

The exact same shape of this previous SI also shows in the maps of the Li and Mn counts. Although, this is striking and might be interpreted of both Mn and Li loss at first, there is a different explanation for this. Careful analysis of the relative composition shows that in those maps the effect disappears. Those maps are not shown here due to the distrust in absolute quantifications of content expressed in the EELS method chapter 4. Despite removing plural scattering via the built-in function of `Digital Micrograph` before any calculation of elemental counts in the edges, this function cannot express the whole effect. The simple explanation is thus that the deposited carbon layer due to bad vacuum diverted some intensity away from the edges by plural scattering. This can be confirmed by the fact, that the effect is very weak in the plasmon center map.

5.8.4. Dispersion tuning

During the many manganese valence quantifications performed during this thesis, it became obvious that the values sometimes appeared to be shifted. Tests of the dispersion tuning have therefore been performed, in which the EEL spectrometer was used with a 100 V wobbler and an integration time of 1 ms for five frames to capture the zero loss peak at its position of 0 eV and shifted by 100 eV.

Fig. 5.33 (a) shows the results of testing this in state the instrument was left in by the previous user and after the automated tuning procedure implemented for the spectrometer in fig. 5.33 (b). It can be clearly observed that after centering the first peak at approximately zero, the second peaks of both situations are not at 100 V. Exact determination of the energy difference results in 99.198 eV and 99.215 eV.

This observation arose only late in this thesis as most of the experiments for this thesis had already been performed and trust in the reproducibility of the experimental

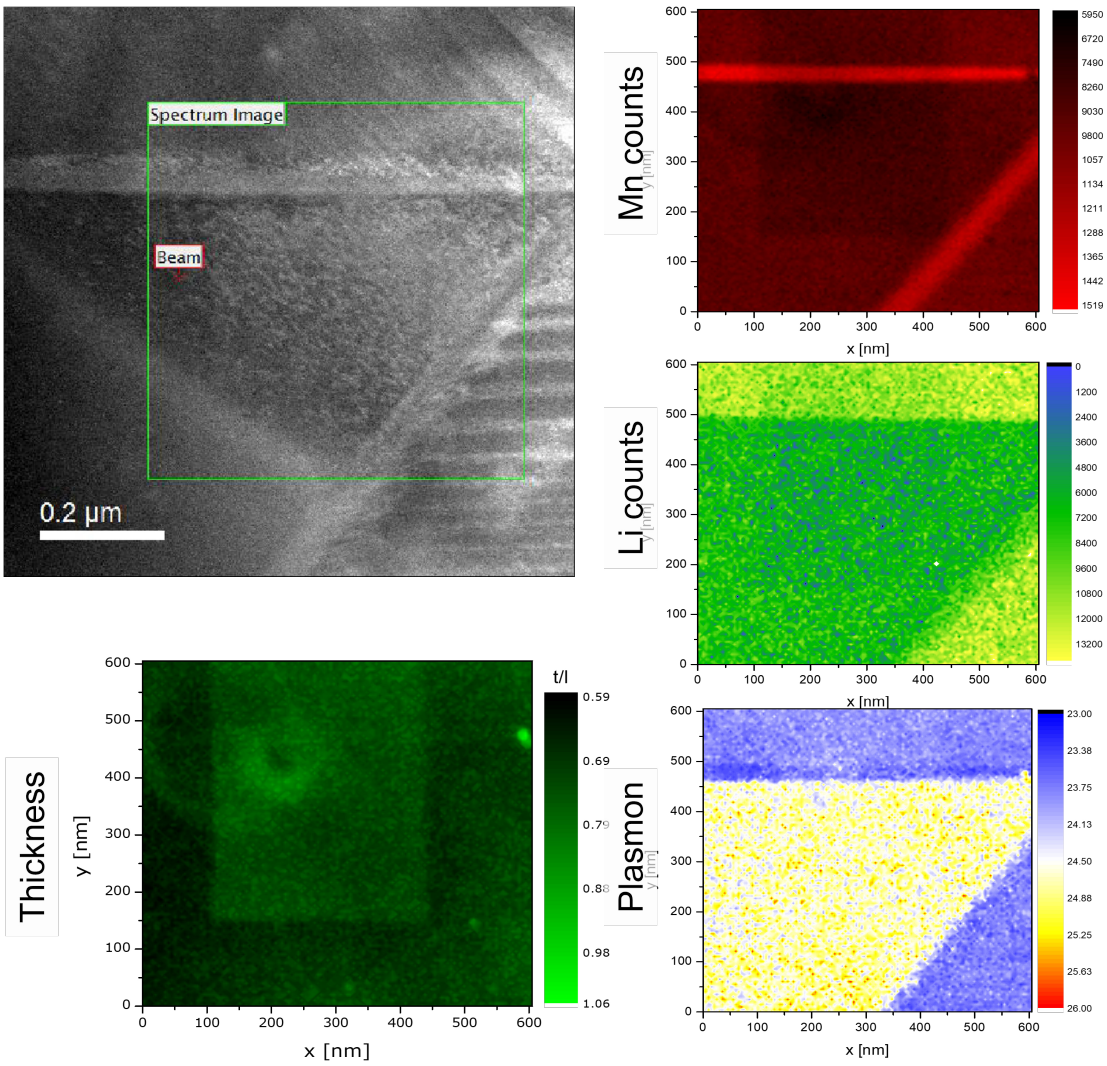

Figure 5.32.: Investigation of the beam stability of the specimen. A prior region (comp fig. 5.25) clearly shows in the thickness map due to carbon deposition. This leads to slight artifacts in Mn/Li counts and almost unnoticeable effects in the plasmon map.

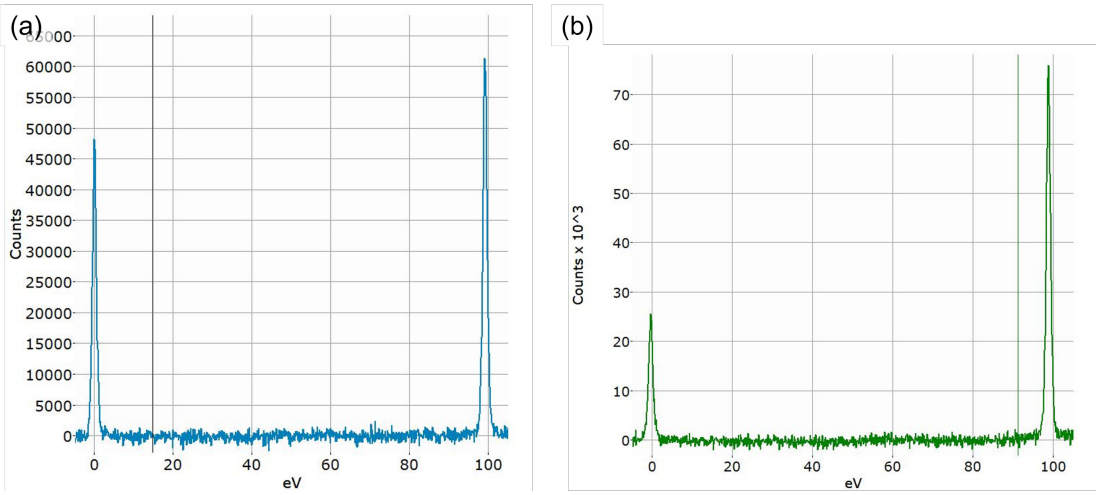

Figure 5.33.: Test of the automatic dispersion tuning of the EEL spectometer. (a) shows an obtained vacuum spectrum with a 100 eV wobbler activated first coming to the TEM. (b) shows the same after the automated tuning procedure has been performed. With the first peak centered on zero both second peaks are not exactly at 100 eV.

results was built, so that the values were questioned more deeply. This is not ideal, but the influence of 1% deviation on the measured values will be revisited in the discussion.

5.8.5. Long term stability of the reaction front

To further understand the nature of the microstructure forming during in-situ lithiation one sample was revisited after a long time. The goal was so check whether the forming microstructure, if somehow metastable, might relax over time. For this a sample was kept in the TEM holder vacuum pumping stand, where the samples could be stored between TEM sessions if further characterisations were to be carried out, for a time of nine months.

Fig. 5.34 shows the sample used for the microstructure analysis in the paper (comp. section 5.2 or [69]) before and after this long-term storage. Comparing before (a) and after (b) in fig. 5.34, shows that the long-term storage in the pumping stand keeps the sample well-preserved from surface reactions. Kept in membrane boxes the samples degrade in a matter of days (compare images in section A.8). Please note that fig. 5.34 (b) has been taken at 120 kV vs. the regular 300 kV and the weaker contrast is not due to any reaction. Furthermore, the spot damage visible is presumably carbon from STEM-based characterisation at non-perfect vacuum conditions that prevailed in the FEI TITAN for quite some time during this thesis.

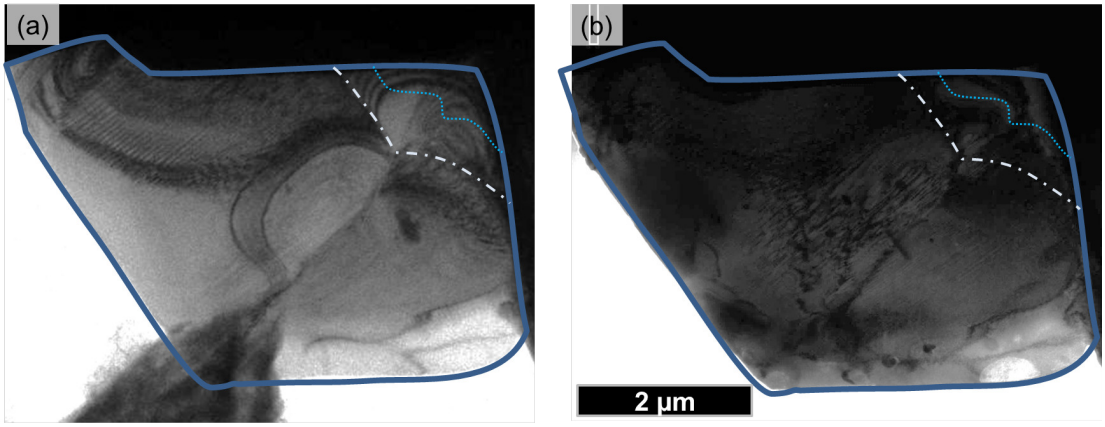

Figure 5.34.: Long-term stability check of a lithiated sample. (a) shows the sample right after in-situ lithiation with the Li-tip still present (300 kV BF). (b) shows the sample after keeping it in a vacuum for nine months (300 kV BF). Both have the sample shape and initial and final slightly moved front position indicated by lines. No obvious long-term reaction and microstructure change happened as the lamellar contrast of the twins is still visible.

Secondly, the reaction front has only moved by less than 1 μm over the time of nine months as has been marked by the two dotted lines as visual aid, since the reaction front may be hard to see at print resolution. Additionally, the twinned contrast is still visible in the sample, probably most visible in the center of Fig. 5.34 (b), but additional images and higher resolution have been used to confirm that it's not only present there.

A better overview image at the reaction front after the ninth months in Fig. 5.35 shows that microstructure doesn't change type and spacing over time as well as when it progresses slowly into the sample without applied bias. Whether this is caused by residual lithium present at the original point of contact with the sample or if maybe the lithium content slightly varies within the $Li_2Mn_2O_4$ phase and then equilibrates to the lowest possible value of that phase cannot be determined this way and might be further point of discussion.

5.8.6. Ex-situ electrochemical lithiation of the sample $LiMn_2O_4$ powder particles

To rule out that the discovered behavior of tetragonal twinning is only inherent to the thin foil geometry of the TEM specimens, electrochemical experiments were conducted on the pristine sample powder. Max Baumung kindly prepared samples from the same micron-sized powder particles used for TEM sample preparation and lithiated them with the same setup normally used in their other experiments (compare e.g [196]). For

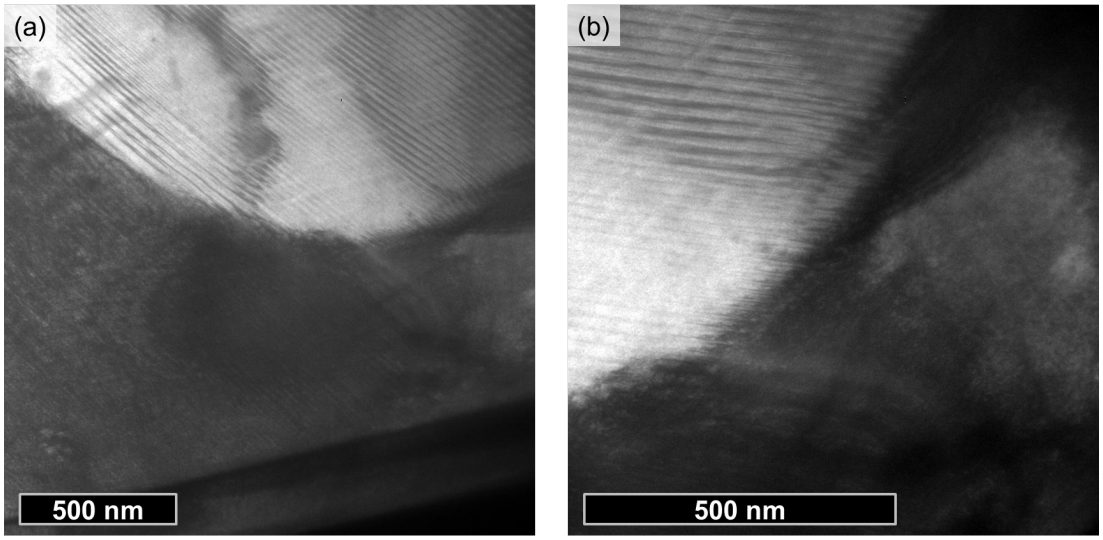

Figure 5.35.: Closer look at the reaction front in Fig. 5.34 (b). Both BFs in (a,b) show that the lamellar structure is preserved. Since the field of view should include the original position directly after in-situ lithiation, no change of microstructure is recognizable between fast and slow, further lithiation.

this the powder was mixed with graphite and lithiated and assembled to a cell with 1.0 mol/L $LiPF_6$/ethylene carbonate (EC) and dimethyl carbonate (DMC) electrolyte using a lithium counter electrode. At a rate of C/10 the potential was then lowered from 4 V to 2 V, where the end voltage ensures a state of $Li_2Mn_2O_4$. This powder was than analyzed by $\theta - 2\theta$-XRD that was inconclusive, because it was dominated by cubic peaks as can be seen in Fig. A.7 in the appendix. But several additional peaks and intensity shifts can be detected that are in agreement with tetragonal phase formation, but are much less visible than expected for a full transformation.

Parallel to the XRD analysis the particles where examined in the SEM to look for changes in the morphology in comparison to the well-facetted micron-sized particles in the pristine sample material. The normal morphology of the pristine sample material is well established by the many SEM images taken during the FIB-based TEM speciment preparation process. As can be seen in Fig. 5.36 all large particles show the same characteristic change to their surface. The previously smooth[8] $\{111\}_c$ and $\{100\}_c$ facets now show cystallographically oriented steps as would be fitting to a deformation process.

[8] Of course defects have been discussed in the sample preparation section, but the particles definetely looked different and the amount of defects was much lower without this characteristic of obvious surface steps.

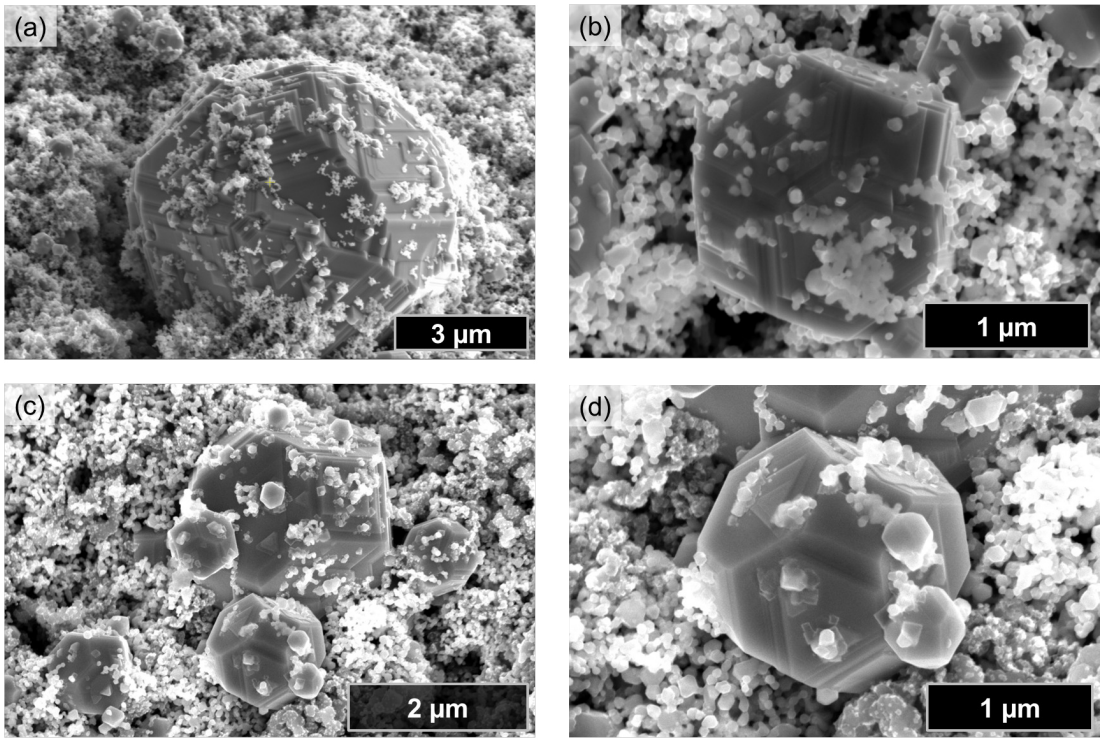

Figure 5.36.: Morphology of ex-situ electrochemically lithiated $LiMn_2O_4/Li_2Mn_2O_4$ particles. All shown particles have developed crystallographically oriented steps (parallel to both the edges between $\{111\}_c$-$\{111\}_c$ and $\{100\}_c$-$\{111\}_c$facets) consistent with twin formation on $\{101\}_p$ planes. (a) shows the particle later used to prepare a sample for further TEM analysis. (b,c,d) Additional images of futher particles show the same change in surface. Note how those changes are also visible in the particles smaller than $1\,\mu$m.

It is well known that surface steps will form on the surface of a sample during tetragonal transformation (see sec. 2.4) to stay close to the original global shape of the samole. Further analysis shows that the steps are parallel to edges between presumed $\{100\}_p$ and $\{111\}_p$ surfaces, which is consistent $0\bar{1}1_p$ planes.

Imaging of a cross-section of one particle (compare Fig. 5.36 (a)) inside the *FEI Helios FIB*[9] by low voltage STEM shows a high density of defects including dislocations and planar defects as well as high internal stresses (see Fig. 5.37). The planar defects inside the sample are of at least two different types, but could not be further determined inside the FIB. But the high density of defects and the bent nature of the sample also didn't

[9]Performed by Volker Radisch.

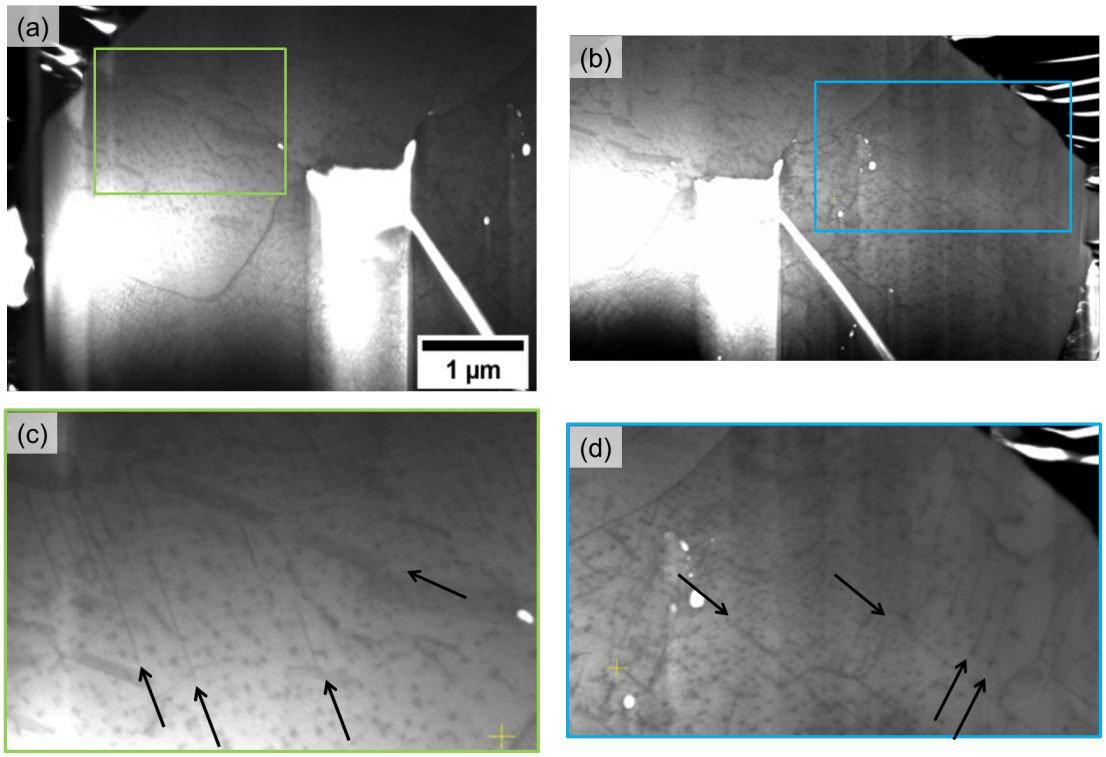

Figure 5.37.: Low voltage STEM micrographs of the lithiated sample microstructure. The scans performed using the designated detector inside the *FEI Helios FIB* show a strongly deformed sample with high residual stresses. A closer look in (c,d) shows a high presence of planar faults (some marked by arrows) as expected during step formation on the surfaces.

yield any additional results by conventional TEM.

6. Discussion

As detailed in the published paper in section 5.2 [69] a total of 15 in-situ lithiation experiments were performed during this thesis. The result was a sharp interface moving into the sample identifiable in brightfield conditions. This allowed tracking the interface over time and identify the diffusion-controlled nature of the reaction as well as the influence of different defects on the reaction (compare sec. 5.6).

The result of the lithiation was a lamellar microstructure in all experiments, which was identified as twins of the tetragonal phase. The samples showed one to three different domains with twin thicknesses of a few to hundreds of nanometers. Some particles of our nominally-$LiMn_2O_4$ sample powder also showed tetragonal particles with a very similar microstructure. The in-situ lithiation proved to be non-reversible in the TEM.

EELS allowed the investigation of both phases of the reaction from $LiMn_2O_4$ to $Li_2Mn_2O_4$ and the interface between the two. The results showed a concurrent change in Li, that almost doubled across the interface, and Mn valence. For this multiple methods of determination were examined for transfer to $Li_xMn_2O_4$ and the one most suitable for the in-situ samples in terms of reliability and spatial resolution was selected. Additional methods were used for comparison and confirmation (compare chapter 4).

This chapter will classify the most important of the results just mentioned, try to explain them and compare them with the relevant literature. It will also assess the significance of these results and what next steps can be derived from them.

6.1. Values measured by EELS

Chapter 4 has already gone into the details of the methods concerning manganese valence and elemental quantification as well as a discussion of the differences and reliabilty of the methods to establish the most suitable one. The result of this was the selection of using the difference in O-K and Mn-L_3 as a measure of valence with the calibration by Zhang, et. al. [92]. Occasionally additional methods like the Mn-L position as well as the plasmon peak center have been used supplementary or based on available data. They were in good agreement with the last two being able to provide more spatial resolution with the drawback that they have no calibration.

Possible beam damage of the sample needed to be excluded for meaningful results. For this the operating voltage was always chosen as 300 kV. This was done as Li is one of the few elements where beam damage cross-section actually rises and falls within the range of typical TEM voltages [170], so that higher is better in this case. It has been reported several times that Li_2O can be decomposed under the electrom beam of a TEM both willingly and unwillingly [172, 248]. And it has been experimentally confirmed that it takes four to five times longer for Li_2O_2 to decay at 200 kV than at 80 kV [249], while the damage is actually argued to be oxygen release [250]. This was once observed accidentally in the TEM when the beam was focused too much on the Li tip with high intensity.

Due to the fact that Li_2O_x is an anode material and $LiMn_2O_4$ a cathode material, lithium is much more strongly incorporated into the $LiMn_2O_4$ structure. Therefore, it was assumed that under conventional TEM conditions the tip would show damage before the sample, so that checks for any damage could be performed. The control experiments of sample damage under STEM-EELS conditions didn't show strong damage, but only sample contamination by carbon deposition. Slight damages cannot totally be ruled out, but for Li_2MnO_3 damage doesn't occur until $2.6 \times 10^8\,e/Å^2$ [251].

The influence of the dispersion error can be estimated according to the calibration equation 4.11 [92]: $\Delta E = 2.65(6)\,eV \cdot V_{Mn} + 103.45(23)\,eV$. According to this equation the difference should be $\Delta E(3.5) = 112.7\,eV$ and $\Delta E(3.0) = 111.4\,eV$. If those energy differences were really measured with a dispersion that is 1% lower this would yield valences of 2.58 and 3.07, which is an extreme shift that was not observed during measurements. What is interesting that the valence difference between the two values drops by 3% in total terms, but the absolute difference is still almost 0.486 and close to the value expected.

This leads to the conclusion that the absolute valence values need to be interpreted with a grain of salt, while the absolute values of their difference across the interface more reliably point at the expected values.

Interpretation of the measured valences therefore needs to be done carefully. But despite always writing $Li_2Mn_2O_4$ this refers more to the structure than to the exact lithium content. Nevertheless, the overall tendency in all experiments with EELS quantification has always been a less than exact doubling of the lithium counts and a valence difference lower than the expected value of 0.5 (for example compare the values given in sec. 5.2: 3.05(11) and 3.45(12) with $\Delta_V = 0.4(2)$ and $\Delta_{Li} \approx +80\%$). The changes in the edges have been comparable the same effects seen soft-XAS of different manganese compounds [183], although they claim that EELS doesn't have the necessary energy resolution for good analysis. Many papers disagreeing with this are in the method section. A very detailed XANES study on $Li_xMn_2O_4$ by Okamura, et. al. [59] supported

by theoretical calculations shows that also in their case $Li_2Mn_2O_4$ is only lithiated to 77.4 in the tetraonal phase based on the volume proportions of $LiMn_2O_4$ and $Li_2Mn_2O_4$ structures at an overall lithium content of $x_{Li} = 1.6$. In an additional work using XRD on different sample sizes it is also suggested that the phase separating region in $Li_xMn_2O_4$ rather lies between $x = 1.0$ and $x \approx 1.75$ for larger particles comparable to those of this work [153].

Going with those results and assuming that the valence difference can be trusted as well as the lithium counts, the change in lithium content of +80% is the value belonging to a valence change of 0.4, that we reported in [69].

Other possible explanations are manyfold, but there it is difficult to chose one over the other and no clear indication that one of them is the reason for deviations in the manganese valences measured. Still, it could be possible that the samples surfaces was damaged during the preparation in the FIB creating a passive surface layer that does not change during lithiation and therefore doesn't contribute to valence changes. It has been reported, that the Ga ions used for sputtering in the FIB can be incorporated into the spinel structure [113].Plus, it would have been possible that one of the twin variants has a lesser chemical change, for which no hints were found upon analysis of the twinned regions. Another possibility that can't be ruled out is any non-stochiometry of the $LiMn_2O_4$ in the particles. This appears reasonable as off-stochiometric defects and full particles were found during this thesis. As laid out in sec. 2.2.2 there are multiple stable lithium manganese oxide spinels with slight deviations to $LiMn_2O_4$ (e.g. $Li_{1+y}Mn_{2-y}O_4$ and $LiMn_2O_{4-\delta}$), but the lack of any further information about it makes any speculation unnecessary.

6.2. Formation of a twinned microstructure during tetragonal transformation

The results of this thesis show that during the in-situ lithiation of $LiMn_2O_4$ a complex, twinned microstructure forms. The relationship of the cubic $LiMn_2O_4$ and the tetragonal $Li_2Mn_2O_4$ was confirmed to be via the similarity of both phases' backbone of oxygen/manganese atoms that keep their spinel-like 3d arrangement of MnO_6 octahedra. For easier comparison of the two phases structural information was often compared via the pseudo-cubic notation of the $Li_2Mn_2O_4$ phase, where the simplifaction of symmetry of the a-axes was ignored so that a_c and a_p pointed in the same direction and the length difference was just a few percent.

The two investigations found in battery literature that come closes to the in-situ experiments of this thesis are the work of Lee, et. al. that performed in-situ lithiation with an ionic liquid electrolyte (ILE) on $LiMn_2O_4$ nanowires [38, 39]. They also observed

a tetragonal transformation to $Li_2Mn_2O_4$, but via orthorhombic intermediate phase, which is not mentioned in the latter of the two publications. In their results there is no indication of any twinning, but strong rotations of the nanowires' orientation are seen in the cases where a defect is present along the long axis of the nanowires.

Indications can be found starting at early research of lithium manganese oxide that the transformation from cubic $LiMn_2O_4$ to tetragonal $Li_2Mn_2O_4$ might involve more than just an intercalation of the lithium into the structure and a simple, same-time distortion of the unit cell: Tarascon, et. al. [252] already showed in 1991 that particle size of $LiMn_2O_4$ plays a crucial role for capacity retention. Thackeray, et. al. [36] who used some ex-situ TEM characterisation on their particles in 1998, came to the conclusion that "Preliminary data of $Li_{1.05}Mn_{1.95}O_4$ [...] indicate that the electron diffraction patterns of the electrodes when discharged to 2.89 V [i.e. lithiated] are complex." Little later, ex-situ TEM analysis of orthorhombic $LiMn_2O_4$, that normally degenerates to spinel over time, cycled to 2 V showed indications of the formation of nano-domains with very fine strain contours [226] No exact nature of those nano-domains was presented, but due to the non-ideal orientation of their diffaction patterns I encountered many times during this thesis, I would come to the conclusion that those could occur under twin formation. This is also consistent with the observations of Levi, et. al. [253] during XRD characterisation of $LiMn_2O_4$ with two different sample sizes (agglomerates up to 60 μm vs. solid particles of 1 – 10 μm), in which they "[...] suggest that the peculiarity of the electrochemical behavior of this compound is connected with the existence of a layered component in this material." This would be in agreement with our lamellar and therefore in a sense layered microstructure.

The size of battery electrode particles plays an important role in the results obtained during experiments – like just mentioned at the beginning of the last paragraph. This was most concisely shown for $LiMn_2O_4$ by Okubo, et. al. [153] who performed ex-situ XRD measurements at multiple voltage steps during a lithiation cycle. For four different particle size on the order of 9 – 210 nm (depending on the type of measurement used), they saw that the particle size can strongly influence the upper boundary of the phase-separating region between $LiMn_2O_4$ and $Li_2Mn_2O_4$ (smaller Δx_{Li} for larger particles). They even claim that at the samallest particles size the transformation becomes a solid solution; losing its phase-separating characteristic. Thin films of 30 – 117 nm thicknesses – consisting of a very compacted structure of circa 20 nm grains – have also shown that only the thinnest film worked well upon cycling emphasizing the stress building up within the samples [254]. But the effect of particle size has been studied for many other battery electrodes with the result that it has an influence, e.g. [255–259].

The thickness of the samples used in this thesis can be estimated by a formula for the

inelastic mean free path λ found in the EELS ATLAS [150]:

$$\lambda = (106\,\mathrm{nm})\,\frac{F(E_0/E_m)}{\ln(2\beta E_0/E_m)}$$

This formular includes the relativistic factor for the electron voltage E_0, β the collection angle and the effective material-dependent energy loss can be calculated as $E_m = 7.6Z^{0.36}$. This includes the effective atomic number (compare [149])

$$Z_{\mathrm{eff}} = \frac{\Sigma f_i Z_i^{1.3}}{\Sigma f_i Z_i^{0.3}}$$

which results in circa 135 nm. Given that the inelastic scattering length of manganese at 200 keV is 106 nm [260] this appears plausible. With this result it is safe to assume that most of the FIB lamellas used in this thesis are 100 nm, because they often showed $\lambda \geq 0.7$ as they needed to be stable on contact by the lithium tip.

Comparing this to the many studies performed on small particles (see examples of sizes above), the in-situ samples used are larger in their thinnest direction than most of those particles. Not to mention that, the two other directions are as large as the commercial battery particles bought from SIGMA ALDRICH. Of course, the aspect ratio might play a role, but I am convinced that the results of this thesis are more transferable to real world battery electrode particles than those of somewhere near 50 nm diameter!

One can argue that lithiation of micron-sized particles must start with a lithiation from the surface so that the first part of the lithiation is that of a thin film (for this compare [237]). The results of a quick check of **ex-situ lithiated micron-sized particles** (see sec. 5.8.6) showed that similar to the results of Thackeray, et. al. ([36] / early in this sec. 6.2) that the reality is a little more complex. Still, the huge amount of observed steps on the sample surface of each and every single particle that was imaged are consistent with on $(101)_{\mathrm{p}}$ planes. The same can be said about the planar defects observed. But one has to note the caveats of FIB-preparation from ex-situ samples so that a full study of many particles and different influences would have been needed for reliable results and full on characterisation of the microstructure within the TEM sample.

The tetragonal samples found in pre-characterisation after TEM lamellae were already prepared in the FIB (compare sec. 5.1), indicate that a similar microstructure in $Li_2Mn_2O_4$ is natural to lithium manganese oxide. This provides the first indication that the twinned microstructure formed during in-situ lithiation is not singular to our experimental conditions. Johannes Maier in his PhD thesis of atom probe characterisation of doped $LiMn_2O_4$ also pberved electron diffraction patterns consistent with twinning in one of his tips, while the results of the sample measured later on by APT showed a Li content of $Li_2Mn_2O_4$ [189].

Comparison to other manganite spinels shows that many manganese oxides show twinning upon cooling due to the Jahn-Teller effect when they are thermally prepared. The TEM study of Couderc, et. al. [235] on tetragonal Mn_3O_4 spinel ($a = 5.75$ Å, $c = 9.42$ Å) shows a c/a-ratio of 1.158, which is almost the same as the literature values of $LiMn_2O_4$. And the twinning plane of $\{112\}_t$ ($\{101\}_p$) is the same as the one observed in this thesis. The twin variants size 50 – 250 nm observed by them, partially overlap with our determined values. The exact values for the example published in [69] of up to 30 nm are not totally different.

Nano-twin domains found by TEM were also reported for mixed cation spinels[1] that showed lamellar contrast down to the same periodicity observed by us [234]. Additionally, Yoon, et. al. reported that twins can appear in layered material[2] after full lithiation with 50 – 95 nm. It has also been shown that if $LiMn_2O_4$ is annealed to more than 600 °C in a oxygen free atmosphere a oxygen deficiency can form [91, 227, 261]. Careful characterisation of many of those samples ($LiMnO_{4-\delta}$ with $x = 0.07$) showed that this can also leed to twinning in the as-prepared state [70], but with very strong variations of c/a-ratio. Despite that, the microstructure is very similar.

Many TEM studies don't give an exact result for the twinning plane, e.g. [234]. This is understandable, though, if one takes a look at the twinning law for the diffraction indizes (hkl)' of a twinning on a $[101]_p$ plane [262]:

$$(h',k',l') = \left(h\frac{\left(\frac{c}{a}\right)^2 + 2l - h}{\left(\frac{c}{a}\right)^2 + 1}, \bar{k}, \frac{2h\left(\frac{c}{a}\right)^2 + l - l\left(\frac{c}{a}\right)^2}{\left(\frac{c}{a}\right)^2 + 1} \right)$$

Taking into account the fact both variants need to be in zone axis to be well visible, one variant might be smaller than the other and the fact that the experiments were performed in a single-tilt holder, is an excuse for the fact that only a limited amount of full studies of the microstructure.

The interface between twins was observed to be close or the same as the twinning plane. Based on this observation one can try to estimate the boundary type as shown in fig. 6.1. It shows the sketch of the projection of the unit cells (blue / red) along $[101]_p$ and overlapping their lattices to form the coincidence lattice (large dots). Comparing the area of the coincidence site lattice (green) to the area of one unit cell gives a ratio of Σ4. The smaller a Σ the more ordered an interface should be according to textbooks of material science, e.g. [136]. A Σ4 boundary makes it plausible that the twinning plane $\{101\}_p$ / $\{112\}_t$ is also the boundary between both variants. This could also explain why, once formed, the defect densities at the interfaces can (sic!) be much lower than the defect densities between domains. Still distortions were often observed

[1] $(Co, Fe, Mn)_3O_4$
[2] $Li[Ni_{0.75}Co_{0.1}Mn_{0.15}]O_2$

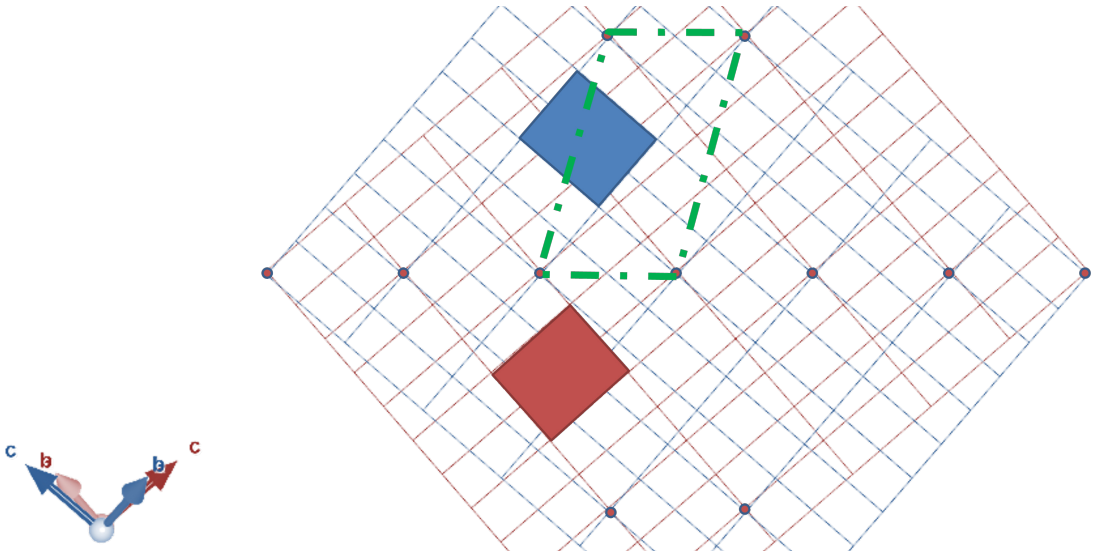

Figure 6.1.: Sketch of the unit cell orientations in $[101]_p$ orientation to estimate the boundary type. Comparison of the coincidence lattice indicated by dots and a collective unit cell (green) and the projected unit cells of both variants (red/blue) yields Σ4.

at the boundaries, which might explain the contrasts observed in STEM at the interfaces. At the same time under many imaging conditions and more arbitrary orientations one variant will be in a better orientation than the other so that a diffraction contrast will be visible.

Influences on the microstructure [3] were tried to be pinpointed with the collection of all the data available from this thesis. Twin formation is often stress induced during the formation of a microstructure that can be described under the framework originally developed for martensite (see sec. 2.4). To look for any connection of the free surface (as determined by the closest out-of-plane orientation in pre-characterisation) and the number of twin domains observed, the data was drawn into a stereographic projection of the cubic system (see fig. 6.2).

In our paper, we came to the following conclusion: "Assuming an equibiaxial stress state in the plane of the TEM foil, the largest reduction in strain energy is predicted when (i) the c-axis of the tetragonal phase is aligned along the [100] direction of the pristine cubic phase that was closest to the foil out-of-plane normal, and (ii) the observed twin domains reflect the twinning planes with the largest resolved shear stresses. Thus, we would predict three different twin domains for foils with a near-<111>c

[3] The beginning of this part was published as supplementary information of the paper [69]

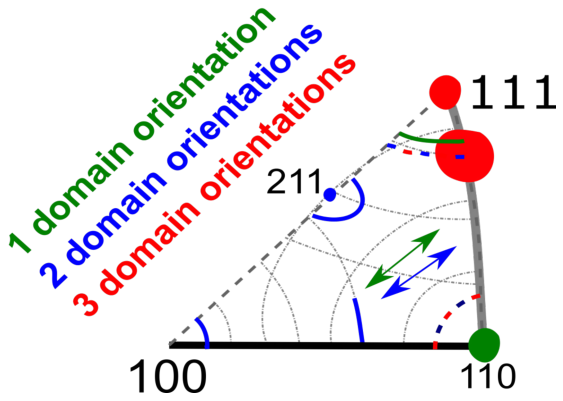

Figure 6.2.: Dependence of the number of domains on the TEM foil out-of-plane orientation. Due to uncertainties in the determination of the out-of-plane orientations, the range of possible normal directions for each foil are indicated by lines, arcs, or spots. The TEM foil normal is assumed here to be parallel to the TEM grid normal, although it may in fact be several degrees off. The color of the markings indicates the number of observed twin domains.

out-of-plane orientation, two different twin domains for foils with a near-<100>c out-of-plane orientations, and one twin domain for foils with near-<110>c out-of-plane orientations. Since we did not always measure the out of plane orientation of the tetragonal phase, we are unable to test the first assumption. However, the summary of the in-situ test observations, Figure S10, does indeed show that the number of twin domains does show a tendency to adhere to the behavior expected for microstructure formation governed by stress relief."

Fig. 6.3 describes one of the previous situations a little further. Fig. 6.3 (a) serves as a reminder of the twinning planes and relationships between cubic and tetragonal unit cells. Assuming a $[001]_c$ out of plane orientation in fig. 6.3 (b) two twinning planes would help to distribute stress that arises by either of the in-plane orientations $[100]_{[}p]$. Technically, there are four different domains in this sample all drawn as a solid arrow for the original elongation (i.e. possible c-axis) and the twin variant at one of the planes. As one can see the ones of the same color are indistinguishable, but if the deformation of the cube was drawn according to the c-axes there was a small difference. Note, that a c-axis out-of-plane would be reflected onto itself by both of the twinning planes as it is perpendicular to their normal.

This would have been very hard see with the bright fields of the in-situ experiments. So the number of domains was always counted as the clearly distinguishable plane directions. In hindsight, the sample in fig. 5.17, where due the free edges of the surface and the very defected domain boundary running diagonally through the sample, a curious flip of the lamellar structure direction happened at the center of the sample. This

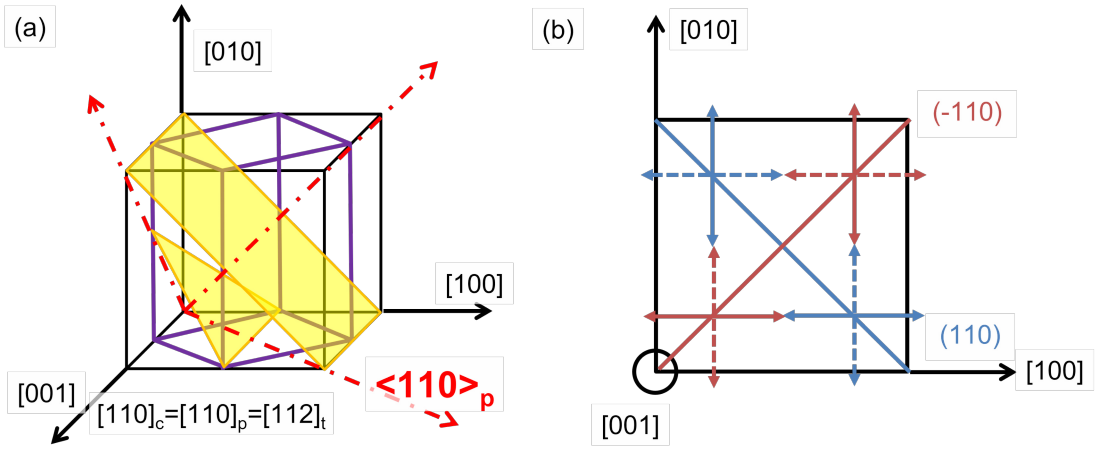

Figure 6.3.: Sketch of one of the twinning planes and the twin variants it can form. (a) shows the same plane drawn for both the cubic as $(110)_c$ and the tetragonal unit cell as $(112)_(t)$ and the three different plane normals $<110>_c$. (b) shows the possible twin variants with the solid arrow being the base and the dashed one being the twin for two planes (blue/red).

is somewhat comparable to the four possibilities drawn in fig. 6.3 (b). Determination of the exact small tilt between the orientations at the interface between $LiMn_2O_4$ and $Li_2Mn_2O_4$ would have allowed to establish an orientation relationship like in martensitic transformations. But the fact basically all TEM samples are (at least slightly) bent over distances of microns makes this impossible.

Additionally, there might be conflicting factors. While, in the case drawn in fig. 6.3 (b) the out-of-plane axis is reflected onto itself by the two planes, one might argue that this doesn't matter as most of the strain can be relaxed to the free surface of the sample. The distortion of the a-axes is much smaller during the tetragonal transformation. The situation would also be very interesting if one and only of the c-axes were to lie within the sample plane. Then one might argue, that only the two other axes form to not have the full 12% distortion directly in the sample plane.

All attempts to identify factors influence twin thickness and spacing produced data that is not strong enough to come to a conclusion (see sec. 5.5). As shown in the paper, the only strong effect observed was the cases were twins split into smaller variants where the sample got much thinner. A very similar effect is known for martensites and was observed by Timo Wuttke in his in-situ work on shape memory alloys [198].

Classifying the nature of the transformation is also very helpful to understand the expected effects taking place during the transformation. The classification of phase

transformations and their large and small differences and their conceptual descriptions is a large field in itself.[4] Historically phase transformations are classified based on the mechanism of the transformation rather than the properties of the product phase [142]. What's interesting is the fact that normally all those classifications consider a transformation that is driven by a temperature change at an unchanged stochiometry of the whole system (e.g. [140, 142, 143, 263]). It might be, that formally a reaction is not even considered, but as so many similarities to martensitic transformations are obvious, I will continue for the sake of comparison. Following this through and excluding all other possibilities, one comes to the conclusion that it must be a diffusional-displacive transformation (compare [141]), although this is also thermally induced. Christian, et. al. summarize it as a mixed category that "[...] is clearly non-martensitic, but it has a crystallography which apparently follows that of a comparable martensitic transformation and this must imply fully coherent or semicoherent interfaces."

In the end, the martensitic crystallographic theory appears to be applicable and it might be interesting to follow up with further research into exact similarities and differences. Especially, since martensite normally transforms by undercooling until a new region of martensite is almost instantly formed [130]. The transformation of $LiMn_2O_4$ to $Li_2Mn_2O_4$ classifies as a first-order phase transition [130] because the chemical potential of Li changes discontinuosly at $x = 1$. This can be seen in the voltage curve of $Li_xMn_2O_4$ in fig. 2.3 by the jump from $> 3.5\,V$ to $3\,V$.[5] Still, a huge driving force for the reaction is available as the formation of $Li_2Mn_2O_4$ provides approximately a voltage of $3\,V$ per lithium, but the speed of the transformation is limited by the availability of lithium. This is most likely the reason why the reaction was found to be diffusion-limited.

Intermediate phases were not identified with total uncertainty in this thesis although this was one of the research questions of this thesis. This was partly based on the previous results by Lee, et. al. that saw an orthorhombic intermediate structure. Another part was the complex nature of simultaneous effects during the transition a structural (distortion of the unit cell, change of previous lithium from tet. to oct. sites), a stochiometric (change in lithium) and a chemical (change in manganses valence values). With the knowledge of the microstructure formation one might even add this, because the mathematical models of the martensitic transformation often involve a transition layer between austenite and martensite [264].

One has to add that in the case of this kind of in-situ study one can only address the question of a spatially(!) intermediate phase that is at least metastable, because of the temporal resolution of the TEM and the fact that for very precise measurements ex-situ analysis has to be performed, which requires time to prepare.

[4] If interested compare e.g. [140, 142, 143, 263]

[5] A nice work of the direct relationship of Gibbs' free energy and the open-circuit voltage is [40].

The one case described in sec. 5.4 was the closest to capturing a untermediate state as according to EELS a transformation has taken place while no twinned microstructure was visible. Despite this, one might reason that martensites are a metastable phase [130] and that the observed $Li_2Mn_2O_4$ microstructure is therefore an intermediate phase itself. But the control experiment checking one sample after a long time showed no change in the microstructure. The interface had moved, but one possible explanation for this is lithium redistribution to the lowest possible lithium content in all regions of the sample. This would be based on the idea that if $Li_2Mn_2O_4$ can form at a level of $x_{Li} = 1.7$ (compare the phase boundaries in [153]), then it were energetically more favorable for a half lithiated sample with the transformed region at $x_{Li} = 1.8$ to transform an additional 6% of the sample with a level of $x_{Li} = 1.7$.

Another hint might be the fact that in the HRTEM images of the interface no immediate structural change was visible in localized FFTs. In addition, live at the TEM on occasions it appeared like there might be localized distortions in front of the twinned interface, that pointed in slightly different directions that did not yet form a full transformation[6], but any tries to capture this or find it in images by FFT did not work. TEM images are always the average of the whole sample projected along the electron beam direction, which also showed in the EELS data. There the interfaces were not localized to a few nanometers either, which is likely because the interface is just not parallel to the beam and e.g. at an angle of 45° could continously change over a distance equal to the thickness of the sample. Even if some scatterplots make it look like there might an intermediate phase (comp. fig. A.4).

Reversibility of the reaction could not be achieved despite biases of more than 10 V applied in the opposite direction on two occasions. This is a hint that the reaction is indeed irreversible, because many groups have shown reversion of in-situ lithiation of battery electrode materials at much lower voltage differences: First example is the work by Lee, et. al. on $LiMn_2O_4$ nanowires [38]. But there are other cases without liquid electrolyte on Si nanowires [166], aluminum nanowires [164] and SnO_2 nanowires [158], to name a few.

Displacive reactions can be reversible with probably the most-known material class of this characteristic being shape-memory alloys (SMA) that can cycle between both states of the martensitic transformation. As the same crystallography applies to the $LiMn_2O_4$-$Li_2Mn_2O_4$ transition one might expect reversibility, but there are also examples of irreversible martensitic transformations like for example in some steels [145, 265]. The topic of reversibility is studied extensively for SMA like the NiTi-based ones, for which a strong loss is observed when deformation and dislocation accumulation are ob-

[6] This could be similar to the effects described in [131], where locally different tetragonal distortions varying in strength and directions were described for other (doped) lithium manganese oxides. Compare also [262].

served [239, 240]. A common, undistorted plane is needed to achieve high reversibility [241], which is sometimes argued to be necessary but not sufficient [140]. It is my understanding that the undercooling necessary in martensitic transformations minimizes the amount of interfaces in the transformed region to the amount necessary for an optimal balance also taking into account stress built-up in the sample. The high ΔG of the lithium manganese oxide transformation might allow for higher defect densities than normally observed in thermally driven formation of a twinned microstructure.

It is therefore likely that the twinned microstructure plays an important role in the non-reversibility. Especially, looking at the extreme dislocation accumulation observed at domain interfaces. Twinning can distribute a fraction of the stresses of the transformation, but it does not change anything about the total volume change of $\Delta V \approx 5-6\%$ during the transformation. This is also the reason why fracture of the electrode particles is often discussed [236], which was not observed in this thesis. In the context of the work of Kirchheim, et. al. at the origin of this work – the Institute of Materials Physics in Göttingen – one might even ask whether Li acts as a defectant and might get trapped at all the interfaces within the sample and at the same time make them energetically less costly.

6.3. Influence of defects on the diffusion in $Li_xMn_2O_4$

Before starting the discussion of lithium in $Li_xMn_2O_4$, it is pretty safe to assume that the diffusion in the experimental setup occurs inside the sample as was concluded in [69]. Firstly, comparing the approximated diffusion coefficient it was multitudes lower than for other surface diffusions (like on carbon [129]) and fell in the range generally observed for $LiMn_2O_4$. Secondly, it is energetically unlikely that Li would diffuse on the surface over long distances of $LiMn_2O_4$ as intercalation releases approximately 3 eV, the voltage of the second voltage region of a $LiMn_2O_4$-battery (compare fig. 2.3 or [56]).

It is important to remind oneself again of the mechanism of diffusion in $Li_xMn_2O_4$, to discuss the influence of defects on the diffusion. The diffusion in $Li_xMn_2O_4$ is known to occur via a diamond sublattice of the structure, which connects the Li in tetrahedral positions via octahedral vacancies [113]. This is sketched in fig. 6.4 with the transparent gray octahedral voids connecting two green tetrahedral lithium positions (diagonally). The tetrahedral sites next to the filled ones are empty and the energy of filling them is so high, that this process leads to the coordinated movement of all Li onto the octahedral sites (as summarized in sec. 2.2.1 for $Li_xMn_2O_4$). The diffusion paths in $Li_xMn_2O_4$] are therefore three-dimensional. All other tetrahedral sites in the lattice are similar to the blueish tones and are nearest-neighbors to manganese.

That the diffusion behavior can be very complex has been shown in many theoretical papers where especially the influence of valence on the diffusion is discussed. The exact effects are not yet understood as papers disagree on the values of activation en-

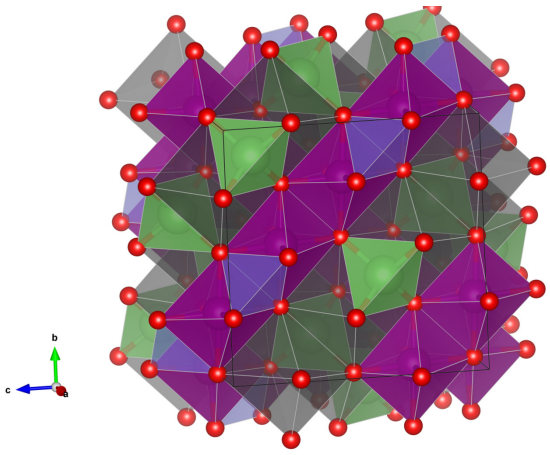

Figure 6.4.: Sketch of the diffusion path in $LiMn_2O_4$ indicated by the transparent gray octahedral voids that facilitate the lithium movement.

ergy required for diffusion and the trends with varying lithium content in the range of $Li_xMn_2O_4$ ($x \leq 1$), e.g. [113, 114]. In-situ delithiation in an atom probe has shown that high rates can lead to the formation of strongly uneven lithium distributions [188, 232]. Another influence that comes to mind that might influence the diffusivity of lithium is the presence of strains in the material thus shrinking or enlarging the involved voids. But as no further information as well as hints regarding this were observed in this work, this shall not further be discussed. However, those influences might be used to enhance the modell for the influence of defects that will be presented later on in this chapter.

Urban, et. al. make a very good argument that to understand the basic diffusion and capacity behavior of lithium transition metal (TM) oxides as battery electrodes it might just need percolation theory and the amount of cation disorder in the structure [116]. On the basis of the previously described network of diffusion via moving through alternating tetrahedral and octahedral voids (tet-oct-tet), they investigated the existing diffusional network in different crystal structures like rocksalt, layered and spinel like structures while also varying cation disorder and lithium excess/deficit (Li positions replaced by random TM or vice versa). On the basis of those networks they could then perform Monte-Carlo simulations investigating at which values of disorder and excess/deficit those networks would break down. This way it is possible to describe the behavior of different battery electrodes just by lithium content, cation disorder and crystal structure without even specifying the transition metal species.

As this suggests that the local diffusional network of an electrode material is the main factor influencing the lithium transport behavior, the following sections will transfer this to the results of this thesis. The focus will be how different kinds of defects might influence the local percolation network and thus give a suggestion of how the different

diffusion behaviors of sec. 5.6 might be explained.

The defects observed in this work are on {111} planes, which is well-known for spinels including twinning on those planes [138], which were also nicely characterized by Carter, et. al. by conventional TEM [266]. This also makes sense in the way that is known that in $Li_xMn_2O_4$ the structure and its characteristics are determined mostly by the Mn-O skeleton [267]. As generally described in chapter 2.2.1 the is also based on an oxygen fcc lattice, which also supports the formation of stacking faults and other similar primarily on {111} planes (compare e.g. [130]).

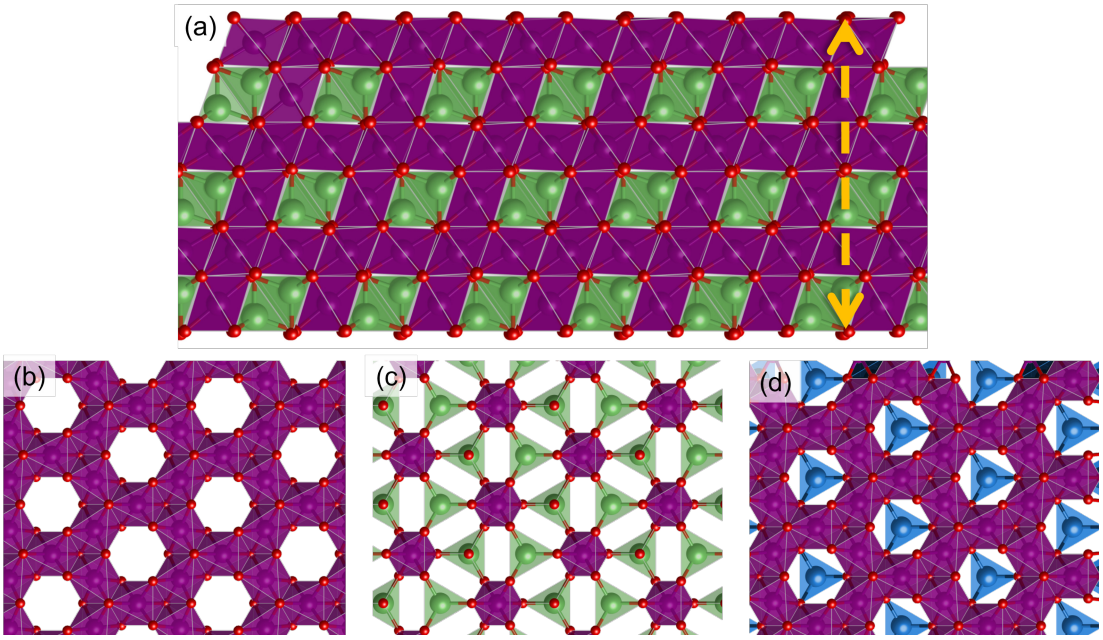

Figure 6.5.: Sketch of the $LiMn_2O_4$ with focus on the {111} planes. (a) shows the stacking sequence of the {111} planes viewed from the side made up of a pure Mn/O and a Li/Mn/O plane. (b,c) shows the top view of the two types of planes. When the layer containing Li is dyed blue (for distinction) their relative positions becomes clearer (c).

Fig. 6.5 shows a sketch of the $LiMn_2O_4$ structure with a focus on the {111} planes. Viewing those planes from the side (compare fig. 6.5 (a)) shows that the structure is made of oxygen layers, that are alternatingly either filled with just manganese in its octahedral voids or lithium (tetrahedral) + manganese (octahedral). This then leads to a structural repetetion after three layers oxygen-wise (oxygen again at same horizontal position) or six layers (indicated by yellow arrow) regarding the full structure. Looking at those two differing layers from the top in fig. 6.5 (b,c) shows the different chemical

nature of the layers even clearer than before. By stacking them in fig. 6.5 (d) with the lithium layer dyed in blue it is visible, that the Li is situated directly next to a octahedral void, as expected. Additionally, the single manganese octahedra in the mixed plane are directly below points where three octahedra meet[7].

6.3.1. Mn_3O_4(Hausmannite)

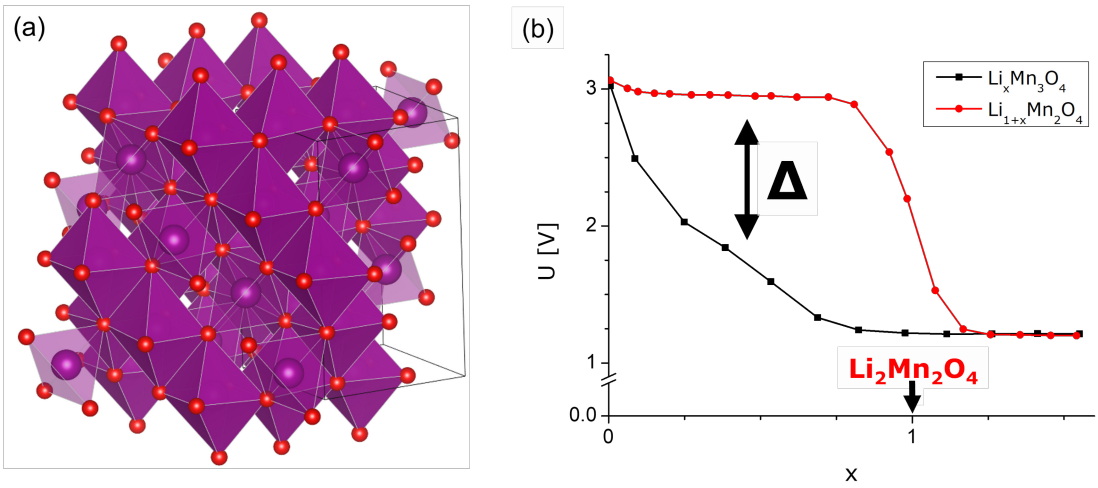

Figure 6.6.: (a) shows the structure of Mn_3O_4 (cut to a pseudo-cubic shape for comparison with $LiMn_2O_4$). The differences are mostly Mn in tetrahedral voids and a tetragonal distortion. (b) Comparison of open circuit voltages of $Li_{1+x}Mn2O_4$ and $Li_xMn_3O_4$ extracted from [55].

As sec. 5.6.2 showed an inclusion of Mn_3O_4 on or between {111} planes leads to the result that the sample region behind it is not lithiated at least as long as other unsecluded regions are still available. Mn_3O_4 is structurally very similar to $LiMn_2O_4$ as they both have the spinel arrangements of octahedral chains and the same amount of tetrahedral voids filled [55]. The difference only lies in the fact that the tetrahedral voids are filled by Mn vs. Li, which leads to a tetragonal distortion of Mn_3O_4 due to the thus different valence (see fig. 6.6). The crystal structure of Mn_3O_4 with its $a = 5.75$ Å, $c = 9.42$ Å [235], which is equivalent to a pseudo-cubic length of $a_p = 8.14$ Å that more similar to the lattice parameter of $LiMn_2O_4$ than $LiMn_2O_4$ vs. $Li_2Mn_2O_4$. It is thus very likely that Mn_3O_4 can form by segregation, presumably on already present planar faults, during the sample preparation process if the total stochiometry is slightly off. Especially, as the fact that tetragonal particles were multiply found during this thesis

[7] Looking very closely, it is the position where the tetrahedral void formed by then four MnO_6 octahedra is facing downwards

is a strong indication that the stochiometry during preparation might not have been perfect.

The properties of Mn_3O_4 present two different contributions to explain the lithiation inbiting behavior of the hausmannite defect, that likely add up. Firstly, taking a look at the comparison of the open circuit voltages of Mn_3O_4 and $LiMn_2O_4$ extracted from [55] shows that they differ by more than a volt for most of the region of added Li[8]. It is thus energetically much more likely that Li is added into an additional part of the $LiMn_2O_4$ structure than into the Mn_3O_4 defect, because the open-circuit voltage is proportional to the chemical potential of Li added to the structure. But Mn_3O_4 is not totally unlithiatable as the voltage is still positive.

Secondly, Thackeray, et. al. also remark in the same publication that very similar to the lithiation of $LiMn_2O_4$ additional Li in the Mn_3O_4 structure should very quickly replace all tetrahedral manganese atoms into octahedral positions [55]. If one connects this with the previously explained diffusion network of the spinel structure, this means that every displaced $Mn_{tet.}$ that is displaced into $Mn_{oct.}$ now blocks a possible diffusion chanel at this position. This doesn't have an effect for a few such defects as the diffusional network of spinel is three-dimensional. Though, according to the reasoning in the also previously-mentioned percolation paper (compare [116]), it should quickly lead to a break-down of the lithium transportation network.

The fact that slight amounts of lithium were measured[9] in the region of the defect fit both explanations of the previous two paragraphs. Firstly, for little Li uptake ($x < 0.2$) the open-circuit voltages of $LiMn_2O_4$ and Mn_3O_4 are not yet as different as for more lithium (see $x = 0.75$) and the energetical penalty thus that large. Secondly, a small amount of lithium might be able to diffuse into the structure of Mn_3O_4 displacing Mn and only then making Mn_3O_4 a diffusion structure with much higher activation energies. Although, already previously higher activation energies for diffusion through the lattice should be expected with the additional Mn in the diffusion channels – though on tetrahedral sites.

6.3.2. Stacking faults or defects of very limited thickness

The results of sec. 5.6.1 showed that stacking faults or what appeared to be stacking faults on {111} planes, can show three different effects: **Blocking** of lithium transport across the defect, **enhanced** transport in the defect plane and a **neutral** behavior, that looked non-differentiable to no defect being present in their region.

[8] Please be aware that both curves show the range of adding slightly more than 1 additional Li to the existing structures of Mn_3O_4/$LiMn_2O_4$, which is different to most of the rest of this thesis.

[9] Those results should not be overinterpreted as lithium quantification of a small region is probably the most error-prone quantification shown in this work. Additionally, measurements with energies in the plasmon region show the highest delocalization (compare e.g. [149]). But the vertical integration leads to good quantitative data of Mn and O, so that a proper discussion shall be made.

This is important as during the preparation of electrode materials in battery production, the particles are mechanically deformed (calendering), which will introduce additional defects. For comparison see the increased defect density of the $LiMn_2O_4$ after trying a differing sample preparation method involving mechanical load in sec. A.4. Even though, the defect density can probably be kept lower by careful production parameter choice the introduction of additional defects seems unavoidable. The deformation modes of spinels will then also involve SFs [138]. Additionally, like the bought particles show there are always slight local stochiometric deviations that can also lead to defects.

Literature of defects in $LiMn_2O_4$ or batteries in general is scarce to non-existent as very often bulk sample methods are used, which makes this thesis and its methods valuable as reasoned in the introduction. On the other hand, there is no direct comparison for above findings, but as the previous section showed just the comparison of diffusion behavior with simple reasoning about the diffusional network can go a long way. Therefore, fig. 6.7 shows five different conceivable defects of $LiMn_2O_4$ that are comparable to those shown in fig. 6.5, but now introducing defects by stacking faults, i.e. a limited amount of Shockley partials of the oxygen lattice, except for (d). This is reasonable, because many publications support the idea that the properties of the crystal lattice are determined in descending order by oxygen, manganese and lithium (e.g. [267]). There are two interesting atom-probe publications, though, that indicate that defects in (doped) $LiMn_2O_4$ can lead to lithium-poor regions in a sample [188] and that segregation might occur at grain boundaries [231]. Due to the nature of the instrument used an exact crystallography of the observed defects is not available.

Neutral behavior can therefore be expected for extrinsic / intrinsic stacking faults of the oxygen lattice with examples shown in fig. 6.7 (a/b). This kind of local distortion should not be a huge barrier for diffusion whether it is two or one plane that are tilted. It might be even more reasonable to assume that the one layer intrinsic stacking fault (other than shown in b) should rather be on a Li-Mn-O plane with more higher-coordinated MnO_6 octahedra. Same as the two previous defects a localized twinning of the structure on a {111} plane, which is common for spinels [138] also doesn't block any connections of the tet-oct-tet diffusion network. An influence of distortion at the interface of any defect will be discussed in the next paragraph, but just looking at the diffusion network there are three possibilities to explain a neutral behavior: intrinsic/extrinsic stacking faults and twins of a few layers, whichever influences the activation energy least.

Enhanced diffusion in the plane of the defect could stem from two different effects. Firstly, a stacking fault created by the removal of a plane that leads to a more open tunnel like structure of the Mn-O octahedra (compare fig. 6.7 (d)). More open struc-

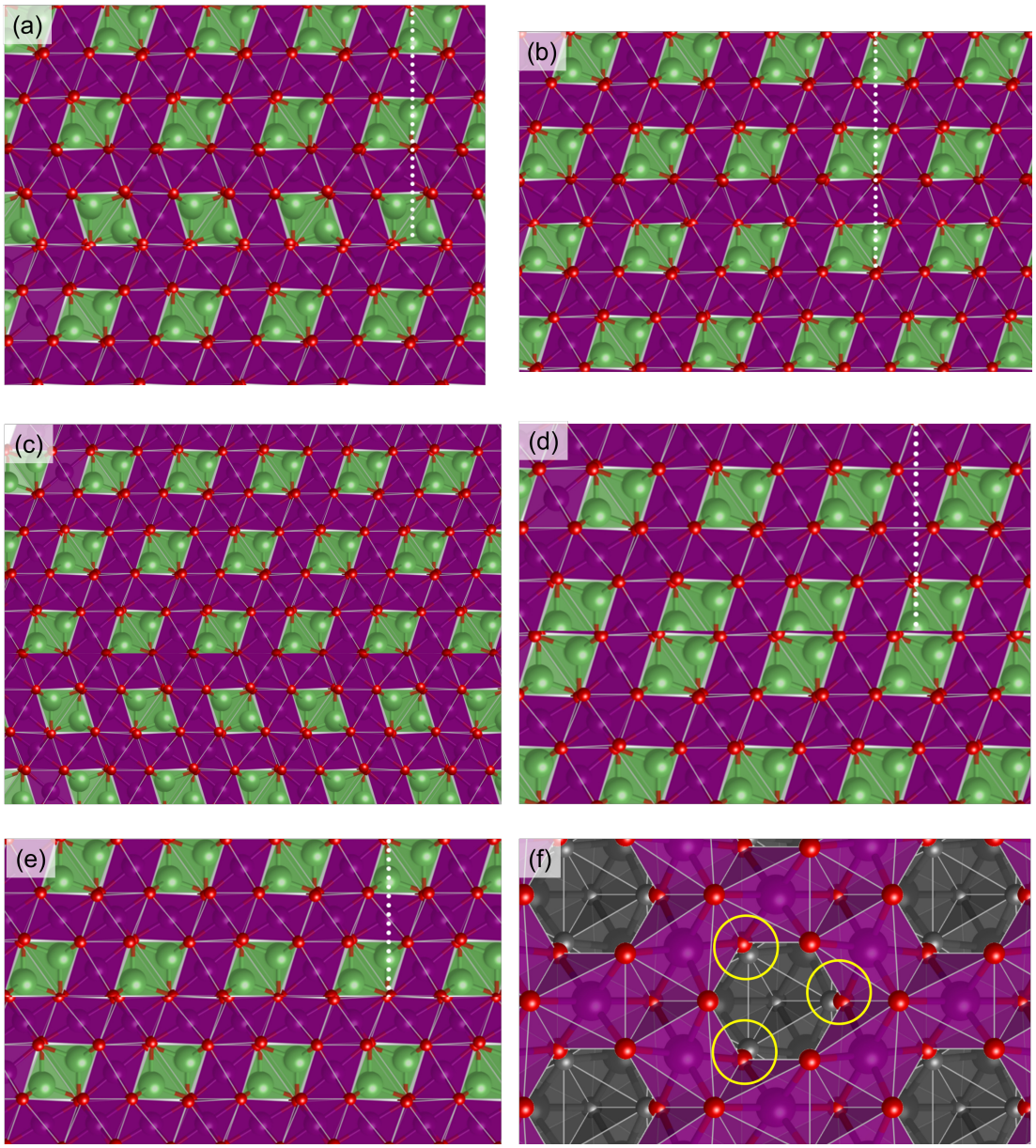

Figure 6.7.: Sketches of conceivable defects in $LiMn_2O_4$. A extrinsic (a) and intrinsic (b) stacking fault of the oxygen lattice. A twin on a {111} plane (c). A localized Mn deficit created by the removal of a plane only containing Mn octahedra (d), but continued as concerning the oxygen lattice. (e) shows a plane displaced by half of a full translation - a anti-phase boundary, which looking at it from the top leads to Mn octahedra (black) residing below voids in the {111} plane (f).

tures of manganese oxides are natural [81] and the locally different stochiometry will likely still resemble motifs found in other manganese oxides. It is highly likely that due to coulombic interaction not all the Li drawn would really be present in those tunnels leading to a higher amount of voids, which could then enhance transport in-plane.

Any off-stoichiometry like this should also lead to a space-charge formation in the vincinity of the defect as the mobile lithium will likely redistribute. Those kinds of effects were recently published in ionic solids [268, 269]. This could provide a starting point for enhanced diffusion due to different fields within vs. perpendicular to the defects.

In-situ lithiation of SnO_2 has shown that a twin-boundary can assist the transport in its plane [118]. A more concise study by STEM of $LiCoO_2$ [117] has shown that twin-boundaries in this material show a lowered calculated voltage of 0.2 V in the region of the interface. Addtionally, "Li migration along the twin boundary has an activation energy, E_a, of 0.20 eV, while Li migration across the twin boundary has a higher E_a of 0.40 eV. This corresponds to a diffusion constant difference of three orders of magnitude at normal operating temperature." This is in line with the very different speed in-plane that was observed.

Multiple different other effects might also play a role like localized strains increasing voids or the effect of the Mn valence of the sorrounding that is suggested in many theoretical papers e.g. [270]. In the end, it seems very likely that a combination of additional voids and space-charge layers by locally differing stochiometry can explain an enhancement.

Blocking of the diffusion perpendicular to the defect plane can of course also be explained in some ways by the just described effect of a possible twin boundary that creates a very strong space-charge layer. Nevertheless, two other, simpler approaches based again on the diffusion network are also possible. On the one hand, there might be a off-stochiometry that has a local structure of Mn_3O_4, but only extends a few layers and is thus hard to differentiate from a stacking fault. On the other hand, it is known that spinels can form anti-phase boundaries (comp. sec. 2.3). An APB is shown in both fig. 6.7 (e,f) which is a full dislocation of the oxygen lattice (3 of 6 Shockley partials required for a full translation of $LiMn_2O_4$). Looking at this from the top in fig. 6.7 (f) one can see that in case of an APB the layer below (black) now leads to MnO_6 octahedra blocking diffusion in out-of-plane direction. Due to the simple way of sketching this situation one can also see that this also isn't a perfect fit (encircled).[10] In general, any defect that places octahedral Mn atoms into the diffusion network would be a strong hinderence as it requires a different diffusion mechanism. The reasoning behind this can also be found in [32], which shows that at exact $Li_2Mn_2O_4$ (Li==2) almost no

[10] The same oxygen atoms top-of-bottom and bottom-of-top layer are not in the exact same localtions so that some distortion would need to occur.

transport should occur.

6.4. Summarizing comparison to the research questions and outlook

Are there other factors responsible for the capacity decay besides the pure tetragonal transformation? Finding the complex and unexpected twinned microstructure that presumably prevented delithiation in in-situ experiments provides an additional mechanism for capacity loss in $LiMn_2O_4$ based cathode materials. When one looks at other cubic-to-tetragonal phase transitions one can fully understand that the stress building up in the sample due to the change in unit cell can best be accomodated by a most likely stress-driven twinned microstructure. The fact that this has not been highlighted in any other publications shows the importance of working with sample dimensions as realistic as possible: In this case two of the three dimensions are realistic, while the third is at least at the same length scale of many small particles studied ex-situ in the TEM. Hints that this microstructure might form regularly show up in some early works on $LiMn_2O_4$, but weren't followed up by further publications. Additionally, the comparison to other microstructures in tetragonal particles and similar materials show that a twinned microstructure is not a special result of our sample stochiometry, geometry and the experimental approach. Nevertheless, the preliminary results of ex-situ particles show that the stress states are likely more complex when lithiation starts from all sides. Looking at the phase transition of $LiMn_2O_4$ to $Li_2Mn_2O_4$ with effects observed in martensites in mind, might in the future lead to tuning of the properties so that reversibility comes closer to that of shape memory alloys.

Are there intermediate steps in the transformation? With the similarity to martensitic crystallography of the $LiMn_2O_4$ to $Li_2Mn_2O_4$ transformation, the formation of an intermediate phase or transition layer would be plausible. But in comparison to the very good reproducibility of the microstructure formation, the hints of this in observations of this thesis are just not strong enough to make a statement. The hope of gathering more data or fine-tuning the observation conditions by moving the phase-interface back and forth as originally intended, were prevented by the fact that delithiation wasn't possible. Without this and the anyways limited temporal resolution of the TEM looking for a temporally intermediate phase was not possible.

Which influence do defects have on the lithiation behavior? With the result that the reaction observed during in-situ experiments is diffusion-controlled further investigations into the dynamics were performed. The results of lithiation in the presence of defects have shown that they can block or enhance lithium transport as well as leave

diffusion relatively unaffected. On the basis of publications that showed that many of transition metal oxides diffusional parameters can be understood by percolation models, models were provided how those behaviors might be understood on the basis of different kinds of stacking faults imaginable for $LiMn_2O_4$. Space-charge at those might also play an important role in terms of both enhancing and blocking lithium transport. Full analysis of all defects in the sample materials was not within the scope of this work.

Outlook Both the observation of the twinned microstructure and the influence of the defects has implications for real world application. It shows that the more common electrochemical methods should in the future maybe supplemented by structural characterisation. So far fractured particles are discussed in terms of sudden mechanical failure. In the future, one might look into whether some observed results are better explained by considering a stabilizing microstructure or fatique that is based on the concepts of dislocation accumulation during cycling as in shape-memory alloys. Further research into the results of the ex-situ lithiated particles is also necessary to shine a light at the effects when the results of this thesis are applied to full particles. This could also be supplemented by lithiation experiments of thin films, that more similar to the geometry of the TEM samples and might serve as an intermediate step in comparison of the results.

Considering the mechanical deformation of battery particles during calendering of the electrodes is likely introducing defects, looking further into this aspect and whether it might explain some capacity not realized even during the first cycles could be worthwile. Additionally, to understand those effects more clearly better characterisation of the initial defects is required. This will be continued by colleagues at the institute to give a better picture in another publication. Adding to this, this might be the chance to also involve researches from theoretical physics or chemistry to provide insights into the stability of different defects and their properties.

In case additional EEL spectroscopy is to be performed on $Li_xMn_2O_4$ or other battery materials, I would advise looking into more powerful means of analysis of the large amounts of data collected by spectrum images. This might involve making own calibrations based on additional mathematical modesl used in other spectroscopy methods like principal component analysis or partial least squares.

7. Conclusion

This thesis addresses the need to further understand failure mechanisms in the environmentally friendly battery cathode material $LiMn_2O_4$. It had been shown over twenty years ago, that regions of tetragonal $Li_2Mn_2O_4$ can be found after one cycle to $LiMn_2O_4$ – presumably due to local overpotentials. Also noting that the diffraction patterns in the $Li_2Mn_2O_4$ region are complex. [36] Additionally it was concluded that partial Mn^{3+} dissolution into the electrolyte cannot solely explain the capacity losses of $LiMn_2O_4$. [27] Obtaining further information on the $Li_2Mn_2O_4$ phase transformation connected to those losses requires additional localized microscopy and cannot be realized by ensemble methods like electrochemistry and XRD combined with ex-situ particle analysis. Thus, in-situ lithiation experiments in the TEM were performed on FIB-specimen preserving the micrometer size of commercial $LiMn_2O_4$ particles at least in two dimensions. The sample was contacted locally by a solid Li using a STM-TEM-holder, making the approach both more stable in the vacuum of the TEM and protecting the sample from electrolyte creeping onto it, which would prevent chemical analysis of the sample. This approach allowed in-situ observation of the lithiation dynamics of the sample as well as analysis of the whole sample, the interface between $LiMn_2O_4$ and $Li_2Mn_2O_4$ and the microstructure of the transformed region by diffraction, high-resolution imaging and EEL spectrocopy.

This thesis was guided by three research questions: 1. Are there other factors responsible for the capacity decay besides the pure tetragonal transformation? 2. Which influence do defects have on the lithiation behavior? 3. Are there intermediate steps in the transformation?

This main findings of this thesis are:

- Sharp interfaces are visible in the TEM when $LiMn_2O_4$ is lithiated, because mismatch between cubic and tetragonal unit cells leads to localized bending contours allowing to pin-point the interface position.
- Tracking the interface allowed to determine that the reaction front between $LiMn_2O_4$ and $Li_2Mn_2O_4$ is diffusion-controlled.
- Multiple EELS methods were compared and a few selected that showed the best spatial resolution and reliability. Using these methods it was possible to investigate the interface to confirm that structural and chemical interface are aligned within experimental resolution.

- An intermediate phase at the interface was not found, but could have been hidden due to limitations of the methods used.
- Upon lithiation the expected tetragonal structure formed. However, the tetragonal regions formed a presumably stress-driven twinned microstructure not previously reported. This makes the $LiMn_2O_4$-$Li_2Mn_2O_4$ reaction a diffusional-displace transformation.
- Comparison of this microstructure to similar materials and preliminary ex-situ lithiations showed that the microstructure is not unique to in-situ TEM setup, but most likely more complex in ex-situ particles. This needs to be further addressed in the future.
- Attempts to delithiate the twinned samples were unsuccessful. This suggests that this microstructure provides an additional explanation of capacity decay when tetragonal regions form in $LiMn_2O_4$ batteries due to overpotentials.
- The knowledge about the interface and the diffusion-controlled reaction allowed to study the influence of defects on the diffusion during the lithiation of $LiMn_2O_4$. Some defects substantially altered the diffusion, others showed no effect. Unfortunately, the exact nature of the stacking faults couldn't be investigated within the scope of this project, but further analysis of the defects will be performed to strengthen a publication of those results.
- Still, a model was developed to explain the different effects of stacking faults on the lithiation reaction.

This thesis reinforces the importance of in-situ work and microstructural characterisation in battery material research. Only this way was it possible to find a previously-unreported microstructure formation that provides an additional explanation for capacity decay in $LiMn_2O_4$. Additionally, this finding could guide further research into how the investigated region could be made fully accessible for battery applications by e.g. structuring the electrode or tuning unit cell parameters. Knowledge of shape-memory alloys might provide a guide, as we need to make the most of our limited ressources. An intermediate phase could not be found, but comparison with literature on diffusional-displacive reactions might provide ideas on how to research this question further probably with other methods or approaches. The influence of defects on the lithiation behavior might prove as the most impactful result as it is transferable to most electrode materials, because those are most of the time deformed during battery assembly.

A. Appendix

A.1. Crystallographic visualisations

All crystal structures in this thesis have been produced with VESTA (see [245]), which has been crucial to understanding the similarities and differences of all the different phases of ltihium-manganese-oxides. Sample structures for those can be downloaded from the internet, e.g. the CRYSTALLOGRAPHY OPEN DATABASE (`http://www.crystallography.net/cod/`). All alterations after this like cuts on certain planes, et cetera, are original work.

A.2. X-Ray diffraction data of the pristine sample material

The X-ray-diffraction data in fig. A.1 was collected in a BRUKER D8 DISCOVERY over the duration of a night under monochromated conditions. The experimental data is consistent with the cubic $LiMn_2O_4$ phase (a=8.24 Å) as the peak structured as well as the measured lattice constant of $a_{exp} = 8.247(4)$ Å agree. This has been calculated using the large peaks at 111, 311, 400 and 440, but also the smaller ones at 222m 331, 511 and 531 (see e.g. [271]).

The two additional spots are caused by aluminum stub of the sample used for the FIB/SEM process and were thus excluded from the lattice calculations before. While our observations show otherwise, no other phase can be distinguished in XRD measurements.[1]

A.3. Additional figures concerning the EELS quantification method

Fig. A.2 shows the two diffent corrections used two remove the continuum background before the integration of the $Mn\text{-}L_3$ and $Mn\text{-}L_2$ to calculate the ratio. From experience, both methods work equally well. The biggest difference can be seen in their influence on the $Mn\text{-}L_3$ edge. In the end they might both work well, but the results of the resulting ratios are not comparable. Maybe the different treatment of the whitelines in

[1] Further attempts in the context of a bachelor thesis at the Institute of Materials Physics, Göttingen to make these visible by using additional methods like *Rietveld refinement* were unsuccessful.

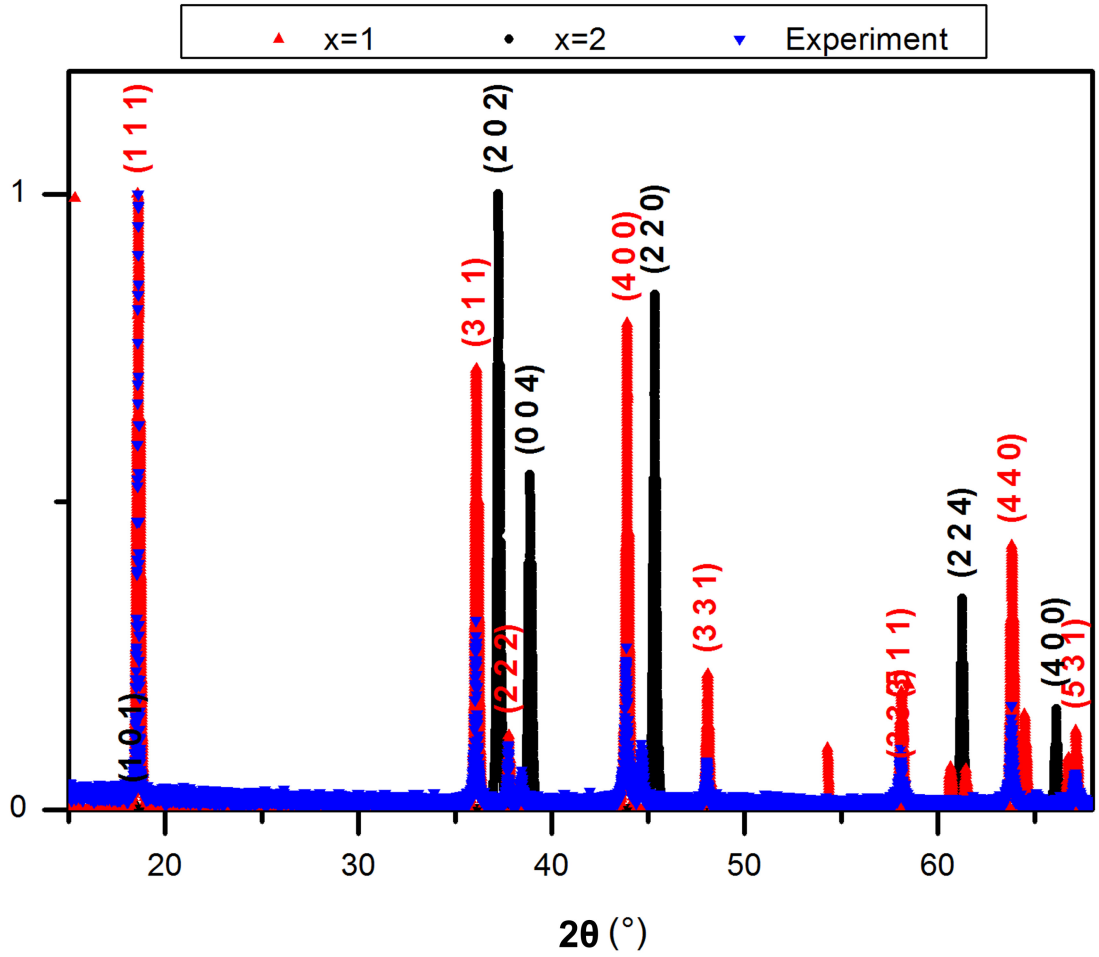

Figure A.1.: $\theta - 2\theta$-X-ray diffraction data on one of the exactly same powder samples on a SEM stub also used as the basis for FIB preparation. Behind the experimental data (blue) the theoretical peak structure for the cubic spinel ($LiMn_2O_4$) and the tetragonal phase ($Li_2Mn_2O_4$) are displayed. The two differing peaks at 37° and 45° can be attributed to the aluminum of the SEM holder. To do: Achse falsch. 2θ

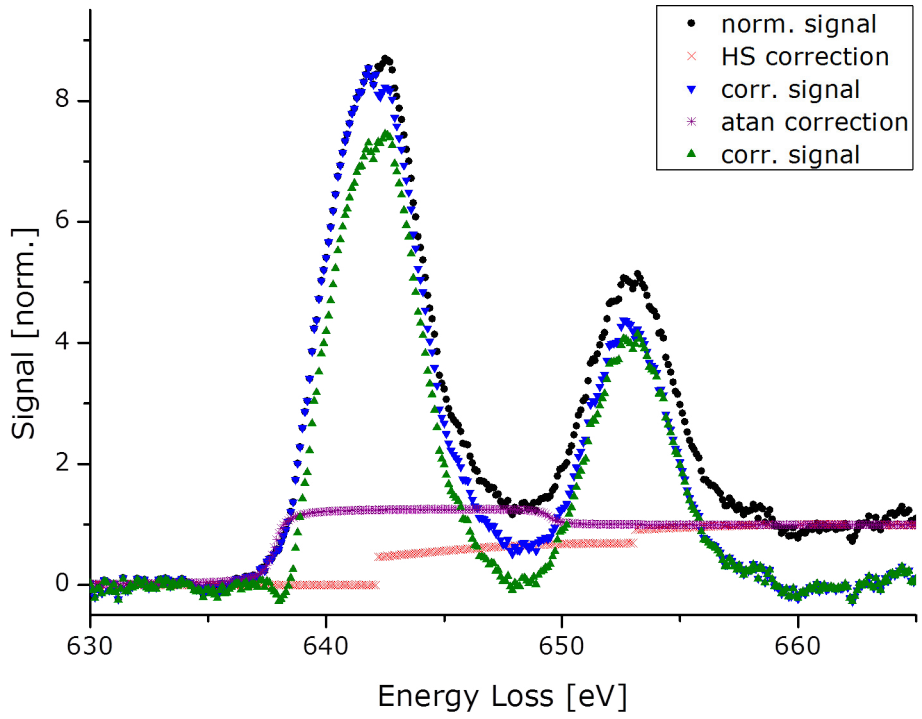

Figure A.2.: The two different continuum contribution corrections - exported Hartree-Slater-function vs. fitted linear combination of two atans - in direct comparison.

combination with all the other procedural differences is the reason why the calibration curves in fig. 4.7 are so different. While, the physics is all the same for the data none of the procedures are particularly physics-based and therefore don't have to yield the same results.

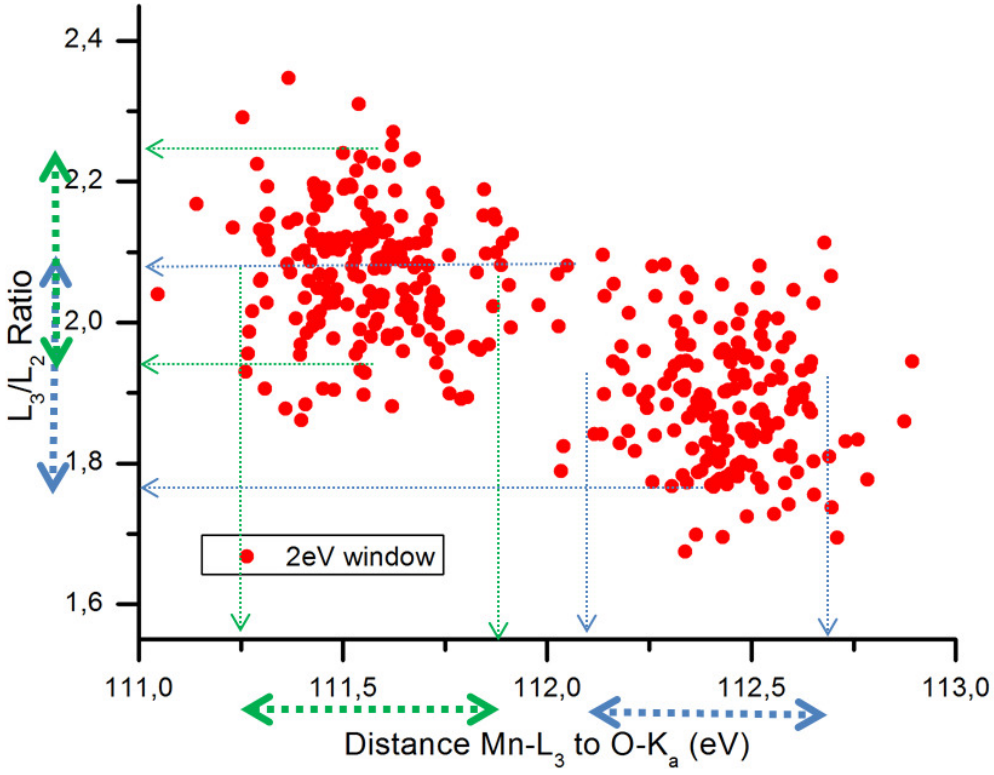

Figure A.3.: All data points of the SI used in this chapter, plotted based on the L_3/L_2 ratio and against the distance of the O–Kand Mn–L_3edge, which results after quantification of the two presented methods. For the ratio of the two edges, a 2 eV wide window was used as an example for all possibilities. To guide the eye the approximate projection of the two regions have been indicated on both axes.

In order to compare the two main methods of the chapter 4 the two base parameters of the methods are plotted against each other in Fig. A.3. The L_3/L_2-ratio was evaluated with a 2 eV wide window, since this window showed the lowest fluctuations and apparently has a lower susceptibility to noise in direct comparison to the wider windows. However, the window width is narrower than the literature method with the

smallest window width (see [217]). The distance between and O−K and Mn−L_3 edge corresponds to the method of Zhang, et. al. [92] Based on all data of the chapter, two clouds are clearly visible. This separation is due to a clear separation of the data on the x-axis so that midpoints at about 111.5 eV and 112.5 eV are obtained comparable to the values of the histograms. However, this separation would not be possible based on the ratio of the Mn−L edges. To guide the eye with this the approximate projections of the clouds on the two axes have been visualized.

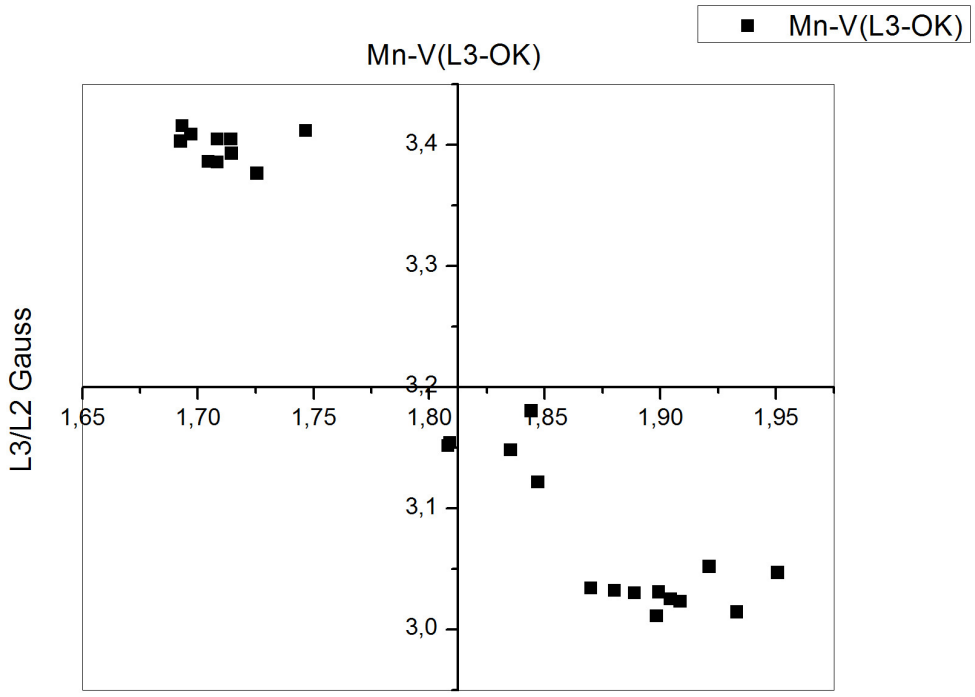

Figure A.4.: Scatter plot of the Mn−L edge ratio determined by dividing the fitted maxima and the approach of Zhang, et. al. Visually there is a very good correlation between both methods.

A preliminary judgement can be made on the suitability of a Mn−L edge ratio method based on fitting instead of integration by a scatter plot of these data points and the Zhang-method. There appears to be a high correlation between both methods. So it seems that using the ratio method on the basis of fitted data would be promising, but of course requires making a own calibration.

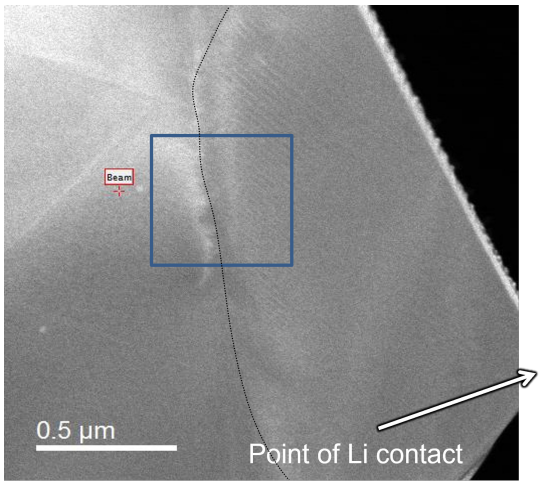

Figure A.5.: Sample situation of the data used for chap. 4 and for EELS data in the paper (fig. 5.8).

The sample, its point of lithium contact, the approximate interface position and the SI used for chap. 4 and fig. 5.8 are shown in fig. A.5.

A.4. Alternative sample preparation attempts

Preliminary alternative sample preparations were perfomed with the intention of preparing multiple particles at once embedded in a conductive matrix to either perform direct in-situ lithiation multiple times or prepare a selected particles from it by FIB liftout of already thinned sample region. The method selected is based on [272] and works (slightly changed) by pressing the powder on a holey carbon grid between thin gold foils. The sample can then be thinned by ion milling in a conventional PIPS.

As can be seen in fig. A.6 by the three representaive BF-TEM images selected, after thinning particles in the PIPS, the thinned regions are approximately $1\,\mu$m large. However, relatively strong contrasts can be seen in almost all of these particles, indicating increased defect density or a very inhomogeneous thickness. This inhomogeneous thickness is also evident on a larger scale, as the samples prepared in the PIPS tend to have a wedge shape (compare (a)).

However, in order to follow the evolution of the material during in-situ lithiation, the areas should be as contrast-free as possible. So this preparation method was discarded after a few trials. However, it produces very high quality thin areas close to the surfaces

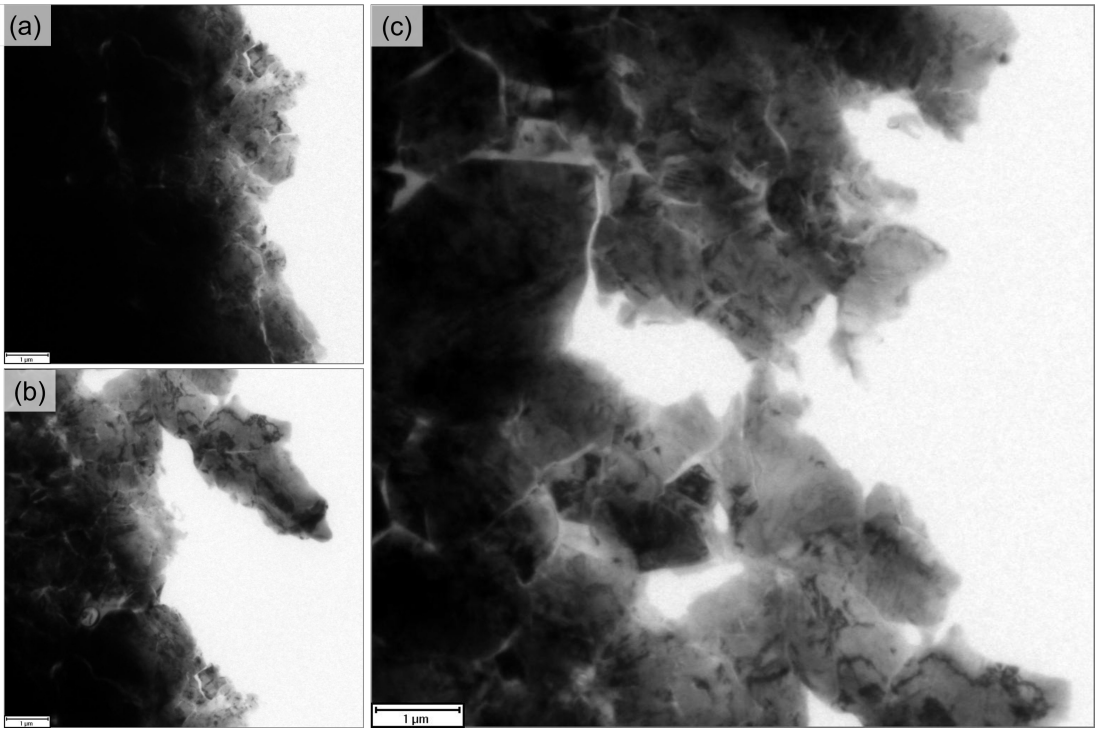

Figure A.6.: Examples of alternatively prepared particles. To do: TEMP

for HRTEM and involves less effort, so it could be well used for other objectives.

A.5. Additional ex-situ electromchemical lithiation data

This XRD scan was performed on powder particles prepared to check if tendencies to form twins during the formation of $Li_2Mn_2O_4$ via lithiation are also present ex-situ in micron-sized particles. For more information on the preparation see sec. 5.8.6. The goal of this preliminary experiments was to prepare as much $Li_2Mn_2O_4$ on the basis of the original pristine powder used also for TEM specimen preparation as possible. As visible in Fig. A.7 though some additional peaks are present the transformation does appear to be much less than complete. Further experiments are needed in the future. Indications that a lot of the particles might still have transformed at least at the surface can be found in sec. 5.8.6.

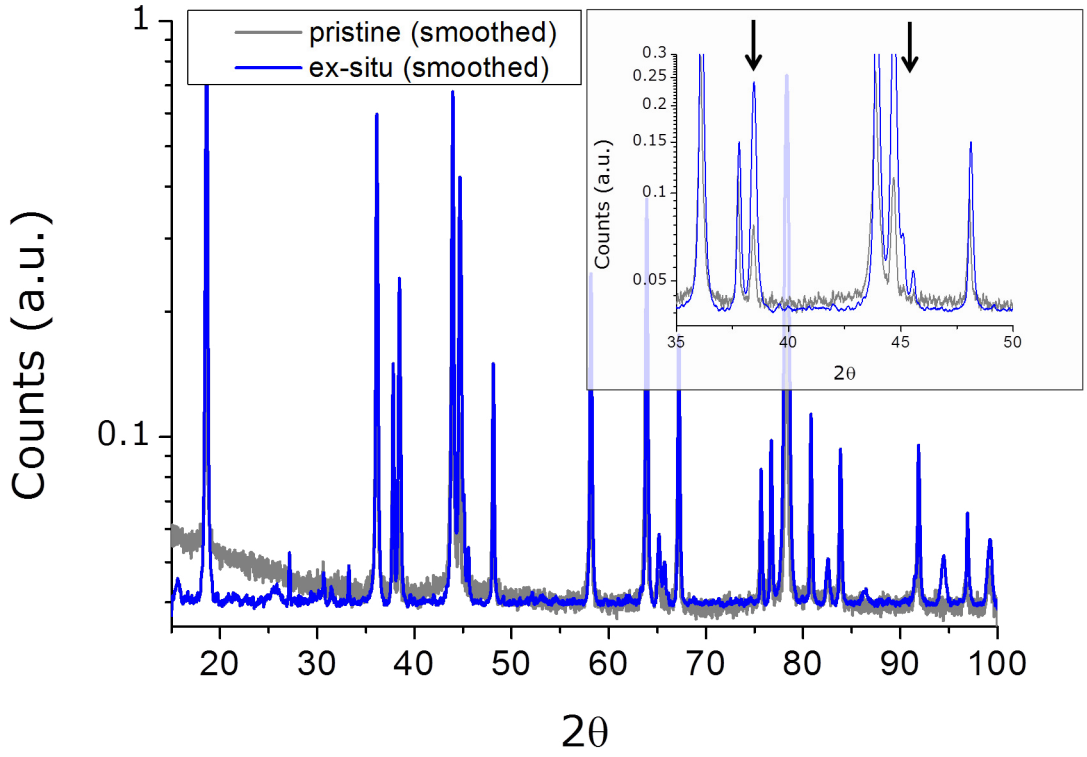

Figure A.7.: θ-2θ-scan data collected on the ex-situ lithiated $LiMn_2O_4$-powder (blue). A similar scan performed on the pristine $LiMn_2O_4$-powder is shown as a baseline for comparison in the background. Overall, the change is less than would be expected, but additional spots and intensity shifts can be detected. Two examples for each are marked by arrows in the upper right inset at positions where peaks of the tetragonal $Li_2Mn_2O_4$ could be expected.

A.6. Details of the laser-assisted APT-Analysis

This APT data was measured and reconstructed by Björn Pfeiffer, but is necessary as supplementary figure of the paper. I performed the TEM characterisation and prepared the data comparison on the cylindrically averaged data.

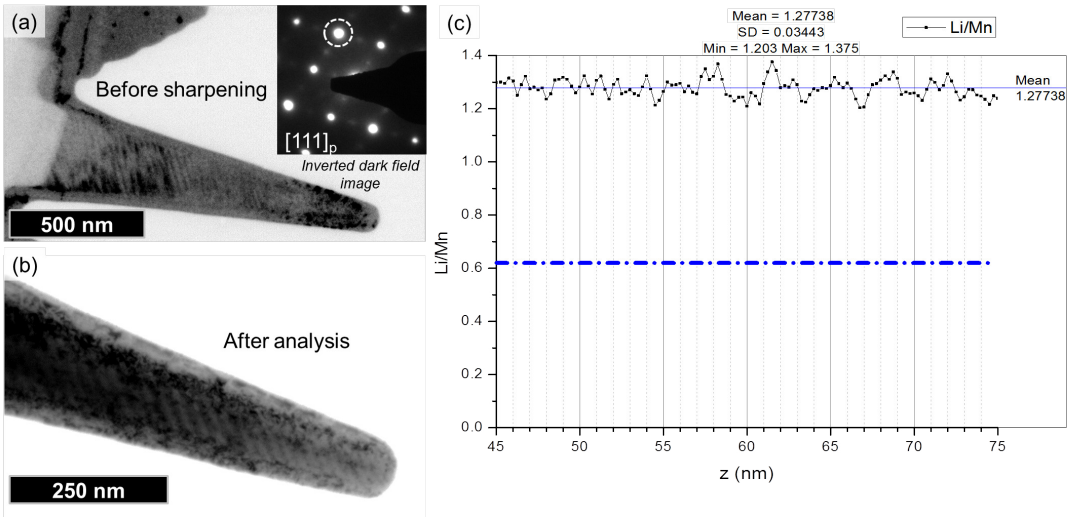

Figure A.8.: Details of the atom probe data. (a,b) show the tip sample used in the Tomographic Atom Probe before and after analysis. It is visible that the twins reach far to the front of the tip and that the analysed volume reaches well into the non-damaged, twinned part of the sample. (c) The Li/Mn-ratio of the volume indicated in Fig. 5.10 is plotted for the central part of the cylinder along the cylindric axis to exclude the surface regions influenced by sample preparation. The data of measured profile are shown and a typical value for measurements in the pristine sample material is indicated. [232]To do: evtl. gedrehte Page?

Fig. A.8 shows additional information to Fig. 5.10. Even though the contrast diminishes towards the tip and the noise of the preparation-induced surface layer is influencing image quality Fig. A.8 (a,b) show that the volume analysed by TAP clearly reaches into the twinned region of the sample. Since the detector of the TAP also only pics up the central part of the sample variations in the Li/Mn-ratio should be visible in the reconstruction, if the two twin variants have a different stochiometry. To check this an analysis cylinder has been used to measure the ratio perpendicular to the twin interfaces (angle to tip direction determined from TEM, other angle by rotation around tip axis and checking for variations). As can be seen in Fig. A.8 (c) the sample has an average Li/Mn-ratio of $1.28(3)$ which is approximately double the detected rounded composition measured in the pristine sample material, which yields $Li_{1.2}Mn_2O_{2.3}$ (indi-

cated with blue line). [232] This also confirms that sample has clearly been lithiated to the tetragonal $Li_2Mn_2O_4$-phase. The measured distance is long enough to include multiple twin boundaries, so that it can be concluded that the variants are chemically identical within the noise level of 2.7 %, with maximum point deviations of ≈ 8 %.

A.7. Origin of the STEM contrast

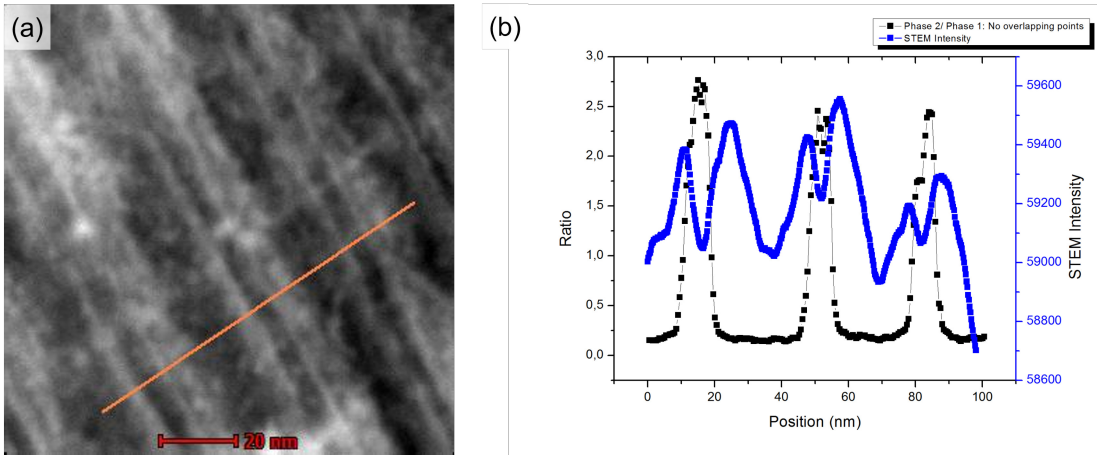

Figure A.9.: Comparison of the Nanodiffraction data and the STEM intensity shows a connection.

The strucutural information of the scanning nanodiffraction can be compared with the intensity data extracted from the according overview image (see fig. A.9). This quickly shows that the contrasts in this STEM image are high at the interfaces. The STEM intensity therefore varies twice for each twin variant. It is not correlated to the variants itself. This should not be overinterpreted, though, as different camera lengths in STEM can alter the contrast obtained and the nanodiffraction mode uses a different camera legth (SI1.05m) in comparison to EELS (38 mm).

A.8. Importance of storing samples in vacuum after in-situ lithiation

Fig. A.10 shows the importance of storing samples that are supposed to be revisited for characterisation under vacuum conditions as the might otherwise react with air presumably humidity, but this has not been further investigated. Sadly this kind of direct transfer of the sample to vacuum conditions is only possible for a limited number of

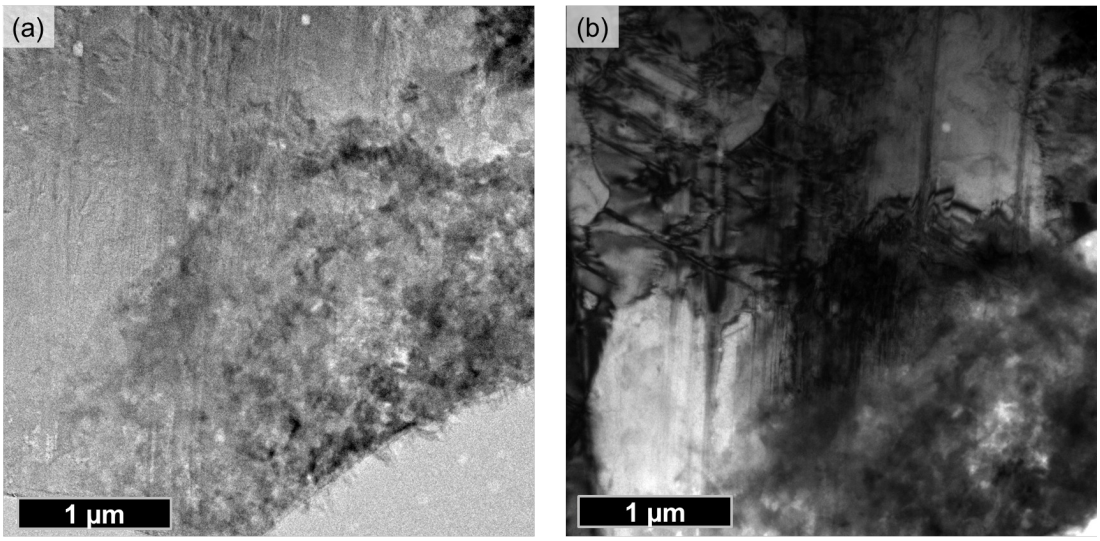

Figure A.10.: Samples get damaged over time when not stored in vacuum. (a) TEM shows the damaged caused to a sample kept in a conventional membrane sample box and therefore in air. (b) BF imaging shows that the twinned structure is still visible in non-damaged areas. Both images show that the damage might start by a reaction starting at the Li-contacted edge. Time elapsed since in-situ experiment: Three weeks.

samples so that some samples were lost that in a later point in time might have provided answers only coming up then that required special characterisation not performed directly after the in-situ experiment.

Also just FIB-prepared samples get damaged being in air contact over a long time as can be seen in Fig. A.11. This sample was pre-characterised and found to be unfit for an in-situ experiment but still revisted after a long time and showed the severe damage. Since all collaborators in our institute haven't registered significant reactions even in the sample powders kept under ambient conditions, I presume that the damage is also influence by the thinner nature of the samples.

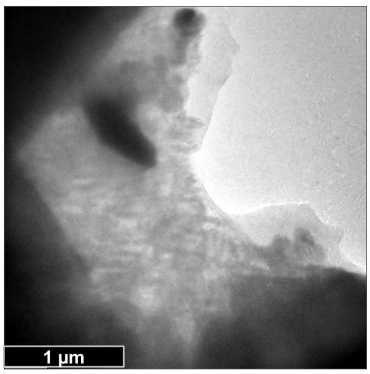

Figure A.11.: FIB-prepared samples also get damaged under ambient conditions over a long time. The damage looks similar to Fig. A.10. Defocus of image to enhance the contrast of the presumably Li-reaction product on the surface.

A.9. The structure of spinel

Any kind of spinel can be produced on the basis of the spinel symmetry by specifying the following positions along the body diagonal without the X at 32e getting any specified relaxation u from the position: [78]

- (0,0,0), 1/4(1,1,1): 8a
- 1/8(1,1,1): 16c
- 3/8(1,1,1), 7/8(1,1,1): 32e
- 1/2(1,1,1), 3/4(1,1,1): 8b
- 5/8(1,1,1,): 16d

When comparing take into consideration that there are two different choices of origin so that some descriptions may differ while producing the same crystal.

An alternative description of the whole spinel structure is given in [78] as: "A-site cations share corners withe neighboring B-site octahedra. No edge sharing occurs between A-site tetrahedra and other A- or B-site polyhedra. B-site octahedra share six of twelve X-X edges with nearest-neighbor B-site octahedra. The other six edges are shared with octahedra that surround 16c vacant sites. The X-X edges that are shared by the B cations form chains in the lattice along the <110> directions. Because no intervening anions obstruct neighboring B-site cations, B-B distances are short, which facilitates electrical conductivity in some spinels, via electron hopping between B-sites."
https://en.wikipedia.org/wiki/Spinel_group

A.10. Additional image sequence of SF interaction with the interface

An additional image sequence showing the influence of the stacking faults on the lithiation behavior is shown in fig. A.12. The results of the image sequence are summarized in sec. 5.6.1 and included in fig. 5.22 as the arrows number two and three. Due to additional strains/contrasts of the already transformed $Li_2Mn_2O_4$ region the further reaction is hard to observe in the still images. The red arrow marks a lamellar contrast that previously wasn't visible suggesting that the region below it is now transformed. Moving images also show the movement in parts of the region from right to left. The white arrows show the movement of the reaction front from right to left through the region directly above - once enclosed by two SFs.

Another video shows the beginnings of the reaction of the next region above the ones in the still images.

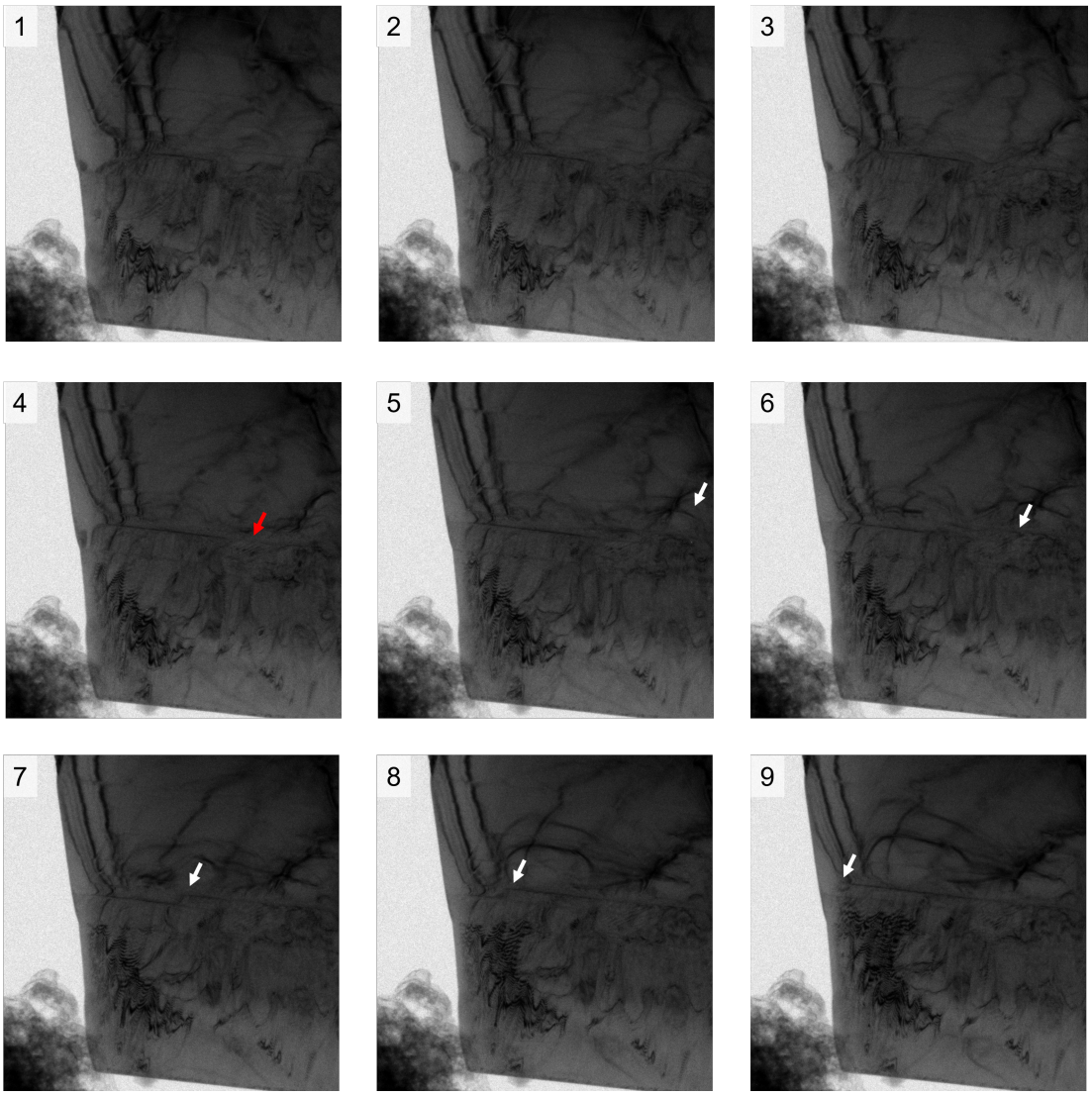

Figure A.12.: Further reaction of regions between stacking faults. During the 140 s of this image series two additional regions enclosed by SFs are lithiated subsequently. The first region is hard to see, but in the second part white arrows mark the reaction front. Field of view: 2.708 μm

List of Figures

Bibliography

[1] F. Giudice, "Volta : an aristocrat who had inventions," *Phys. World*, vol. 17, no. 2, pp. 41–43, 2004.

[2] T. Placke, R. Kloepsch, S. Dühnen, and M. Winter, "Lithium ion, lithium metal, and alternative rechargeable battery technologies: the odyssey for high energy density," *J. Solid State Electrochem.*, vol. 21, no. 7, pp. 1939–1964, 2017.

[3] J. Sudworth and A. R. Tiley, *Sodium Sulfur Battery*. Springer Science & Business Media, 1985.

[4] Vattenfall InCharge, "The history of the electric car: It all started in 1832," 2020. [Online]. Available: https://incharge.vattenfall.de/en/knowledge-hub/articles/the-history-of-the-electric-car-it-all-started-in-1832

[5] M. Armand and J.-M. Tarascon, "Building better batteries," *Nature*, vol. 451, no. 7179, pp. 652–657, 2008. [Online]. Available: http://www.nature.com/doifinder/10.1038/451652a

[6] B. L. Ellis, K. Town, and L. F. Nazar, "New composite materials for lithium-ion batteries," *Electrochim. Acta*, vol. 84, pp. 145–154, 2012. [Online]. Available: http://dx.doi.org/10.1016/j.electacta.2012.04.113

[7] M. S. Whittingham, "Electrical Energy Storage and Intercalation Chemistry," *Science (80-.).*, vol. 192, no. 4244, pp. 1126–1127, jun 1976. [Online]. Available: https://science.sciencemag.org/content/192/4244/1126/tab-pdfhttps://www.sciencemag.org/lookup/doi/10.1126/science.192.4244.1126

[8] M. M. Thackeray, J. R. Croy, E. Lee, A. Gutierrez, M. He, J. S. Park, B. T. Yonemoto, B. R. Long, J. D. Blauwkamp, C. S. Johnson, Y. Shin, and W. I. F. David, "The quest for manganese-rich electrodes for lithium batteries: strategic design and electrochemical behavior," *Sustain. Energy Fuels*, vol. 00, pp. 1–23, 2018. [Online]. Available: http://dx.doi.org/10.1039/C8SE00157Jhttp://xlink.rsc.org/?DOI=C8SE00157J

[9] A. K. Padhi, K. S. Nanjundaswamy, and J. B. Goodenough, "Phospho-olivines as Positive-Electrode Materials for Rechargeable Lithium Batteries," *J. Electrochem. Soc.*, vol. 144, no. 4, pp. 1188–1194, apr 1997. [Online]. Available: https://iopscience.iop.org/article/10.1149/1.1837571

[10] J. M. Tarascon and M. Armand, "Issues and challenges facing rechargeable lithium batteries," *Nature*, vol. 414, no. 6861, pp. 359–367, 2001. [Online]. Available: http://www.ncbi.nlm.nih.gov/pubmed/11713543

[11] A. Manthiram, "An Outlook on Lithium Ion Battery Technology," *ACS Cent. Sci.*, vol. 3, no. 10, pp. 1063–1069, oct 2017. [Online]. Available: http://pubs.acs.org/doi/10.1021/acscentsci.7b00288

[12] J. Tarascon and D. Guyomard, "The Li1+xMn2O4/C rocking-chair system: a review," *Electrochim. Acta*, vol. 38, no. 9, pp. 1221–1231, jun 1993. [Online]. Available: http://linkinghub.elsevier.com/retrieve/pii/0013468693800533

[13] M. S. Whittingham, "Lithium Batteries and Cathode Materials," *Chem. Rev.*, vol. 104, no. 10, pp. 4271–4302, oct 2004. [Online]. Available: https://pubs.acs.org/doi/10.1021/cr020731c

[14] ——, "Ultimate limits to intercalation reactions for lithium batteries," *Chem. Rev.*, vol. 114, no. 23, pp. 11 414–11 443, 2014.

[15] J. Qi and D. Dah-Chuan Lu, "Review of battery cell balancing techniques," in *2014 Australas. Univ. Power Eng. Conf.* IEEE, sep 2014, pp. 1–6. [Online]. Available: http://ieeexplore.ieee.org/document/6966514/

[16] J. K. Barillas, J. Li, C. Günther, and M. A. Danzer, "A comparative study and validation of state estimation algorithms for Li-ion batteries in battery management systems," *Appl. Energy*, vol. 155, pp. 455–462, oct 2015. [Online]. Available: https://linkinghub.elsevier.com/retrieve/pii/S0306261915007357

[17] S. Wen, "Cell balancing buys extra run time and battery life," *Analog Appl. J.*, vol. 1, 2009.

[18] K. Sann, E. Rahimzei, and M. Dr. Vogel, "Kompendium : Li - Ionen - Batterien," *VDE Verband der Elektrotechnik*, p. 66, 2015.

[19] M. Wayland, "Tesla will change the type of battery cells it uses in all its standard-range cars," 2021. [Online]. Available: https://www.cnbc.com/2021/10/20/tesla-switching-to-lfp-batteries-in-all-standard-range-cars.html

[20] K. K. Turekian, N. Haven, K. Hans, and W. M.-i. D. Universitat, "KARL K. TUREKIAN Dept. Geology, Yale University, New Haven, Conn. KARL HANS WEDEPOHL Mineralogische-Institut der Universitat, Gottingen, Germany Distribution of the Elements in Some Major Units of the Earth's Crust," *America (NY).*, no. February, pp. 175–192, 1961.

[21] J. O. Besenhard, Ed., *Handbook of Battery Materials*. Wiley, dec 1998. [Online]. Available: https://onlinelibrary.wiley.com/doi/book/10.1002/9783527611676

[22] M. M. Thackeray, "Manganese oxides for lithium batteries," *Prog. Solid State Chem.*, vol. 25, no. 1-2, pp. 1–71, jan 1997. [Online]. Available: http://linkinghub.elsevier.com/retrieve/pii/S0079678697810035

[23] J. Ma, P. Hu, G. Cui, and L. Chen, "Surface and Interface Issues in Spinel LiNi 0.5 Mn 1.5 O 4 : Insights into a Potential Cathode Material for High Energy Density Lithium Ion Batteries," *Chem. Mater.*, vol. 28, no. 11, pp. 3578–3606, jun 2016. [Online]. Available: http://pubs.acs.org/doi/abs/10.1021/acs.chemmater.6b00948

[24] A. Manthiram, X. Yu, and S. Wang, "Lithium battery chemistries enabled by solid-state electrolytes," *Nat. Rev. Mater.*, vol. 2, no. 4, p. 16103, apr 2017. [Online]. Available: http://dx.doi.org/10.1038/natrevmats.2016.103http://www.nature.com/articles/natrevmats2016103

[25] J. C. Hunter, "Preparation of a new crystal form of manganese dioxide: λ-MnO2," *J. Solid State Chem.*, vol. 39, no. 2, pp. 142–147, sep 1981. [Online]. Available: http://linkinghub.elsevier.com/retrieve/pii/0022459681903236

[26] A. Bhandari and J. Bhattacharya, "Review—Manganese Dissolution from Spinel Cathode: Few Unanswered Questions," *J. Electrochem. Soc.*, vol. 164, no. 2, pp. A106–A127, 2017.

[27] Y. Y.-Y. Xia, Y. Zhou, and M. Yoshio, "Capacity Fading on Cycling of 4 V Li/LiMn2O4 Cells," *J. Electrochem. Soc.*, vol. 144, no. 8, p. 2593, 1997. [Online]. Available: http://jes.ecsdl.org/cgi/doi/10.1149/1.1837870

[28] R. Gummow, A. de Kock, and M. M. Thackeray, "Improved capacity retention in rechargeable 4 V lithium/lithium-manganese oxide (spinel) cells," *Solid State Ionics*, vol. 69, no. 1, pp. 59–67, apr 1994. [Online]. Available: http://linkinghub.elsevier.com/retrieve/pii/0167273894904502

[29] S.-c. Park, Y.-m. Kim, S.-c. Han, S. Ahn, C.-h. Ku, and J.-y. Lee, "The elevated temperature performance of LiMn2O4 coated with LiNi1-XCoXO2 (X = 0.2 and 1)," *J. Power Sources*, vol. 107, no. 1, pp. 42–47, apr 2002. [Online]. Available: https://linkinghub.elsevier.com/retrieve/pii/S0378775301009788

[30] C. Zhan, T. Wu, J. Lu, and K. Amine, "Dissolution, migration, and deposition of transition metal ions in Li-ion batteries exemplified by Mn-based cathodes – a critical review," *Energy Environ. Sci.*, vol. 11, no. 2, pp. 243–257, 2018. [Online]. Available: http://xlink.rsc.org/?DOI=C7EE03122J

[31] K. Amine, J. Liu, S. Kang, I. Belharouak, Y. Hyung, D. Vissers, and G. Henriksen, "Improved lithium manganese oxide spinel/graphite Li-ion cells for high-power applications," *J. Power Sources*, vol. 129, no. 1, pp. 14–19, apr 2004. [Online]. Available: https://linkinghub.elsevier.com/retrieve/pii/S0378775303010735

[32] M. D. Radin, S. Hy, M. Sina, C. Fang, H. Liu, J. Vinckeviciute, M. Zhang, M. S. Whittingham, Y. S. Meng, and A. Van der Ven, "Narrowing the Gap between Theoretical and Practical Capacities in Li-Ion Layered Oxide Cathode Materials," *Adv. Energy Mater.*, vol. 7, no. 20, pp. 1–33, 2017.

[33] M. R. Palacin and A. de Guibert, "Why do batteries fail?" *Science (80-.).*, vol. 351, no. 6273, pp. 1 253 292–1 253 292, feb 2016. [Online]. Available: http://www.sciencemag.org/cgi/doi/10.1126/science.1253292

[34] W. Li, B. Song, and A. Manthiram, "High-voltage positive electrode materials for lithium-ion batteries," *Chem. Soc. Rev.*, vol. 46, no. 10, pp. 3006–3059, 2017. [Online]. Available: http://xlink.rsc.org/?DOI=C6CS00875E

[35] "How to Prolong Lithium-based Batteries," 2021. [Online]. Available: https://batteryuniversity.com/article/bu-808-how-to-prolong-lithium-based-batteries

[36] M. M. Thackeray, Y. Shao-Horn, A. J. Kahaian, K. D. Kepler, E. Skinner, J. T. Vaughey, and S. a. Hackney, "Structural Fatigue in Spinel Electrodes in High Voltage (4 V) Li/LixMn2O4 Cells," *Electrochem. Solid-State Lett.*, vol. 1, no. 1, p. 7, 1998. [Online]. Available: http://esl.ecsdl.org/cgi/doi/10.1149/1.1390617

[37] J. Conder, C. Marino, P. Novák, and C. Villevieille, "Do imaging techniques add real value to the development of better post-Li-ion batteries?" *J. Mater. Chem. A*, vol. 6, no. 8, pp. 3304–3327, 2018. [Online]. Available: http://pubs.rsc.org/en/Content/ArticleLanding/2018/TA/C7TA10622Jhttp://xlink.rsc.org/?DOI=C7TA10622J

[38] S. Lee, Y. Oshima, E. Hosono, H. Zhou, K. Kim, H. M. Chang, R. Kanno, and K. Takayanagi, "In situ TEM observation of local phase transformation in a rechargeable LiMn2O4 nanowire battery," *J. Phys. Chem. C*, vol. 117, no. 46, pp. 24 236–24 241, nov 2013. [Online]. Available: https://pubs.acs.org/doi/10.1021/jp409032r

[39] ——, "Phase Transitions in a LiMn2O4 Nanowire Battery Observed by Operando Electron Microscopy," *ACS Nano*, vol. 9, no. 1, pp. 626–632, jan 2015. [Online]. Available: http://dx.doi.org/10.1021/nn505952khttp://pubs.acs.org/doi/abs/10.1021/nn505952k

[40] A. Van der Ven, J. Bhattacharya, and A. A. Belak, "Understanding Li Diffusion in Li-Intercalation Compounds," *Acc. Chem. Res.*, vol. 46, no. 5, pp. 1216–1225, may 2013. [Online]. Available: http://pubs.acs.org/doi/abs/10.1021/ar200329rhttp://pubs.acs.org/doi/10.1021/ar200329r

[41] M. Nič, J. Jirát, B. Košata, A. Jenkins, and A. McNaught, Eds., *IUPAC Compendium of Chemical Terminology*. Research Triangle Park, NC: IUPAC, jun 2009. [Online]. Available: http://goldbook.iupac.org

[42] J. B. Goodenough, M. S. Whittingham, and A. Yoshino, "They developed the world's most powerful battery," 2019. [Online]. Available: https://www.nobelprize.org/prizes/chemistry/2019/popular-information/{#}:{~}:text=TheNobelPrizeinChemistry2019isawardedtoJohn,asmobilephonesandlaptops.

[43] N. Bensalah and H. Dawood, "Review on Synthesis, Characterizations, and Electrochemical Properties of Cathode Materials for Lithium Ion Batteries," *J. Mater. Sci. Eng.*, vol. 5, no. 4, 2016. [Online]. Available: https://www.omicsgroup.org/journals/review-on-synthesis-characterizations-and-electrochemical-properties-of-cathode-materials-for-lithium
php?aid=75026

[44] J.-M. Tarascon and D. Guyomard, "Li Metal-Free Rechargeable Batteries Based on Li(1+x)Mn2O4 Cathodes (0 \leq x \leq 1) and Carbon Anodes," *J. Electrochem. Soc.*, vol. 138, no. 10, 1991.

[45] A. S. Wills, N. P. Raju, and J. E. Greedan, "Low-Temperature Structure and Magnetic Properties of the Spinel LiMn2O 4: A Frustrated Antiferromagnet and Cathode Material," *Chem. Mater.*, vol. 11, no. 6, pp. 1510–1518, jun 1999. [Online]. Available: http://pubs.acs.org/doi/abs/10.1021/cm981041l

[46] K. Hoang, "Understanding the electronic and ionic conduction and lithium overstoichiometry in LiMn 2 O 4 spinel," *J. Mater. Chem. A*, vol. 2, no. 43, pp. 18 271–18 280, 2014. [Online]. Available: http://xlink.rsc.org/?DOI=C4TA04116J

[47] V. Massarotti, D. Capsoni, M. Bini, G. Chiodelli, C. Azzoni, M. Mozzati, and A. Paleari, "Electric and Magnetic Properties of LiMn2O4- and Li2MnO3-Type Oxides," *J. Solid State Chem.*, vol. 131, no. 1, pp. 94–100, jun 1997. [Online]. Available: https://linkinghub.elsevier.com/retrieve/pii/S0022459697973497

[48] C. B. Azzoni, M. C. Mozzati, A. Paleari, M. Bini, D. Capsoni, and V. Massarotti, "Stoichiometry Effects on the Electrical Conductivity of Lithium-Manganese Spinels," *Zeitschrift für Naturforsch. A*, vol. 54, no. 10-11, pp. 579–684, jan 1999. [Online]. Available: https://www.degruyter.com/view/j/zna.1999.54.issue-10-11/zna-1999-10-1104/zna-1999-10-1104.xml

[49] J. Rodriguez-Carvajal, G. Rousse, C. Masquelier, and M. Hervieu, "Verwey-like Transition in a Lithium Battery Material: The Spinel LiMn2O4," Laboratoire Léon Brillouin (CEA-CNRS); Laboratoire de Chimie des Solides (Université Paris-Sud); CRISMAT (ISMRA, Caen Cedex), Tech. Rep., 1999.

[50] J. Molenda, "Transport properties of LiMn2O4," *Solid State Ionics*, vol. 117, no. 1-2, pp. 41–46, feb 1999. [Online]. Available: http://linkinghub.elsevier.com/retrieve/pii/S016727389800246X

[51] K. Miura, A. Yamada, and M. Tanaka, "Electric states of spinel LixMn2O4 as a cathode of the rechargeable battery," *Electrochim. Acta*, vol. 41, no. 2, pp. 249–256, feb 1996. [Online]. Available: https://linkinghub.elsevier.com/retrieve/pii/001346869500304W

[52] R. J. Gummow, "An Investigation of Spinel-Related and Orthorhombic LiMnO2 Cathodes for Rechargeable Lithium Batteries," *J. Electrochem. Soc.*, vol. 141, no. 5, p. 1178, 1994. [Online]. Available: http://jes.ecsdl.org/cgi/doi/10.1149/1.2054893

[53] R. J. Tilley, "Spinel, MgAl2O4 and AB2O4 Spinels," in *Defects in Solids*. Wiley, 2008, ch. S1: Crysta, pp. 459–460.

[54] J. B. Goodenough, M. M. Thackeray, W. I. F. David, and P. G. Bruce, "Lithium insertion/extraction reactions with manganese oxides," *Rev. Chim. minérale*, vol. 21, no. 4, pp. 435–455, 1986.

[55] M. M. Thackeray, W. I. F. David, P. G. Bruce, J. B. Goodenough, S. P. Road, W. I. F. David, P. G. Bruce, and J. B. Goodenough, "Lithium insertion into manganese spinels," *Mater. Res. Bull.*, vol. 18, pp. 461–472, 1983.

[56] T. Ohzuku, "Electrochemistry of Manganese Dioxide in Lithium Nonaqueous Cell," *J. Electrochem. Soc.*, vol. 136, no. 11, p. 3169, 1989. [Online]. Available: http://jes.ecsdl.org/cgi/doi/10.1149/1.2096421

[57] J. C. Knight, S. Therese, and A. Manthiram, "Delithiation Mechanisms in Acid of Spinel LiMn 2-x M x O 4 (M = Cr, Fe, Co, and Ni) Cathodes," *J. Electrochem. Soc.*, vol. 162, no. 3, pp. A426–A431, dec 2015. [Online]. Available: http://jes.ecsdl.org/cgi/doi/10.1149/2.0661503jeshttp://jes.ecsdl.org/lookup/doi/10.1149/2.0661503jes

[58] A. N. Grundy, B. Hallsteat, and R. J. Gauckler, "Assessment of the Mn-O system," *J. Phase Equilibra*, vol. 24, no. 1, pp. 27–29, 2003.

[59] T. Okumura, Y. Yamaguchi, M. Shikano, and H. Kobayashi, "Further Findings of X-ray Absorption Near-Edge Structure in Lithium Manganese Spinel Oxide using First-Principles Calculations," *J. Mater. Chem. A*, vol. 2, pp. 8017–8025, 2014. [Online]. Available: http://dx.doi.org/10.1039/C3TA15412B

[60] A. van der Ven, C. Marianetti, D. Morgan, and G. Ceder, "Phase transformations and volume changes in spinel LixMn2O4," *Solid State Ionics*, vol. 135, pp. 21–32, 2000.

[61] G. Li, "Phase segregation of LixMn2O4 (0.6<x<1) in non-equilibrium reduction processes," *Solid State Ionics*, vol. 130, no. 3-4, pp. 221–228, may 2000. [Online]. Available: http://linkinghub.elsevier.com/retrieve/pii/S0167273800006652

[62] H. Berg, "The LiMn2O4 to Î»-MnO2 phase transition studied by in situ neutron diffraction," *Solid State Ionics*, vol. 144, no. 1-2, pp. 65–69, 2001. [Online]. Available: http://www.sciencedirect.com/science/article/pii/S0167273801008943

[63] W. Liu, K. Kowal, and G. C. Farrington, "Mechanism of the Electrochemical Insertion of Lithium into LiMn2O4 Spinels," *J. Electrochem. Soc.*, vol. 145, no. 2, pp. 459–465, feb 1998. [Online]. Available: http://jes.ecsdl.org/cgi/doi/10.1149/1.1838285https://iopscience.iop.org/article/10.1149/1.1838285

[64] M. M. Thackeray, P. Johnson, L. Picciotto, P. Bruce, and J. Goodenough, "Electrochemical extraction of lithium from LiMn2O4," *Mater. Res. Bull.*, vol. 19, no. 2, pp. 179–187, 1984. [Online]. Available: https://doi.org/10.1016/0025-5408(84)90088-6

[65] H. Björk, T. Gustafsson, and J. O. Thomas, "Single-crystal studies of electrochemically delithiated LiMn2O4," *Electrochem. commun.*, vol. 3, no. 4, pp. 187–190, apr 2001. [Online]. Available: http://linkinghub.elsevier.com/retrieve/pii/S1388248101001291https://linkinghub.elsevier.com/retrieve/pii/S1388248101001291

[66] Y.-Y. Xia, T. Sakai, T. Fujieda, X. Q. Yang, X. Sun, Z. F. Ma, J. McBreen, and M. Yoshio, "Correlating Capacity Fading and Structural Changes in Li1+yMn2-yO4-δ Spinel Cathode Materials: A Systematic Study on the Effects of Li/Mn Ratio and Oxygen Deficiency," *J. Electrochem. Soc.*, vol. 148, no. 7, p. A723, 2001. [Online]. Available: http://jes.ecsdl.org/cgi/doi/10.1149/1.1376117

[67] F. Le Cras, P. Strobel, M. Anne, and D. Bloch, "Lithium intercalation in low temperature Li-Mn-O compounds: a new monoclinic phase and structural in situ studies," *J. Power Sources*, vol. 65, no. 1-2, p. 225, mar 1997. [Online]. Available: http://linkinghub.elsevier.com/retrieve/pii/S0378775397025639

[68] W. I. F. David, M. M. Thackeray, L. De Picciotto, and J. Goodenough, "Structure refinement of the spinel-related phases Li2Mn2O4 and Li0.2Mn2O4," *J. Solid State Chem.*, vol. 67, no. 2, pp. 316–323, apr 1987. [Online]. Available: http://linkinghub.elsevier.com/retrieve/pii/0022459687903690

[69] T. Erichsen, B. Pfeiffer, V. Roddatis, and C. A. Volkert, "Tracking the Diffusion-Controlled Lithiation Reaction of LiMn2O4 by In Situ TEM," *ACS Appl. Energy Mater.*, vol. 3, no. 6, pp. 5405–5414, jun 2020. [Online]. Available: https://pubs.acs.org/doi/10.1021/acsaem.0c00380

[70] Z. Xu, J. Wang, X. Quan, S. Hu, and Q. Wu, "Formation and distribution of tetragonal phases in the Li1+αMn2-αO4-δ at room temperature: Direct evidence from a transmission electron microscopy study," *J. Power Sources*, vol. 248, pp. 1201–1210, feb 2014. [Online]. Available: http://dx.doi.org/10.1016/j.jpowsour.2013.10.059http://linkinghub.elsevier.com/retrieve/pii/S0378775313017254

[71] S. Mishra and G. Ceder, "Structural stability of lithium manganese oxides," *Phys. Rev. B*, vol. 59, no. 9, pp. 6120–6130, 1999.

[72] A. Paolone, P. Roy, G. Rousse, C. Masquelier, and J. Rodriguez-Carvajal, "Infrared spectroscopy investigation of the charge ordering transition in LiMn2O4," *Solid State Commun.*, vol. 111, no. 8, pp. 453–458, jul 1999. [Online]. Available: http://linkinghub.elsevier.com/retrieve/pii/S0038109899002082

[73] H. Hayakawa, T. Takada, H. Enoki, and E. Akiba, "New findings on the structural phase transitions of spinel LiMn2O4 at low temperature," *J. Mater. Sci. Lett.*, vol. 17, no. 10, pp. 811–812, 1998.

[74] C. Ouyang, S. Shi, and M. Lei, "Jahn–Teller distortion and electronic structure of LiMn2O4," *J. Alloys Compd.*, vol. 474, no. 1-2, pp. 370–374, apr 2009. [Online]. Available: http://linkinghub.elsevier.com/retrieve/pii/S0925838808010633

[75] T. Takada, H. Hayakawa, H. Enoki, E. Akiba, H. Slegr, I. Davidson, and J. Murray, "Structure and electrochemical characterization of Li1+xMn2-xO4 spinels for rechargeable lithium batteries," *J. Power Sources*, vol. 81-82, pp. 505–509, sep 1999. [Online]. Available: http://linkinghub.elsevier.com/retrieve/pii/S0378775398002250

[76] I. Tomeno, Y. Kasuya, and Y. Tsunoda, "Charge and spin ordering in LiMn2O4," *Phys. Rev. B*, vol. 64, no. 9, p. 094422, aug 2001. [Online]. Available: https://link.aps.org/doi/10.1103/PhysRevB.64.094422

[77] J. M. Paulsen and J. R. Dahn, "Phase Diagram of Li-Mn-O Spinel in Air," *Chem. Mater.*, vol. 11, no. 11, pp. 3065–3079, nov 1999. [Online]. Available: http://pubs.acs.org/doi/abs/10.1021/cm9900960

[78] K. E. Sickafus, J. M. Wills, and N. W. Grimes, "Structure of spinel," *J. Am. Ceram. Soc.*, vol. 82, no. 12, pp. 3279–3292, dec 1999. [Online]. Available: http://doi.wiley.com/10.1111/j.1151-2916.1999.tb02241.x

[79] M. M. Thackeray, "Spinel Electrodes for Lithium Batteries," *J. Am. Ceram. Soc.*, vol. 82, no. 12, pp. 3347–3354, dec 1999. [Online]. Available: http://www.ncbi.nlm.nih.gov/entrez/query.fcgi?db=pubmed{&}cmd=Retrieve{&}dopt=AbstractPlus{&}list{_}uids=11133718817669169373related:3cBAlEbqgpoJhttp://doi.wiley.com/10.1111/j.1151-2916.1999.tb02250.x

[80] R. Chen, M. Knapp, M. Yavuz, R. Heinzmann, D. Wang, S. Ren, V. Trouillet, S. Lebedkin, S. Doyle, H. Hahn, H. Ehrenberg, and S. Indris, "Reversible Li + Storage in a LiMnTiO 4 Spinel and Its Structural Transition Mechanisms," *J. Phys. Chem. C*, vol. 118, no. 24, pp. 12 608–12 616, jun 2014. [Online]. Available: http://pubs.acs.org/doi/10.1021/jp501618n

[81] J. E. Post, "Manganese oxide minerals: Crystal structures and economic and environmental significance," *Proc. Natl. Acad. Sci.*, vol. 96, no. 7, pp. 3447–3454, mar 1999. [Online]. Available: http://www.pnas.org/content/96/7/3447.abstracthttp://www.pnas.org/cgi/doi/10.1073/pnas.96.7.3447

[82] B. Ammundsen and J. Paulsen, "Novel lithium-ion cathode materials based on layered manganese oxides," *Adv. Mater.*, vol. 13, no. 12-13, pp. 943–956, 2001.

[83] S. Miao, M. Kocher, P. Rez, B. Fultz, Y. Ozawa, R. Yazami, and C. C. Ahn, "Local electronic structure of layered Li(x)Ni0.5Mn0.5O2 and Li(x)Ni(1/3)Mn(1/3)Co(1/3)O2." *J. Phys. Chem. B*, vol. 109, no. 49, pp. 23 473–23 479, 2005.

[84] G. Vitins, "Lithium Intercalation into Layered LiMnO2," *J. Electrochem. Soc.*, vol. 144, no. 8, p. 2587, 1997. [Online]. Available: http://jes.ecsdl.org/cgi/doi/10.1149/1.1837869

[85] Y. Shin and A. Manthiram, "Influence of the lattice parameter difference between the two cubic phases formed in the 4 V region on the capacity fading of spinel manganese oxides," *Chem. Mater.*, vol. 15, no. 15, pp. 2954–2961, 2003.

[86] M. Yonemura, A. Yamada, H. Kobayashi, M. Tabuchi, T. Kamiyama, Y. Kawamoto, and R. Kanno, "Synthesis, structure, and phase relationship in lithium manganese oxide spinel," *J. Mater. Chem.*, vol. 14, no. 13, pp. 1948–1958, 2004.

[87] J. Sugiyama, T. Atsumi, T. Hioki, S. Noda, and N. Kamegashira, "Nonstoichiometry and defect structure of spinel LiMn2O4-δ," *J. Power Sources*, vol. 68, no. 2, pp. 641–645, oct 1997. [Online]. Available: http://linkinghub.elsevier.com/retrieve/pii/S0378775396025955

[88] R. Kanno, M. Yonemura, T. Kohigashi, Y. Kawamoto, M. Tabuchi, and T. Kamiyama, "Synthesis and structures of lithium manganese oxide spinel, LiMn2O4-d," *J. Power Sources*, vol. 97-98, pp. 423–426, 2001.

[89] J. Sugiyama, T. Atsumi, T. Hioki, S. Noda, and N. Kamegashira, "Oxygen nonstoichiometry of spinel LiMn2O4-δ," *J. Alloys Compd.*, vol. 235, no. 2, pp. 163–169, mar 1996. [Online]. Available: http://linkinghub.elsevier.com/retrieve/pii/0925838895021248

[90] Y. Koyama, I. Tanaka, H. Adachi, Y. Uchimoto, and M. Wakihara, "First Principles Calculations of Formation Energies and Electronic Structures of Defects in Oxygen-Deficient LiMn2O4," *J. Electrochem. Soc.*, vol. 150, no. 1, p. A63, 2003. [Online]. Available: http://jes.ecsdl.org/cgi/doi/10.1149/1.1522720

[91] X. Hao, O. Gourdon, B. J. Liddle, and B. M. Bartlett, "Improved electrode kinetics in lithium manganospinel nanoparticles synthesized by hydrothermal methods: identifying and eliminating oxygen vacancies," *J. Mater. Chem.*, vol. 22, no. 4, pp. 1578–1591, 2012. [Online]. Available: http://xlink.rsc.org/?DOI=C1JM15583K

[92] S. Zhang, K. J. T. Livi, A.-C. Gaillot, a. T. Stone, and D. R. Veblen, "Determination of manganese valence states in (Mn3+, Mn4+) minerals by electron energy-loss spectroscopy," *Am. Mineral.*, vol. 95, no. 11-12, pp. 1741–1746, nov 2010. [Online]. Available: http://ammin.geoscienceworld.org/cgi/doi/10.2138/am.2010.3468

[93] C. Röhr, "Übergangsmetalle II: VII. Nebengruppe/7. Gruppe/Mangan-Gruppe." [Online]. Available: http://ruby.chemie.uni-freiburg.de/Vorlesung/metalle{_}mn{_}gruppe.html{#}mn

[94] H. A. Jahn and E. Teller, "Stability of Polyatomic Molecules in Degenerate Electronic States: I - Orbital Degeneracy," *Proc. R. Soc. London*, vol. 161, pp. 220–235, 1937.

[95] Z. X. Nie, C. Y. Ouyang, J. Z. Chen, Z. Y. Zhong, Y. L. Du, D. S. Liu, S. Q. Shi, and M. S. Lei, "First principles study of Jahn-Teller effects in LixMnPO4," *Solid State Commun.*, vol. 150, no. 1-2, pp. 40–44, 2010. [Online]. Available: http://dx.doi.org/10.1016/j.ssc.2009.10.010

[96] C. Liu, Z. G. Neale, and G. Cao, "Understanding electrochemical potentials of cathode materials in rechargeable batteries," *Mater. Today*, vol. 19, no. 2, pp. 109–123, mar 2016. [Online]. Available: http://dx.doi.org/10.1016/j.mattod.2015.10.009https://linkinghub.elsevier.com/retrieve/pii/S1369702115003181

[97] M. M. Markowitz and D. A. Boryta, "Lithium Metal-Gas Reactions." *J. Chem. Eng. Data*, vol. 7, no. 4, pp. 586–591, oct 1962. [Online]. Available: http://pubs.acs.org/doi/abs/10.1021/je60015a047{%}5Cnhttp://pubs.acs.org/cgi-bin/doilookup/?10.1021/je60015a047http://pubs.acs.org/doi/abs/10.1021/je60015a047

[98] Y. Sun, Y. Li, J. Sun, Y. Li, A. Pei, and Y. Cui, "Stabilized Li3N for efficient battery cathode prelithiation," *Energy Storage Mater.*, vol. 6, pp. 119–124, jan 2017. [Online]. Available: https://linkinghub.elsevier.com/retrieve/pii/S2405829716302379

[99] J. Phillips and J. Tanski, "Structure and kinetics of formation and decomposition of corrosion layers formed on lithium compounds exposed to atmospheric gases," *Int. Mater. Rev.*, vol. 50, no. 5, pp. 265–286, oct 2005. [Online]. Available: http://www.ingentaselect.com/rpsv/cgi-bin/cgi?ini=xref{&}body=linker{&}reqdoi=10.1179/174328005X41122http://www.tandfonline.com/doi/full/10.1179/174328005X41122

[100] A. Rabenau, "Lithium nitride and related materials case study of the use of modern solid state research techniques," *Solid State Ionics*, vol. 6, no. 4, pp. 277–293, jul 1982. [Online]. Available: http://linkinghub.elsevier.com/retrieve/pii/0167273882900121

[101] U. V. Alpen, A. Rabenau, and G. H. Talat, "Ionic conductivity in Li 3 N single crystals," *Appl. Phys. Lett.*, vol. 30, no. 12, pp. 621–623, jun 1977. [Online]. Available: http://aip.scitation.org/doi/10.1063/1.89283

[102] W. Li, G. Wu, C. M. Araújo, R. H. Scheicher, A. Blomqvist, R. Ahuja, Z. Xiong, Y. Feng, and P. Chen, "Li+ion conductivity and diffusion mechanism in α-Li3N and β-Li3N," *Energy Environ. Sci.*, vol. 3, no. 10, pp. 1524–1530, 2010. [Online]. Available: http://xlink.rsc.org/?DOI=c0ee00052c

[103] B. A. Boukamp and R. A. Huggins, "Lithium ion conductivity in lithium nitride," *Phys. Lett. A*, vol. 58, no. 4, pp. 231–233, 1976.

[104] T. Lapp, "Ionic conductivity of pure and doped Li3N," *Solid State Ionics*, vol. 11, no. 2, pp. 97–103, oct 1983. [Online]. Available: https://linkinghub.elsevier.com/retrieve/pii/0167273883900450

[105] A. Rabenau, "Lithium nitride, Li3N, an unusual ionic conductor," in *Festkörperprobleme 18*. Berlin, Heidelberg: Springer Berlin Heidelberg, 1978, pp. 77–108. [Online]. Available: http://link.springer.com/10.1007/BFb0107778

[106] R. M. Biefeld, "Ionic Conductivity of Li2O-Based Mixed Oxides and the Effects of Moisture and LiOH on Their Electrical and Structural Properties," *J. Electrochem. Soc.*, vol. 126, no. 1, p. 1, 1979. [Online]. Available: http://www.scopus.com/inward/record.url?eid=2-s2.0-0018287019{&}partnerID=40{&}md5=39d8c1576f61e3df9f90f7061db64c5ehttp://jes.ecsdl.org/cgi/doi/10.1149/1.2128980

[107] A. Chadwick, K. Flack, J. Strange, and J. Harding, "Defect structures and ionic transport in lithium oxide," *Solid State Ionics*, vol. 28-30, pp. 185–188, sep 1988. [Online]. Available: http://linkinghub.elsevier.com/retrieve/pii/S0167273888800304

[108] J. H. Strange, S. M. Rageb, A. V. Chadwick, K. W. Flack, and J. H. Harding, "Conductivity and NMR study of ionic mobility in lithium oxide," *J. Chem. Soc. Faraday Trans.*, vol. 86, no. 8, pp. 1239–1241, 1990.

[109] T. R. Jow, S. A. Delp, J. L. Allen, J.-P. Jones, and M. C. Smart, "Factors Limiting Li ⁺ Charge Transfer Kinetics in Li-Ion Batteries," *J. Electrochem. Soc.*, vol. 165, no. 2, pp. A361–A367, 2018. [Online]. Available: http://jes.ecsdl.org/lookup/doi/10.1149/2.1221802jes

[110] C. Ouyang, S. Shi, Z. Wang, X. Huang, and L. Chen, "Experimental and theoretical studies on dynamic properties of Li ions in LixMn2O4," *Solid State Commun.*, vol. 130, no. 7, pp. 501–506, 2004.

[111] C. Ouyang, Y. Du, S. Shi, and M. Lei, "Small polaron migration in LixMn2O4: From first principles calculations," *Phys. Lett. A*, vol. 373, no. 31, pp. 2796–2799, jul 2009. [Online]. Available: https://linkinghub.elsevier.com/retrieve/pii/S0375960109006847

[112] A. Kraytsberg, Y. Ein-Eli, A. Kraytsberg, and Y. Ein-Eli, "Higher, stronger, better ... A review of 5 volt cathode materials for advanced lithium-ion batteries," *Adv. Energy Mater.*, vol. 2, no. 8, pp. 922–939, 2012.

[113] M. Nakayama, M. Kaneko, and M. Wakihara, "First-principles study of lithium ion migration in lithium transition metal oxides with spinel structure," *Phys. Chem. Chem. Phys.*, vol. 14, no. 40, p. 13963, 2012. [Online]. Available: http://xlink.rsc.org/?DOI=c2cp42154b

[114] B. Xu and S. Meng, "Factors affecting Li mobility in spinel LiMn2O4-A first-principles study by GGA and GGA+U methods," *J. Power Sources*, vol. 195, no. 15, pp. 4971–4976, 2010. [Online]. Available: http://dx.doi.org/10.1016/j.jpowsour.2010.02.060

[115] J. Lee, A. Urban, X. Li, D. Su, G. Hautier, and G. Ceder, "Unlocking the Potential of Cation-Disordered Oxides for Rechargeable Lithium Batteries," *Science (80-.).*, vol. 343, no. 6170, pp. 519–522, jan 2014. [Online]. Available: http://www.sciencemag.org/cgi/doi/10.1126/science.1246432

[116] A. Urban, J. Lee, and G. Ceder, "The Configurational Space of Rocksalt-Type Oxides for High-Capacity Lithium Battery Electrodes," *Adv. Energy Mater.*, vol. 4, no. 13, p. 1400478, sep 2014. [Online]. Available: http://doi.wiley.com/10.1002/aenm.201400478

[117] H. Moriwake, A. Kuwabara, C. A. J. Fisher, R. Huang, T. Hitosugi, Y. H. Ikuhara, H. Oki, and Y. Ikuhara, "First-Principles Calculations of Lithium-Ion Migration at a Coherent Grain Boundary in a Cathode Material, LiCoO 2," *Adv. Mater.*, vol. 25, no. 4, pp. 618–622, jan 2013. [Online]. Available: http://doi.wiley.com/10.1002/adma.201202805

[118] A. Nie, L.-y. Gan, Y. Cheng, Q. Li, Y. Yuan, F. Mashayek, H. Wang, R. Klie, U. Schwingenschlogl, and R. Shahbazian-Yassar, "Twin Boundary-Assisted Lithium Ion Transport," *Nano Lett.*, vol. 15, no. 1, pp. 610–615, jan 2015. [Online]. Available: http://pubs.acs.org/doi/abs/10.1021/nl504087zhttps://pubs.acs.org/doi/10.1021/nl504087z

[119] J. Zheng, D. Crain, and D. Roy, "Kinetic aspects of Li intercalation in mechano-chemically processed cathode materials for lithium ion batteries: Electrochemical characterization of ball-milled LiMn2O4," *Solid State Ionics*, vol. 196, no. 1, pp. 48–58, aug 2011. [Online]. Available: http://dx.doi.org/10.1016/j.ssi.2011.06.004http://linkinghub.elsevier.com/retrieve/pii/S0167273811003043

[120] F. Wunde, S. Nowak, J. Mürter, E. Hadjixenophontos, F. Berkemeier, and G. Schmitz, "Ion transport and phase transformation in thin film intercalation electrodes," *Int. J. Mater. Res.*, vol. 108, no. 11, pp. 984–998, 2017.

[121] M. Park, X. Zhang, M. Chung, G. B. Less, and A. M. Sastry, "A review of conduction phenomena in Li-ion batteries," *J. Power Sources*, vol. 195, no. 24, pp. 7904–7929, dec 2010. [Online]. Available: http://dx.doi.org/10.1016/j.jpowsour.2010.06.060http://linkinghub.elsevier.com/retrieve/pii/S0378775310010463

[122] C. Julien, E. Haro-Poniatowski, M. Camacho-Lopez, L. Escobar-Alarcon, and J. Jimenez-Jarquin, "Growth of LiMn2O4 thin films by pulsed-laser deposition and their electrochemical properties in lithium microbatteries," *Mater. Sci. Eng. B*, vol. 72, no. 1, pp. 36–46, mar 2000. [Online]. Available: http://linkinghub.elsevier.com/retrieve/pii/S092151079900598X

[123] Z. Quan, S. Ohguchi, M. Kawase, H. Tanimura, and N. Sonoyama, "Preparation of nanocrystalline LiMn2O4 thin film by electrodeposition method and its electrochemical performance for lithium battery," *J. Power Sources*, vol. 244, pp. 375–381, 2013. [Online]. Available: http://dx.doi.org/10.1016/j.jpowsour.2012.12.087

[124] H. Gao, Q. Wu, Y. Hu, J. P. Zheng, K. Amine, and Z. Chen, "Revealing the Rate-Limiting Li-Ion Diffusion Pathway in Ultrathick Electrodes for Li-Ion Batteries," *J. Phys. Chem. Lett.*, vol. 9, no. 17, pp. 5100–5104, 2018.

[125] M.-J. Lee, S. Lee, P. Oh, Y. Kim, and J. Cho, "High Performance LiMn 2 O 4 Cathode Materials Grown with Epitaxial Layered Nanostructure for Li-Ion Batteries," *Nano Lett.*, vol. 14, no. 2, pp. 993–999, feb 2014. [Online]. Available: http://pubs.acs.org/doi/10.1021/nl404430e

[126] K. Kamazawa, H. Nozaki, M. Harada, K. Mukai, Y. Ikedo, K. Iida, T. J. Sato, Y. Qiu, M. Tyagi, and J. Sugiyama, "Interrelationship between Li+ diffusion, charge, andmagnetism in 7LiMn2O4 and 7Li1.1Mn1.9O4 spinels: Elastic, inelastic, and quasielastic neutron scattering," *Phys. Rev. B*, vol. 83, no. 9, p. 094401, mar 2011. [Online]. Available: https://link.aps.org/doi/10.1103/PhysRevB.83.094401

[127] M. Jäckle and A. Groß, "Microscopic properties of lithium, sodium, and magnesium battery anode materials related to possible dendrite growth," *J. Chem. Phys.*, vol. 141, no. 17, p. 174710, nov 2014. [Online]. Available: http://dx.doi.org/10.1063/1.4901055http://aip.scitation.org/doi/10.1063/1.4901055

[128] A. Loburets, A. Naumovets, and Y. Vedula, "Surface diffusion of lithium on (011) face of tungsten," *Surf. Sci.*, vol. 120, no. 2, pp. 347–366, aug 1982. [Online]. Available: http://linkinghub.elsevier.com/retrieve/pii/0039602882901558

[129] L. Mandeltort and J. T. Yates, "Rapid atomic Li surface diffusion and intercalation on graphite: A surface science study," *J. Phys. Chem. C*, vol. 116, no. 47, pp. 24 962–24 967, 2012.

[130] R. W. Cahn and P. Haasen, Eds., *Physical Metallurgy*, 4th ed. Amsterdam: North Holland, 1996.

[131] Y. M. Chiang, H. Wang, and Y. I. Jang, "Electrochemically induced cation disorder and phase transformations in lithium intercalation oxides," *Chem. Mater.*, vol. 13, no. 1, pp. 53–63, 2001.

[132] M. H. Lewis, "The defect structure and mechanical properties of spinel single crystals," *Philos. Mag.*, vol. 17, no. 147, pp. 481–499, 1968. [Online]. Available: http://www.tandfonline.com/doi/abs/10.1080/14786436808217737

[133] P. J. Vaughan and D. L. Kohlstedt, "Cation stacking faults in magnesium germanate spinel," *Phys. Chem. Miner.*, vol. 7, no. 6, pp. 241–245, dec 1981. [Online]. Available: http://link.springer.com/10.1007/BF00311975

[134] S. Parsons, "Introduction to twinning," *Acta Crystallogr. - Sect. D Biol. Crystallogr.*, vol. 59, no. 11, pp. 1995–2003, 2003.

[135] G. Chapuis and A. Authier, "Online Dictionary of Crystallography," 2021. [Online]. Available: https://dictionary.iucr.org/

[136] G. Gottstein, *Physical Foundations of Materials Science*. Berlin, Heidelberg: Springer Berlin Heidelberg, 2004. [Online]. Available: http://link.springer.com/10.1007/978-3-662-09291-0

[137] B. Roos, B. Kapelle, G. Richter, and C. A. Volkert, "Surface dislocation nucleation controlled deformation of Au nanowires," *Appl. Phys. Lett.*, vol. 105, no. 20, p. 201908, nov 2014. [Online]. Available: http://aip.scitation.org/doi/10.1063/1.4902313

[138] J. Hornstra, "Dislocations, stacking faults and twins in the spinel structure," *J. Phys. Chem. Solids*, vol. 15, no. 3-4, pp. 311–323, 1960. [Online]. Available: http://linkinghub.elsevier.com/retrieve/pii/0022369760902547

[139] S. Drev, A. Rečnik, and N. Daneu, "Twinning and epitaxial growth of taaffeite-type modulated structures in BeO-doped MgAl2O4," *CrystEngComm*, vol. 15, no. 14, p. 2640, 2013. [Online]. Available: http://xlink.rsc.org/?DOI=c3ce26997c

[140] D. Dunne, "Martensite," *Metals (Basel).*, vol. 8, no. 6, 2018.

[141] B. C. Muddle, J. F. Nie, and G. R. Hugo, "Application of the theory of martensite crystallography to displacive phase transformations in substitutional nonferrous alloys," *Metall. Mater. Trans. A*, vol. 25, no. 9, pp. 1841–1856, 1994.

[142] J. W. Christian, G. B. Olson, and M. Cohen, "Classification of Displacive Transformations : What is a Martensitic Transformation ?" *Le J. Phys. IV*, vol. 05, no. C8, pp. C8–3–C8–10, dec 1995. [Online]. Available: http://www.edpsciences.org/10.1051/jp4:1995801

[143] J. A. Klostermann, "The concept of the habit plane and the phenomenological theories of the martensite transformation," *J. Less-Common Met.*, vol. 28, no. 1, pp. 75–94, 1972.

[144] Z. Zhang, R. D. James, and S. Müller, "Energy barriers and hysteresis in martensitic phase transformations," *Acta Mater.*, vol. 57, no. 15, pp. 4332–4352, 2009.

[145] E. Hornbogen, "Review Thermo-mechanical fatigue of shape memory alloys," *J. Mater. Sci.*, vol. 39, no. 2, pp. 385–399, 2004.

[146] K. Bhattacharya, S. Conti, G. Zanzotto, and J. Zimmer, "Crystal symmetry and the reversibility of martensitic transformations," *Nature*, vol. 428, no. 6978, pp. 55–59, 2004.

[147] W. Grogger, F. Hofer, G. Kothleitner, and B. Schaffer, "An introduction to high-resolution EELS in transmission electron microscopy," *Top. Catal.*, vol. 50, no. 1-4, pp. 200–207, 2008.

[148] D. B. Williams and C. B. Carter, "Transmission Electron Microscopy: A Textbook for Materials Science," in *Mater. Sci.*, 2nd ed. Springer, 2009, vol. V1-V4, p. 760. [Online]. Available: http://www.loc.gov/catdir/enhancements/fy0820/96028435-d.html

[149] R. Egerton, *Electron Energy-Loss Spectroscopy in the Electron Microscope*. Boston, MA: Springer US, 2011. [Online]. Available: http://link.springer.com/10.1007/978-1-4419-9583-4{%}5Cnhttp://www.springerlink.com/index/10.1007/978-1-4419-9583-4http://link.springer.com/10.1007/978-1-4419-9583-4

[150] C. C. Ahn, Ed., *Transmission Electron Energy Loss Spectrometry in Materials Science and The EELS Atlas*. Weinheim, FRG: Wiley, sep 2004. [Online]. Available: http://doi.wiley.com/10.1002/3527605495https://onlinelibrary.wiley.com/doi/book/10.1002/3527605495

[151] J. A. Mundy, Q. Mao, C. M. Brooks, D. G. Schlom, and D. A. Muller, "Atomic-resolution chemical imaging of oxygen local bonding environments by electron energy loss spectroscopy," *Appl. Phys. Lett.*, vol. 101, no. 4, 2012.

[152] J. Rodríguez-Carvajal, G. Rousse, C. Masquelier, and M. Hervieu, "Electronic Crystallization in a Lithium Battery Material: Columnar Ordering of Electrons and Holes in the Spinel LiMn2O4," *Phys. Rev. Lett.*, vol. 81, no. 21, pp. 4660–4663, nov 1998. [Online]. Available: https://link.aps.org/doi/10.1103/PhysRevLett.81.4660

[153] M. Okubo, Y. Mizuno, H. Yamada, J. Kim, E. Hosono, H. Zhou, T. Kudo, and I. Honma, "Fast Li-ion insertion into nanosized LiMn2O4 without domain boundaries," *ACS Nano*, vol. 4, no. 2, pp. 741–752, 2010.

[154] A. Mosbah, A. Verbaere, and M. Tournoux, "Phases LixMnO2λ rattachees au type spinelle," *Mater. Res. Bull.*, vol. 18, no. 11, pp. 1375–1381, nov 1983. [Online]. Available: https://linkinghub.elsevier.com/retrieve/pii/0025540883900454

[155] L. Laffont, C. Delacourt, P. Gibot, M. Y. Wu, P. Kooyman, C. Masquelier, and J. M. Tarascon, "Study of the LiFePO 4 /FePO 4 Two-Phase System by High-Resolution Electron Energy Loss Spectroscopy," *Chem. Mater.*, vol. 18, no. 23, pp. 5520–5529, nov 2006. [Online]. Available: http://pubs.acs.org/doi/abs/10.1021/cm0617182

[156] H. Ohnishi, Y. Kondo, and K. Takayanagi, "Quantized conductance through individual rows of suspended gold atoms," *Nature*, vol. 395, no. 6704, pp. 780–783, oct 1998. [Online]. Available: http://www.nature.com/articles/27399

[157] M. W. Larsson, L. R. Wallenberg, A. I. Persson, and L. Samuelson, "Probing of Individual Semiconductor Nanowhiskers by TEM-STM," *Microsc. Microanal.*, vol. 10, no. 1, pp. 41–46, 2004.

[158] J. Y. Huang, L. Zhong, C. M. Wang, J. P. Sullivan, W. Xu, L. Q. Zhang, S. X. Mao, N. S. Hudak, X. H. Liu, A. Subramanian, H. Fan, L. Qi, A. Kushima, and J. Li, "In Situ Observation of the Electrochemical Lithiation of a Single SnO2 Nanowire Electrode," *Science (80-.).*, vol. 330, no. 6010, pp. 1515–1520, dec 2010. [Online]. Available: http://www.sciencemag.org/cgi/doi/10.1126/science.1195628

[159] X. H. Liu, L. Q. Zhang, L. Zhong, Y. Liu, H. Zheng, J. W. Wang, J. H. Cho, S. A. Dayeh, S. T. Picraux, J. P. Sullivan, S. X. Mao, Z. Z. Ye, and J. Y. Huang, "Ultrafast electrochemical lithiation of individual Si nanowire anodes," *Nano Lett.*, vol. 11, no. 6, pp. 2251–2258, 2011.

[160] L. Zhong, X. H. Liu, G. F. Wang, S. X. Mao, and J. Y. Huang, "Multiple-stripe lithiation mechanism of individual SnO2 nanowires in a flooding geometry," *Phys. Rev. Lett.*, vol. 106, no. 24, pp. 18–21, 2011.

[161] M. Gu, Y. Li, X. Li, S. Hu, X. Zhang, W. Xu, S. Thevuthasan, D. R. Baer, J.-G. Zhang, J. Liu, and C. Wang, "In Situ TEM Study of Lithiation Behavior of Silicon Nanoparticles Attached to and Embedded in a Carbon Matrix," *ACS Nano*, vol. 6, no. 9, pp. 8439–8447, sep 2012. [Online]. Available: http://pubs.acs.org/doi/abs/10.1021/nn303312m

[162] X. H. Liu, Y. Liu, A. Kushima, S. Zhang, T. Zhu, J. Li, and J. Y. Huang, "In Situ TEM Experiments of Electrochemical Lithiation and Delithiation of Individual Nanostructures," *Adv. Energy Mater.*, vol. 2, no. 7, pp. 722–741, jul 2012. [Online]. Available: http://doi.wiley.com/10.1002/aenm.201200024

[163] X. H. Liu, S. Huang, S. T. Picraux, J. Li, T. Zhu, and J. Y. Huang, "Reversible Nanopore Formation in Ge Nanowires during Lithiation–Delithiation Cycling: An In Situ Transmission Electron Microscopy Study," *Nano Lett.*, vol. 11, no. 9, pp. 3991–3997, sep 2011. [Online]. Available: http://pubs.acs.org/doi/abs/10.1021/nl2024118

[164] Y. Liu, N. S. Hudak, D. L. Huber, S. J. Limmer, J. P. Sullivan, and J. Y. Huang, "In situ transmission electron microscopy observation of pulverization of aluminum nanowires and evolution of the thin surface Al2O3 layers during lithiation-delithiation cycles," *Nano Lett.*, vol. 11, no. 10, pp. 4188–4194, 2011.

[165] X. H. Liu and J. Y. Huang, "In situ TEM electrochemistry of anode materials in lithium ion batteries," *Energy Environ. Sci.*, vol. 4, no. 10, p. 3844, 2011. [Online]. Available: http://xlink.rsc.org/?DOI=c1ee01918j

[166] X. H. Liu, H. Zheng, L. Zhong, S. Huang, K. Karki, L. Q. Zhang, Y. Liu, A. Kushima, W. T. Liang, J. W. Wang, J.-H. Cho, E. Epstein, S. A. Dayeh, S. T. Picraux, T. Zhu, J. Li, J. P. Sullivan, J. Cumings, C. Wang, S. X. Mao, Z. Z. Ye, S. Zhang, and J. Y. Huang, "Anisotropic Swelling and Fracture of Silicon Nanowires during Lithiation," *Nano Lett.*, vol. 11, no. 8, pp. 3312–3318, aug 2011. [Online]. Available: http://pubs.acs.org/doi/abs/10.1021/nl201684d

[167] Y. Zhu, J. W. Wang, Y. Liu, X. H. Liu, A. Kushima, Y. Liu, Y. Xu, S. X. Mao, J. Li, C. Wang, and J. Y. Huang, "In Situ Atomic-Scale Imaging of Phase Boundary Migration in FePO 4 Microparticles During Electrochemical Lithiation," *Adv. Mater.*, vol. 25, no. 38, pp. 5461–5466, oct 2013. [Online]. Available: http://doi.wiley.com/10.1002/adma.201301374

[168] J. Niu, A. Kushima, X. Qian, L. Qi, K. Xiang, Y.-M. Chiang, and J. Li, "In situ observation of random solid solution zone in LiFePO4 electrode." *Nano Lett.*, vol. 14, no. 7, pp. 4005–10, 2014. [Online]. Available: http://dx.doi.org/10.1021/nl501415b

[169] Y. Yuan, A. Nie, S. Santhanagopalan, D. Desheng Meng, and R. Shahbazian-Yassar, "In-situ TEM Study on Electrochemical Behavior of α-MnO2 Nanowire," *Microsc. Microanal.*, vol. 20, no. S3, pp. 496–497, aug 2014. [Online]. Available: http://www.journals.cambridge.org/abstract{_}S1431927614004206

[170] F. Wang, J. Graetz, M. S. Moreno, C. Ma, L. Wu, V. Volkov, Y. Zhu, W. E. T. Al, F. Wang, J. Graetz, M. S. Moreno, C. Ma, L. Wu, V. Volkov, and Y. Zhu, "Chemical distribution and bonding of lithium in intercalated graphite: Identification with optimized electron energy loss spectroscopy," *ACS Nano*, vol. 5, no. 2, pp. 1190–1197, feb 2011. [Online]. Available: http://pubs.acs.org/doi/abs/10.1021/nn1028168http://pubs.acs.org/doi/10.1021/nn1028168https://pubs.acs.org/doi/10.1021/nn1028168

[171] X. H. Liu, L. Zhong, S. Huang, S. X. Mao, T. Zhu, and J. Y. Huang, "Size-dependent fracture of silicon nanoparticles during lithiation," *ACS Nano*, vol. 6, no. 2, pp. 1522–1531, 2012.

[172] F. Wang, S.-W. Kim, L. Wu, D. Su, Y. Zhu, and J. Graetz, "In situ TEM-EELS For Tracking Lithium Reactions in Battery Electrodes," *Microsc. Microanal.*, vol. 19, no. S2, pp. 1490–1491, 2013.

[173] K. Yamamoto, Y. Iriyama, T. Asaka, T. Hirayama, H. Fujita, C. A. Fisher, K. Nonaka, Y. Sugita, and Z. Ogumi, "Dynamic visualization of the electric potential in an all-solid-state rechargeable lithium battery," *Angew. Chemie - Int. Ed.*, vol. 49, no. 26, pp. 4414–4417, 2010.

[174] K. Yamamoto, Y. Iriyama, and T. Hirayama, "Operando observations of solid-state electrochemical reactions in Li-ion batteries by spatially resolved TEM EELS and electron holography," *Microscopy*, vol. 66, no. 1, pp. 50–61, oct 2016. [Online]. Available: https://academic.oup.com/jmicro/article/2645982/Operando-observations-of-solidstate

[175] Y. S. Meng, T. McGilvray, M.-C. Yang, D. Gostovic, F. Wang, D. Zeng, Y. Zhu, and J. Graetz, "In Situ Analytical Electron Microscopy for Probing Nanoscale Electrochemistry," *Interface Mag.*, vol. 20, no. 3, pp. 49–53, 2016.

[176] D. Santhanagopalan, D. Qian, T. McGilvray, Z. Wang, F. Wang, F. Camino, J. Graetz, N. Dudney, and Y. S. Meng, "Interface limited lithium transport in solid-state batteries," *J. Phys. Chem. Lett.*, vol. 5, no. 2, pp. 298–303, 2014.

[177] Y. Gong, Y. Chen, Q. Zhang, F. Meng, J. A. Shi, X. Liu, X. Liu, J. Zhang, H. Wang, J. Wang, Q. Yu, Z. Zhang, Q. Xu, R. Xiao, Y. S. Hu, L. Gu, H. Li, X. Huang, and L. Chen, "Three-dimensional atomic-scale observation of structural evolution of cathode

material in a working all-solid-state battery," *Nat. Commun.*, vol. 9, no. 1, pp. 1–8, 2018. [Online]. Available: http://dx.doi.org/10.1038/s41467-018-05833-x

[178] R. R. Unocic, X.-G. Sun, R. L. Sacci, L. a. Adamczyk, D. H. Alsem, S. Dai, N. J. Dudney, and K. L. More, "Direct Visualization of Solid Electrolyte Interphase Formation in Lithium-Ion Batteries with In Situ Electrochemical Transmission Electron Microscopy," *Microsc. Microanal.*, vol. 20, no. 04, pp. 1029–1037, aug 2014. [Online]. Available: http://www.ncbi.nlm.nih.gov/pubmed/24994021http://www.journals.cambridge.org/abstract{_}S1431927614012744

[179] P. Abellan, B. L. Mehdi, L. R. Parent, M. Gu, C. Park, W. Xu, Y. Zhang, I. Arslan, J.-G. Zhang, C.-M. Wang, J. E. Evans, and N. D. Browning, "Probing the Degradation Mechanisms in Electrolyte Solutions for Li-Ion Batteries by in Situ Transmission Electron Microscopy," *Nano Lett.*, vol. 14, no. 3, pp. 1293–1299, mar 2014. [Online]. Available: http://dx.doi.org/10.1021/nl404271khttp://pubs.acs.org/doi/abs/10.1021/nl404271k

[180] Z. Zeng, X. Zhang, K. Bustillo, K. Niu, C. Gammer, J. Xu, and H. Zheng, "In Situ Study of Lithiation and Delithiation of MoS<inf>2</inf> Nanosheets Using Electrochemical Liquid Cell Transmission Electron Microscopy," *Nano Lett.*, vol. 15, no. 8, pp. 5214–5220, 2015.

[181] H. Yamaguchi, A. Yamada, and H. Uwe, "Jahn-Teller transition of LiMn2O4 studied by x-ray-absorption spectroscopy," *Phys. Rev. B*, vol. 58, no. 1, pp. 8–11, jul 1998. [Online]. Available: http://link.aps.org/doi/10.1103/PhysRevB.58.8

[182] S. Kobayashi, I. R. M. Kottegoda, Y. Uchimoto, and M. Wakihara, "XANES and EXAFS analysis of nano-size manganese dioxide as a cathode material for lithium-ion batteries," *J. Mater. Chem.*, vol. 14, no. 12, p. 1843, 2004. [Online]. Available: http://xlink.rsc.org/?DOI=b315443b

[183] R. Qiao, T. Chin, S. J. Harris, S. Yan, and W. Yang, "Spectroscopic fingerprints of valence and spin states in manganese oxides and fluorides," *Curr. Appl. Phys.*, vol. 13, no. 3, pp. 544–548, may 2013. [Online]. Available: http://linkinghub.elsevier.com/retrieve/pii/S1567173912003951

[184] N. Nagamura, S. Ito, K. Horiba, T. Shinohara, M. Oshima, S.-i. Nishimura, A. Yamada, and N. Mizuno, "Spectromicroscopic analysis of lithium intercalation in spinel LiMn\n 2\n O\n 4\n for lithium-ion battery by 3D nano-ESCA," *J. Phys. Conf. Ser.*, vol. 502, p. 012013, 2014. [Online]. Available: http://stacks.iop.org/1742-6596/502/i=1/a=012013?key=crossref.36edeee1f9cfd2b2cc49dcf41b923a7f

[185] D. Tang, Y. Sun, Z. Yang, L. Ben, L. Gu, and X. Huang, "Surface Structure Evolution of LiMn 2 O 4 Cathode Material upon Charge/Discharge," *Chem. Mater.*, vol. 26, no. 11, pp. 3535–3543, jun 2014. [Online]. Available: http://pubs.acs.org/doi/10.1021/cm501125e

[186] S. Kuppan, Y. Xu, Y. Liu, and G. Chen, "Phase transformation mechanism in lithium manganese nickel oxide revealed by single-crystal hard X-ray microscopy," *Nat. Commun.*, vol. 8, pp. 1–10, 2017. [Online]. Available: http://dx.doi.org/10.1038/ncomms14309

[187] J. Lim, Y. Li, D. H. Alsem, H. So, S. C. Lee, P. Bai, D. A. Cogswell, X. Liu, N. Jin, Y.-s. Yu, N. J. Salmon, D. A. Shapiro, M. Z. Bazant, T. Tyliszczak, and W. C. Chueh, "Origin and hysteresis of lithium compositional spatiodynamics within battery primary particles," *Science (80-.).*, vol. 353, no. 6299, pp. 566–571, aug 2016. [Online]. Available: http://www.sciencemag.org/lookup/doi/10.1126/science.aaf4914https://www.sciencemag.org/lookup/doi/10.1126/science.aaf4914

[188] B. Pfeiffer, "In-situ Deinterkalation von Lithiummanganoxid mittels Atomsondentomographie," Promotion, Universität Göttingen, 2017.

[189] J. Maier, "Mikrostruktur von Lithium-Mangan-Oxid," Promotion, Universität Göttingen, 2016.

[190] D. C. Joy, D. E. Newbury, and D. L. Davidson, "Electron channeling patterns in the scanning electron microscope," *J. Appl. Phys.*, vol. 53, no. 8, 1982.

[191] I. Gutierrez-Urrutia, S. Zaefferer, and D. Raabe, "Electron channeling contrast imaging of twins and dislocations in twinning-induced plasticity steels under controlled diffraction conditions in a scanning electron microscope," *Scr. Mater.*, vol. 61, no. 7, pp. 737–740, oct 2009. [Online]. Available: http://dx.doi.org/10.1016/j.scriptamat.2009.06.018http://linkinghub.elsevier.com/retrieve/pii/S1359646209004199

[192] ——, "Coupling of Electron Channeling with EBSD: Toward the Quantitative Characterization of Deformation Structures in the SEM," *JOM*, vol. 65, no. 9, pp. 1229–1236, sep 2013.

[193] R. Benedek and M. M. Thackeray, "Simulation of the surface structure of lithium manganese oxide spinel SURFACES," *Phys. Rev. B*, vol. 83, no. May, pp. 1–8, 2011. [Online]. Available: http://link.aps.org/doi/10.1103/PhysRevB.83.195439

[194] J.-S. Kim, K. Kim, W. Cho, W. H. Shin, R. Kanno, and J. W. Choi, "A Truncated Manganese Spinel Cathode for Excellent Power and Lifetime in Lithium-Ion Batteries," *Nano Lett.*, vol. 12, no. 12, pp. 6358–6365, dec 2012. [Online]. Available: http://pubs.acs.org/doi/10.1021/nl303619s

[195] C. Jiang, Z. Tang, S. Wang, and Z. Zhang, "A truncated octahedral spinel LiMn 2 O 4 as high-performance cathode material for ultrafast and long-life lithium-ion batteries," *J. Power Sources*, vol. 357, pp. 144–148, jul 2017. [Online]. Available: http://dx.doi.org/10.1016/j.jpowsour.2017.04.079http://linkinghub.elsevier.com/retrieve/pii/S037877531730575X

[196] M. Baumung, F. Schönewald, T. Erichsen, C. A. Volkert, and M. Risch, "Influence of particle size on the apparent electrocatalytic activity of LiMn2O4 for oxygen evolution," *Sustain. Energy Fuels*, vol. 3, no. 9, pp. 2218–2226, 2019. [Online]. Available: http://xlink.rsc.org/?DOI=C8SE00551F

[197] K. Svensson, Y. Jompol, H. Olin, and E. Olsson, "Compact design of a transmission electron microscope-scanning tunneling microscope holder with three-dimensional coarse motion," *Rev. Sci. Instrum.*, vol. 74, no. 11, pp. 4945–4947, 2003.

[198] T. Wuttke, "TEM in-situ Untersuchungen an Ti-Ni basierten Formgedächtnislegierungen," Dissertation, Georg-August-Universität Göttingen, 2018.

[199] A. Kelling, K. R. Mangipudi, I. Knorr, T. Liese, H.-U. Krebs, and C. A. Volkert, "Investigating fracture of nanoscale metal–ceramic multilayers in the transmission electron microscope," *Scr. Mater.*, vol. 115, pp. 42–45, apr 2016. [Online]. Available: https://linkinghub.elsevier.com/retrieve/pii/S1359646215300981

[200] T. Kramer, M. Scherff, D. Mierwaldt, J. Hoffmann, and C. Jooss, "Role of oxygen vacancies for resistive switching in noble metal sandwiched Pr 0.67 Ca 0.33 MnO 3-δ," *Appl. Phys. Lett.*, vol. 110, no. 24, p. 243502, jun 2017. [Online]. Available: http://aip.scitation.org/doi/10.1063/1.4985645

[201] T. Wuttke, "TEM in-situ Lithiierung von Silicium," Masterarbeit, Universität Göttingen, 2012.

[202] S. Mildner, M. Beleggia, D. Mierwaldt, T. W. Hansen, J. B. Wagner, S. Yazdi, T. Kasama, J. Ciston, Y. Zhu, and C. Jooss, "Environmental TEM Study of Electron Beam Induced Electrochemistry of Pr0.64Ca0.36MnO3 Catalysts for Oxygen Evolution," *J. Phys. Chem. C*, vol. 119, no. 10, pp. 5301–5310, mar 2015. [Online]. Available: http://pubs.acs.org/doi/10.1021/jp511628c

[203] J. H. Paterson and O. L. Krivanek, "Elnes of 3d transition-metal oxides," *Ultramicroscopy*, vol. 32, no. 4, pp. 319–325, 1990. [Online]. Available: http://www.sciencedirect.com/science/article/pii/030439919090078Z

[204] R. F. Egerton, "Electron energy-loss spectroscopy in the TEM," *Reports Prog. Phys.*, vol. 72, no. 1, p. 016502, 2008.

[205] M. K. Kinyanjui, P. Axmann, M. Wohlfahrt-Mehrens, P. Moreau, F. Boucher, U. Kaiser, M. K. K. Kaiser, P. Axmann, M. Wohlfahrt-Mehrens, P. Moreau, F. Boucher, and U, "Origin of valence and core excitations in LiFePO 4 and FePO 4," *J. Phys. Condens. Matter*, vol. 22, no. 27, p. 275501, jul 2010. [Online]. Available: http://stacks.iop.org/0953-8984/22/i=27/a=275501http://stacks.iop.org/0953-8984/22/i=27/a=275501?key=crossref.56361df1896adab6788d8ca234bc3d16

[206] M. K. Kinyanjui, P. Axmann, M. Mancini, G. Gabrielli, P. Balasubramanian, F. Boucher, M. Wohlfahrt-Mehrens, and U. Kaiser, "Understanding the spectroscopic signatures of Mn valence changes in the valence energy loss spectra of Li-Mn-Ni-O spinel oxides," *Phys. Rev. Mater.*, vol. 1, no. 7, p. 074402, dec 2017. [Online]. Available: https://link.aps.org/doi/10.1103/PhysRevMaterials.1.074402

[207] S. Kobayashi, C. A. J. Fisher, A. Kuwabara, Y. Ukyo, and Y. Ikuhara, "Quantitative analysis of Li distributions in battery material Li1-xFePO4 using Fe M2,3-edge and valence electron energy loss spectra," *J. Electron Microsc. (Tokyo).*, vol. 66, no. 4, pp. 254–260, 2017. [Online]. Available: https://academic.oup.com/jmicro/article/66/4/254/3738799

[208] X. Mu, A. Kobler, D. Wang, V. Chakravadhanula, S. Schlabach, D. Szabó, P. Norby, and C. Kübel, "Comprehensive analysis of TEM methods for LiFePO4/FePO4 phase mapping: spectroscopic techniques (EFTEM, STEM-EELS) and STEM diffraction techniques (ACOM-TEM)," *Ultramicroscopy*, vol. 170, pp. 10–18, nov 2016. [Online]. Available: http://linkinghub.elsevier.com/retrieve/pii/S0304399116301012

[209] H. Kurata and C. Colliex, "Electron-energy-loss core-edge structures in manganese oxides," *Phys. Rev. B*, vol. 48, no. 4, pp. 2102–2108, 1993.

[210] J. Graetz, C. C. Ahn, R. Yazami, and B. Fultz, "An Electron Energy-Loss Spectrometry Study of Charge Compensation in LiNi 0.8 Co 0.2 O 2," *J. Phys. Chem. B*, vol. 107, no. 13, pp. 2887–2891, apr 2003. [Online]. Available: http://pubs.acs.org/doi/abs/10.1021/jp026484y

[211] T. Akita and N. Taguchi, "Practical analysis of Li distribution by EELS," *Surf. Interface Anal.*, vol. 48, no. 11, pp. 1226–1230, 2016.

[212] P. Gao, R. Ishikawa, E. Tochigi, A. Kumamoto, N. Shibata, and Y. Ikuhara, "Atomic-Scale Tracking of a Phase Transition from Spinel to Rocksalt in Lithium Manganese Oxide," *Chem. Mater.*, vol. 29, no. 3, pp. 1006–1013, feb 2017. [Online]. Available: http://www.journals.cambridge.org/abstract{_}S1431927615002469https://pubs.acs.org/doi/10.1021/acs.chemmater.6b03659

[213] D. Mierwaldt, S. Mildner, R. Arrigo, A. Knop-Gericke, E. Franke, A. Blumenstein, J. Hoffmann, and C. Jooss, "In Situ XANES/XPS Investigation of Doped Manganese Perovskite Catalysts," *Catalysts*, vol. 4, no. 4, pp. 129–145, apr 2014. [Online]. Available: http://www.mdpi.com/2073-4344/4/2/129/http://www.mdpi.com/2073-4344/4/2/129

[214] M. Varela, M. P. Oxley, W. Luo, J. Tao, M. Watanabe, A. R. Lupini, S. T. Pantelides, and S. J. Pennycook, "Atomic-resolution imaging of oxidation states in manganites," *Phys. Rev. B*, vol. 79, no. 8, p. 085117, feb 2009. [Online]. Available: https://link.aps.org/doi/10.1103/PhysRevB.79.085117

[215] L. Garvie and A. Craven, "High-resolution parallel electron energy-loss spectroscopy of Mn L2,3-edges in inorganic manganese compounds," *Phys. Chem. Miner.*, vol. 21, no. 4, pp. 191–206, aug 1994. [Online]. Available: http://link.springer.com/10.1007/BF00202132

[216] P. A. van Aken and B. Liebscher, "Quantification of ferrous/ferric ratios in minerals: new evaluation schemes of Fe L 23 electron energy-loss near-edge spectra," *Phys. Chem. Miner.*, vol. 29, no. 3, pp. 188–200, apr 2002. [Online]. Available: http://link.springer.com/10.1007/s00269-001-0222-6

[217] H. Tan, J. Verbeeck, A. M. Abakumov, and G. Van Tendeloo, "Oxidation state and chemical shift investigation in transition metal oxides by EELS," *Ultramicroscopy*, vol. 116, pp. 24–33, 2012. [Online]. Available: http://dx.doi.org/10.1016/j.ultramic.2012.03.002

[218] T. Riedl, T. Gemming, and K. Wetzig, "Extraction of EELS white-line intensities of manganese compounds: Methods, accuracy, and valence sensitivity," *Ultramicroscopy*, vol. 106, no. 4-5, pp. 284–291, mar 2006. [Online]. Available: http://linkinghub.elsevier.com/retrieve/pii/S0304399105002147

[219] X. Gao, Y. H. Ikuhara, C. A. Fisher, H. Moriwake, A. Kuwabara, H. Oki, K. Kohama, R. Yoshida, R. Huang, and Y. Ikuhara, "Structural Distortion and Compositional Gradients Adjacent to Epitaxial LiMn<inf>2</inf>O<inf>4</inf> Thin Film Interfaces," *Adv. Mater. Interfaces*, vol. 1, no. 8, pp. 1–10, 2014.

[220] D. B. Loomer, T. A. Al, L. Weaver, and S. Cogswell, "Manganese valence imaging in Mn minerals at the nanoscale using STEM-EELS," *Am. Mineral.*, vol. 92, no. 1, pp. 72–79, jan 2007. [Online]. Available: http://ammin.geoscienceworld.org/cgi/doi/10.2138/am.2007.2252https://pubs.geoscienceworld.org/ammin/article/92/1/72-79/134305

[221] J. Graetz, C. C. Ahn, H. Ouyang, P. Rez, and B. Fultz, "White lines and d -band occupancy for the 3 d transition-metal oxides and lithium transition-metal oxides," *Phys. Rev. B*, vol. 235103, no. 69, pp. 1–6, 2004.

[222] Z. L. Wang, J. Bentley, and N. D. Evans, "Valence state mapping of cobalt and manganese using near-edge fine structures," *Micron*, vol. 31, no. 4, pp. 355–362, 2000.

[223] V. Mauchamp, F. Boucher, G. Ouvrard, and P. Moreau, "Ab initio simulation of the electron energy-loss near-edge structures at the Li K edge in Li, Li 2 O , and Li Mn 2 O 4," *Phys. Rev. B*, vol. 74, no. 11, p. 115106, sep 2006. [Online]. Available: http://link.aps.org/doi/10.1103/PhysRevB.74.115106

[224] F. Espinosa-Magaña, L. Alvarez-Contreras, O. Morales-Rivera, M. Ochoa-Lara, S. Loya-Mancilla, and A. Aguilar-Elguezabal, "Electron energy-loss spectroscopy of LiMn2O4, LiMn1.6Ti0.4O4 and LiMn1.5Ni0.5O4," *J. Phys. Chem. Solids*, vol. 70, no. 6, pp. 972–977, jun 2009. [Online]. Available: http://linkinghub.elsevier.com/retrieve/pii/S0022369709000997

[225] J. Cho and M. M. Thackeray, "Structural Changes of LiMn2O4 Spinel Electrodes during Electrochemical Cycling," *J. Electrochem. Soc.*, vol. 146, no. 10, p. 3577, 1999.

[226] Y.-I. Jang, "Electrochemical Cycling-Induced Spinel Formation in High-Charge-Capacity Orthorhombic LiMnO2," *J. Electrochem. Soc.*, vol. 146, no. 9, p. 3217, 1999. [Online]. Available: http://jes.ecsdl.org/cgi/doi/10.1149/1.1392457

[227] X. Hao, X. Lin, W. Lu, and B. M. Bartlett, "Oxygen Vacancies Lead to Loss of Domain Order, Particle Fracture, and Rapid Capacity Fade in Lithium Manganospinel (LiMn2O4) Batteries," *ACS Appl. Mater. Interfaces*, vol. 6, no. 14, pp. 10 849–10 857, jul 2014. [Online]. Available: http://pubs.acs.org/doi/10.1021/am500671e

[228] S.-H. Kang, J. B. Goodenough, and L. K. Rabenberg, "Nanocrystalline Lithium Manganese Oxide Spinel Cathode for Rechargeable Lithium Batteries," *Electrochem. Solid-State Lett.*, vol. 4, no. 5, p. A49, 2001. [Online]. Available: http://esl.ecsdl.org/cgi/doi/10.1149/1.1357696

[229] J. H. Rask, B. A. Miner, and P. R. Buseck, "Determination of manganese oxidation states in solids by electron energy-loss spectroscopy," *Ultramicroscopy*, vol. 21, no. 4, pp. 321–326, jan 1987. [Online]. Available: http://linkinghub.elsevier.com/retrieve/pii/0304399187900301

[230] F. M. De Groot, M. Grioni, J. C. Fuggle, J. Ghijsen, G. A. Sawatzky, and H. Petersen, "Oxygen 1s X-ray-absorption edges of transition-metal oxides," *Phys. Rev. B*, vol. 40, no. 8, pp. 5715–5723, 1989.

[231] J. Maier, B. Pfeiffer, C. A. Volkert, and C. Nowak, "Three-Dimensional Microstructural Characterization of Lithium Manganese Oxide with Atom Probe Tomography," *Energy Technol.*, vol. 4, no. 12, pp. 1565–1574, dec 2016. [Online]. Available: http://doi.wiley.com/10.1002/ente.201600210

[232] B. Pfeiffer, J. Maier, J. Arlt, and C. Nowak, "In Situ Atom Probe Deintercalation of Lithium-Manganese-Oxide," *Microsc. Microanal.*, vol. 23, no. 02, pp. 314–320, apr 2017. [Online]. Available: https://www.cambridge.org/core/product/identifier/S1431927616012691/type/journal{_}article

[233] C. Zener, "Theory of Growth of Spherical Precipitates from Solid Solution," *J. Appl. Phys.*, vol. 20, no. 10, pp. 950–953, oct 1949. [Online]. Available: http://aip.scitation.org/doi/10.1063/1.1698258

[234] Y. Horibe, S. Takeyama, and S. Mori, "Large-scale phase separation with nano-twin domains in manganite spinel (Co,Fe,Mn)3O4," in *AIP Conf. Proc.*, vol. 050005, 2016, p. 050005. [Online]. Available: http://aip.scitation.org/doi/abs/10.1063/1.4961358

[235] J. J. Couderc, S. Fritsch, M. Brieu, G. Vanderschaeve, M. Fagot, and A. Rousset, "A transmission electron microscopy study of lattice defects in Mn3O4 hausmannite," *Philos. Mag. B*, vol. 70, no. 5, pp. 1077–1094, nov 1994. [Online]. Available: https://www.tandfonline.com/doi/full/10.1080/01418639408240274

[236] J. Christensen and J. Newman, "A Mathematical Model of Stress Generation and Fracture in Lithium Manganese Oxide," *J. Electrochem. Soc.*, vol. 153, no. 6, p. A1019, 2006. [Online]. Available: http://jes.ecsdl.org/cgi/doi/10.1149/1.2185287

[237] A. F. Bower, P. R. Guduru, and E. Chason, "Analytical solutions for composition and stress in spherical elastic–plastic lithium-ion electrode particles containing a propagating phase boundary," *Int. J. Solids Struct.*, vol. 69-70, pp. 328–342, sep 2015. [Online]. Available: https://linkinghub.elsevier.com/retrieve/pii/S0020768315002280

[238] G. B. Olson, H. K. D. H. Bhadeshia, and M. Cohen, "Coupled diffusional/displacive transformations: Part II. Solute trapping," *Metall. Trans. A*, vol. 21, no. 3, pp. 805–809, 1990.

[239] N. B. Morgan and C. M. Friend, "A review of shape memory stability in NiTi alloys," *Le J. Phys. IV*, vol. 11, no. PR8, pp. Pr8–325–Pr8–332, 2001.

[240] A. R. Pelton, "Nitinol fatigue: A review of microstructures and mechanisms," *J. Mater. Eng. Perform.*, vol. 20, no. 4-5, pp. 613–617, 2011.

[241] X. Yang, L. Ma, and J. Shang, "Martensitic transformation of Ti50(Ni50-xCux) and Ni50(Ti50-xZrx) shape-memory alloys," *Sci. Rep.*, vol. 9, no. 1, pp. 1–8, 2019.

[242] C.-M. Wang, "In situ transmission electron microscopy and spectroscopy studies of rechargeable batteries under dynamic operating conditions: A retrospective and perspective view," *J. Mater. Res.*, vol. 30, no. 03, pp. 326–339, feb 2015. [Online]. Available: http://www.journals.cambridge.org/abstract{_}S0884291414002817

[243] M. Wohlfahrt-Mehrens, C. Vogler, and J. Garche, "Aging mechanisms of lithium cathode materials," *J. Power Sources*, vol. 127, no. 1-2, pp. 58–64, mar 2004. [Online]. Available: https://linkinghub.elsevier.com/retrieve/pii/S0378775303009376

[244] D. J. Larson, D. T. Foord, A. K. Petford-Long, H. Liew, M. G. Blamire, A. Cerezo, and G. D. W. Smith, "Field-ion specimen preparation using focused ion-beam milling," *Ultramicroscopy*, vol. 79, no. 1-4, pp. 287–293, sep 1999. [Online]. Available: http://linkinghub.elsevier.com/retrieve/pii/S0304399199000558

[245] K. Momma and F. Izumi, "VESTA 3 for three-dimensional visualization of crystal, volumetric and morphology data," *J. Appl. Crystallogr.*, vol. 44, no. 6, pp. 1272–1276, dec 2011. [Online]. Available: http://scripts.iucr.org/cgi-bin/paper?S0021889811038970

[246] J. Schindelin, I. Arganda-Carreras, E. Frise, V. Kaynig, M. Longair, T. Pietzsch, S. Preibisch, C. Rueden, S. Saalfeld, B. Schmid, J.-Y. Tinevez, D. J. White, V. Hartenstein, K. Eliceiri, P. Tomancak, and A. Cardona, "Fiji: an open-source platform for biological-image analysis," *Nat. Methods*, vol. 9, no. 7, pp. 676–682, jul 2012. [Online]. Available: http://www.nature.com/articles/nmeth.2019

[247] B. Pfeiffer, T. Erichsen, E. Epler, C. A. Volkert, P. Trompenaars, and C. Nowak, "Characterization of Nanoporous Materials with Atom Probe Tomography," *Microsc. Microanal.*, vol. 21, no. 3, pp. 557–563, jun 2015. [Online]. Available: https://www.cambridge.org/core/product/identifier/S1431927615000501/type/journal{_}article

[248] N. Jiang, "On the in situ study of Li ion transport in transmission electron microscope," *J. Mater. Res.*, vol. 30, no. 03, pp. 424–428, feb 2015. [Online]. Available: http://www.journals.cambridge.org/abstract{_}S0884291414003550

[249] S. Basak, J. Jansen, Y. Kabiri, and H. W. Zandbergen, "Towards optimization of experimental parameters for studying Li-O 2 battery discharge products in TEM using in situ EELS," *Ultramicroscopy*, vol. 188, pp. 52–58, may 2018. [Online]. Available: https://doi.org/10.1016/j.ultramic.2018.03.005http://linkinghub.elsevier.com/retrieve/pii/S0304399117304448

[250] F. Beuneu, P. Vajda, G. Jaskierowicz, and M. Lafleurielle, "Formation of two kinds of non-spherical lithium colloids in electron-irradiatedO single crystals," *Phys. Rev. B - Condens. Matter Mater. Phys.*, vol. 55, no. 17, pp. 11 263–11 269, 1997.

[251] P. J. Phillips, H. Iddir, D. P. Abraham, and R. F. Klie, "Direct observation of the structural and electronic changes of Li2MnO3 during electron irradiation," *Appl. Phys. Lett.*, vol. 105, no. 11, p. 113905, sep 2014. [Online]. Available: http://scitation.aip.org/content/aip/journal/apl/105/11/10.1063/1.4896264http://aip.scitation.org/doi/10.1063/1.4896264

[252] J. M. Tarascon, "The Spinel Phase of LiMn2O4 as a Cathode in Secondary Lithium Cells," *J. Electrochem. Soc.*, vol. 138, no. 10, p. 2859, 1991. [Online]. Available: http://jes.ecsdl.org/cgi/doi/10.1149/1.2085330

[253] E. Levi, M. D. Levi, G. Salitra, D. Aurbach, R. Oesten, U. Heider, and L. Heider, "In situ XRD study of Li deintercalation from two different types of LiMn2O4 spinel," *Solid State Ionics*, vol. 126, no. 1, pp. 109–119, 1999.

[254] B. Put, P. M. Vereecken, N. Labyedh, A. Sepulveda, C. Huyghebaert, I. P. Radu, and A. Stesmans, "High Cycling Stability and Extreme Rate Performance in Nanoscaled LiMn 2 O 4 Thin Films," *ACS Appl. Mater. Interfaces*, vol. 7, no. 40, pp. 22 413–22 420, oct 2015. [Online]. Available: http://pubs.acs.org/doi/10.1021/acsami.5b06386

[255] D. Li and H. Zhou, "Two-phase transition of Li-intercalation compounds in Li-ion batteries," *Mater. Today*, vol. 17, no. 9, pp. 451–463, 2014.

[256] H. Liu, J. Wang, X. Zhang, D. Zhou, X. Qi, B. Qiu, J. Fang, R. Kloepsch, G. Schumacher, Z. Liu, and J. Li, "Morphological Evolution of High-Voltage Spinel LiNi 0.5 Mn 1.5 O 4 Cathode Materials for Lithium-Ion Batteries: The Critical Effects of Surface Orientations and Particle Size," *ACS Appl. Mater. Interfaces*, vol. 8, no. 7, pp. 4661–4675, feb 2016. [Online]. Available: http://pubs.acs.org/doi/10.1021/acsami.5b11389

[257] R. Arabolla Rodriguez, N. Della Santina Mohallem, M. Avila Santos, D. A. Sena Costa, L. Andrey Montoro, Y. Mosqueda Laffita, L. A. Tavera Carrasco, E. L. Perez-Cappe, R. Arabolla Rodríguez, N. Della Santina Mohallem, M. Avila Santos, D. A. Sena Costa, L. Andrey Montoro, Y. Mosqueda Laffita, L. A. Tavera Carrasco, and E. L. Perez-Cappe, "Unveiling the role of Mn-interstitial defect and particle size on the Jahn-Teller distortion of the LiMn2O4 cathode material," *J. Power Sources*, vol. 490, no. January, p. 229519, apr 2021. [Online]. Available: https://doi.org/10.1016/j.jpowsour.2021.229519https://linkinghub.elsevier.com/retrieve/pii/S0378775321000689

[258] M. Z. Bazant, "Theory of Chemical Kinetics and Charge Transfer based on Nonequilibrium Thermodynamics," *Acc. Chem. Res.*, vol. 46, no. 5, pp. 1144–1160, may 2013. [Online]. Available: http://pubs.acs.org/doi/abs/10.1021/ar300145c

[259] M. Tang, W. C. Carter, and Y.-M. Chiang, "Electrochemically Driven Phase Transitions in Insertion Electrodes for Lithium-Ion Batteries: Examples in Lithium Metal Phosphate Olivines," *Annu. Rev. Mater. Res.*, vol. 40, no. 1, pp. 501–529, jun 2010. [Online]. Available: https://www.annualreviews.org/doi/10.1146/annurev-matsci-070909-104435

[260] K. Iakoubovskii, K. Mitsuishi, Y. Nakayama, and K. Furuya, "Mean free path of inelastic electron scattering in elemental solids and oxides using transmission electron microscopy: Atomic number dependent oscillatory behavior," *Phys. Rev. B*, vol. 77, no. 10, p. 104102, mar 2008. [Online]. Available: https://link.aps.org/doi/10.1103/PhysRevB.77.104102

[261] R. Huang, Y. H. Ikuhara, T. Mizoguchi, S. D. Findlay, A. Kuwabara, C. A. J. Fisher, H. Moriwake, H. Oki, T. Hirayama, and Y. Ikuhara, "Oxygen-Vacancy Ordering at Surfaces of Lithium Manganese(III,IV) Oxide Spinel Nanoparticles," *Angew. Chemie Int. Ed.*, vol. 50, no. 13, pp. 3053–3057, mar 2011. [Online]. Available: http://doi.wiley.com/10.1002/anie.201004638

[262] M. Sugiyama, R. Oshima, and F. Eiichi Fujita, "Mechanism of FCC-FCT Thermoelastic Martensite Transformation in Fe-Pd Alloys," *Trans. Japan Inst. Met.*, vol. 27, no. 10, pp. 719–730, 1986. [Online]. Available: https://www.jim.or.jp/journal/e/pdf3/27/10/719.pdf

[263] G. Olson, H. Bhadeshia, and M. Cohen, "Coupled diffusional/displacive transformations," *Acta Metall.*, vol. 37, no. 2, pp. 381–390, feb 1989. [Online]. Available: https://linkinghub.elsevier.com/retrieve/pii/0001616089902228

[264] K. F. Hane and T. W. Shield, "Symmetry and microstructure in martensites," *Philos. Mag. A*, vol. 78, no. 6, pp. 1215–1252, dec 1998. [Online]. Available: http://www.tandfonline.com/doi/abs/10.1080/01418619808239984

[265] J. Bhattacharya and C. Wolverton, "Prediction of Quaternary Spinel Oxides as Li-Battery Cathodes: Cation Site Preference, Metal Mixing, Voltage and Phase Stability," *J. Electrochem. Soc.*, vol. 161, no. 9, pp. A1440–A1446, jun 2014. [Online]. Available: http://jes.ecsdl.org/cgi/doi/10.1149/2.0961409jes

[266] C. B. Carter, Z. Elgat, T. M. Shaw, C. B. Carter, and Z. Elgat, "Lateral twin boundaries in spinel," *Philos. Mag. A Phys. Condens. Matter, Struct. Defects Mech. Prop.*, vol. 55, no. 1, pp. 21–38, 1987.

[267] Y. Liu, T. Fujiwara, H. Yukawa, and M. Morinaga, "Chemical bonding in lithium intercalation compound LixMn2O4 (x=0,1,2)," *Electrochim. Acta*, vol. 46, no. 8, pp. 1151–1159, jan 2001. [Online]. Available: http://linkinghub.elsevier.com/retrieve/pii/S0013468600006927

[268] R. A. De Souza and E. C. Dickey, "The effect of space-charge formation on the grain-boundary energy of an ionic solid," *Philos. Trans. R. Soc. A Math. Phys. Eng. Sci.*, vol. 377, no. 2152, p. 20180430, aug 2019. [Online]. Available: https://royalsocietypublishing.org/doi/10.1098/rsta.2018.0430

[269] A. R. Genreith-Schriever, J. P. Parras, H. J. Heelweg, and R. A. De Souza, "The Intrinsic Structural Resistance of a Grain Boundary to Transverse Ionic Conduction," *ChemElectroChem*, vol. 7, no. 23, pp. 4694–4694, dec 2020. [Online]. Available: https://onlinelibrary.wiley.com/doi/10.1002/celc.202001357

[270] W.-W. Liu, D. Wang, Z. Wang, J. Deng, W.-M. Lau, and Y. Zhang, "Influence of magnetic ordering and Jahn–Teller distortion on the lithiation process of LiMn 2 O 4," *Phys. Chem. Chem. Phys.*, vol. 19, no. 9, pp. 6481–6486, 2017. [Online]. Available: http://xlink.rsc.org/?DOI=C6CP08324B

[271] M. Jayalakshmi, M. Mohan Rao, and F. Scholz, "Electrochemical Behavior of Solid Lithium Manganate (LiMn2O4) in Aqueous Neutral Electrolyte Solutions," *Langmuir*, vol. 19, no. 20, pp. 8403–8408, sep 2003. [Online]. Available: https://pubs.acs.org/doi/10.1021/la0340448

[272] Q. Xu, V. Kumar, T. de Kruijff, J. Jansen, and H. W. Zandbergen, "Preparation of TEM samples for hard ceramic powders," *Ultramicroscopy*, vol. 109, no. 1, pp. 8–13, dec 2008. [Online]. Available: http://linkinghub.elsevier.com/retrieve/pii/S0304399108001927http://www.sciencedirect.com/science/article/pii/S0304399108001927/pdfft?md5=945365e6ce1db95a3cd010bf3e7cce3a{&}pid=1-s2.0-S0304399108001927-main.pdf

B. Acknowledgements

First and foremost I want to thank Prof. Cynthia Volkert for the chance to work on this project and for the long support and many discussions during this endeavor. I also thank Prof. Michael Seibt for his willingness to take on the role of Co-referent and him and the rest of the TEM meeting for the critical input during many of our sessions. Many of those were collaborators in the CRC 1073, which strongly broadend my scientific horizon. A few of those absolutely need to be mentioned by name: Daniel, Marian and Vladimir provided valueable insights about all aspects of TEM during long conversations.

This work would have been the same or might not even exist if it weren't for the support of the Nano group not excluding all the former members - be it through their uplifting words or by providing a helping hand on many small occasions. Same applies to our great technicians at the institute, e.g. Volker, Tobi and Matthias, knowing things many a doctoral student can dream of!

It has been a pleasure to work with the partners of my project C05 over the time of those years Björn, Carsten, Florian and Max, who shared more coffees with me than I'd like to admit. The experience of sharing an office with so many totally different characters during my time at the IMP has been enlightening and I will miss many aspects of it at my new work. One of those aspects will be not having a fellow scout to revel in the experiences of my youth, Niklas.

The people that were absolutely irreplacable to the completion of this thesis on so many levels are Hendrik, Anja, Mona and the members of my family. Words cannot do their support justice!

To all those above, all those I didn't mention by name and also the reader that made it to this page: Thank you!